

UNIVERSITY OF SOUTHAMPTON
FACULTY OF NATURAL AND ENVIRONMENTAL SCIENCES
School of Chemistry

**Energy decomposition analysis for large-scale first principles quantum
mechanical simulations of biomolecules**

by

Maximillian J. S. Phipps

Thesis for the degree of Doctor of Philosophy

January 2017

UNIVERSITY OF SOUTHAMPTON

ABSTRACT

FACULTY OF NATURAL AND ENVIRONMENTAL SCIENCES

School of Chemistry

Doctor of Philosophy

ENERGY DECOMPOSITION ANALYSIS FOR LARGE-SCALE FIRST
PRINCIPLES QUANTUM MECHANICAL SIMULATIONS OF BIOMOLECULES

by Maximillian J. S. Phipps

Kohn-Sham density functional theory (DFT) is an extraordinarily powerful and versatile tool for calculating the properties of materials. In its conventional form, this approach scales cubically with the size of the system under study. This scaling becomes prohibitive when investigating larger arrangements such as biomolecules and nanostructures. More recently linear-scaling approaches have been developed that overcome this limitation, allowing calculations to be performed on systems many thousands of atoms in size. An example of such an approach is the ONETEP code which uses a plane wave-like basis set and is based upon the use of spherically-localised orbitals.

A simple yet common calculation performed using ab initio codes is the total (ground state) energy calculation. By comparing the energy of isolated parts of a system to the energy of the combined system, we are able to obtain the energy of interaction. This quantity is useful as it provides a relative measure of the enthalpic stability of an interaction which can be compared to other systems. Equally, however, this quantity gives little indication of the driving forces that lead to the interaction energy we observe.

A number of approaches have been developed that aim to identify these driving forces. Energy decomposition analysis (EDA) refers to the set of methods that decompose the interaction energy into physically relevant energy components which add to the full interaction energy. Few studies have applied EDA approaches to larger systems in the thousand-atom regime, with the vast majority of investigations focussing on small system studies (less than 100 atoms in size). These methods have shown varying degrees of success.

In this work, we have evaluated the suitability of a selection of popular EDA methods in decomposing the interaction energies of small biomolecule-like systems. Based on the results of this review, we developed a linear-scaling EDA approach in the ONETEP code that separates the intermolecular interaction energy into chemically distinct components (electrostatic, exchange, correlation, Pauli repulsion, polarisation, and charge transfer). The intermediate state used to calculate polarisation, also known as the absolutely localised molecular orbital (ALMO) state, has the key advantage of being fully antisymmetric and variationally optimised. The linear-scaling capability of the scheme is based on use of an adaptive purification approach and sparse matrix equations. We demonstrate the accuracy of this approach in reproducing the energy component values of its Gaussian basis counterparts, and present a remedy to the limitation of polarisation and charge transfer basis set dependence that is based on the property of strict localisation of the ONETEP orbitals. Additionally, we show the method to have mild exchange-correlation functional and atomic coordinate dependence.

We have demonstrated the high value of our method by applying it to the thrombin protein interacting with a number of small binders. Here, we used our scheme in combination with electron density difference (EDD) plots to identify the key protein and ligand regions that contribute to polarisation and charge transfer. In our studies, we assessed convergence of the EDA components with protein truncation up to a total system size of 4975 atoms. Additionally, we applied our EDA to binders that had been partitioned into smaller fragments. Here, we accurately quantified the bonding contributions of key ligand moieties with particular regions of the protein cavity. We assessed how accurately the ligand binding components are reproduced by the fragment contributions using an additivity measure. Using this measure, we showed the fragment binding components to add up to the full ligand binding component with overall minimal additivity error. We also investigated the energy components of a series of small thrombin S1 pocket binders all less than 30 atoms in size. In this study, we demonstrate the EDA and EDD plots as tools for understanding the relative importance of different binder structural features and positionings within the pocket.

Overall, we show our EDA method to be a stable and powerful approach for the analysis of interaction energies in systems of large size. The application of this method is not limited to biomolecular studies, and we expect that this approach can be readily applied to analyses within other fields, for example materials, catalysts, and nanostructures.

Contents

Declaration of Authorship	xix
Acknowledgements	xxi
Abbreviations	xxiii
Introduction	1
Thesis outline	2
List of related publications	5
1 Quantum mechanical principles	7
1.1 The wavefunction	7
1.2 The Schrödinger equation	8
1.3 The Born-Oppenheimer approximation	10
1.4 Antisymmetry of the wavefunction and the Pauli exclusion principle	11
1.5 The variational principle	12
1.6 The Hartree-Fock equations	14
2 Density functional theory	21
2.1 The Hohenberg-Kohn theorems	23
2.1.1 Theorem 1	23
2.1.2 Theorem 2	24
2.2 The Kohn-Sham equations	25
2.3 The exchange-correlation functional	28
2.4 Basis sets	30
2.4.1 Slater-type orbitals	31
2.4.2 Gaussian-type orbitals	31
2.4.3 Plane waves	32
2.5 Basis set superposition error	33
2.6 Core electrons	34
2.7 Linear-scaling density functional theory	36
2.7.1 The near-sightedness of electronic matter	36
2.7.2 Localised orbitals	37
2.7.3 The Li-Nunes and Vanderbilt method	38
2.8 The ONETEP package	38
2.8.1 The non-orthogonal generalised Wannier function basis set .	39
2.8.2 The ONETEP Kohn-Sham energy expression	42

2.8.3	Inner loop optimisation: the density kernel	43
2.8.4	Outer loop optimisation: the NGWFs	45
3	Current biomolecular energy decomposition analysis approaches	49
3.1	Previous applications of energy decomposition analysis	50
3.2	Common EDA wavefunctions	53
3.3	Common EDA charge densities	55
3.4	Kitaura-Morokuma EDA	56
3.4.1	Kitaura-Morokuma EDA theory	56
3.4.2	The extended transition state approach	61
3.4.3	Assessment	62
3.5	Reduced variational space EDA	64
3.5.1	Reduced variational space EDA theory	64
3.5.2	Assessment	68
3.6	Pair interaction EDA	68
3.6.1	The fragment molecular orbital and the pair interaction energy	69
3.6.2	Pair interaction EDA theory	72
3.6.3	Assessment	73
3.7	Absolutely localised molecular orbital EDA and block-localised wave- function EDA	74
3.7.1	The absolutely localised molecular orbital and block-localised wavefunction	74
3.7.2	Absolutely localised molecular orbital and block-localised wavefunction EDA theory	75
3.7.3	Assessment	78
3.8	Natural EDA	80
3.8.1	The natural bond orbital basis set	80
3.8.2	The five-term natural EDA theory	82
3.8.3	The self polarisation energy term and the three-term natural EDA	86
3.8.4	Assessment	88
3.9	Symmetry-adapted perturbation theory	89
3.9.1	SAPT theory	89
3.9.2	SAPT treatment of polarisation and charge transfer	92
3.9.3	Assessment	93
3.10	Natural bond orbital second-order perturbation theory analysis . .	94
4	An evaluation of current biomolecular energy decomposition anal- ysis approaches	95
4.1	Calculations	96
4.2	Analysis	99
4.2.1	Test Set 1: Hydrogen bonding interactions	104
4.2.2	Test Set 2: Water-cations	108
4.2.3	Test Set 3: Ammonium- π systems	110
4.2.4	Test Set 4: π -cations	111
4.2.5	Test Set 5: π interacting systems	113

4.2.6	Test Set 6: Halogenated systems	115
4.2.7	Dispersion energy treatments	118
4.2.8	Observed EDA scheme advantages and weaknesses	124
4.3	Summary	129
5	The ONETEP energy decomposition analysis	133
5.1	ONETEP EDA theory	134
5.1.1	The localised and absolutely localised energy decomposition analyses	135
5.1.1.1	The absolutely localised energy decomposition analysis	135
5.1.1.2	The frozen density analysis	137
5.1.2	Self-consistent field theory for molecular interactions	139
5.1.2.1	Overview of the Stoll SCF-MI equations	139
5.1.2.2	Derivation of the Stoll SCF-MI equations	140
5.1.3	Construction of the frozen density kernels	144
5.1.4	The polarisation component	146
5.1.5	Calculation of the polarised density kernel	146
5.1.5.1	Inner loop optimisation: the density kernel	147
5.1.5.2	Outer loop optimisation: the NGWFs	150
5.1.6	The charge transfer component	151
5.1.7	Parallelisation and numerical eigensolvers	151
5.1.8	Linear scaling reformulation of the EDA	153
5.1.8.1	Reformulation of the Stoll SCF-MI	153
5.1.8.2	The adaptive McWeeny purification transformation	155
5.1.8.3	The lambda function	159
5.2	Electron density difference plots	160
5.3	Results and discussion	160
5.3.1	Validation	160
5.3.1.1	Calculations	161
5.3.1.2	Analysis	164
5.3.2	Basis set dependence	169
5.3.2.1	Calculations	170
5.3.2.2	Analysis	170
5.3.3	Exchange-correlation functional dependence	172
5.3.3.1	Calculations	172
5.3.3.2	Analysis	173
5.3.4	Atomic coordinate dependence	174
5.3.4.1	Calculations	175
5.3.4.2	Analysis	176
5.3.5	Electron density difference water trimer test example	178
5.3.5.1	Calculations	179
5.3.5.2	Analysis	179
6	Applications of the ONETEP energy decomposition analysis	185
6.1	Thrombin - C24	186

6.1.1	Calculations	186
6.1.2	Analysis	188
6.2	Thrombin - small fragmented binders	195
6.2.1	Calculations	195
6.2.2	Analysis: ligand fragmentations	197
6.2.2.1	Frozen density component	198
6.2.2.2	Polarisation, charge transfer and dispersion	204
6.2.3	Analysis: S1 pocket binders	211
6.2.3.1	5AFY and 5AHG	213
6.2.3.2	4UD9 and 5AFY	216
6.2.3.3	4UD9 and 5AF9	220
6.2.3.4	4UEH and 4UE7	223
7	Conclusions	229
7.1	Future work	231
	Appendices	235
A	EDA benchmarking tests	237
B	EDA validation tests	247
C	Thrombin - C24 ligand EDA	251
D	Thrombin - fragment binder EDA	253
	References	257

List of Figures

1.1	A representation of the relative energy of H_2 during dissociation when calculated using the RHF and UHF approximations.	19
2.1	A one-dimensional representation of the $D_0(\mathbf{r})$ psinc function centered at 0, with 15 grid points in the cell dimension.	40
3.1	The Kitaura–Morokuma electrostatics, exchange and polarisation EDA components for the AB complex.	58
3.2	The partitioning of the Fock and overlap matrices for the KM EDA scheme for the evaluation of the charge transfer component. The set of matrices (a) that involve only the diagonal exchange and electrostatics interactions produces the energy E^{ESX} and the set of matrices (b) that involve these diagonal blocks and also the charge transfer blocks produces the energy $E^{\text{ESX+CT}}$. The labels ‘ <i>occ</i> ’ and ‘ <i>vir</i> ’ denote the sets of orbitals that are occupied and virtual on the monomers A and B	59
3.3	The treatment of BSSE for the exchange term within the KM EDA scheme. A BSSE correction due to the presence of the occupied orbitals of adjacent monomers is introduced to the exchange term. .	60
3.4	The treatment of BSSE for the charge transfer term within the KM EDA scheme. A BSSE correction due to the presence of the virtual orbitals of adjacent monomers is introduced to the charge transfer term.	61
3.5	The ALMO EDA and BLW EDA scheme for a complex AB	78
3.6	The treatment of charge transfer within the ALMO EDA and BLW EDA schemes. The (positive) BSSE is introduced to the charge transfer term because both BSSE and charge transfer are effects resulting from the delocalisation of monomer MOs, caused by including basis functions from the neighbouring fragments.	79
3.7	The partitioning of the NBO Fock matrix for the AB complex involved in the construction of the $n_{AB}^{\text{loc},AB}(\mathbf{r})$ charge density. Delocalising interactions described by the hashed blocks of the Fock matrix are not included in this charge density construction, where the labels ‘ <i>occ</i> ’ and ‘ <i>vir</i> ’ denote the sets of orbitals that are occupied and virtual on the monomers A and B	84
3.8	The evaluation of ΔE_{DEF} for a complex AB . Non-classical effects of polarisation are captured within the ΔE_{DEF} component along with intrafragmental electrostatic energy effects.	85

3.9	The evaluation of self energy component for a monomer A in the field of monomer B . This component is a portion of the deformation component that is electrical in origin, with the remainder of the deformation component resulting from Pauli repulsion contributions.	87
3.10	The NEDA scheme for a complex AB .	89
4.1	Converged EDA component values (in kcal/mol) of the test sets 1 and 2. The results of test set 1 are given by plots (a), (c), (e), (g) and (i), and test set 2 by plots (b), (d), (f), (h) and (j). The EDA results of the electrostatic components are shown within plots (a) and (b), the exchange/exchange–correlation components within plots (c) and (d), the Heitler–London interaction components within plots (e) and (f), the polarisation components within plots (g) and (h), and the charge transfer components within plots (i) and (j). The NEDA polarisation energies corrected with self energy term are given by POL+SE within plots (g) and (h). The green bars of the polarisation and charge transfer plots (g)–(j) represent the SAPT(KS) contributions, where the non–hashed bars represent the electrostatic contribution of this term only and where the hashed bars also include exchange in this term. The full BLYP–D3/6-311G* level interaction energy ΔE is given within plots (a) and (b).	101
4.2	Converged EDA component values (in kcal/mol) of the test sets 3 and 4. The results of test set 3 are given by plots (a), (c), (e), (g) and (i), and test set 4 by plots (b), (d), (f), (h) and (j). The EDA results of the electrostatic components are shown within plots (a) and (b), the exchange/exchange–correlation components within plots (c) and (d), the Heitler–London interaction components within plots (e) and (f), the polarisation components within plots (g) and (h), and the charge transfer components within plots (i) and (j). The NEDA polarisation energies corrected with self energy term are given by POL+SE within plots (g) and (h). The green bars of the polarisation and charge transfer plots (g)–(j) represent the SAPT(KS) contributions, where the non–hashed bars represent the electrostatic contribution of this term only and where the hashed bars also include exchange in this term. The full BLYP–D3/6-311G* level interaction energy ΔE is given within plots (a) and (b).	102

- 4.3 Converged EDA component values (in kcal/mol) of the test sets 5 and 6. The results of test set 5 are given by plots (a), (c), (e), (g) and (i), and test set 6 by plots (b), (d), (f), (h) and (j). ‘Bz Bz (p-displaced)’ represents the parallel displaced benzene dimer. The EDA results of the electrostatic components are shown within plots (a) and (b), the exchange/exchange–correlation components within plots (c) and (d), the Heitler–London interaction components within plots (e) and (f), the polarisation components within plots (g) and (h), and the charge transfer components within plots (i) and (j). The NEDA polarisation energies corrected with self energy term are given by POL+SE within plots (g) and (h). The green bars of the polarisation and charge transfer plots (g)–(j) represent the SAPT(KS) contributions, where the non–hashed bars represent the electrostatic contribution of this term only and where the hashed bars also include exchange in this term. The full BLYP–D3/6-311G* level interaction energy ΔE is given within plots (a) and (b). 103
- 4.4 The –D3 correction for dispersion (blue), and SAPT(KS) dispersion (green) energy values (in kcal/mol). The energy values for test sets 1–6 are given by plots (a)–(f) respectively. ‘Bz Bz (p-displaced)’ represents the parallel displaced benzene dimer. The non–hashed green bar represents the electrostatic contribution of dispersion only and the hashed bar represents the exchange plus electrostatic contribution of this term. 119
- 5.1 A diagrammatic representation of the quantities involved in the construction of the frozen density kernel $K_{\text{orth}}^{A\alpha,B\beta}$ for a system comprising of two fragments ‘frag1’ and ‘frag2’. Empty matrix sub-blocks represent zero blocks, and sub-blocks containing dots represent non-zero blocks. The diagonal intrafragmental MO overlap sub-blocks of $\sigma_{Ai,Bj}$ are identity due to orthonormality of the KS states within fragments, and non-zero for the sub-blocks representing interfragment MO overlaps due to lack of orthonormality. 146
- 5.2 The modified kernel of a system comprising three fragments {X,Y,Z}, where the index A of $K_{\text{orth,col}(A)}^{B\beta,C\gamma}$ is set to fragment X. The shaded blocks are set to zero, with the non-shaded blocks equal to the relevant blocks of the (full supermolecule, orthogonalised MO) kernel $K_{\text{orth}}^{B\beta,A\alpha}$ 154
- 5.3 The standard McWeeny purification transformation mapping of the unpurified to purified eigenvalues of the density kernel (orbital occupancies). The lower and upper orbital occupancy bounds $\left[\frac{1-\sqrt{3}}{2}\right], \left[\frac{1+\sqrt{3}}{2}\right]$ that ensure stability of the transformation with respect to flipping is shown by the blue vertical lines. 156

5.4	The steepest descent step length λ for various extremal orbital occupancies f . The step length is set to 0.5 (red) when in the occupancy interval that guarantees preservation of occupancy number $(\left[\frac{1-\sqrt{3}}{2}\right], \left[\frac{1+\sqrt{3}}{2}\right])$. When outside of this interval, the step length is determined analytically (blue) using Eq. 5.69. The overall value of λ is given by the solid black line.	158
5.5	Frozen density analysis energy components for test sets 1 and 2. EDA component values are given in kcal/mol and were calculated with the PBE-D2 functional. ONETEP EDA calculations (yellow) were performed with a psinc basis set with a kinetic energy cutoff of 1200 eV. Q-CHEM ALMO EDA calculations (blue) and GAMESS-US LMO EDA calculations (green) were performed with an aug-cc-pVTZ Gaussian basis set. The ALMO frozen density component is the sum of the electrostatic, exchange, Pauli-repulsion and correlation energy components as shown in Eq. 5.6	165
5.6	EDA energy components for test sets 1 and 2. EDA component values are given in kcal/mol and were calculated with the PBE-D2 functional. ONETEP EDA calculations (yellow) were performed with a psinc basis set with a kinetic energy cutoff of 1200 eV. Q-CHEM ALMO EDA calculations (blue) were performed with an aug-cc-pVTZ Gaussian basis set. Values of Grimme's -D2 correction for dispersion are also provided (grey).	166
5.7	The ONETEP (6 Bohr to 9 Bohr NGWF radii) and ALMO (aug-cc-pVDZ to aug-cc-pV5Z) EDA of PBE-D2/aug-cc-pVTZ geometry optimised (a) water dimer, (b) methanol - methanol, and (c) benzene - ammonium systems. The PBE/1200 eV level ΔE (green) is partitioned into the frozen density (blue), polarisation (red), and charge transfer (yellow) energy components as described in Eq. 5.2. The -D2 correction for dispersion of Grimme is independent of basis set size and so was not included for clarity.	171
5.8	Superposition of the optimised 1G30 systems used to quantify atomic coordinate sensitivity.	176
5.9	The (a) UUU and (b) UUU _{rot} water trimer test systems. Hydrogen bonding extends throughout the system in the case of the UUU system, but is broken between the lower water molecules in the case of the UUU _{rot} system.	180
5.10	Polarisation EDD plots of the (a) UUU and (b) UUU _{rot} water trimer test systems calculated using the PBE exchange-correlation functional with an 800 eV psinc basis set cutoff energy and 8 Bohr NGWF radii. The isosurface contour levels are displayed at 0.01 electrons per cubic Angstrom with green surfaces representing electron gain and magenta surfaces representing electron loss	182
5.11	Polarisation EDD plots of the (a) UUU and (b) UUU _{rot} water trimer test systems calculated using the PBE exchange-correlation functional with an 800 eV psinc basis set cutoff energy and 8 Bohr NGWF radii. The isosurface contour levels are displayed at 0.01 electrons per cubic Angstrom with green surfaces representing electron gain and magenta surfaces representing electron loss	183

6.1	The C24 ligand (pdb:1KTS).	187
6.2	The binding pocket of the untruncated (4975 atom) protein system. The C24 ligand has been highlighted in orange.	188
6.3	Frozen density analysis of the thrombin-C24 complexes calculated at the PBE-D2/800 eV level of theory (component values are given in kcal/mol). Error of the energy components is shown with re- spect to the full, untruncated (4975 atom) protein system. The frozen density component is formally equivalent to adding the elec- trostatic, exchange, Pauli-repulsion and correlation energy compo- nents as shown in Eq. 5.6	189
6.4	EDA components of the thrombin-C24 complexes calculated at the PBE-D2/800 eV level of theory (component values are given in kcal/mol). Error of the energy components is shown with respect to the full, untruncated (4975 atom) protein system. The full inter- action energy ΔE is equivalent to adding the frozen density com- ponent, polarisation, charge transfer, and Grimme -D2 dispersion energy components.	190
6.5	EDD plots of polarisation for the (a) 3Å system and (b) untrun- cated system. The isosurface contour levels are displayed at 0.0175 electrons per cubic Angstrom with green surfaces representing elec- tron gain and magenta surfaces representing electron loss. The C24 ligand has been highlighted in orange. The EDD plots show the contributions of functional groups to polarisation and charge trans- fer.	192
6.6	EDD plots of charge transfer for the (a) 3Å system, and (b) untrun- cated system. The isosurface contour levels are displayed at 0.0175 electrons per cubic Angstrom with green surfaces representing elec- tron gain and magenta surfaces representing electron loss. The C24 ligand has been highlighted in orange. The EDD plots show the contributions of functional groups to polarisation and charge trans- fer.	193
6.7	The ligand fragmentation scheme for the 4UDW, 2ZGX, and 5AFZ ligands. The bond partitions of the ligands are shown by the dashed blue lines, with each fragment produced capped with a hydrogen atom. The F1, F2, and F3 ligands refer to the fragment indexes 1, 2, and 3.	198
6.8	Frozen density analysis of the fragmented 4UDW, 2ZGX, and 5AFZ complexes calculated at the PBE-D2/800 eV level of theory (com- ponent values are given in kcal/mol). F1, F2, and F3 refer to the fragments that compose the full reference ligand. For each energy component, the fragmentation error equals the sum of the fragment contributions subtracted from the contribution of the full reference ligand (Eq. 6.2).	200

6.9	EDA components of the fragmented 4UDW, 2ZGX, and 5AFZ complexes calculated at the PBE-D2/800 eV level of theory (component values are given in kcal/mol). D2 refers to the dispersion energy correction of Grimme. F1, F2, and F3 refer to the fragments that compose the full reference ligand. For each energy component, the fragmentation error equals the sum of the fragment contributions subtracted from the contribution of the full reference ligand (Eq. 6.2). The total ΔE in combination with the cost of ligand desolvation ΔE_{desolv} is also shown.	201
6.10	Superposition of the 4UDW and 2ZGX F2 fragments.	202
6.11	EDD plots of (a) polarisation and (b) charge transfer for the 4UDW system. The isosurface contour levels are displayed at 0.025 electrons per cubic Angstrom with green surfaces representing electron gain and magenta surfaces representing electron loss. The ligand of the 4UDW system has been highlighted in orange.	205
6.12	EDD plots of (a) polarisation and (b) charge transfer for the 2ZGX system. The isosurface contour levels are displayed at 0.025 electrons per cubic Angstrom with green surfaces representing electron gain and magenta surfaces representing electron loss. The ligand of the 2ZGX system has been highlighted in orange.	206
6.13	EDD plots of (a) polarisation and (b) charge transfer for the 5AFZ system. The isosurface contour levels are displayed at 0.025 electrons per cubic Angstrom with green surfaces representing electron gain and magenta surfaces representing electron loss. The ligand of the 5AFZ system has been highlighted in orange.	207
6.14	EDD plots of (a) polarisation and (b) charge transfer for the F2 fragment region of 4UDW with Ser214. The isosurface contour levels are displayed at 0.025 electrons per cubic Angstrom with green surfaces representing electron gain and magenta surfaces representing electron loss. The ligand of the 4UDW system has been highlighted in orange.	208
6.15	EDD plots of (a) polarisation and (b) charge transfer for the 5AFZ system F3 fragment interaction with thrombin. The isosurface contour levels are displayed at 0.015 electrons per cubic Angstrom with green surfaces representing electron gain and magenta surfaces representing electron loss. The ligand of the 5AFZ system has been highlighted in orange.	209
6.16	Frozen density analysis of the fragmented thrombin S1 pocket complexes calculated at the PBE-D2/800 eV level of theory (component values are given in kcal/mol).	214
6.17	EDA components of the fragmented thrombin S1 pocket complexes calculated at the PBE-D2/800 eV level of theory (component values are given in kcal/mol). D2 refers to the dispersion energy correction of Grimme. The total ΔE in combination with the cost of ligand desolvation ΔE_{desolv} is also shown.	215

6.18	EDD plots of (a) polarisation and (b) charge transfer for the 5AFY system. The isosurface contour levels are displayed at 0.025 electrons per cubic Angstrom with green surfaces representing electron gain and magenta surfaces representing electron loss. The ligand of the 5AFY system has been highlighted in orange.	217
6.19	EDD plots of (a) polarisation and (b) charge transfer for the 5AHG system. The isosurface contour levels are displayed at 0.025 electrons per cubic Angstrom with green surfaces representing electron gain and magenta surfaces representing electron loss. The ligand of the 5AHG system has been highlighted in orange.	218
6.20	EDD plots of (a) polarisation and (b) charge transfer for the 4UD9 system. The isosurface contour levels are displayed at 0.025 electrons per cubic Angstrom with green surfaces representing electron gain and magenta surfaces representing electron loss. The ligand of the 4UD9 system has been highlighted in orange.	221
6.21	EDD plots of (a) polarisation and (b) charge transfer for the 5AF9 system. The isosurface contour levels are displayed at 0.025 electrons per cubic Angstrom with green surfaces representing electron gain and magenta surfaces representing electron loss. The ligand of the 5AF9 system has been highlighted in orange.	222
6.22	EDD plots of (a) polarisation and (b) charge transfer for the 4UEH system. The isosurface contour levels are displayed at 0.025 electrons per cubic Angstrom with green surfaces representing electron gain and magenta surfaces representing electron loss. The ligand of the 4UEH system has been highlighted in orange.	226
6.23	EDD plots of (a) polarisation and (b) charge transfer for the 4UE7 system. The isosurface contour levels are displayed at 0.025 electrons per cubic Angstrom with green surfaces representing electron gain and magenta surfaces representing electron loss. The ligand of the 4UE7 system has been highlighted in orange.	227

List of Tables

4.1	Test set 1 (hydrogen bonding interactions) BLYP-D3/6-311G* geometry optimised systems for EDA (intermolecular distances are given in Å)	97
4.2	Test set 2 (water-cations) BLYP-D3/6-311G* geometry optimised systems for EDA (intermolecular distances are given in Å)	98
4.3	Test set 3 (ammonium- π systems) BLYP-D3/6-311G* geometry optimised systems for EDA (intermolecular distances are given in Å)	99
4.4	Test set 4 (π -cations) BLYP-D3/6-311G* geometry optimised systems for EDA (intermolecular distances are given in Å)	100
4.5	Test set 5 (π interacting systems) BLYP-D3/6-311G* geometry optimised systems for EDA (intermolecular distances are given in Å)	104
4.6	Test set 6 (halogenated systems) BLYP-D3/6-311G* geometry optimised systems for EDA (intermolecular distances are given in Å)	105
4.7	A summary of the EDA approaches investigated	125
5.1	Test set 1 of PBE-D2/aug-cc-pVTZ geometry optimised systems for EDA (intermolecular distances are given in Å)	162
5.2	Test set 2 of PBE-D2/aug-cc-pVTZ geometry optimised systems for EDA (intermolecular distances are given in Å)	163
5.3	The water - ammonium ONETEP EDA energy components using a 1200eV basis set kinetic energy cutoff.	173
5.4	The benzene - dimethylacetamide (DMA) ONETEP EDA energy components using a 1200eV basis set kinetic energy cutoff.	173
5.5	The PBE-D2/800eV ONETEP EDA energy components and errors for the 1G30 optimised systems used to quantify atomic coordinate sensitivity.	177
5.6	The water trimer ONETEP EDA energy components using a 800eV basis set kinetic energy cutoff.	179
6.1	A summary of the fragments of the thrombin-C24 complexes used in the ONETEP EDA, where ‘ ∞ ’ refers to the full, untruncated protein (charges given in parenthesis).	187
6.2	Small fragment binders of the thrombin S1 pocket for EDA.	212
A.1	The BLYP/6-311G* level ALMO EDA and NEDA results performed on the BLYP-D3/6-311G* optimised geometries of test sets 1 and 2.	238
A.2	The BLYP/6-311G* level DCBS and MCBS SAPT(KS) results performed on the BLYP-D3/6-311G* optimised geometries of test sets 1 and 2.	239

A.3	The HF/6-311G* level KM EDA and RVS EDA results performed on the BLYP-D3/6-311G* optimised geometries of test sets 1 and 2.	240
A.4	The BLYP/6-311G* level ALMO EDA and NEDA results performed on the BLYP-D3/6-311G* optimised geometries of test sets 3 and 4.	241
A.5	The BLYP/6-311G* level DCBS and MCBS SAPT(KS) results performed on the BLYP-D3/6-311G* optimised geometries of test sets 3 and 4.	242
A.6	The HF/6-311G* level KM EDA and RVS EDA results performed on the BLYP-D3/6-311G* optimised geometries of test sets 3 and 4.	243
A.7	The BLYP/6-311G* level ALMO EDA and NEDA results performed on the BLYP-D3/6-311G* optimised geometries of test sets 5 and 6.	244
A.8	The BLYP/6-311G* level DCBS and MCBS SAPT(KS) results performed on the BLYP-D3/6-311G* optimised geometries of test sets 5 and 6.	245
A.9	The HF/6-311G* level KM EDA and RVS EDA results performed on the BLYP-D3/6-311G* optimised geometries of test sets 5 and 6.	246
B.1	The ALMO, LMO and ONETEP EDA energy components for the PBE-D2/aug-cc-pVTZ optimised systems of Test Set 1.	248
B.2	The ALMO, LMO and ONETEP EDA energy components for the PBE-D2/aug-cc-pVTZ optimised systems of Test Set 2.	249
C.1	The PBE-D2/800eV ONETEP EDA energy components of the thrombin-C24 systems.	251
D.1	The PBE-D2/800eV ONETEP EDA energy components of the full and fragmented thrombin-ligand systems 4UDW, 2ZGX and 5AFZ.	254
D.2	The PBE-D2/800eV ONETEP EDA energy components of the thrombin S1 pocket binder systems 4UD9, 5AFY, 5AHG, 5AF9, 4UEH, and 4UE7.	255

Declaration of Authorship

I, **Maximillian J. S. Phipps**, declare that the thesis entitled *Energy decomposition analysis for large-scale first principles quantum mechanical simulations of biomolecules* and the work presented in the thesis are both my own, and have been generated by me as the result of my own original research. I confirm that:

- this work was done wholly or mainly while in candidature for a research degree at this University;
- where any part of this thesis has previously been submitted for a degree or any other qualification at this University or any other institution, this has been clearly stated;
- where I have consulted the published work of others, this is always clearly attributed;
- where I have quoted from the work of others, the source is always given. With the exception of such quotations, this thesis is entirely my own work;
- I have acknowledged all main sources of help;
- where the thesis is based on work done by myself jointly with others, I have made clear exactly what was done by others and what I have contributed myself;
- parts of this work have been published as:
 - Energy decomposition analysis approaches and their evaluation on prototypical protein-drug interaction patterns. Phipps, M. J. S., Fox, T., Tautermann, C. S., and Skylaris, C.-K. *Chem. Soc. Rev.*, **44**, 3177–3211 (2015).
 - Energy decomposition analysis based on absolutely localised molecular orbitals for large-scale density functional theory calculations in drug design. Phipps, M. J. S., Fox, T., Tautermann, C. S., and Skylaris, C.-K. *J. Chem. Theory Comp.*, **12**, 3135–3148 (2016).

Signed:.....

Date:.....

Acknowledgements

The past years that I have spent at the University of Southampton have been a thoroughly enjoyable time, both academically and socially. I am grateful for the support I have received during this time, without which this work would likely not have been possible.

Firstly, I would like to thank my supervisor, Chris-Kriton Skylaris, for the stimulating and insightful discussions we have shared and the support he has provided. I would also like to thank the BBSRC and Boehringer Ingelheim for an industrial CASE PhD studentship (BBSRC Grant reference: BB/I015922/1). The practical insight provided over the past few years by my industrial sponsors at Boehringer Ingelheim, Thomas Fox and Christofer Tautermann, has been invaluable in translating theory into productive application.

The friendly people I have had the fortune to meet here in Southampton have also made this time particularly cherished. Unquestionably, the members of the Skylaris group current and past, Alberto Zoccante, Álvaro Serrano, Ben Lowe, Chris Cave-Ayland, Chris Pittock, Chris Sampson, Frank Longford, Gabriele Boschetto, Jacek Dziedzic, James Womack, Joly Aarons, Karl Wilkinson, Lucas Verga, Peter Cherry, Stephen Fox, Tom Ellaby, Valerio Vitale and Hongtao Xue have made a memorable mark on how I will remember my time spent here.

Lastly, but most importantly, I also wish to thank my family for their endless support during my time producing this work.

Abbreviations

ALMO	Absolutely localised molecular orbital
AO	Atomic orbital
BLW	Block-localised wavefunction
BSSE	Basis set superposition error
CI	Configuration interaction
CP	Counterpoise
CSOV	Constrained space orbital variation
CT	Charge transfer
DCBS	Dimer-centered basis set
DFT	Density functional theory
DMA	Dimethylacetamide
EDA	Energy decomposition analysis
EDD	Electron density difference
ETS	Extended transition state
FMO	Fragment molecular orbital
HF	Hartree-Fock
KM	Kitaura-Morokuma
KS	Kohn-Sham
LMO	Localised molecular orbital
MAD	Mean absolute deviation
MCBS	Monomer-centered basis set
MCSCF	Multi-configurational self-consistent field
MM	Molecular mechanics
MO	Molecular orbital
MP2	Second-order Møller-Plesset perturbation theory
NAO	Natural atomic orbital
NBO	Natural bond orbital
NEDA	Natural EDA
NGWF	Nonorthogonal generalized Wannier functions
PIEDA	Pair interaction energy decomposition analysis
PIE	Pair interaction energy

QM	Quantum mechanical
QTAIM	Quantum theory of atoms in molecules
RHF	Restricted HF
ROHF	Restricted open shell HF
RVS	Reduced variational space
SAPT	Symmetry-adapted perturbation theory
SCF MI	SCF for molecular interactions
SCF	Self-consistent field
UHF	Unrestricted open shell HF

Introduction

Intermolecular interactions are key in the formation of many systems of interest, determining the overall structure and properties of materials [1; 2]. Many fields of science benefit from the insights gained studying these interactions, for example biomolecular [3; 4] and supramolecular chemistry [5; 6], as well as condensed matter physics [7; 8]. Understanding the chemical phenomena that give rise to these interactions (e.g. electrostatics, polarisation and charge transfer) would be of great value to such investigations, providing key insight into the driving forces of binding. Unfortunately, these quantities are not accessible by physical experimentation alone. With the development of first principles methods however, the opportunity to calculate these quantities using *in silico* methods has arisen.

Energy decomposition analysis (EDA) is a valuable analytical tool that partitions the intermolecular interaction energy into energy components of chemical interest, typically electrostatic, exchange, correlation, Pauli repulsion, polarisation, and charge transfer contributions. Applying such a separation of the intermolecular interaction energy is not without complication and there is not a single, universal approach by which this separation is applied. As such, a high degree of diversity [9–18] exists in the EDA schemes described within literature. With such diversity, the EDA schemes may also display greater strengths to particular applications, for example transition metal and halogen bonding [19–22] or forcefield development [23–25].

In this work, we have sought to investigate the strengths and weaknesses of the

popular EDA approaches presented in literature, in particular focussing our studies on the application of EDA to biomolecular systems. Biomolecular systems are often very large (e.g. proteins) and therefore difficult to calculate using conventional density functional theory (DFT) approaches which typically scale cubically with system size. To overcome this limitation, we have developed a new EDA scheme capable of analysing interaction energies of systems many thousands of atoms in size which we have implemented within the linear-scaling ONETEP DFT package. We have demonstrated the high value of our method by applying it to a wide range of systems including a thrombin protein system 4975 atoms in size. We also demonstrate the high level of information obtained using electron density difference (EDD) plots which show the key charge redistributions that occur during polarisation and charge transfer. This work has provided a new EDA method which we expect to be highly valuable not only in the field of drug design, but also in the wider scientific disciplines such as materials science (e.g. studies of catalysts, polymers, and nanostructures).

A chapter-by-chapter outline of the work contained in this thesis now follows.

Thesis outline

This Ph.D. thesis is arranged as eight chapters. In Chapters 1 and 2, we outline the theories and approximations of quantum mechanics upon which this work is based. Specifically, we introduce the theories of quantum mechanics used to develop the theories of ab initio calculations in Chapter 1, and further detail the DFT framework and linear-scaling ONETEP approach in Chapter 2.

Following this, in Chapter 3 we present an overview of the popular EDA approaches in literature which we consider to show high relevance for biomolecular studies. Here, we present the theory of these methods using a common framework of shared quantities which allows for their simple comparison.

We have sought to investigate the strengths and weaknesses of the EDA approaches for biomolecular studies in Chapter 4. We attempt to comprehensively assess the schemes by benchmarking against six test sets of systems. These test sets are composed of pairs of small molecules that display a variety of biomolecule-like interactions, such as π - π stacking and dispersion interactions. Here, we also consider the various treatments for dispersion which may be used alongside the EDA approaches.

In Chapter 5 we introduce our EDA approach which has been implemented within the ONETEP code. Here, we also present our extension based on adaptive purification that results in the computational cost of this method scaling linearly with system size. Our EDA scheme is validated against its Gaussian basis set EDA counterparts, and its sensitivity to basis set, exchange-correlation functional, and atomic coordinates quantified. Within this chapter we also introduce and demonstrate the high value of EDD plots. These plots are used to identify key regions of systems where electron density redistributions occur through polarisation and charge transfer effects.

We apply our EDA scheme to a number of large thrombin systems up to 4975 atoms in size in Chapter 6. Here, we use the EDA results to identify the key driving forces of thrombin-ligand binding, and also assess the convergence of the EDA components with system size. In this chapter, we also demonstrate application of the EDA to fragment molecules. Specifically, we partition a set of thrombin binders into small fragments and study their interaction with the thrombin protein using our EDA. In doing this, we are able to gain insight into the important contributions of specific ligand moieties to binding. The error associated with the EDA components due to ligand fragmentation is also quantified, allowing us to evaluate the effect of the approximations we make. We also present a study of the binding components of small S1 pocket binders interacting with thrombin using the EDA and EDD plots. By considering the interactions of relatively simple molecules, we are able to comprehensively analyse the results we obtain and understand the driving forces of the interactions.

In Chapter [7](#) we provide a summary of our investigations and detail future work that we consider to be of important value for the field of biomolecular simulation and task of interaction energy analysis.

List of related publications

- The work presented in Chapters 3 and 4 has been published as:

Energy decomposition analysis approaches and their evaluation on prototypical protein-drug interaction patterns. M. J. S. Phipps, T. Fox, C. S. Tautermann, and C.-K. Skylaris, *Chem. Soc. Rev.*, **44**, 3177–3211 (2015).

- Some, but not all, of the work presented in Chapters 5 and 6 has been published as:

Energy decomposition analysis based on absolutely localised molecular orbitals for large-scale density functional theory calculations in drug design. M. J. S. Phipps, T. Fox, C. S. Tautermann, and C.-K. Skylaris, *J. Chem. Theory Comp.*, **12**, 3135–3148 (2016).

Chapter 1

Quantum mechanical principles

Quantum mechanics, the foundations of which were developed in the early 20th century, is a branch of science that describes the physics of very small systems on the atomic scale. Through applying the equations of quantum mechanics to physical models of scientific interest using computational means, we are able to gain insight into the properties and behaviours of systems. In this chapter, we provide a brief introduction to the quantum mechanical theories of key relevance to our work. We begin by describing the wavefunction, used within the Schrödinger equation. Next, we introduce the approximation of Born and Oppenheimer that separates the nuclear and electronic problem into the more feasible subject of electronic wavefunctions in an external potential. The framework provided by the variational principle is discussed which enables the equations of quantum mechanics to be solved. Finally, we introduce the Hartree-Fock approximation which is used to estimate the ground state energy of a system.

1.1 The wavefunction

The wavefunction is a central concept in the theory of quantum mechanics. This quantity provides a complete quantum mechanical description of a system and is a function of particles' coordinates and time [26]. The wavefunction is not

itself an observable, and quantum mechanical operators must be applied to the wavefunction in order to calculate physical properties.

We now describe a number of important properties of the wavefunction. The probability density for a (normalised) wavefunction Ψ of a system of one particle with coordinate \mathbf{r} , spin s and time t is defined as

$$|\Psi(\mathbf{r}, s, t)|^2 \quad . \quad (1.1)$$

Integrated over all space, the probability will be equal to 1 as the particle must exist within space, i.e.,

$$\int_{-\infty}^{\infty} |\Psi(\mathbf{r}, s, t)|^2 d\mathbf{r} = 1 \quad . \quad (1.2)$$

1.2 The Schrödinger equation

In quantum chemistry calculations, we typically seek to obtain the (approximate) solution to the non-relativistic time-independent Schrödinger equation,

$$\begin{aligned} \hat{H}\Psi &= E\Psi \\ &= E\Psi(\mathbf{r}_1, \mathbf{r}_2, \dots, \mathbf{r}_N, s_1, s_2, \dots, s_N, \mathbf{R}_1, \mathbf{R}_2, \dots, \mathbf{R}_{N_{\text{nuc}}}, S_1, S_2, \dots, S_{N_{\text{nuc}}}) \end{aligned} \quad (1.3)$$

where \hat{H} is the Hamiltonian operator, E is the total energy of the system, Ψ is the wavefunction for a system of N electrons and N_{nuc} nuclei each with spin s and S and coordinate \mathbf{r} and \mathbf{R} respectively. The Schrödinger equation is an eigenvalue problem for a system of interacting particles of electrons and nuclei, with the Hamiltonian operating on the wavefunction to obtain the total energy as our observable.

The Hamiltonian of the system is expressed using the kinetic energy operator, \hat{T} , and the potential energy operator, \hat{V} ,

$$\hat{H} = \hat{T} + \hat{V} \quad (1.4)$$

Defining \hat{T}_e and \hat{T}_n as the electronic and nuclear kinetic energy operators, and \hat{V}_{ee} , \hat{V}_{ne} , and \hat{V}_{nn} as the electron–electron, nuclear–electron, and nuclear–nuclear potential energy operators, the molecular Schrödinger equation is re-expressed as,

$$(\hat{T}_e + \hat{T}_n + \hat{V}_{ee} + \hat{V}_{ne} + \hat{V}_{nn})\Psi = E\Psi \quad (1.5)$$

These operators are expressed as¹,

$$\hat{T}_e = - \sum_{i=1}^N \frac{1}{2} \nabla_i^2 \quad (1.6a)$$

$$\hat{T}_n = - \sum_{A=1}^{N_{\text{nuc}}} \frac{1}{2M_A} \nabla_A^2 \quad (1.6b)$$

$$\hat{V}_{ee} = + \sum_{i=1}^N \sum_{j>i}^N \frac{1}{r_{ij}} \quad (1.6c)$$

$$\hat{V}_{ne} = - \sum_{i=1}^N \sum_{A=1}^{N_{\text{nuc}}} \frac{Z_A}{r_{iA}} \quad (1.6d)$$

$$\hat{V}_{nn} = + \sum_{A=1}^{N_{\text{nuc}}} \sum_{B>A}^{N_{\text{nuc}}} \frac{Z_A Z_B}{R_{AB}} \quad (1.6e)$$

where the position vectors r_{ij} , r_{iA} and R_{AB} are given by,

$$r_{ij} = |\mathbf{r}_i - \mathbf{r}_j| \quad (1.7a)$$

$$r_{iA} = |\mathbf{r}_i - \mathbf{R}_A| \quad (1.7b)$$

$$R_{AB} = |\mathbf{R}_A - \mathbf{R}_B| \quad (1.7c)$$

and where M_A is the mass ratio of nucleus A to an electron, Z_A is the atomic number of nucleus A , and ∇_i^2 and ∇_A^2 are both the Laplace operator involved in

¹In atomic units, $\hbar = m_e = e = 4\pi\epsilon_0 = 1$

differentiation with respect to the coordinates of electron i and nucleus A ,

$$\nabla_i^2 = \frac{\partial^2}{\partial \mathbf{r}_{\mathbf{x}i}} + \frac{\partial^2}{\partial \mathbf{r}_{\mathbf{y}i}} + \frac{\partial^2}{\partial \mathbf{r}_{\mathbf{z}i}} \quad (1.8a)$$

$$\nabla_A^2 = \frac{\partial^2}{\partial \mathbf{r}_{\mathbf{x}A}} + \frac{\partial^2}{\partial \mathbf{r}_{\mathbf{y}A}} + \frac{\partial^2}{\partial \mathbf{r}_{\mathbf{z}A}} \quad (1.8b)$$

where the Cartesian coordinates $\mathbf{r} = \{\mathbf{r}_{\mathbf{x}}, \mathbf{r}_{\mathbf{y}}, \mathbf{r}_{\mathbf{z}}\}$.

1.3 The Born-Oppenheimer approximation

We may simplify the Schrödinger equation that contains five operators to a form that involves only three. The Born–Oppenheimer approximation [27] is a fundamental backbone of quantum chemistry that approximates the molecular Schrödinger equation as separable into electronic and nuclear parts,

$$\Psi(\{\mathbf{x}_i\}, \{\mathbf{x}_A\}) = \Psi_{\text{elec}}(\{\mathbf{x}_i\}, \{\mathbf{x}_A\}) \Psi_{\text{nuc}}(\{\mathbf{x}_A\}) \quad (1.9)$$

where the spatial and spin coordinate is given by $\mathbf{x} = \{\mathbf{r}, s\}$, Ψ_{nuc} is the nuclear wavefunction, and where Ψ_{elec} is the electronic wavefunction that depends parametrically on the nuclear coordinates.

This approximation, also known as the adiabatic approximation, is grounded in the fact that electrons are significantly less massive than the nuclei they orbit. This mass difference results in the nuclei moving significantly slower than the electrons, so much so that the electrons may be treated as moving in the field of fixed nuclei.

When we apply this approximation, the kinetic energies of the nuclei are approximated to zero and the nuclear–nuclear potential \hat{V}_{nn} becomes a constant value.

The total system energy E is therefore representable as a correction to the electronic energy E_{elec} by the energy of nuclear–nuclear interactions E_{nuc} as,

$$E = E_{\text{elec}} + E_{\text{nuc}} \quad (1.10a)$$

$$E_{\text{nuc}} = \sum_{A=1}^{N_{\text{nuc}}} \sum_{B>A}^{N_{\text{nuc}}} \frac{Z_A Z_B}{R_{AB}} \quad (1.10b)$$

with the total electronic energy expressed as,

$$(\hat{T}_e + \hat{V}_{ee} + \hat{V}_{ne})\Psi_{\text{elec}} = E_{\text{elec}}(\{\mathbf{x}_A\}) \Psi_{\text{elec}}(\{\mathbf{x}_i\}, \{\mathbf{x}_A\}) \quad (1.11)$$

As the scope of this work does not consider the vibrational or rotational problems of the nuclei, we consider solely the electronic problem given in Eq. 1.11 from this point onwards. We therefore now discontinue use of the subscript label ‘elec’ and refer only to the electronic Hamiltonians and wavefunctions. ²

1.4 Antisymmetry of the wavefunction and the Pauli exclusion principle

Antisymmetry of the electronic wavefunction is an important quantum mechanical property that relates to the exchange of electrons in a system. To demonstrate this principle, we now consider the case of an N electron wavefunction with two exchanging electrons i and j . Due to the indistinguishability of electrons, the probability of finding both electrons in space must remain constant, and therefore

$$|\Psi(\mathbf{x}_1, \dots, \mathbf{x}_i, \dots, \mathbf{x}_j, \dots, \mathbf{x}_N)|^2 = |\Psi(\mathbf{x}_1, \dots, \mathbf{x}_j, \dots, \mathbf{x}_i, \dots, \mathbf{x}_N)|^2 \quad (1.12)$$

In the case of integer spin bosonic particles, the wavefunction is symmetric with respect to coordinate exchange. For half-spin fermionic particles (and therefore electrons), the wavefunction must be antisymmetric with respect to coordinate

²Additionally, the parametric dependence of Ψ_{elec} on the nuclear coordinates will not explicitly appear in the form of Ψ_{elec} from this point onwards.

exchange, and so

$$\Psi(\mathbf{x}_1, \dots, \mathbf{x}_i, \dots, \mathbf{x}_j, \dots, \mathbf{x}_N) = -\Psi(\mathbf{x}_1, \dots, \mathbf{x}_j, \dots, \mathbf{x}_i, \dots, \mathbf{x}_N) \quad . \quad (1.13)$$

This antisymmetry principle demonstrates respect of the Pauli exclusion principle [28] that no more than one electron can occupy the same state, as in the case of two electrons occupying the same state (i.e. $i = j$) the wavefunction would vanish.

1.5 The variational principle

The variational principle states that for a normalised wavefunction Ψ satisfying boundary conditions the Hamiltonian expectation value $\langle \Psi | \hat{H} | \Psi \rangle$ is an upper bound to the exact ground state energy, E_0 , i.e.

$$\langle \Psi | \hat{H} | \Psi \rangle \geq E_0 \quad . \quad (1.14)$$

As this means that the energy of any approximated wavefunction is always too high, a trial wavefunction can always be improved by finding another wavefunction with lower energy. This fact gives rise to the variational method, in which we begin with a (normalised) trial wavefunction and optimise its parameters to minimise the value of $\langle \Psi | \hat{H} | \Psi \rangle$, which we take as our estimate of the exact ground state energy.

We begin the proof of this theory by observing that there is an infinitely large set of exact solutions to the Schrödinger equation, i.e.

$$\hat{H}|\Psi_\alpha\rangle = E_\alpha|\Psi_\alpha\rangle \quad \alpha = 0, 1, \dots, \infty \quad (1.15)$$

where α refers to a solution of the Schrödinger equation, and where we use E_0 to refer to the ground state energy (i.e. $E_0 \leq E_1 \leq \dots \leq E_\alpha \leq \dots$). Due to the Hermiticity of the Hamiltonian operator \hat{H} , the eigenfunctions $\{\Psi_\alpha\}$ are

orthonormal

$$\langle \Psi_\alpha | \Psi_\beta \rangle = \delta_{\alpha\beta} \quad . \quad (1.16)$$

Pre-multiplying Eq. 1.15 by $\langle \Psi_\beta |$ and taking into account Eq. 1.16, we observe

$$\langle \Psi_\beta | \hat{H} | \Psi_\alpha \rangle = E_\alpha \delta_{\alpha\beta} \quad . \quad (1.17)$$

Noting completeness of the set of the eigenfunctions $\{\Psi_\alpha\}$ (due to the Hermiticity of \hat{H}), we can express any function $\tilde{\Psi}$ satisfying the same boundary conditions as $\{\Psi_\alpha\}$ as a linear combination,

$$|\tilde{\Psi}\rangle = \sum_{\alpha} |\Psi_\alpha\rangle c_\alpha = \sum_{\alpha} |\Psi_\alpha\rangle \langle \Psi_\alpha | \tilde{\Psi} \rangle \quad (1.18a)$$

$$\langle \tilde{\Psi} | = \sum_{\alpha} c_\alpha^* \langle \Psi_\alpha | = \sum_{\alpha} \langle \tilde{\Psi} | \Psi_\alpha \rangle \langle \Psi_\alpha | \quad . \quad (1.18b)$$

For a given normalised trial wavefunction $\tilde{\Psi}$, we note using Eqs. 1.16, 1.18a and 1.18b that

$$\begin{aligned} \langle \tilde{\Psi} | \tilde{\Psi} \rangle &= 1 \\ &= \sum_{\alpha\beta} \langle \tilde{\Psi} | \Psi_\alpha \rangle \langle \Psi_\alpha | \Psi_\beta \rangle \langle \Psi_\beta | \tilde{\Psi} \rangle \\ &= \sum_{\alpha\beta} \langle \tilde{\Psi} | \Psi_\alpha \rangle \delta_{\alpha\beta} \langle \Psi_\beta | \tilde{\Psi} \rangle \\ &= \sum_{\alpha} \langle \tilde{\Psi} | \Psi_\alpha \rangle \langle \Psi_\alpha | \tilde{\Psi} \rangle \\ &= \sum_{\alpha} \left| \langle \Psi_\alpha | \tilde{\Psi} \rangle \right|^2 \end{aligned} \quad (1.19)$$

Similarly, using Eqs. 1.17, 1.18a, and 1.18b we also note

$$\begin{aligned}
 \langle \tilde{\Psi} | \hat{H} | \tilde{\Psi} \rangle &= \sum_{\alpha\beta} \langle \tilde{\Psi} | \Psi_\alpha \rangle \langle \Psi_\alpha | \hat{H} | \Psi_\beta \rangle \langle \Psi_\beta | \tilde{\Psi} \rangle \\
 &= \sum_{\alpha\beta} \langle \tilde{\Psi} | \Psi_\alpha \rangle E_\beta \delta_{\alpha\beta} \langle \Psi_\beta | \tilde{\Psi} \rangle \\
 &= \sum_{\alpha} E_\alpha \left| \langle \Psi_\alpha | \tilde{\Psi} \rangle \right|^2 .
 \end{aligned} \tag{1.20}$$

Finally, by noting that $E_\alpha \geq E_0$ for all α , we find

$$\begin{aligned}
 \langle \tilde{\Psi} | \hat{H} | \tilde{\Psi} \rangle &\geq \sum_{\alpha} E_0 \left| \langle \Psi_\alpha | \tilde{\Psi} \rangle \right|^2 \\
 \therefore \langle \tilde{\Psi} | \hat{H} | \tilde{\Psi} \rangle &\geq E_0 \sum_{\alpha} \left| \langle \Psi_\alpha | \tilde{\Psi} \rangle \right|^2 \\
 \therefore \langle \tilde{\Psi} | \hat{H} | \tilde{\Psi} \rangle &\geq E_0
 \end{aligned} \tag{1.21}$$

where we have taken into account the requirement of wavefunction normalisation given in Eq. 1.16.

This principle tells us that because our wavefunction is approximated, the ground state solution to the Schrödinger equation obtained will have an energy above the true ground state energy. Therefore, the lower the energy we obtain, the ‘better’ our approximated wavefunction represents the exact ground state wavefunction. The variational principle allows for what is known as the variation method: by varying the parameters of a normalised trial wavefunction until the expectation value reaches a minimum we are able to estimate the energy of the exact ground state.

1.6 The Hartree-Fock equations

In this section, we introduce the important Hartree-Fock (HF) approximation [29; 30] that is used to find the wavefunction and ground-state energy of a system. This approach serves as a grounding for more sophisticated wavefunction based

techniques, and is also the framework used by many of the EDA schemes discussed later in Chapter 3 of this thesis. For further in-depth details of this method, we refer the reader to the comprehensive literature of Szabo and Ostlund [26].

In the HF approach, the exact electronic wavefunction of a many-electron system is approximated using a number of single electron wavefunctions in what is known as a Slater determinant. This determinant properly expresses the antisymmetry requirement described by Eq. 1.13, as a determinant will change sign on exchanging two columns or rows. The expression of the electronic wavefunction is given as the antisymmetrised product of N orthonormal spin orbitals $\chi(\mathbf{x})$ by

$$\Psi_{\text{HF}} = \frac{1}{\sqrt{N!}} \begin{vmatrix} \chi_1(\mathbf{x}_1) & \chi_2(\mathbf{x}_1) & \cdots & \chi_N(\mathbf{x}_1) \\ \chi_1(\mathbf{x}_2) & \chi_2(\mathbf{x}_2) & \cdots & \chi_N(\mathbf{x}_2) \\ \vdots & \vdots & \ddots & \vdots \\ \chi_1(\mathbf{x}_N) & \chi_2(\mathbf{x}_N) & \cdots & \chi_N(\mathbf{x}_N) \end{vmatrix} \quad (1.22)$$

where the prefactor $\frac{1}{\sqrt{N!}}$ is included to ensure normalisation (Eq. 1.2). As previously discussed, both the spin and spatial coordinate must be specified in order to fully describe an electron. A spin orbital $\chi(\mathbf{x})$ is constructed from a spatial orbital $\psi(\mathbf{r})$ as

$$\chi(\mathbf{x}) = \begin{cases} \psi(\mathbf{r})\alpha(s) \\ or \\ \psi(\mathbf{r})\beta(s) \end{cases} \quad (1.23)$$

where $\alpha(s)$ and $\beta(s)$ are the spin functions that describe the spin state of the spin orbital (spin up or spin down). These spin functions are orthonormal, i.e.

$$\langle \alpha | \beta \rangle = 0 \quad (1.24a)$$

$$\langle \alpha | \alpha \rangle = 1 \quad . \quad (1.24b)$$

In the case of restricted theories, the spatial orbitals are doubly occupied (i.e. two spin orbitals share a single spatial orbital), as will be discussed later.

Within HF theory, the Slater determinant is used as an approximation for the exact electronic wavefunction of the system and its energy minimised using the variational theorem to estimate the exact ground state energy of the system,

$$E_{\text{HF}} = \langle \Psi_{\text{HF}} | \hat{H} | \Psi_{\text{HF}} \rangle \quad . \quad (1.25)$$

In this approach, the one-electron problems for the electron in the field of the nuclei and remaining electrons are solved using a series of one-electron Schrödinger equations,

$$\hat{f}_i(\mathbf{x}_i)\chi_i(\mathbf{x}_i) = \varepsilon_i\chi_i(\mathbf{x}_i) \quad (1.26)$$

where ε_i represents the energy of this one-electron wavefunction χ_i , and the Fock operator \hat{f}_i represents the Hamiltonian as,

$$\hat{f}_i = -\frac{1}{2}\hat{\nabla}_i^2 + \sum_{A=1}^{N_{\text{nuc}}} \frac{Z_A}{r_{iA}} + \hat{v}_{\text{HF},i} \quad (1.27)$$

where $\hat{v}_{\text{HF},i}$ is the Hartree Fock potential acting on the one-electron wavefunction χ_i . The HF potential is the (repulsive) potential felt by the i th electron in the field of all the other $N - 1$ electrons of the system that simplifies the Hamiltonian potential \hat{V}_{ee} described by Eq. 1.6c with an average representation. This is expressed in terms of Coulomb (\hat{J}) and exchange (\hat{K}) operators as

$$\hat{v}_{\text{HF}}(\mathbf{x}_1) = \sum_j^N (\hat{J}_j(\mathbf{x}_1) - \hat{K}_j(\mathbf{x}_1)) \quad . \quad (1.28)$$

The Coulomb operator,

$$\hat{J}_j(\mathbf{x}_1) = \int \frac{|\chi_j(\mathbf{x}_2)|^2}{r_{12}} d\mathbf{x}_2 \quad (1.29)$$

represents the potential felt by an electron at coordinate \mathbf{x}_1 due to the average distribution of charge by an electron in the spin orbital χ_j . We observe that through Eq. 1.1 this operator weights the repulsion felt by an electron at \mathbf{x}_1 by

the probability of an electron being present at \mathbf{x}_2 , This is integrated over all space in order to evaluate the repulsion felt by the average distribution of charge by an electron in χ_j . The expectation value of the Coulomb operator is given by

$$\begin{aligned} J_{ij} &= \langle \chi_i(\mathbf{x}_1) | \hat{J}_j(\mathbf{x}_1) | \chi_i(\mathbf{x}_1) \rangle \\ &= \iint \frac{\chi_i^*(\mathbf{x}_1) \chi_j^*(\mathbf{x}_2) \chi_i(\mathbf{x}_1) \chi_j(\mathbf{x}_2)}{r_{12}} d\mathbf{x}_1 d\mathbf{x}_2 \\ &= \langle ij | ij \rangle \quad . \end{aligned} \quad (1.30)$$

The exchange operator $\hat{K}_j(\mathbf{x}_1)$ has no classical interpretation. We represent this operator by considering its action on a spin orbital $\chi_i(\mathbf{x}_1)$

$$\hat{K}_j(\mathbf{x}_1) \chi_i(\mathbf{x}_1) = \left[\int \frac{\chi_j^*(\mathbf{x}_2) \chi_i(\mathbf{x}_2)}{r_{12}} d\mathbf{x}_2 \right] \chi_j(\mathbf{x}_1) \quad (1.31)$$

From this expression, we observe the *non-local* nature of this operator: the action of \hat{K}_j on $\chi_i(\mathbf{x}_1)$ results in exchange of the coordinates of the spin orbitals $\chi_i(\mathbf{x}_1)$ and $\chi_j(\mathbf{x}_1)$, and therefore the result is dependent on the value of χ_i at all spatial coordinates due to the integration. This is not the case for the Coulomb operator (in which the result of applying $\hat{J}_j(\mathbf{x}_1)$ on $\chi_i(\mathbf{x}_1)$ is dependent only on the value of χ_i at \mathbf{x}_1) and hence is referred to as *local*. The expectation value of the exchange operator is given by

$$\begin{aligned} K_{ij} &= \langle \chi_i(\mathbf{x}_1) | \hat{K}_j(\mathbf{x}_1) | \chi_i(\mathbf{x}_1) \rangle \\ &= \iint \frac{\chi_i^*(\mathbf{x}_1) \chi_j^*(\mathbf{x}_2) \chi_j(\mathbf{x}_1) \chi_i(\mathbf{x}_2)}{r_{12}} d\mathbf{x}_1 d\mathbf{x}_2 \\ &= \langle ij | ji \rangle \quad . \end{aligned} \quad (1.32)$$

We note that the exchange term arises due to antisymmetry of the Slater determinant, and the exchange interaction only exists for electrons of the same spin which we now demonstrate. By observing that the r_{12}^{-1} term is independent of spin, the exchange integral can be separated over the product of two spin orbitals. We now consider the integral for such a product using two different spin orbitals, χ_i with

spin up and χ_j with spin down i.e.

$$\chi_i(\mathbf{x}) = \psi_i(\mathbf{r})\alpha(s) \quad (1.33a)$$

$$\chi_j(\mathbf{x}) = \psi_j(\mathbf{r})\beta(s) \quad . \quad (1.33b)$$

If these spin orbitals depend on the same coordinate \mathbf{x}_2 , we observe that the spin function integral becomes zero due to orthogonality of the $\alpha(s)$ and $\beta(s)$ spins (Eq. 1.24), and therefore the exchange interaction only exists for same spin electrons,

$$\begin{aligned} \hat{K}_j(\mathbf{x}_1)\chi_i(\mathbf{x}_1) &= \left[\int \frac{\chi_j^*(\mathbf{x}_2)\chi_i(\mathbf{x}_2)}{r_{12}} d\mathbf{x}_2 \right] \chi_j(\mathbf{x}_1) \\ &= \left[\int \frac{\psi_j^*(\mathbf{r}_2)\beta(s)\psi_i(\mathbf{r}_2)\alpha(s)}{r_{12}} d\mathbf{x}_2 \right] \chi_j(\mathbf{x}_1) \\ &= \left[\int \frac{\psi_j^*(\mathbf{r}_2)\psi_i(\mathbf{r}_2)}{r_{12}} d\mathbf{r}_2 \int \frac{\beta(s)\alpha(s)}{s} ds \right] \chi_j(\mathbf{x}_1) \\ &= 0 \quad . \end{aligned} \quad (1.34)$$

For systems in which all the electrons are paired (*closed-shell* systems), it is possible to express the wavefunction using spatial orbitals that are the same for both the α and β spins, and with each spatial orbital occupied by two electrons

$$\begin{aligned} |\Psi_0\rangle &= |\chi_1\chi_2\chi_3\chi_4 \cdots \chi_{N-1}\chi_N\rangle \\ &= |\psi_1^\alpha\psi_1^\beta\psi_2^\alpha\psi_2^\beta \cdots \psi_{N/2}^\alpha\psi_{N/2}^\beta\rangle \quad . \end{aligned} \quad (1.35)$$

This form of the HF approximation is termed the *restricted* HF (RHF) approximation. For *open-shell* systems in which the number of electrons is odd (e.g. CH_3^+), or even but without pairwise occupation of a spatial orbital (e.g. a $^3\Sigma_g^-$ oxygen molecule), then two possible solutions exist. In the restricted open-shell HF (ROHF) approach, the singly occupied orbitals are treated as such, and the remaining orbitals are treated using the RHF approximation. In the unrestricted HF (UHF) approach, every spin orbital has its own spatial orbital, with the α and β orbitals each experiencing unique HF potentials. A diagram showing the

application of RHF and UHF approximations to a hydrogen molecule is provided in Fig. 1.1, in which we observe the RHF approximation to fail outside of the closed-shell regime close to the equilibrium geometry.

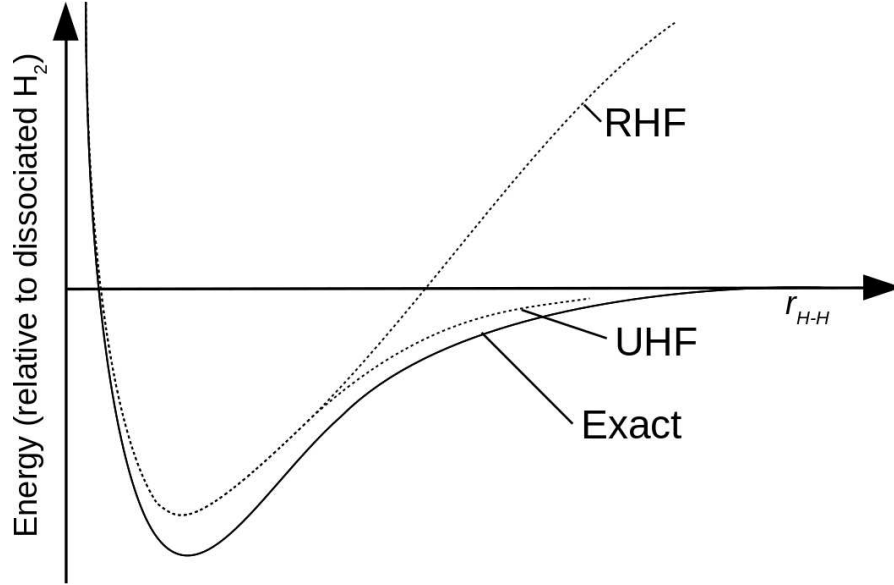


Figure 1.1: A representation of the relative energy of H_2 during dissociation when calculated using the RHF and UHF approximations.

The Fock operator \hat{f}_i (Eq. 1.27) is used with a set of trial orbitals and the one-electron Schrödinger equations (Eq. 1.26) self-consistently solved (due to the dependence of the Fock operator on the molecular orbitals being calculated). Due to the orbitals being derived by optimisation in their own field, the HF method is also referred to in literature as the self-consistent field (SCF) method.

Expanding Eq. 1.25 and applying the variational principle, the optimal spin orbitals minimise the (restricted) HF energy

$$E_{\text{HF}} = \sum_i^N \left(-\frac{1}{2} \hat{\nabla}_i^2 - \sum_{A=1}^{N_{\text{nuc}}} \frac{Z_A}{r_{iA}} \right) + \frac{1}{2} \sum_i^N \sum_j^N (J_{ij} - K_{ij}) \quad (1.36)$$

where the i and j iterate over N occupied spin orbitals. Importantly, we observe that the $j = i$ term in the double summation (that would relate to the interaction of an electron with itself) is permitted. This is because the Coulomb and exchange

integrals reduce to

$$\begin{aligned}
 J_{ii} &= \iint \frac{\chi_i^*(\mathbf{x}_1)\chi_i^*(\mathbf{x}_2)\chi_i(\mathbf{x}_1)\chi_i(\mathbf{x}_2)}{r_{12}} d\mathbf{x}_1 d\mathbf{x}_2 \\
 &= \langle ii|ii \rangle \\
 &= K_{ii}
 \end{aligned} \tag{1.37}$$

and as a result J_{ii} and K_{ii} cancel out in the double summation of Eq. 1.36.

Having calculated the ground-state HF electronic energy, the nuclear–nuclear interaction energy is lastly added to obtain the HF approximation of the total exact ground state energy of the system E_{TOT}

$$E_{\text{TOT}} = E_{\text{HF}} + E_{\text{nuc}} \quad . \tag{1.38}$$

The HF model has been further developed in the post-HF set of methods that treat for the missing electron correlation energy expressed by

$$E_{\text{corr}} = E_0 - E_{\text{HF}} \quad . \tag{1.39}$$

Methods that seek to include this energy include Møller-Plesset perturbation theory [31], coupled cluster [32], configuration interaction (CI) [33], or multi-configurational self-consistent field (MCSCF) approach (e.g. CASSCF [34]).

Chapter 2

Density functional theory

Knowing the exact form of the many-body wavefunction provides us with direct access to all the information we require of our system under study. The Hartree-Fock (HF) approach [29; 30], discussed in Section 1.6, is a valuable tool for quantum mechanical calculations that approximates the many-body wavefunction as an antisymmetrised Slater determinant of single electron molecular orbitals (MOs). Unfortunately, however, the wavefunction is an intrinsically complicated quantity. This is because the wavefunction depends on $4N$ variables (three spatial variables and one variable for spin) for a given N electron problem, and therefore for systems of appreciable size wavefunction based approaches quickly become computationally unwieldy.

Equally, our Hamiltonian operator \hat{H} relies on use of only one and two particle operators. This very fact suggests that the wavefunction is a quantity that contains information redundant for our purposes, and that it is possible to avoid the need for the wavefunction in calculations altogether. Density functional theory (DFT) is a powerful framework that successfully achieves this accomplishment. In DFT, the central quantity used to solve the Schrödinger equation is the electron density, which depends on simply 3 spatial dimensions. The electron density can

be calculated by integration using the many-body wavefunction as

$$n(\mathbf{r}) = N \int \cdots \int |\Psi(\mathbf{r}, \mathbf{r}_2, \cdots, \mathbf{r}_N)|^2 d\mathbf{r}_2, \cdots, d\mathbf{r}_N \quad . \quad (2.1)$$

This powerful approach is made possible by the fact that the Hamiltonian operator of a given system is uniquely defined by the electron density itself, and therefore this quantity is all that is needed for molecular properties to be completely described.

The early foundations of DFT were provided by the Thomas–Fermi model [35; 36] in which electronic structure information is obtained from the density alone. In this model the kinetic energy is accounted for using the uniform electron gas, with additional contributions included for the nuclear-electron and electron-electron interactions cast in terms of the electron density, and all terms of the energy expression rely on the electron density alone. This model was later augmented by Dirac to account for electron exchange interactions, resulting in the Thomas–Fermi–Dirac energy functional [37].

Although these models provided the groundwork for a quantum mechanical approach based on the electron density alone, it was not until 1964 that the pioneering theorems of Hohenberg and Kohn [38] were published, setting out a practical and general method for obtaining accurate chemical information of systems. More recent progress made within the field of DFT has produced new methods that scale as $\mathcal{O}(N)$ with system size. These linear scaling methods, which exploit the near-sightedness of matter, present the opportunity to calculate properties of systems many magnitudes larger than is possible using conventional DFT.

In this chapter, we introduce the framework of density functional theory and the underlying theory of the ONETEP linear-scaling DFT code [39].

2.1 The Hohenberg-Kohn theorems

The existence of modern day density functional theory owes much to the seminal work of Hohenberg and Kohn [38] in which the theorems that permit this framework are laid out. The first of these theorems demonstrates that the electron density uniquely determines the Hamiltonian operator. The second Hohenberg-Kohn theorem shows that the variational principle may be applied to find the (approximate) ground state using the electron density as a basic variable. We now describe these theorems in detail.

2.1.1 Theorem 1

The first Hohenberg and Kohn [38] theorem states that the electron density uniquely determines the Hamiltonian operator and therefore the total energy of the system. The simple proof of this theorem is based on reductio ad absurdum, i.e. we assume that the external potential is not unequivocally determined by the density and show this to result in a contradiction. We begin by assuming the existence of two different external potentials $v_{\text{ext}}(\mathbf{r})$ and $v'_{\text{ext}}(\mathbf{r})$ with respective ground state wavefunctions Ψ_0 and Ψ'_0 which give rise to the same density $n(\mathbf{r})$. We assume these potentials to differ by more than a constant, and therefore the wavefunctions of $v_{\text{ext}}(\mathbf{r})$ and $v'_{\text{ext}}(\mathbf{r})$ must differ, i.e.

$$\Psi_0 \neq \Psi'_0 \quad . \quad (2.2)$$

Defining the Hamiltonians of Ψ_0 and Ψ'_0 as \hat{H} and \hat{H}' respectively, with energies E_0 and E'_0 , and using the variational principle we find

$$E'_0 = \langle \Psi'_0 | \hat{H}' | \Psi'_0 \rangle < \langle \Psi_0 | \hat{H}' | \Psi_0 \rangle = \langle \Psi_0 | \hat{H} | \Psi_0 \rangle + \langle \Psi_0 | \hat{H}' - \hat{H} | \Psi_0 \rangle \quad (2.3)$$

and therefore

$$E'_0 < E_0 + \int [v'_{\text{ext}}(\mathbf{r}) - v_{\text{ext}}(\mathbf{r})] n(\mathbf{r}) d\mathbf{r} \quad . \quad (2.4)$$

Interchanging the primed and unprimed quantities, we equivalently find

$$E_0 < E'_0 + \int [v_{\text{ext}}(\mathbf{r}) - v'_{\text{ext}}(\mathbf{r})] n(\mathbf{r}) d\mathbf{r} \quad . \quad (2.5)$$

Adding Eq. 2.4 and Eq. 2.5 yields the absurdity

$$E_0 + E'_0 < E_0 + E'_0 \quad (2.6)$$

thus demonstrating the first theorem.

2.1.2 Theorem 2

The second Hohenberg and Kohn [38] theorem states that the energy $E[n]$ obtained for a given density n is the lowest energy if and only if n is the true ground state density n_0 , i.e.

$$E[n] \geq E[n_0] \quad . \quad (2.7)$$

The proof of this theorem relies on the first Hohenberg–Kohn theorem. We begin by noting that for the density to preserve the number of particles N which it describes, the following equation must hold true

$$\int n(\mathbf{r}) d\mathbf{r} = N \quad . \quad (2.8)$$

Through the first theorem of Hohenberg and Kohn, for a non-negative density $n(\mathbf{r})$ normalised to N we can define its energy E as a functional of this electronic

density as

$$E[n] = \int n(\mathbf{r}) v_{\text{ext}}(\mathbf{r}) d\mathbf{r} + F[n] \quad (2.9)$$

where $v_{\text{ext}}(\mathbf{r})$ is the external potential, uniquely determined by $n(\mathbf{r})$, and where $F[n]$ is a universal functional of the electron density that contains electron-electron interaction and kinetic energy terms, i.e.

$$F[n(\mathbf{r})] \equiv \langle \Psi | \hat{T} + \hat{V}_{\text{ee}} | \Psi \rangle \quad . \quad (2.10)$$

The energy functional $E[n]$ is equivalent to the wavefunction energy functional

$$E[\Psi] \equiv \langle \Psi | \hat{V}_{\text{ne}} | \Psi \rangle + \langle \Psi | \hat{T} + \hat{V}_{\text{ee}} | \Psi \rangle \quad . \quad (2.11)$$

We note that $E[\Psi]$ will be at its minimum when Ψ is the exact ground state wavefunction, Ψ_0 . If Ψ is not the exact ground state wavefunction then using the variational principle

$$E[\Psi] > E[\Psi_0] = E_0 \quad (2.12)$$

and applying this analogously to the electron density provides us with the equation,

$$E[n] > E[n_0] = E_0 \quad . \quad (2.13)$$

This therefore demonstrates that the ground state solution may be found variationally using the electron density as a variable.

2.2 The Kohn-Sham equations

Whilst the Hohenberg-Kohn theorems provide an argument for central use of the density in obtaining the ground state, these present little applicability for finding the solutions to problems as the exact form of the universal functional $F[n]$ is not known. The pioneering work of Kohn and Sham [40] presented a practical means

by which the solutions to physical problems could be found. This was achieved by representing the interacting electron system at hand in terms of a fictitious system of non-interacting electrons moving in an effective potential, where this fictitious system reproduces the exact ground state density of the system of interacting electrons.

In Kohn-Sham density functional theory, the electron density has the form

$$n(\mathbf{r}) = \sum_{i=1}^N |\psi_i(\mathbf{r})|^2 \quad (2.14)$$

where $\psi_i(\mathbf{r})$ are the one-electron Kohn-Sham (KS) orbitals of a fictitious system of non-interacting electrons which is constructed in such a way that its density is the same as the exact density of the system of interest which has interacting electrons.

A key advantage of Kohn-Sham DFT is that one can calculate exactly the kinetic energy of the non-interacting system T_s as a functional of the orbitals, which can be used as a starting point for calculating the kinetic energy of the interacting system T . The kinetic energy of the non-interacting reference system is given by

$$T_s[n] = \sum_{i=1}^N \left\langle \psi_i \left| -\frac{1}{2} \nabla^2 \right| \psi_i \right\rangle \quad . \quad (2.15)$$

We introduce an exchange-correlation energy functional E_{xc} that accounts for the missing kinetic and correlation effects by repartitioning the Hohenberg-Kohn universal functional as

$$\begin{aligned} F[n] &= T[n] + V_{ee}[n] \\ &= T[n] + T_s[n] - T_s[n] + E_H[n] - E_H[n] + V_{ee}[n] \\ &= T_s[n] + E_H[n] + (T[n] - T_s[n] - E_H[n] + V_{ee}[n]) \\ &= T_s[n] + E_H[n] + E_{xc}[n] \end{aligned} \quad (2.16)$$

$$E_{xc}[n] \equiv T[n] - T_s[n] + V_{ee}[n] - E_H[n] \quad (2.17)$$

where $E_H[n]$ is the Hartree energy (see Eq. 1.30) and where the exchange-correlation energy is a functional of charge density which is approximated in practice due to lack of a known analytic form of this functional.

In the KS formalism, we aim to calculate the density $n(\mathbf{r})$ that minimises E_{KS} for a given KS effective potential $v_{\text{eff}}(\mathbf{r})$ acting on a system of non-interacting electrons. This density is defined by the KS orbitals obtained by solving the set of one-electron Schrödinger equations

$$\hat{h}_{\text{KS}}\psi_i(\mathbf{r}) = \varepsilon_i\psi_i(\mathbf{r}) \quad (2.18)$$

with the Kohn-Sham Hamiltonian

$$\hat{h}_{\text{KS}} = -\frac{1}{2}\nabla^2 + v_{\text{eff}}(\mathbf{r}) \quad (2.19)$$

which contains an effective potential v_{eff} such that the ground state Kohn-Sham density equals the true ground state density. We define the KS effective potential as,

$$v_{\text{eff}}(\mathbf{r}) = v_{\text{ext}}(\mathbf{r}) + \int \frac{n(\mathbf{r}')}{|\mathbf{r} - \mathbf{r}'|} d\mathbf{r}' + v_{\text{xc}}(\mathbf{r}) \quad (2.20)$$

with exchange-correlation potential,

$$v_{\text{xc}}(\mathbf{r}) = \frac{\delta E_{\text{xc}}[n]}{\delta n(\mathbf{r})} \quad (2.21)$$

On calculating v_{eff} from a guessed density $n(\mathbf{r})$ using Eq. 2.20, a new density is found using Eqs. 2.14 and 2.18. These equations are known as the KS equations and are solved in a self-consistent manner to obtain new densities until energy convergence is achieved. The total electronic energy is calculated at each iteration

using the KS energy functional,

$$E_{\text{KS}}[n] = T_s[n] + \int n(\mathbf{r})v_{\text{ext}}(\mathbf{r})d\mathbf{r} + \frac{1}{2} \iint \frac{n(\mathbf{r})n(\mathbf{r}')}{|\mathbf{r} - \mathbf{r}'|} d\mathbf{r}d\mathbf{r}' + E_{\text{xc}}[n] \quad (2.22)$$

where the factor of half is present to correct for double counting.

2.3 The exchange-correlation functional

Within Kohn-Sham DFT, the complexities of the interacting system are contained within the exchange-correlation functional. As previously discussed, the exact form of the exchange-correlation functional $E_{\text{xc}}[n]$ is unknown, and this presents a central problem within the Kohn-Sham model. Many approximate forms of the exchange-correlation functional have been proposed, primarily specialised to solving the particular problem at hand. Here, we briefly introduce a selection of popular functionals used in Kohn-Sham DFT calculations.

We begin by noting the separable nature of the exchange-correlation functional into its exchange $E_{\text{x}}[n]$ and correlation parts $E_{\text{c}}[n]$, i.e.

$$E_{\text{xc}}[n] = E_{\text{x}}[n] + E_{\text{c}}[n] \quad . \quad (2.23)$$

At its simplest, the exchange-correlation functional depends on the local electron density alone without any consideration of local features (for example density gradient). This is the basis for the local density approximation (LDA), in which the exchange-correlation energy is modelled by extrapolation using the per-electron exchange-correlation energy for the uniform electron gas, i.e.

$$E_{\text{xc}}^{\text{LDA}}[n] = \int n(\mathbf{r})\epsilon_{\text{xc}}^{\text{LDA}}(n)d\mathbf{r} \quad (2.24)$$

where $\epsilon_{xc}^{\text{LDA}}(n)$ is the per-electron exchange-correlation energy of the uniform electron gas with density n . The function $\epsilon_{xc}^{\text{LDA}}(n)$ is separable into its exchange $\epsilon_x^{\text{LDA}}(n)$ and correlation $\epsilon_c^{\text{LDA}}(n)$ parts as

$$\epsilon_{xc}^{\text{LDA}}(n) = \epsilon_x^{\text{LDA}}(n) + \epsilon_c^{\text{LDA}}(n) \quad . \quad (2.25)$$

The exchange contribution to $\epsilon_{xc}^{\text{LDA}}(n)$ is analytically known, and is given using the Dirac functional [37]

$$\epsilon_x(n) = -\frac{3}{4} \left(\frac{3}{\pi} \right)^{\frac{1}{3}} n^{\frac{1}{3}}(\mathbf{r}) \quad . \quad (2.26)$$

A number of proposals have been made for the correlation part of $\epsilon_{xc}^{\text{LDA}}(n)$. Examples of popular LDA correlation parameterisations include the Vosko, Wilk and Nusair (VWN) [41] and Perdew and Wang (PW92) [42] models. As may be expected from the simple LDA functional that uses a uniform electron density system as its reference, the highest accuracy results are obtained for systems with more smoothly distributed electron densities.

To improve exchange-correlation functionals beyond the limits of the LDA functional to be able to accurately calculate properties of systems for which the electron density is more non-uniform, we may also include the gradient of electron density, $\nabla n(\mathbf{r})$, in our calculations. Doing so yields the so called generalised gradient approximation (GGA) class of exchange-correlation functionals. Here, the form of the exchange-correlation energy is

$$E_{xc}^{\text{GGA}}[n] = \int \epsilon_{xc}^{\text{GGA}}(n(\mathbf{r}), \nabla n(\mathbf{r})) d\mathbf{r} \quad (2.27)$$

where $\epsilon_{xc}^{\text{GGA}}(n(\mathbf{r}), \nabla n(\mathbf{r}))$ is the GGA exchange-correlation function that depends on the electron density gradient in addition to the electron density. Examples of GGA functionals include the Perdew and Wang (PW91) [43], and Perdew, and Burke and Ernzerhof (PBE) [44] functionals.

The GGA functional model can be extended further to also encompass the higher

order electron density derivatives. Such functionals are known as meta-GGA functionals, for example

$$E_{xc}^{\text{meta-GGA}}[n] = \int \epsilon_{xc}^{\text{meta-GGA}}(n(\mathbf{r}), \nabla n(\mathbf{r}), \nabla^2 n(\mathbf{r})) d\mathbf{r} \quad (2.28)$$

Examples of meta-GGA functionals include the Perdew, Kurth, Zupan, and Blaha (PKZB) [45], and Filatov and Thiel (FT98) [46] functional.

It is also possible to define exchange-correlation functionals that include a contribution from the exact HF non-local exchange energy calculated using the KS states. A popular example of such a hybrid functional is the B3LYP functional [47], in which the form of the functional is given by

$$\begin{aligned} E_{xc}^{\text{B3LYP}}[n] = & (1 - \alpha_0 - \alpha_x) E_x^{\text{LDA}}[n] + \alpha_0 E_x^{\text{HF}}[\{\psi_i\}] + \alpha_x E_x^{\text{B88}}[n] \\ & + (1 - \alpha_c) E_c^{\text{VWN}}[n] + \alpha_c E_c^{\text{LYP}}[n] \end{aligned} \quad (2.29)$$

where $E_x^{\text{LDA}}[n]$ is the LDA exchange energy, $E_x^{\text{HF}}[\{\psi_i\}]$ is the exact HF non-local exchange energy (which depends on the occupied KS orbitals), $E_x^{\text{B88}}[n]$ is the B88 exchange energy of Becke [48], $E_c^{\text{VWN}}[n]$ is the VWN correlation energy, $E_c^{\text{LYP}}[n]$ is the correlation of Lee, Yang and Parr [49], and where α_0 , α_x and α_c are the functional parameters of Stephens et al. [50].

2.4 Basis sets

In order to describe the one-electron MOs we use mathematical functions known as basis functions. The one-electron MOs are expanded as a linear combination of basis functions as

$$\psi_i(\mathbf{r}) = \sum_{\mu}^K C_{\mu i} \phi_{\mu}(\mathbf{r}) \quad (2.30)$$

where K is the number of basis functions, and $C_{\mu i}$ is an expansion coefficient for the basis function $\phi_{\mu}(\mathbf{r})$ of the basis set. The choice of basis set is an important consideration in ab initio calculations, as this is usually a key determining factor

in the speed and accuracy of the calculation. In the following section, we briefly discuss a number of important basis set functions used in DFT calculations.

2.4.1 Slater-type orbitals

The Slater-type orbital basis function [51] was developed for use in early quantum chemistry calculations. This function properly represents the correct form of the cusp at the nucleus, however due to the high computational expense of calculating solutions to integrals using these functions, Slater-type orbitals are in most cases not favoured today. The form of a Slater-type orbital is given by [52],

$$\phi_S(x, y, z; \zeta, i, j, k) = Nx^i y^j z^k e^{-\zeta \sqrt{x^2 + y^2 + z^2}} \quad (2.31)$$

where N is the normalisation constant, i , j , and k are non-negative integer parameters that determine the description of the orbital along the Cartesian axes, and ζ is a constant relating to the effective nuclear charge on the atom this basis function represents.

2.4.2 Gaussian-type orbitals

A more commonly used basis set function is the Gaussian-type orbital [53], developed to attempt to correct the difficulty using Slater functions in evaluating integrals. The functional form of a Gaussian orbital is given by,

$$\phi_G(x, y, z; \alpha, i, j, k) = Nx^i y^j z^k e^{-\alpha(x^2 + y^2 + z^2)} \quad (2.32)$$

where α is an exponent parameter that determines the orbital width. As well as displaying the incorrect representation of zero slope at the nucleus, this function decays at a much faster rate than Slater functions far away from the nucleus. To solve this problem, Slater-type orbitals are approximated using a linear combination of Gaussian-type orbitals, referred to as contracted Gaussian functions. This

approximation has proved to be very successful, with a large number of DFT codes adopting this as their primary basis set choice (e.g. Q-CHEM [54], NWChem [55], GAMESS-US [56]).

2.4.3 Plane waves

An alternate basis set to Slater and Gaussian-type orbitals is the plane wave basis set. This basis set is typically adopted for calculations involving periodic systems, for example bulk solids, surfaces and crystals, as plane waves are solutions to the Schrödinger equation for a particle in a periodic box. The plane wave basis functions normalised to a cubic cell with side length l are given by

$$\psi_{\mathbf{G}}(\mathbf{r}) = \frac{1}{l^{\frac{3}{2}}} e^{i\mathbf{G} \cdot \mathbf{r}} \quad (2.33)$$

where \mathbf{G} is the wave vector. Examples of DFT codes that adopt this basis set include CASTEP [57] and QUANTUM ESPRESSO [58]. As will be shown in Section 2.8.1, the psinc basis set used in the ONETEP code [39; 59] is fundamentally linked to the plane wave basis.

Many hundreds (or even thousands, depending on the cell and grid parameters) of plane waves are used as basis functions in a typical plane wave calculation. A specific advantage of using plane waves as a basis set is the lack of basis set superposition error, which we discuss below in Section 2.5. This is due to the basis functions being present in all regions of space, resulting in the basis set being fully balanced throughout binding energy calculations. However, this fact also results in empty space within the cell effectively having its own associated computational cost. This can be notably disadvantageous when approximating open boundary conditions using the supercell approximation, in which the cell is made additionally larger in order to avoid the system interacting with its own periodic image.

2.5 Basis set superposition error

Basis set superposition error (BSSE) is an error that arises in the calculation of binding energies due to the incompleteness of the basis set. As EDA calculations are grounded on binding energy calculations, appreciation of BSSE is equally important within these types of calculations also. The (BSSE-uncorrected) binding of two molecules A and B that form the complex AB may be expressed as

$$\Delta E(AB) = E_{AB}(AB) - E_A(A) - E_B(B) \quad (2.34)$$

where $E(X)$ is the energy of the molecule or complex X , and where the subscript denotes the basis set used during the energy calculation. The BSSE error arises from the inconsistent treatment of the isolated molecules that are able to access the functions of the partner molecules [60]. This unbalanced basis set which provides the complex with greater variational freedom than the isolated molecules allows the complex to reach an artificially lower energy, therefore resulting in an artificial increase in the calculated binding energy.

The Boys and Bernardi counterpoise correction (CP) [61] for BSSE attempts to re-balance the basis sets used in the binding energy calculation. The CP correction to the binding energy, ΔE_{BSSE} , may be expressed as the total of the CP corrections for the molecules A and B , $\Delta E_{\text{BSSE}}(A)$ and $\Delta E_{\text{BSSE}}(B)$ respectively, as

$$\Delta E_{\text{BSSE}}(A) = E_A(A) - E_{AB}(A) \quad (2.35a)$$

$$\Delta E_{\text{BSSE}}(B) = E_B(B) - E_{AB}(B) \quad (2.35b)$$

$$\Delta E_{\text{BSSE}} = \Delta E_{\text{BSSE}}(A) + \Delta E_{\text{BSSE}}(B) \quad (2.35c)$$

The CP-corrected binding energy is therefore given by

$$\begin{aligned} \Delta E(AB) &= E_{AB}(AB) - E_A(A) - E_B(B) + \Delta E_{\text{BSSE}} \\ &= E_{AB}(AB) - E_{AB}(A) - E_{AB}(B) \quad . \end{aligned} \quad (2.36)$$

This correction has been argued to overestimate the error [62] due to the fact that basis functions on the partner molecule will be occupied and so should not be available, whilst others argue the problem to be a reflection of other errors [60]. Additionally, this correction is one of a number of possible treatments for the BSSE [60].

2.6 Core electrons

The core electrons of an atom are those other than the valence electrons. Since the valence electrons determine almost all of a given system's electronic structure, we may simplify our picture of the core electrons and reduce the computational cost of calculations significantly. This can be done while at the same time still maintaining high physical accuracy. Additionally, the problem of modelling the electron states close to the nuclear centres is an important reason for making this approximation. Due to the requirement for the wavefunctions of the core electrons to be orthogonal, rapid oscillations in the core electron wavefunctions are observed near to the nucleus. Describing these wavefunctions accurately in plane wave DFT would therefore be highly expensive.

The pseudopotential method [63; 64] is an approach that seeks to simplify the core region by describing the core electrons and nucleus by more approximate means. Commonly, pseudopotentials are determined using conventional wavefunction methods, and it may not be immediately clear whether or not such pseudopotentials are suited to DFT calculations. However, in practise this has been shown not to present an issue for example in the work of Russo et al. [65]. Pseudopotentials may incorporate relativistic effects, in which case they are referred to as 'relativistic' pseudopotentials. These effects are of important consideration in heavier elements, as in such elements the electrons closer to the core travel at velocities close to the speed of light.

Norm-conserving pseudopotentials are those that satisfy the condition of norm-conservation. The condition of norm-conservation is expressed by the charge density within the core region for the pseudo wavefunction $\tilde{\phi}(\mathbf{r})$ equalling that of the all-electron wavefunction $\phi(\mathbf{r})$, as

$$\int_0^{r_c} |\tilde{\phi}(\mathbf{r})|^2 d\mathbf{r} = \int_0^{r_c} |\phi(\mathbf{r})|^2 d\mathbf{r} \quad (2.37)$$

where r_c is the cut off distance from the nucleus that defines the core region. This is a desirable property of the pseudopotential, designed to reproduce the scattering properties of the nuclei and maximise transferability to different systems.

The pseudopotential \hat{V}_{ps} can be split into a local \hat{V}_{loc} and non-local \hat{V}_{nl} part as

$$\hat{V}_{\text{ps}} = \hat{V}_{\text{loc}} + \hat{V}_{\text{nl}} \quad . \quad (2.38)$$

The local potential is simple to calculate, but the non-local part is less easily calculated. The Kleinman-Bylander [64] form of the non-local potential is given by

$$\hat{V}_{\text{KB}} = \hat{V}_{\text{loc}} + \sum_{lm} \frac{|\delta\hat{V}_l\phi_{lm}\rangle\langle\phi_{lm}\delta\hat{V}_l|}{\langle\phi_{lm}|\delta\hat{V}_l|\phi_{lm}\rangle} \quad (2.39)$$

where ϕ_{lm} are the pseudo-atom wavefunctions and $\delta\hat{V}_l$ is an operator dependent on the angular momentum l .

An alternative type of pseudopotential used in plane wave DFT calculations is the ultrasoft pseudopotential [66], in which smooth pseudo wavefunctions are used which require lower kinetic energy cut-offs. These pseudopotentials are not norm-conserving. A different approach to the use of pseudopotentials for modelling the core electrons is the projector-augmented wave method (PAW) approach [67], which typically uses the frozen core approximation to model the core electrons.

2.7 Linear-scaling density functional theory

Scaling of ab initio methods with system size is an important consideration when performing calculations as this will largely determine limitations of the size of computable systems. For example, in Hartree-Fock calculations the computational cost scales as $\mathcal{O}(N^4)$ with respect to the number of basis functions due to the bottleneck in calculating the two-electron integrals (without approximations). For other wavefunction-based methods this scaling can be even more prohibitive, e.g. third-order Møller-Plesset perturbation theory (MP3) in which the cost scales as $\mathcal{O}(N^6)$. In Kohn-Sham DFT the cost scales as $\mathcal{O}(N^3)$ due to the bottleneck of diagonalisation of the Hamiltonian matrix, as well as multiplication and inversion of matrices that are dense.

Clearly, performing conventional electronic structure calculations on large systems using these methods would be extremely challenging using the computational resources available today. Examples of larger systems that are of importance for study include proteins, biomolecules and nanostructures. It is clear that in order to investigate such systems, approximations that reduce the computational cost are necessary. From this need, linear-scaling methods ($\mathcal{O}(N)$) have been developed. For further in depth discussions of linear-scaling methods, we refer the reader to the reviews of Goedecker [68] and Bowler and Miyazaki [69].

In this section, we briefly introduce a number of key concepts that relate to the formulation of linear-scaling DFT approaches, and in particular the ONETEP approach.

2.7.1 The near-sightedness of electronic matter

The near-sightedness of electronic matter in many-atom systems was recognised and discussed qualitatively by Walter Kohn in 1996 [70; 71]. This is the idea that regions of large systems are local, i.e. that they are effectively isolated from the interaction from other regions when separated by a large enough distance.

This important concept can be applied in the development of linear-scaling methods. We begin by introducing the one-particle density matrix $\rho(\mathbf{r}, \mathbf{r}')$ for a set of MOs $\{\psi_i\}$,

$$\rho(\mathbf{r}, \mathbf{r}') = \sum_i^{N_{\psi(\text{occ})}} \psi_i(\mathbf{r}) \psi_i^*(\mathbf{r}') \quad (2.40)$$

where $N_{\psi(\text{occ})}$ is the number of (singly) occupied orbitals ($\equiv N$). The electronic density is obtained from the diagonal elements of the one-particle density matrix $\rho(\mathbf{r}, \mathbf{r}')$ as,

$$n(\mathbf{r}) = \sum_i^{N_{\psi(\text{occ})}} \psi_i(\mathbf{r}) \psi_i^*(\mathbf{r}) = \rho(\mathbf{r}, \mathbf{r}) \quad . \quad (2.41)$$

Ismail-Beigi and Arias [72] showed the density matrix $\rho(\mathbf{r}, \mathbf{r}')$ to decay exponentially for insulating systems

$$\rho(\mathbf{r}, \mathbf{r}') \propto e^{-\gamma|\mathbf{r}-\mathbf{r}'|} \quad (2.42)$$

where γ is a constant that depends on the band gap of the system. From this we can expect that truncating elements of $\rho(\mathbf{r}, \mathbf{r}')$ that are above a certain threshold distance \mathbf{r}_{cut} apart, i.e.

$$\rho(\mathbf{r}, \mathbf{r}') = 0 \text{ when } |\mathbf{r} - \mathbf{r}'| > \mathbf{r}_{\text{cut}} \quad (2.43)$$

will reduce computational cost (as we will no longer need to evaluate these elements) with minimal introduction of error (as these interactions provide the least contribution).

2.7.2 Localised orbitals

Another typical requirement for linear-scaling capability is the spatial truncation of the basis set to within a localisation region. For delocalised basis sets such as

plane waves, localisation must be enforced by certain means. The expansion of the nonorthogonal generalised Wannier function (NGWF) [59] basis set within a specified localisation sphere in ONETEP [39; 59] is used to enforce localisation of the basis functions, as will be discussed later.

2.7.3 The Li-Nunes and Vanderbilt method

The Li-Nunes and Vanderbilt (LNV) method [73; 74] is an approach to obtaining the variational solution to the density matrix whilst maintaining idempotency. The enforcement of idempotency of the density matrix is necessary and is equivalent to ensuring orthonormality of the Kohn-Sham states. This is achieved by making use of the McWeeny transformation [75], which is based on the formula

$$\tilde{P} = 3P^2 - 2P^3 \quad . \quad (2.44)$$

With truncation of the density matrix (Eq. 2.43) and use of sparse algebra the computational cost of the LNV approach has the capacity to scale linearly with system size.

2.8 The ONETEP package

The work described in Chapter 5 of this thesis has been implemented in the ONETEP quantum chemistry package. This is a parallelised, linear-scaling Kohn-Sham DFT code based on a reformulation of the plane wave pseudopotential method and is well suited to calculations of systems of very large size using high-performance computing systems.

ONETEP uniquely differs from conventional DFT approaches in two fundamental ways. Firstly, ONETEP uses a strictly localised basis set that is truncated to within a given localisation sphere. Through this, ONETEP exploits the near-sightedness of electronic matter and is able to achieve linear-scaling with respect

to system size. Secondly, the basis set itself is self-consistently optimised during the energy minimisation procedure. Additionally, this plane-wave like basis set affords ONETEP very high accuracy in its results.

In this section, we introduce the theory of the ONETEP approach required to describe our EDA method implementation.

2.8.1 The non-orthogonal generalised Wannier function basis set

Here we introduce the non-orthogonal generalised Wannier functions (NGWFs) that are used as a basis set in ONETEP calculations. In the following equations, the Einstein convention of implicit summation over repeated Greek indices is adopted unless stated otherwise.

We begin expressing the NGWFs $\{|\phi_\alpha\rangle\}$ by their expansion in a basis of N_p periodic cardinal sine (psinc) functions [76; 77] $\{D_p\}$,

$$\phi_\alpha(\mathbf{r}) = \sum_{p=1}^{N_p} D_p(\mathbf{r}) c_{p\alpha} \quad (2.45)$$

where $c_{p\alpha}$ are the expansion coefficients. The psinc functions are centred on a regular grid that spans the whole simulation cell, and the grid point each psinc function is centred on is given by the index p . These cell-periodic psinc functions can be expressed as a sum over a finite set of plane-waves. The expression for a psinc function located at the grid coordinate vector \mathbf{r}_p is given by

$$\begin{aligned} D_p(\mathbf{r}) &= D(\mathbf{r} - \mathbf{r}_p) \\ &= \frac{1}{N_p} \sum_{\mathbf{G}}^{\mathbf{G}_c} e^{i\mathbf{G} \cdot (\mathbf{r} - \mathbf{r}_p)} \end{aligned} \quad (2.46)$$

where \mathbf{G} is a reciprocal lattice vector which is iterated up to the cutoff wavevector \mathbf{G}_c . The reciprocal lattice vector \mathbf{G} is given by

$$\mathbf{G} = m_1 \mathbf{b}_1 + m_2 \mathbf{b}_2 + m_3 \mathbf{b}_3 \quad (2.47)$$

where m_1 , m_2 and m_3 are integers and b_1 , b_2 and b_3 are the primitive lattice vectors of a reciprocal Bravais lattice. The modulus of the cutoff wavevector \mathbf{G}_c , which determines the quality of the psinc basis set, is related to the plane-wave kinetic energy E_c by

$$E_c = \frac{1}{2} |\mathbf{G}_c|^2 \quad . \quad (2.48)$$

Increasing the value of the kinetic energy cutoff increases \mathbf{G}_c and therefore increases the completeness of the basis set (see Eq. 2.46). A one-dimensional plot of the function $D_0(\mathbf{r})$ is displayed in Fig. 2.1.

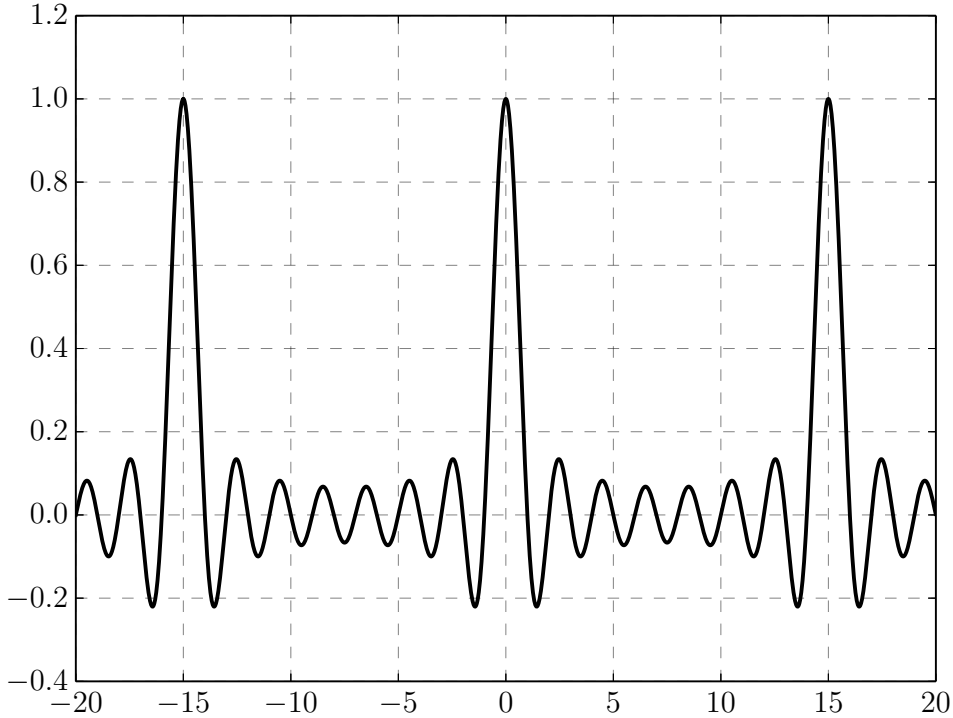


Figure 2.1: A one-dimensional representation of the $D_0(\mathbf{r})$ psinc function centered at 0, with 15 grid points in the cell dimension.

During the optimisation of the NGWF basis functions, strict localisation is enforced by repeated truncation of the expansion coefficient contributions $c_{p\alpha}$ outside

of a localisation sphere R_α , i.e.

$$c_{p\alpha} = 0 \quad \text{if} \quad |\mathbf{R}_\alpha - \mathbf{r}_p| > R_\alpha \quad (2.49)$$

where \mathbf{R}_α is the centre of the localisation region of the NGWF ϕ_α , \mathbf{r}_p is the coordinate of the psinc basis function, and R_α is the NGWF localisation radius.

In the ONETEP formalism, the set of KS orbitals $\{|\psi_i\rangle\}$ can be considered as linear combinations of the set of strictly localised NGWFs $\{|\phi_\alpha\rangle\}$ as,

$$\psi_i(\mathbf{r}) = \phi_\alpha(\mathbf{r}) M_i^\alpha \quad . \quad (2.50)$$

where $\{M_i^\alpha\}$ are the KS MO expansion coefficients.

Orthonormality of $\{|\psi_i\rangle\}$ is a necessary physical constraint for the Pauli principle to be respected, which can be expressed as,

$$\sigma_{ij} = \langle \psi_i | \psi_j \rangle = (M^\dagger)_i^\alpha S_{\alpha\beta} M_j^\beta = \delta_{ij} \quad (2.51)$$

where the NGWF overlap matrix $S_{\alpha\beta}$ is given by,

$$S_{\alpha\beta} = \langle \phi_\alpha | \phi_\beta \rangle \quad (2.52)$$

By substitution of Eq. 2.50 into Eq. 2.40, we introduce the density kernel $K^{\alpha\beta}$ as the representation of the density operator in terms of NGWFs,

$$\rho(\mathbf{r}, \mathbf{r}') = \phi_\alpha(\mathbf{r}) K^{\alpha\beta} \phi_\beta^*(\mathbf{r}') \quad (2.53)$$

where the density kernel matrix $K^{\alpha\beta}$ is given by,

$$K^{\alpha\beta} = \sum_i^{N_\psi} M_i^\alpha f_i (M^\dagger)_i^\beta \quad (2.54)$$

where f_i are the MO occupancies which are equal to 1 for the occupied MOs. In an analogous fashion to truncation of the psinc expansion coefficients outside of

the localisation sphere, the density matrix is also truncated when NGWF centres are separated by more than a specified cutoff radius.

2.8.2 The ONETEP Kohn-Sham energy expression

In ONETEP, a number of different calculation tasks are available. These include, for example, geometry optimisation, population analysis, electrostatic potential, and charge density calculations. Running EDA calculations, such as the approach we have implemented in ONETEP described in this thesis, generally involves performing a series of total energy calculations on a given system under study, and subtracting these energies to yield the EDA energy components. The specific theory of our EDA implementation is described in further detail in Chapter 5, however it is necessary to first introduce the total energy calculation in ONETEP that underlies this approach.

In ONETEP, we typically use pseudopotentials to model core electrons, and calculate the ion-ion interactions using an Ewald sum. The expression of the total energy in ONETEP is given by,

$$E[n] = T[n] + E_{\text{nl}}[n] + E_{\text{loc}}[n] + E_{\text{H}}[n] + E_{\text{xc}}[n] \quad (2.55)$$

where T is the kinetic energy, E_{nl} and E_{loc} are the non-local and local components of the pseudopotential energy, E_{H} is the Hartree energy and E_{xc} is the exchange-correlation energy.

The calculation of the total energy in ONETEP is organised as two nested loops. Having constructed an initial set of NGWFs with expansion coefficients $\{c_{p\alpha}\}$, and a density kernel $K^{\alpha\beta}$, the inner loop begins by minimising the energy of $K^{\alpha\beta}$ with the NGWFs held fixed until convergence. In the outer loop, the kernel is held fixed and the expansion coefficients $\{c_{p\alpha}\}$ optimised. Convergence of both loops yields the ground-state density with ground state energy E_0 .

2.8.3 Inner loop optimisation: the density kernel

During minimisation of the inner loop, constraints must be placed on the kernel to ensure both physicality of the quantities and linear-scaling capability [78]. The kernel must respect the localisation condition

$$K^{\alpha\beta} = 0 \quad \text{when} \quad |\mathbf{R}_\alpha - \mathbf{R}_\beta| > \mathbf{R}_{\text{cut}} \quad (2.56)$$

where \mathbf{R}_α and \mathbf{R}_β are the centres of the localisation regions of the NGWFs ϕ_α and ϕ_β , and \mathbf{R}_{cut} is the kernel cutoff radius [39]. Additionally, the idempotency constraint

$$K^{\alpha\gamma} S_{\gamma\delta} K^{\delta\beta} = K^{\alpha\beta} \quad (2.57)$$

is used to fix the orbital occupancies to one and zero and ensure orbital orthogonality. Finally, the number of electrons in the system must also be conserved as

$$2 \text{tr}[K^{\alpha\gamma} S_{\gamma\beta}] = N \quad (2.58)$$

for a spin unpolarised system.

The LNV method makes use of the McWeeny transformation [75] to enforce the necessary physical constraint of idempotency on the density matrix. As described earlier, enforcing idempotency of the density kernel is equivalent to imposing orthonormality of the Kohn-Sham orbitals. An auxiliary matrix σ is used to define the density matrix ρ as

$$\rho(\mathbf{r}, \mathbf{r}') = 3\sigma^2(\mathbf{r}, \mathbf{r}') - 2\sigma^3(\mathbf{r}, \mathbf{r}') \quad (2.59)$$

where σ is defined in terms of the auxiliary density kernel L as

$$\sigma(\mathbf{r}, \mathbf{r}') = \phi_\alpha(\mathbf{r}) L^{\alpha\beta} \phi_\beta(\mathbf{r}') \quad . \quad (2.60)$$

Given an auxiliary kernel L with occupancies in the range $(\left[\frac{1-\sqrt{5}}{2}\right], \left[\frac{1+\sqrt{5}}{2}\right])$, a ‘weakly idempotent’ kernel K (i.e. with occupancies in the range $[0, 1]$) is produced using the purification transformation

$$K = 3LSL - 2LSLSL \quad . \quad (2.61)$$

By optimising the auxiliary kernel L to minimise the energy $E[\rho]$, the density kernel will automatically be driven towards idempotency. This approach therefore avoids the $\mathcal{O}(N^3)$ problem of matrix diagonalisation, which would otherwise be needed for orbital orthonormalisation.

At each inner loop iteration m , a new auxiliary density kernel $L^{(m+1)}$ is found by line-search using a direct energy minimisation method such as the conjugate-gradients or steepest-descents techniques. The search direction for this direct energy minimisation is based on the gradient [79]

$$\frac{\partial E}{\partial L^{\alpha\beta}} = 6(SLH + HLS)_{\beta\alpha} - 4(SLSLH + SLHLS + HLSLS)_{\beta\alpha} \quad . \quad (2.62)$$

Whilst the LNV approach is used to drive the density kernel to idempotency in ONETEP, conservation of the number of electrons is also enforced. The chemical potential μ is used as a Lagrange multiplier to solve this problem and ensure that the functional minimum has the correct electron count. Instead of minimising the energy, we now seek to minimise the grand potential $\Omega = E - \mu N$. During the minimisation, μ remains an unknown quantity. Three methods are used in ONETEP to impose this normalisation [78]. Firstly, the purified electron number may be constrained as (for the spin unpolarised case)

$$\begin{aligned} 2 \operatorname{tr}(\rho) &= 2 \operatorname{tr}(KS) \\ &= 2 \operatorname{tr}(3LSLS - 2LSLSLS) \\ &= N \quad . \end{aligned} \quad (2.63)$$

Secondly, the unpurified electron number may be constrained as,

$$\begin{aligned} 2 \operatorname{tr}(\sigma) &= 2 \operatorname{tr}(LS) \\ &= N \quad . \end{aligned} \quad (2.64)$$

Thirdly, a normalised and purified density kernel can be directly constructed by rescaling using the purification transformation

$$\rho = N \frac{3\sigma^2 - 2\sigma^3}{2 \operatorname{tr}(3\sigma^2 - 2\sigma^3)} \quad . \quad (2.65)$$

The gradient of the electron number is expressed as

$$\frac{\partial N}{\partial L_{\alpha\beta}} = 12(SLS - SL SLS)_{\alpha\beta} \quad (2.66)$$

and is used to fix the electron count to remain constant during the calculation.

At each step m , a new auxiliary kernel $L^{(m+1)}$ is calculated, and the McWeeny purification transformation (Eq. 2.61) used to construct a near-idempotent density kernel $K^{(m+1)}$. This procedure has linear scaling cost, enabled by the sparsity of H , L and S due to the localisation constraints imposed during the calculation.

2.8.4 Outer loop optimisation: the NGWFs

Having converged the inner loop to obtain the optimised kernel K for the set of NGWFs $\{|\phi_\alpha\rangle\}$, the outer loop optimises the expansion coefficients $c_{p\alpha}$. This optimisation is performed whilst imposing the constraints of strict localisation of the functions (using Eq. 2.49), idempotency of the density kernel, and conservation of the electron count. A line-search step is performed to minimise the energy with respect to the NGWFs. The search direction is again calculated using direct energy minimisation methods using the gradient [79] of the NGWFs,

$$\frac{\delta E}{\delta \phi_\alpha^*(\mathbf{r})} = 2[\hat{H}\phi_\beta(\mathbf{r})K^{\beta\alpha} + \phi_\beta(\mathbf{r})Q^{\beta\alpha}] \quad (2.67)$$

where,

$$Q = 3LHL - 2LSLHL - 2LHLSL \quad . \quad (2.68)$$

For a fully converged density kernel, the Hamiltonian and density kernel commute,

$$HKS = SKH, \quad (2.69)$$

and the kernel has the relationship

$$KSK = K = L = LSL \quad (2.70)$$

due to convergence of K and idempotency of this quantity. These two relationships can be used to simplify the expression of Q given in Eq. 2.68 above. Substituting Eq. 2.70 into Eq 2.68 yields

$$\begin{aligned} Q &= 3KHK - 2KSKHK - 2KHKSK \\ &= 3KHK - 2KHK - 2KHK \\ &= -KHK \\ &= -KHKSS^{-1} \end{aligned} \quad (2.71)$$

and by substituting Eq. 2.69 into this expression we obtain

$$\begin{aligned} Q &= -KSKHS^{-1} \\ &= -KHS^{-1} \quad . \end{aligned} \quad (2.72)$$

The derivative of the electron number with respect to the NGWFs is given by

$$\frac{\delta N}{\delta \phi_{\alpha}^*(\mathbf{r})} = 12\phi_{\beta}^*(\mathbf{r})(SLS - SLSLS)^{\beta\alpha} \quad (2.73)$$

and is used to constrain the electron number of the system during the NGWF optimisation step. On convergence of the NGWF gradient, which indicates that

the psinc basis has been optimised, the ground-state energy has been found.

ONETEP uses sparse algebra in calculation of the quantities involved during the optimisation of the inner and outer loops. By also using a kernel cutoff with the strictly localised basis functions, the code achieves an overall linear-scaling cost. ONETEP is also highly parallelised and able to efficiently partition the computational problems that must be solved over many CPUs. For this reason, ONETEP is highly suited to the calculation of large-scale systems using high-performance computing systems.

Chapter 3

Current biomolecular energy decomposition analysis approaches

A primary aim of this work is to identify the EDA method or methods with greatest suitability to the analysis of interaction energies in biomolecular systems. Towards this goal, we introduce here the theory of a selection of important EDA approaches and assess their theoretical strengths and weaknesses. In [Chapter 4](#) that follows this, we quantify the success of these EDA approaches by benchmarking against six test sets of molecules that display biomolecular-like interactions.

The EDA schemes can be categorized by the nature of their underlying theory. The character of the schemes may be described as either variational, in which the interaction energy is decomposed by use of intermediate wavefunctions or electron densities, or alternatively as perturbation based, in which the interaction between the fragments is seen as a perturbation to the non-interacting fragments and the interaction is constructed as corrections resulting from different physical effects. In this chapter, we begin by providing an overview of notable studies applying EDA in literature. Next, we introduce a number of common quantities which we use to describe the theory of the EDA approaches. Using this framework, we

describe the variational and perturbation based EDAs, and summarise each of these approaches.

3.1 Previous applications of energy decomposition analysis

Investigations using EDA approaches are naturally well suited to evaluations of molecular bonding forces, and EDA has been used in a wide range of applications in quantum chemistry. The EDA studies in literature typically feature systems of relatively small size (up to tens of atoms) for both the variational [12–15; 80–89] and perturbation approaches [90–93], and for biomolecular systems approaches such as molecular mechanics (MM) are sometimes combined with the QM region [94; 95]. Here we discuss a number of these applications in literature.

EDA calculations in the literature have typically been performed to evaluate newly developed EDA methodologies, to quantify the driving forces of association in the studied systems, or for both reasons. The water dimer has been frequently adopted as a theoretical test model for the purpose of evaluating new EDA approaches [12; 13; 15; 80; 81; 83; 84; 96] as this system is exemplary of a typical hydrogen bonding interaction. Other small interacting systems also studied include the benzene dimer system [14; 88; 93], the water – alkali metal cation series [15; 80; 82; 83] and the ammonia – hydrogen fluoride [81; 86; 90] system.

EDA calculations of drug – water clusters have also been performed. For example, investigations were performed by Esrafil and Behzadi [97] on the hydrogen bonding interaction of aspirin (and fluorine-substituted aspirin) with (water)_{n=1–3}. This work included symmetry-adapted perturbation theory (SAPT) and natural bond orbital (NBO) second-order perturbation theory analyses, as well as density partitioning using Bader’s quantum theory of atoms in molecules (QTAIM) [98] approach.

Investigations of larger biomolecules are also noted in the EDA literature. These are typically performed by EDA calculations on smaller derived truncated systems, rather than on the whole biomolecular system itself. Truncated active-site systems of a Cl^-/H^+ exchange transporter protein (EcClC) were studied with Kitaura-Morokuma (KM) EDA and natural EDA (NEDA) by Church et al. [99] for example. A number of EDA investigations of cytochrome P450 have also been performed [94; 95; 100]. Thellamurege investigated the interaction of a water molecule with cytochrome P450, specifically with the ferric heme group and compound I intermediate of this biomolecule [100]. This investigation was performed using the LMO EDA [14] and the extended transition state (ETS) EDA developed by Ziegler and Rauk [101–103]. The results revealed electrostatic and polarisation effects to be dominant in the interactions within these systems.

The possibility of EDA on larger systems also has been evidenced. Hirao performed an EDA of the ONIOM(B3LYP:AMBER) QM/MM interaction energy of the compound I intermediate of cytochrome P450cam to investigate the effect of the protein environment on this state [95]. This work found electrostatics to be the most dominant contribution to the interaction energy, followed by van der Waals and polarisation contributions. The calculations of this investigation involved thousands of atoms present in the protein environment, and even though this involved a QM/MM-based variant of EDA, this study offers an example of EDA application to an entire protein. An earlier investigation by Hirao using this method was also performed on the non-heme diiron enzyme myo-inositol oxygenase [94]. The aim of this investigation was to assess the effects of the protein environment and intracuster dispersion in the process of oxygen binding to this enzyme. This found dispersion to be the most dominant contribution to the interaction energy, which was enhanced to a lesser degree by electrostatic, van der Waals, and polarisation effects. This work notes that because entropic effects do not favour the bonding of oxygen, overall this process is almost thermoneutral. This demonstrates a limitation of pure interaction energy investigations: the interaction energy (or enthalpy) itself is also one of the components that control the

thermodynamics of binding, the other being the entropy of binding.

Another established approach to large scale energy calculations is the fragment molecular orbital (FMO) framework of Kitaura et al. [104–107]. This approach involves the partitioning of a system into a number of smaller fragments, with the total system energy calculated using the FMOs of these fragments. This fragmentation reduces computational cost whilst maintaining accuracy and a number of studies have been performed on important protein–receptor systems using the FMO approach investigating binding affinities and the interaction energies of fragments. Examples of these studies include calculations performed on the human immunodeficiency virus type 1 (HIV-1) protease complexed with lopinavir [108; 109], the HIV-1 antibody 2G12 [110; 111], the influenza virus surface protein hemagglutinin [112–122], prion protein [123–125], the estrogen receptor [126–128], the vitamin D receptor [129–132], and the retinoid X receptor [133–135]. The pair interaction EDA (PIEDA) scheme [96] has been developed in the FMO framework, and a discussion of the PIEDA approach is included later in this chapter. The PIEDA scheme has been used to investigate contributions to stabilisation in various conformers in the evolution of amide stacking in larger γ -peptides [136], and to investigate DNA recognition modulation in artificial zinc–finger proteins using PIEDA maps [137].

Investigations are not limited to low atomic mass compositions. EDA calculations of the bonding in more exotic systems have been published, such as in the transition metal–oxime bond [138] and the transition metal–imine bond [139] by Bayat et al., and work by Marjolin et al. [140] has sought to seek the components of interactions within mono aqua complexes of various lanthanide and actinide cations. This work investigating lanthanide and actinide cation interactions was achieved using a modified constrained space orbital variation (CSOV) EDA scheme [11; 141] with small and large core pseudopotentials.

3.2 Common EDA wavefunctions

It is useful to adopt a unified notation of the wavefunctions (and their derived charge densities) shared between the EDA schemes we consider in this chapter. Starting with the direct calculation of the interaction energy, we define the commonly used electronic Slater determinant wavefunctions $\Psi_A^{0,AB}$, $\Psi_B^{0,AB}$ and Ψ_{AB} and other related intermediate wavefunctions used to express the EDA theory. We denote the lower index as distinguishing the fragment(s) described by the wavefunction, and the upper index as distinguishing the basis in which the MOs of the wavefunction are expanded. The upper index zero describes wavefunctions constructed using the optimised MOs of fragments in isolation. The Boys and Bernardi [61] counterpoise (CP) corrected binding energy calculation may be expressed as,

$$\Delta E = E[\Psi_{AB}] - E[\Psi_A^{0,AB}] - E[\Psi_B^{0,AB}] \quad (3.1)$$

where Ψ_{AB} , $\Psi_A^{0,AB}$, and $\Psi_B^{0,AB}$ are the variationally optimised wavefunctions for the AB complex and the isolated monomers A and B calculated in the full AB basis. Furthermore, two similar sets of wavefunctions $\Psi_A^{0,AB_{occ}}$, $\Psi_B^{0,AB_{occ}}$ and $\Psi_A^{0,AB_{vir}}$, $\Psi_B^{0,AB_{vir}}$ may be derived to facilitate the partitioning of the CP correction into a contribution from ghost occupied orbitals of the adjacent fragments and from ghost virtual orbitals of the adjacent fragments. These wavefunctions are constructed in the same manner as $\Psi_A^{0,AB}$, and $\Psi_B^{0,AB}$, but using either the occupied or virtual orbitals of the adjacent fragments as given by the upper index. We define the wavefunctions for the monomers calculated in their own basis as,

$$\Psi_A^{0,A} = \hat{A} \left(\prod_a^{\text{on } A} \psi'_a \right) \quad (3.2a)$$

$$\Psi_B^{0,B} = \hat{B} \left(\prod_b^{\text{on } B} \psi'_b \right) \quad (3.2b)$$

where \hat{A} is the antisymmetriser and $\{\psi'_a\}$ and $\{\psi'_b\}$ represent the optimised MOs of the isolated monomers A and B respectively.

A number of many-electron intermediate wavefunctions are defined for the complex AB using combinations of the MOs of the monomers A and B . The first set of wavefunctions of this type, $\Psi_{AB}^{0,A/B,\text{Hartree}}$ and $\Psi_{AB}^{0,AB,\text{Hartree}}$, are constructed as the Hartree product of the individual monomer Slater determinant wavefunctions. This means that interfragmental exchange is not included in the energies of these two wavefunctions. As before, a key feature of these wavefunctions is the basis in which the individual monomer MOs are optimised. The wavefunction $\Psi_{AB}^{0,A/B,\text{Hartree}}$ is constructed using the MOs of the individual monomers A and B optimised in isolation in their own basis, and the wavefunction $\Psi_{AB}^{0,AB,\text{Hartree}}$ is constructed using the monomer MOs optimised in isolation in the full AB basis:

$$\Psi_{AB}^{0,A/B,\text{Hartree}} = \left[\Psi_A^{0,A} \cdot \Psi_B^{0,B} \right] \quad (3.3a)$$

$$\Psi_{AB}^{0,AB,\text{Hartree}} = \left[\Psi_A^{0,AB} \cdot \Psi_B^{0,AB} \right] \quad . \quad (3.3b)$$

The second set of wavefunctions of this type are $\Psi_{AB}^{0,A/B}$ and $\Psi_{AB}^{0,AB}$ which are constructed in the same manner as $\Psi_{AB}^{0,A/B,\text{Hartree}}$ and $\Psi_{AB}^{0,AB,\text{Hartree}}$ but taking the antisymmetric product of the monomer MOs as,

$$\Psi_{AB}^{0,A/B} = \hat{A} \left(\Psi_A^{0,A} \cdot \Psi_B^{0,B} \right) \quad (3.4a)$$

$$\Psi_{AB}^{0,AB} = \hat{A} \left(\Psi_A^{0,AB} \cdot \Psi_B^{0,AB} \right) \quad . \quad (3.4b)$$

These wavefunctions do not obey the Pauli exclusion principle due to lack of orthogonality of the MOs between the different fragments. This presents a source of difficulty when attempting to rigorously ascribe physical meaningfulness to energy components that are calculated using these wavefunctions.

3.3 Common EDA charge densities

In this section we describe the charge densities corresponding to the intermediate wavefunctions above which are used to provide a description of the NEDA scheme theory [12; 13; 82; 83]. Similar to the wavefunction indices' definitions, we use the lower index to denote the fragment(s) described by the charge density and the upper index to denote the basis in which the density is constructed. The construction of charge densities within the NEDA scheme proceeds by decomposition of the charge density of the AB supermolecule rather than by construction from the monomer charge densities, and all charge densities of this scheme are calculated in the full AB basis. We also distinguish densities optimised in isolation by an upper index zero.

The charge densities n_{AB}^{AB} , $n_A^{0,AB}$ and $n_B^{0,AB}$ describe the charge densities of the fully optimised AB supermolecule and the isolated monomers A and B respectively. The descriptions of these charge densities complement the commonly used wavefunctions Ψ_{AB} , $\Psi_A^{0,AB}$ and $\Psi_B^{0,AB}$ respectively. The charge density of the AB supermolecule, n_{AB}^{AB} , is given by,

$$\begin{aligned} n_{AB}^{AB}(\mathbf{r}) = & \sum_{\alpha}^{\text{on } A} Z_{\alpha} \delta(\mathbf{r} - \mathbf{R}_{\alpha}) - 2 \sum_a^{\text{on } A} |\psi_a(\mathbf{r})|^2 \\ & + \sum_{\beta}^{\text{on } B} Z_{\beta} \delta(\mathbf{r} - \mathbf{R}_{\beta}) - 2 \sum_b^{\text{on } B} |\psi_b(\mathbf{r})|^2 \end{aligned} \quad (3.5)$$

where the nuclei of A and B are located at coordinates \mathbf{R}_{α} and \mathbf{R}_{β} with charge Z_{α} and Z_{β} respectively, and where $\{\psi_a\}$ and $\{\psi_b\}$ are the MOs of A and B respectively. The isolated monomer charge densities $n_A^{0,AB}(\mathbf{r})$ and $n_B^{0,AB}(\mathbf{r})$ are constructed in a similar manner as,

$$n_A^{0,AB}(\mathbf{r}) = \sum_{\alpha}^{\text{on } A} Z_{\alpha} \delta(\mathbf{r} - \mathbf{R}_{\alpha}) - 2 \sum_a^{\text{on } B} |\psi'_a(\mathbf{r})|^2 \quad (3.6a)$$

$$n_B^{0,AB}(\mathbf{r}) = \sum_{\beta}^{\text{on } B} Z_{\beta} \delta(\mathbf{r} - \mathbf{R}_{\beta}) - 2 \sum_b^{\text{on } B} |\psi'_b(\mathbf{r})|^2 \quad (3.6b)$$

where a and b span the MOs $\{\psi'_a\}$ and $\{\psi'_b\}$ of the isolated monomers A and B , and where these MOs have been variationally optimised in the full AB basis.

3.4 Kitaura-Morokuma EDA

The KM scheme [142; 143], extended from the scheme of Morokuma [9], is one of the earliest energy decomposition analysis schemes developed. This scheme is a widely used variational scheme limited to the RHF level of theory and which therefore excludes electronic correlation terms within the decomposition.

3.4.1 Kitaura-Morokuma EDA theory

The decomposition of the interaction energy within the KM EDA consists of the following terms [142; 143]:

$$\Delta E = \Delta E_{\text{ES}} + \Delta E_{\text{EX}} + \Delta E_{\text{POL}} + \Delta E_{\text{CT}} + \Delta E_{\text{MIX}} \quad (3.7)$$

where ΔE_{ES} is the electrostatic interaction between the monomers with their charge distributions undistorted, ΔE_{EX} is the exchange repulsion contribution that describes the interaction of exchange between the undistorted monomer charge distributions (and includes the short-range repulsion resulting from orbital overlap between the two fragments), ΔE_{POL} is the polarisation interaction on distorting the charge distributions of the monomers in the presence of their neighbouring monomer, ΔE_{CT} is the charge transfer energy that results from electron transfer from the occupied MOs of one monomer into the virtual MOs of its neighbouring monomer, and where the term ΔE_{MIX} describes contributions to the interaction energy that are not ascribable to a particular component.

We express the components of the KM EDA scheme except the charge transfer component in terms of energy functionals of the common wavefunctions described above. The electrostatic energy, ΔE_{ES} , is evaluated as the Coulomb energy on

taking the relaxed charge densities of the monomers in isolation to complex geometry,

$$\Delta E_{\text{ES}} = E[\Psi_{AB}^{0,A/B,\text{Hartree}}] - E[\Psi_A^{0,A}] - E[\Psi_B^{0,B}] \quad . \quad (3.8)$$

The exchange energy, ΔE_{EX} , is taken as the energy on forming the fully antisymmetrised wavefunction from the Hartree product intermediate wavefunction,

$$\Delta E_{\text{EX}} = E[\Psi_{AB}^{0,A/B}] - E[\Psi_{AB}^{0,A/B,\text{Hartree}}] \quad . \quad (3.9)$$

The definitions of the electrostatic and exchange terms take this general form in the majority of EDA schemes we discuss. After calculating these two components, the energy change on restricted variational optimisation of the Hartree product intermediate wavefunction leads to calculation of the polarisation energy component ΔE_{POL} ,

$$\Delta E_{\text{POL}} = E[\Psi_{AB}^{A/B,\text{Hartree}}] - E[\Psi_{AB}^{0,A/B,\text{Hartree}}] \quad (3.10)$$

where the intermediate wavefunction $\Psi_{AB}^{A/B,\text{Hartree}}$ is constructed by relaxation of the fragment orbitals of the Hartree product intermediate wavefunction $\Psi_{AB}^{0,A/B,\text{Hartree}}$ in the field of the neighbouring monomer. This term is denoted ΔE_{PL} within the original KM EDA, but to ensure continuity with the other schemes discussed in this thesis we term this component ΔE_{POL} . A diagram of the KM EDA scheme electrostatics, exchange and polarisation components is given within Fig. 3.1.

The charge transfer component is calculated as the energy resulting from charge transfer from the occupied MOs of one monomer to the virtual MOs of the other and vice versa. The calculation of this component may be described as the energy difference between two intermediate wavefunctions: one that includes this interfragmental interaction, and one that does not. The calculation of this energy component is more clearly demonstrated by use of modified overlap and Fock matrices for the AB complex. The charge transfer energy component of this scheme

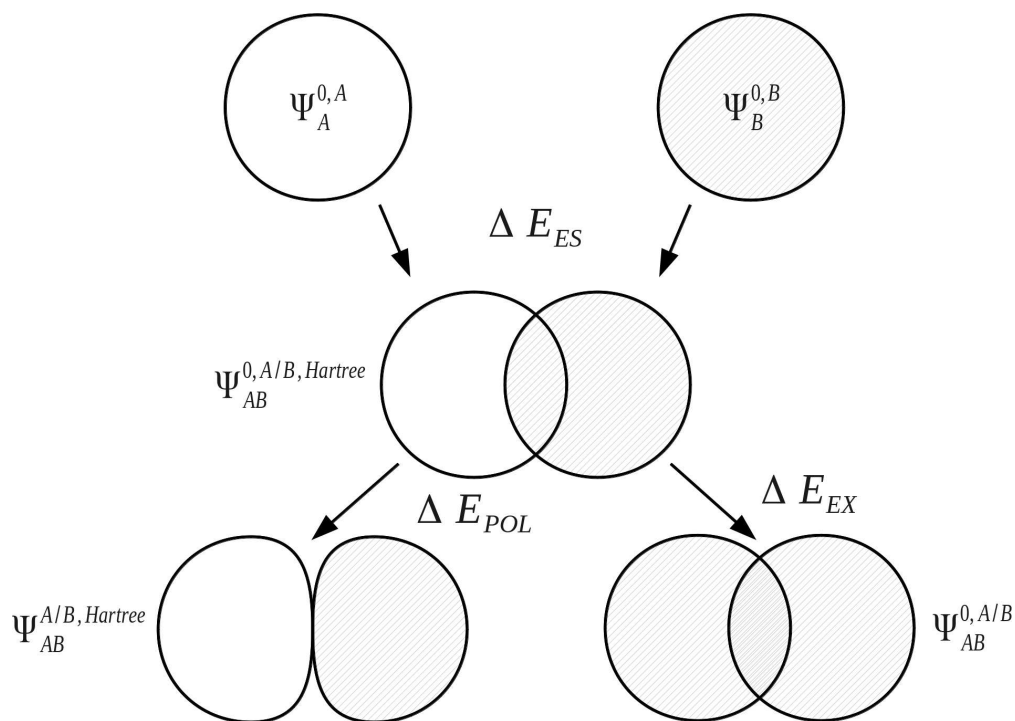


Figure 3.1: The Kitaura–Morokuma electrostatics, exchange and polarisation EDA components for the AB complex.

is calculated by setting to zero certain blocks of the complex Fock and overlap matrices that express specific chemical effects during the iteration cycles. The matrices of the complex are partitioned into blocks that involve the occupied and virtual orbitals of each monomer. The contribution of charge transfer effects to the interaction energy may be calculated as the difference between the energy of an intermediate set of matrices that have non-zero diagonal blocks which we name ‘ESX’ blocks that give an energy E^{ESX} , and another set of intermediate matrices that involve both the diagonal ‘ESX’ blocks and those blocks required to describe charge transfer effects which we name ‘CT’ blocks with energy $E^{\text{ESX+CT}}$. These matrices are shown diagrammatically within Fig. 3.2.

$$\Delta E_{\text{CT}} = E^{\text{ESX+CT}} - E^{\text{ESX}} \quad . \quad (3.11)$$

	<i>occ A vir A occ B vir B</i>					<i>occ A vir A occ B vir B</i>			
<i>occ A</i>	ESX				<i>occ A</i>	ESX			CT
<i>vir A</i>		ESX			<i>vir A</i>		ESX	CT	
<i>occ B</i>			ESX		<i>occ B</i>		CT	ESX	
<i>vir B</i>				ESX	<i>vir B</i>	CT			ESX
	(a)					(b)			

Figure 3.2: The partitioning of the Fock and overlap matrices for the KM EDA scheme for the evaluation of the charge transfer component. The set of matrices (a) that involve only the diagonal exchange and electrostatics interactions produces the energy E^{ESX} and the set of matrices (b) that involve these diagonal blocks and also the charge transfer blocks produces the energy $E^{\text{ESX+CT}}$. The labels ‘*occ*’ and ‘*vir*’ denote the sets of orbitals that are occupied and virtual on the monomers *A* and *B*.

A remainder ‘mixing’ term is defined to describe the contribution to the interaction energy not ascribable to any particular component of the scheme,

$$\Delta E_{\text{MIX}} = \Delta E - (\Delta E_{\text{ES}} + \Delta E_{\text{POL}} + \Delta E_{\text{CT}} + \Delta E_{\text{EX}}) \quad . \quad (3.12)$$

The KM theory described herein follows the implementation of Chen and Gordon [84]. Treatment of BSSE in this scheme applies the CP correction to the ΔE_{EX} and ΔE_{CT} terms only and the components ΔE_{ES} , ΔE_{POL} and ΔE_{MIX} remain as in the original KM EDA scheme. This treatment splits the CP correction to the interaction energy into two: one correction for the exchange component calculated by including the set of occupied orbitals of the adjacent fragments, and a second correction for the charge transfer component calculated by including the set of virtual orbitals of the adjacent fragments. The CP corrections to the ΔE_{EX}

term are given as,

$$\Delta E_{\text{BSSE,EX}(A)} = E[\Psi_A^{0,A}] - E[\Psi_A^{0,AB_{\text{occ}}}] \quad (3.13a)$$

$$\Delta E_{\text{BSSE,EX}(B)} = E[\Psi_B^{0,B}] - E[\Psi_B^{0,A_{\text{occ}}B}] \quad (3.13b)$$

$$\Delta E_{\text{BSSE,EX}} = \Delta E_{\text{BSSE,EX}(A)} + \Delta E_{\text{BSSE,EX}(B)} \quad (3.13c)$$

and the correction to ΔE_{CT} is given as,

$$\Delta E_{\text{BSSE,CT}(A)} = E[\Psi_A^{0,A}] - E[\Psi_A^{0,AB_{\text{vir}}}] \quad (3.14a)$$

$$\Delta E_{\text{BSSE,CT}(B)} = E[\Psi_B^{0,B}] - E[\Psi_B^{0,A_{\text{vir}}B}] \quad (3.14b)$$

$$\Delta E_{\text{BSSE,CT}} = \Delta E_{\text{BSSE,CT}(A)} + \Delta E_{\text{BSSE,CT}(B)} \quad (3.14c)$$

The calculations of these BSSE components are further described within Fig. 3.3 and 3.4.

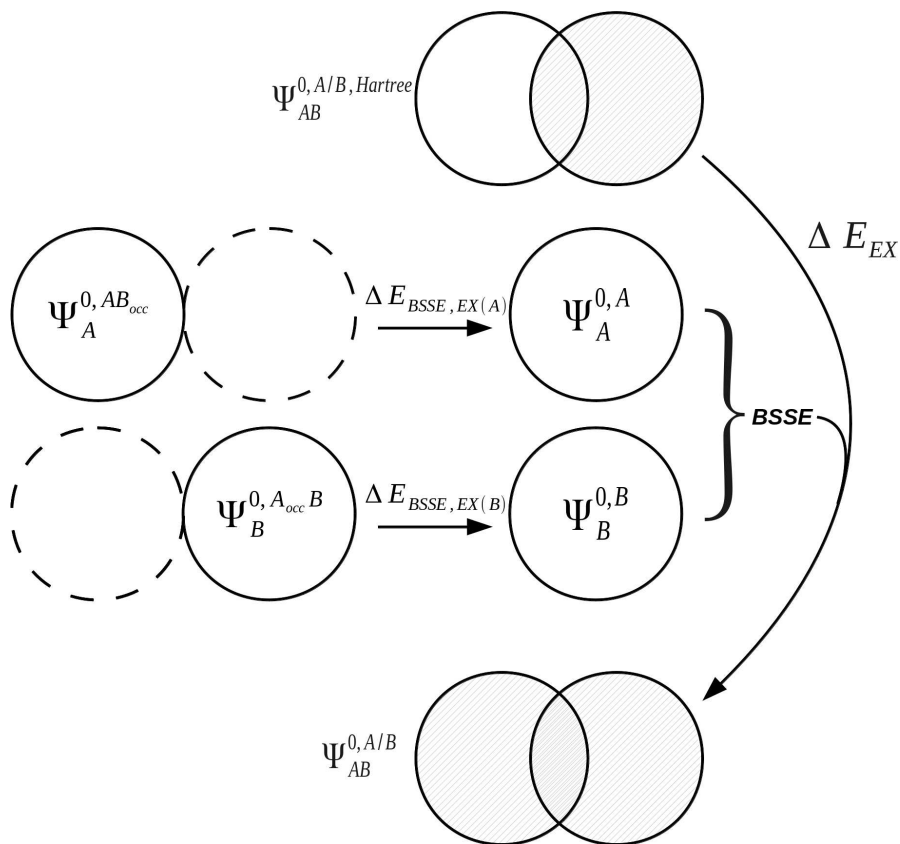


Figure 3.3: The treatment of BSSE for the exchange term within the KM EDA scheme. A BSSE correction due to the presence of the occupied orbitals of adjacent monomers is introduced to the exchange term.

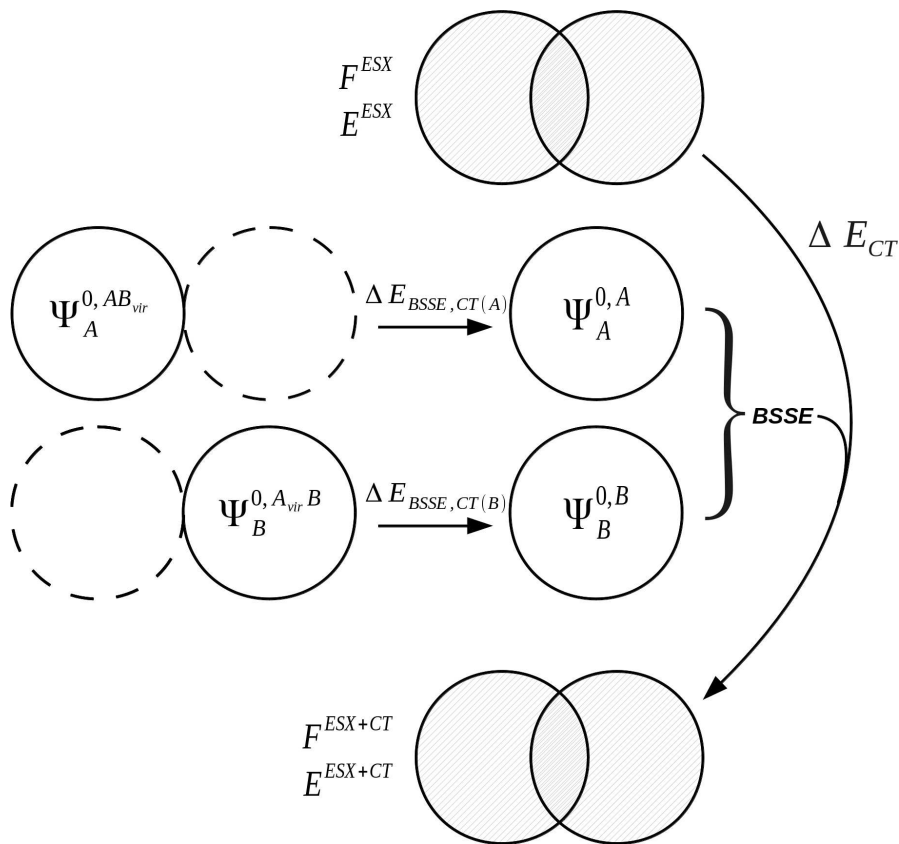


Figure 3.4: The treatment of BSSE for the charge transfer term within the KM EDA scheme. A BSSE correction due to the presence of the virtual orbitals of adjacent monomers is introduced to the charge transfer term.

3.4.2 The extended transition state approach

It is relevant at this point to mention Ziegler and Rauk's equally important ETS EDA scheme [101–103] which was developed independently but around the time of the KM EDA and which share a number of similarities. This scheme approaches the problem of decomposing the interaction energy by describing an electrostatic energy component (identical to the ΔE_{ES} energy component of the KM EDA), a Pauli exchange repulsion energy term ΔE_{Pauli} , and an orbital interaction term ΔE_{orb} :

$$\Delta E = \Delta E_{ES} + \Delta E_{Pauli} + \Delta E_{orb} \quad . \quad (3.15)$$

This decomposition also includes a geometric deformation energy term to distort the fragment equilibrium geometries to their geometries when in complex. To

maximise consistency of the definition of ΔE in this thesis, and due to the simple evaluation of this component, we do not include this term within Eq. 3.15. The Pauli exchange repulsion term is related to the exchange energy component of the KM EDA scheme (see Eq. 3.9), with its evaluation at the DFT level calculated as the exchange–correlation energy difference between a version of the wavefunction $\Psi_{AB}^{0,A/B,\text{Hartree}}$ in which all the orbitals are Löwdin orthogonalised [144] and the fragment wavefunctions $\Psi_A^{0,A}$ and $\Psi_B^{0,B}$, [19]

$$\Delta E_{\text{Pauli}} = E_{\text{xc}}[\Psi_{AB}^{0,A/B,\text{Hartree}}] - \left(E_{\text{xc}}[\Psi_A^{0,A}] + E_{\text{xc}}[\Psi_B^{0,B}] \right) \quad . \quad (3.16)$$

The final orbital interaction term contains interaction energy information relating to the charge transfer and polarisation interaction components and other orbital mixing interactions. This term is somewhat similar to the mixing term of the KM EDA as it is calculated as a remainder term that is required for the energy components to add up to the full interaction energy.

3.4.3 Assessment

A number of issues are observed that relate to the KM EDA scheme. The definition of the mixing term has no physical equivalent and has the potential to be even greater in magnitude than the total interaction energy itself [145]. The components of this decomposition are also observed to be highly basis set dependent and the charge transfer and polarisation energies are numerically unstable with large basis sets and at short intermolecular distance [146–148]. This is a result of the improper antisymmetrisation of the intermediate wavefunctions used in evaluating these terms: electrons from one fragment are permitted to occupy space already occupied by the electrons of the other fragment and so the Pauli exclusion principle remains unenforced [149]. Later EDA schemes such as the reduced variational space (RVS) analysis [10; 84], CSOV [11; 141], and NEDA [12; 13; 82; 83] schemes have been developed which attempt to overcome these limitations.

As seen within other schemes, the description of ΔE_{ES} and ΔE_{EX} as individual terms remains problematic due to their wavefunction definitions not obeying the Pauli principle. These terms are often combined in schemes derived from the KM EDA to produce a new term that is defined by the addition of the electrostatic and exchange terms. This combined term avoids the problem of using improperly antisymmetrised wavefunctions in the decomposition. The ΔE_{CT} and ΔE_{POL} KM EDA components are also observed to share the problem of using improperly antisymmetrised wavefunctions in their calculation. These terms may be combined as a new ΔE_{CTPLX} term which is defined by the addition of the polarisation and charge transfer components with inclusion of the exchange integral: this is performed in an alternative scheme [150] intended for the analysis of strong transition metal – ligand interactions.

The ETS scheme has been coupled in recent years with the natural orbitals for chemical valence (NOCV) approach [151–154] in what is termed ETS–NOCV [19]. This method allows the orbital interaction energy ΔE_{orb} to be divided into its orbital origins and visualised. In this approach, a deformation density matrix describing the change in density of the ΔE_{orb} interaction is constructed and diagonalised to yield NOCVs [19]. Complementary pairs of NOCVs are used to visualise the interactions, with energetic estimations of these interactions computed from the KS matrix of a transition state density (midway between the supermolecule and fragment densities). This approach therefore provides both a qualitative and quantitative analysis of chemical bonding. The ETS–NOCV scheme has been applied to organometallic [21; 155–157] and coordination compounds [20; 155–157], as well as metal–metal bonding [19; 156] and boronic [158; 159] systems. More unusual organometallic analyses have also been performed using the ETS–NOCV approach, including systems involving gold [160] and silver [161] interactions for example. The ETS EDA scheme has also been applied to purely organic molecules, for example in investigating conjugation and hyperconjugation stabilisations in conjugated molecules [162], heterobenzene molecules [163; 164],

benzene [164], five-membered aromatic compounds [164], cyclic and acyclic conjugated carbenes [164], and hetero- and anti-aromatic compounds [164]. Additionally, a number of review articles have been published on applications of the ETS scheme to both inorganic [165; 166] and organic systems [85; 167]. Other approaches that seek to provide a measure of the electron density delocalisation between molecules include the NBO approach [168–172], Bader’s QTAIM [98; 173], the electron localisation function [174; 175], and the Hirshfeld analysis [176], as well as the various population analysis schemes [144; 170; 177].

3.5 Reduced variational space EDA

The RVS scheme [10; 84] corrects a number of the unsatisfactory tendencies of the KM scheme that result as a consequence of the terms not correctly satisfying the Pauli exclusion principle in their calculation [149]. The CSOV analysis [11; 141] is similar to the RVS scheme and differs subtly in its treatment of charge transfer and polarisation. By ensuring proper antisymmetrisation of the wavefunctions of the decomposition, the Pauli exclusion principle within the RVS scheme is enforced correctly. Effectively, this scheme combines the electrostatics and exchange terms of the KM EDA and modifies the evaluations of the polarisation and charge transfer components.

3.5.1 Reduced variational space EDA theory

The RVS EDA method is closely related to the KM scheme but has a small number of distinct differences. The first is the inclusion of the electrostatic and exchange terms as a single ESX contribution (due to the fact that the wavefunctions corresponding to the isolated ΔE_{ES} and ΔE_{EX} not obeying the Pauli principle) [84]. The second is the different restrictions of variational space available for orbital optimisation to the KM EDA scheme. Lastly, the treatment of BSSE in the RVS EDA is slightly more complicated than in the KM EDA scheme. Notably, the

equivalent mixing term, ΔE_{MIX} , to that in the KM EDA scheme has a much greater tendency to become so small that it becomes insignificant in the RVS scheme.

The form of the RVS EDA interaction energy partitioning is,

$$\Delta E = \Delta E_{\text{ESX}} + \Delta E_{\text{POL}} + \Delta E_{\text{CT}} + \Delta E_{\text{MIX}} \quad (3.17)$$

where the ΔE_{ESX} term is equal to the sum of the ΔE_{ES} and ΔE_{EX} components of the KM EDA,

$$\Delta E_{\text{ESX}} = E[\Psi_{AB}^{0,A/B}] - E[\Psi_A^{0,A}] - E[\Psi_B^{0,B}] \quad (3.18)$$

and where the construction of the intermediate wavefunction $\Psi_{AB}^{0,A/B}$ ensures orthogonality between the monomers by Gram–Schmidt orthogonalisation [10; 84]. A number of other schemes apply this reduction of terms, including the ALMO and BLW EDA schemes discussed within this chapter.

The remaining components are modifications to their KM EDA equivalents. The polarisation energy component differs from the KM EDA evaluation by variational optimisation of the fully antisymmetrised wavefunction $\Psi_{AB}^{0,A/B}$ (rather than the non-antisymmetrised wavefunction $\Psi_{AB}^{0,A/B,\text{Hartree}}$). The subspace available for variational optimisation of the orbitals is reduced by freezing the occupied orbitals of the neighbouring monomer and omitting its virtual orbital subspace to prevent charge transfer. For the two-fragment system AB , orbital optimisation in the field of the neighbouring monomer produces two wavefunctions $\Psi_{AB}^{\text{RVS-POL}(A),A/B}$ and $\Psi_{AB}^{\text{RVS-POL}(B),A/B}$ relating to the polarised states of fragments A and B respectively. The polarisation energies for these two wavefunctions are then calculated by subtraction of the energy of the non-polarised state wavefunction $\Psi_{AB}^{0,A/B}$ from the energies of these polarised state wavefunctions. Addition of these two polarisation

energies produces the total polarisation energy E_{POL} .

$$\Delta E_{\text{POL}(A)} = E[\Psi_{AB}^{\text{RVS-POL}(A),A/B}] - E[\Psi_{AB}^{0,A/B}] \quad (3.19a)$$

$$\Delta E_{\text{POL}(B)} = E[\Psi_{AB}^{\text{RVS-POL}(B),A/B}] - E[\Psi_{AB}^{0,A/B}] \quad (3.19b)$$

$$\Delta E_{\text{POL}} = \Delta E_{\text{POL}(A)} + \Delta E_{\text{POL}(B)} \quad . \quad (3.19c)$$

This is formally a similar process to that within the KM EDA. Within the KM scheme however, this interaction instead effectively involves the simultaneous polarisation of the orbitals of each fragment in the field of their neighbouring fragment and also excludes an interfragmental exchange contribution.

Repeating a similar process of orbital optimisation but with extension of the variational space to include the virtual orbitals of the neighbouring fragment allows charge transfer to occur, producing the two wavefunctions $\Psi_{AB}^{\text{RVS-CT}(A),A/B}$ and $\Psi_{AB}^{\text{RVS-CT}(B),A/B}$ relating to the polarised and charge transferred states of fragments A and B respectively. The difference between the energies of these wavefunctions and their polarised-only counterparts, $\Psi_{AB}^{\text{RVS-POL}(A),A/B}$ and $\Psi_{AB}^{\text{RVS-POL}(B),A/B}$, provides the charge transfer energies of fragments A and B . The BSSE contributions from each fragment for charge transfer are introduced at this point in the decomposition. We denote the CP corrected charge transfer energies $E_{\text{BSSE,CT}(A)}$ and $E_{\text{BSSE,CT}(B)}$ for the CP correction to charge transfer originating from monomers A and B respectively, and the total of these two energies as $\Delta E_{\text{BSSE,CT}}$. The BSSE contributions from each fragment are introduced in a form similar to Eqs. 3.14a and 3.14b. This CP correction is referred to as the CP correction with virtual orbitals (VCP) in literature [84]. Addition of the BSSE contributions from the

fragments produces the total charge transfer energy $E_{\text{CT}+\text{BSSE}}$:

$$\begin{aligned} \Delta E_{\text{CT}+\text{BSSE}(A)} = & E[\Psi_{AB}^{\text{RVS}-\text{CT}(A),A/B}] - E[\Psi_{AB}^{\text{RVS}-\text{POL}(A),A/B}] \\ & + \Delta E_{\text{BSSE,CT}(A)} \end{aligned} \quad (3.20a)$$

$$\begin{aligned} \Delta E_{\text{CT}+\text{BSSE}(B)} = & E[\Psi_{AB}^{\text{RVS}-\text{CT}(B),A/B}] - E[\Psi_{AB}^{\text{RVS}-\text{POL}(B),A/B}] \\ & + \Delta E_{\text{BSSE,CT}(B)} \end{aligned} \quad (3.20b)$$

$$\Delta E_{\text{CT}+\text{BSSE}} = \Delta E_{\text{CT}(A)} + \Delta E_{\text{CT}(B)} \quad . \quad (3.20c)$$

In the RVS EDA literature [84], the charge transfer component is labelled simply E_{CT} . To reinforce that this component includes a BSSE correction contribution we have relabelled this component as $\Delta E_{\text{CT}+\text{BSSE}}$.

The mixing component, ΔE_{MIX} , of the RVS EDA is calculated as the difference between the CP corrected interaction energy and the total of the energy components. The form of the RVS EDA residual energy is given as,

$$\Delta E_{\text{MIX}} = \Delta E_{\text{RVS}} - (\Delta E_{\text{ESX}} + \Delta E_{\text{POL}} + \Delta E_{\text{CT}}) \quad . \quad (3.21)$$

In the RVS literature [84], this residual energy component is termed ΔE_{RES} . To maintain consistency with the naming convention of the mixing term of the KM EDA, we refer to this component as ΔE_{MIX} .

The CP correction applied to the interaction energy is not the full CP correction, and its calculation involves use of the virtual orbitals of the partner monomer rather than its full set of orbitals. The form of the RVS EDA CP corrected interaction energy is therefore,

$$\Delta E_{\text{RVS}} = E[\Psi_{AB}] - E[\Psi_A^{0,A}] - E[\Psi_B^{0,B}] + \Delta E_{\text{BSSE,CT}} \quad (3.22)$$

$$= E[\Psi_{AB}] - E[\Psi_A^{0,AB_{\text{vir}}}] - E[\Psi_B^{0,A_{\text{vir}}B}] \quad (3.23)$$

where $\Delta E_{\text{BSSE,CT}}$ is the CP correction to the charge transfer component. As the interaction energy is defined with a partial CP correction, the interaction energy

obtained from the RVS EDA differs to the interaction energy calculated from the KM EDA (in which the full CP correction is applied).

3.5.2 Assessment

This approach partially remedies the shortcomings of the KM EDA by use of fully antisymmetrised intermediate wavefunctions, and the Pauli exclusion principle is fully enforced within this scheme. However, by reducing the electrostatics and exchange contributions to one term the level of information provided by the scheme is decreased. This advantage and disadvantage is present in all KM EDA derived schemes in which the electrostatic and exchange terms may be combined. Also the theoretical description of polarisation is extended to include some exchange, and this may be useful or not depending on the chemical interpretation attributed to this term.

Despite its improvements upon the KM EDA, this scheme is however currently limited to the HF level of theory. The closely related CSOV scheme typically used in the investigation of metallic systems has been used with multi-configurational SCF (MCSCF) wavefunctions [178], and has been extended from its original HF implementation [11; 141] to the DFT level [179; 180] by simply using the KS orbitals in the EDA procedure. Subtle difference in the CSOV analysis theory cause the polarisation and charge transfer energies to be slightly dependent on their order of evaluation. Two CSOV analyses are therefore possible for any one system, and in some cases it is convenient to perform both calculations to validate results [141].

3.6 Pair interaction EDA

The PIEDA [96] scheme is a reformulation of the original KM EDA approach in the FMO description of Kitaura et al. [104–107]. The PIEs referred to by PIEDA are the interaction energies of the fragments produced, and for this reason

PIEs are also known as interfragment interaction energies (IFIEs) [181]. The FMO prescription is one that is also naturally well suited to the analyses of large systems (such as proteins) and hence is of interest for the study of biomolecular systems.

The FMO framework is implemented at many levels of theory, namely the RHF, DFT, second-order Møller–Plesset perturbation theory (MP2), CC, MCSCF, time-dependent DFT (TDDFT), and configuration interaction (CI) theories [182]. This is also partially inherited within the PIEDA approach and the ability to access the MP2 and CC correlated levels of theories [106; 182] is of merit to the approach. The KM EDA-type energy components are however limited to evaluation at the RHF level of theory, with the addition of a dispersion term ΔE_{DI} to ensure a correct representation of the interaction energy at these correlated levels of theories.

3.6.1 The fragment molecular orbital and the pair interaction energy

The FMO [104–107] framework is adopted within the PIEDA approach of Fedorov and Kitaura [96]. There are two different approaches to the construction of the fragments within FMO theory: an approach based upon the use of hybrid orbital projection (HOP) operators [104] known as the HOP method, and an alternative approach using the adaptive frozen orbitals (AFO) [183] scheme. The FMO approach we describe here is the HOP method which is used in PIEDA and serves as an introduction to the FMO formalism.

In the FMO approach, selected chemical bonds are detached at an atom with the two bonding electrons assigned to one of the fragments. Ideally, this detachment should avoid regions of delocalised charge such as C–N amide bonds in order to maintain the localised nature of the fragments. The atom retaining this bond is named the bond attached atom (BAA), and the atom from which this bond is detached is named the bond detached atom (BDA) [183]. Essentially, the HOP technique is used in order to prevent the BDA electron density from occupying the region of the bond that is now occupied by the BAA.

On the BAA fragment, a pseudoatom replaces the BDA to provide the basis functions used to describe the bond and a proton from the BDA is formally transferred to this pseudoatom. This transfer does not affect the electrostatic field surrounding the fragment, and so the total properties of the system remain unaltered.

A brief description of the general FMO formalism and FMO system energy calculation is as follows [181] :

1. The system is partitioned as determined by the user into a number of fragments with BDAs and BAAs.
2. Initial monomer electron densities are constructed for optimisation.
3. Monomer Fock operators are subsequently constructed using these densities, and the monomer energies evaluated in the electrostatic field of the surrounding fragments.
4. These energies are self-consistently minimised to a converged electrostatic potential.
5. Two-fragment energy calculations (FMO2) are performed in this potential and used to evaluate the total energy of the system. These dimer energies are calculated using the converged fragment densities.
6. Three-fragment calculations (FMO3) may also be performed and used to calculate the total system energy including three-body effects. Similarly, these trimer energies are calculated using the converged fragment densities.

The FMO2 total system energy is expressed as a many-body expansion up to second-order as,

$$E^{\text{FMO2}} = \sum_I^{N_{\text{frag}}} E_I + \sum_{I>J}^{N_{\text{frag}}} (E_{IJ} - E_I - E_J) \quad (3.24)$$

where N_{frag} is the number of fragments comprising the FMO system, E_I and E_J refer to the monomer energies of step 4, and E_{IJ} refers to the (non self-consistently

obtained) dimer energies of step 5. We can re-express this equation in terms of pair interaction energies (PIEs) of the fragments by separating out the electrostatic potential term as,

$$E^{\text{FMO2}} = \sum_I^{N_{\text{frag}}} E'_I + \sum_{I>J}^{N_{\text{frag}}} (E'_{IJ} - E'_I - E'_J) + \sum_{I>J}^{N_{\text{frag}}} \text{tr}(\Delta D^{IJ} V^{IJ}) \quad (3.25)$$

where E'_I and E'_J are the monomer internal energies and E'_{IJ} are the dimer internal energies which exclude the electrostatic interaction energy of the surrounding fragments, and where $\text{tr}(\Delta D^{IJ} V^{IJ})$ is the interaction energy on density relaxation in the electrostatic potential of the surrounding fragments, with the density matrix difference ΔD^{IJ} given by,

$$\Delta D^{IJ} = D^{IJ} - D^I \oplus D^J \quad (3.26)$$

where D^I , D^J , and D^{IJ} are the monomer and dimer density matrices respectively and V^{IJ} is the electrostatic potential matrix of the other fragments acting upon the dimer IJ [182]. The monomer and dimer internal energies are obtained by subtracting the electrostatic interaction energy due to the surrounding fragments from the monomer and dimer energies E_I , E_J and E_{IJ} respectively. For example in the case of the fragment dimer,

$$E'_{IJ} = E_{IJ} - \text{tr}(D^{IJ} V^{IJ}) \quad (3.27)$$

where $\text{tr}(D^{IJ} V^{IJ})$ is the electrostatic interaction of the surrounding fragments given by their electron density and nuclei.

The FMO2 energy form of Eq. 3.25 can be re-expressed in terms of internal monomer energies and PIEs, $\Delta E_{IJ}^{\text{int}}$, as,

$$E^{\text{FMO2}} = \sum_I^{N_{\text{frag}}} E'_I + \sum_{I>J}^{N_{\text{frag}}} \Delta E_{IJ}^{\text{int}} \quad (3.28)$$

The PIE of any arbitrary fragment pair IJ is given by,

$$\Delta E_{IJ}^{\text{int}} = (E'_{IJ} - E'_I - E'_J) + \text{tr}(\Delta D^{IJ} V^{IJ}) \quad (3.29)$$

and it is these interaction energies that are decomposed within the PIEDA scheme.

3.6.2 Pair interaction EDA theory

The PIEDA approach divides the interaction in a manner derived from the KM EDA approach, with the addition of a dispersion term for analyses at levels of theory above RHF.

PIEDA is available in two types. The first type begins using the densities obtained by an FMO calculation. The FMO densities are already polarised by construction, and so PIEDA follows using the KM EDA components described within Eq. 3.7 but without inclusion of the polarisation component [107]. Within PIEDA, the charge transfer component is also combined with the mixing component to produce the component $\Delta E_{\text{CT+MIX}}$. An additional dispersion component ΔE_{DI} is also included in the PIEDA decomposition. This is added in a straightforward manner when running a PIEDA calculation at the MP2 or CC levels of theory, and describes the correlation energy of these theories [182]. PIEDA has also been developed for system calculations in solution [184]. A solvation contribution ΔE_{SOLV} is calculated using an approach combining the polarisable continuum model (PCM) with the FMO framework known as PIEDA/PCM. This contribution describes the solvent screening of the PIEs and is important for obtaining meaningful interaction analyses [185]. The full form of this PIEDA type is

$$\Delta E_{IJ}^{\text{int}} = \Delta E_{\text{ES}} + \Delta E_{\text{EX}} + \Delta E_{\text{CT+MIX}} + \Delta E_{\text{DI}} + \Delta E_{\text{SOLV}} \quad (3.30)$$

where the interaction energy definition used by PIEDA is the pair interaction $\Delta E_{IJ}^{\text{int}}$ described in Eq. 3.29.

The second (full) type of PIEDA adds a polarisation component ΔE_{POL} to the EDA components [182]. The calculation of polarisation requires an additional description of the free state of the fragments. For molecular clusters this is simply obtained as the molecules in isolation, however for systems that involve bond partitioning the description is ambiguous. The state for these bond partitioned fragments uses minimally possible caps, for example in the case of a C–C bond a methyl cap would be used.

The polarisation energy is separated into a destabilising contribution from the monomer internal energies E'_I , and a stabilising contribution from the electrostatic energy component ΔE_{ES} of the first PIEDA [96]. A number of polarisation coupling terms are included in this EDA, namely polarisation–exchange, polarisation–dispersion, polarisation–charge transfer and many–body polarisation terms.

3.6.3 Assessment

As well as the advantage the use of the FMO framework within PIEDA provides by enabling EDA of larger systems, the use of FMO also allows the evaluation of EDA components for select regions of molecules through the localised description of the FMOs. This is a particular benefit of the PIEDA method. The PIEDA method also includes a number of mixing and coupling terms which may be problematic to interpret as within the KM EDA. BSSE within the PIEs is also not treated in the original PIEDA scheme. However, attempts have been made to reduce the BSSE within the PIEs for example through using model core potentials [186] and by using a CP approach [123; 187]. A limitation of using a CP approach to estimate BSSE in fragment based calculations is that many extra calculations are required to evaluate this. A novel approach that uses a statistical model has also been proposed [188] to estimate fragment BSSE contributions, thereby reducing the number of additional calculations required.

3.7 Absolutely localised molecular orbital EDA and block-localised wavefunction EDA

3.7.1 The absolutely localised molecular orbital and block-localised wavefunction

A description of a charge transfer restricted intermediate wavefunction is given by the ALMO EDA scheme [189] and similar BLW EDA scheme of Mo et al. [80; 89] by restricted expansion of the MOs in terms of only atomic orbitals (AOs) localised to a particular fragment. This yields MOs that are localised to each fragment and that are non-orthogonal between the fragments. The following provides a description of the construction of a set of ALMOs for two fragments A and B , with the procedure for the construction of BLW orbitals very similar.

For the subset of AOs localised to each of the fragments A and B , we denote the basis function index within a given subset as μ . The occupied MOs of each fragment are expanded in terms of their respective localised AOs,

$$|\psi_{Ai}\rangle = |\phi_{A\mu}\rangle M_{Ai}^{A\mu} \quad (3.31a)$$

$$|\psi_{Bi}\rangle = |\phi_{B\mu}\rangle M_{Bi}^{B\mu} \quad (3.31b)$$

where $M_{Bi}^{A\mu}$ represents the MO coefficients which are constrained to equal zero for $A \neq B$, and where $|\psi_{Ai}\rangle$ represents a MO localised on fragment A [189]. This orbital expansion constraint ensures a localised MO description on the fragments in a similar fashion to the localisation of AOs on atoms. This expansion also ensures no borrowing of AOs from other fragments to compensate for basis set incompleteness, therefore following this description does not result in basis set superposition error (BSSE) and consequential artificial lowering of interaction energy.

The theory underlying the construction of ALMOs is closely related to that of the block-localised MOs of Mo et al. [80; 89] (the BLW method). The ALMO and BLW wavefunctions may be considered almost identical in their construction,

differing by the method of orbital optimisation within the theories. The procedure by which the ALMOs are variationally optimised is known as SCF for molecular interactions (SCF MI) [189–191]. Orbital optimisation within the BLW approach may follow a similar procedure [190; 192–194], or may be achieved by successive Jacobi rotation [195]. Despite the similarities that exist in the construction of these wavefunctions, a number of small differences are observed in the EDA schemes they are used within as we discuss in the sections dedicated to each method.

3.7.2 Absolutely localised molecular orbital and block-localised wavefunction EDA theory

In the ALMO EDA decomposition, the total binding energy ΔE is expressed by addition of the individual decomposition components [15],

$$\Delta E = \Delta E_{\text{FRZ}} + \Delta E_{\text{POL}} + \Delta E_{\text{CT}} \quad (3.32)$$

where the frozen density component ΔE_{FRZ} describes the exchange and electrostatic interaction of the frozen charge densities when taken to complex geometry and is retermed the Heitler–London energy ΔE_{HL} within the BLW EDA [89]. We refer to this component as ΔE_{FRZ} within this thesis.

In order to evaluate the polarisation and charge transfer components, intermediate wavefunctions Ψ_{AB}^{ALMO} and Ψ_{AB}^{BLW} are constructed for the system. This construction given earlier within Eq. 3.31 follows similar processes within both the ALMO and BLW approaches. Relaxation of the MOs of the common wavefunction $\Psi_{AB}^{0,A/B}$ ensuring conformity to the restricted MO expansion requirement of these ALMO and BLW descriptions when applied to each fragment results in construction of the new intermediate wavefunctions Ψ_{AB}^{ALMO} and Ψ_{AB}^{BLW} respectively.

Both the ALMO and BLW EDA schemes include a geometric distortion energy term associated with the distortion of the monomer nuclear geometries at infinite separation to that found when in complex which provides an additional energy

contribution to ΔE . Within the ALMO EDA scheme this energy component is referred to as the geometric distortion term, ΔE_{GD} , and as the deformation energy ΔE_{def} within the BLW EDA scheme (of significantly different physical interpretation to that of the term of the same name in the NEDA scheme). Including such an important term has obvious implications on the evaluation of the interaction energy. As this term may be considered a simple additional component to our standardised description of the interaction energy, we will not include these terms within our discussion of the theory of the schemes.

Similarly, a dispersion contribution ΔE_{disp} obtainable as a simple ad-hoc procedure is introduced within the BLW EDA scheme and therefore is also not included within our theory discussion. This term is simply evaluated as the difference in energy obtained on performing higher level QM calculations that account for correlation effects above the HF and DFT theory EDA level of theory.

We may express the components of the ALMO and BLW EDA schemes in terms of energy functionals of the common wavefunctions and the wavefunctions Ψ_{AB}^{ALMO} and Ψ_{AB}^{BLW} described above. The frozen density component, ΔE_{FRZ} , is defined simply as the energy change on complexation of the monomers without allowing for orbital relaxation,

$$\Delta E_{\text{FRZ}} = E[\Psi_{AB}^{0,A/B}] - E[\Psi_A^{0,A}] - E[\Psi_B^{0,B}] \quad . \quad (3.33)$$

The frozen density term may also be expressed also as a sum of a Coulomb (ΔE_{ES}) term and an exchange term within HF theory or an exchange-correlation term within DFT ($\Delta E_{\text{EX/XC}}$) as,

$$\Delta E_{\text{FRZ}} = \Delta E_{\text{ES}} + \Delta E_{\text{EX/XC}} \quad (3.34)$$

where these components are not computed explicitly in the ALMO implementation [15] but are within the BLW implementation [89]. The BLW EDA descriptions of these electrostatic and exchange contributions are noted as being identical

in their evaluation to that of their KM EDA counterparts given within Eqs. 3.8 and 3.9. The exchange–correlation analogue to the Hartree product is adopted at the DFT level to evaluate ΔE_{XC} . Within the ALMO and BLW literatures, this electrostatic component is termed Δ_{ELS} and Δ_{ele} respectively.

The use of ALMOs in the expression of $E[\Psi_{AB}^{\text{ALMO}}]$ constrains the variations to intramolecular contributions. Charge transfer is prevented through use of this intermediate wavefunction description whilst allowing polarisation of the MOs. The energy lowering from $\Psi_{AB}^{0,A/B}$ to Ψ_{AB}^{ALMO} is therefore equal to the energy stabilisation on orbital polarisation,

$$\Delta E_{\text{POL}} = E[\Psi_{AB}^{\text{ALMO}}] - E[\Psi_{AB}^{0,A/B}] \quad . \quad (3.35)$$

The final energy component of the decomposition is the charge transfer energy. The contribution of charge transfer is calculated as,

$$\Delta E_{\text{CT}} = E[\Psi_{AB}] - E[\Psi_{AB}^{\text{ALMO}}] + \Delta E_{\text{BSSE}} \quad . \quad (3.36)$$

This term includes the CP correction accounting for the BSSE. The introduction of the BSSE at this stage in the decomposition is justified by the fact that this error needs to be corrected for and that it can be considered as an artificial type of charge transfer. The BSSE associated with this interaction is defined as,

$$\Delta E_{\text{BSSE}}(A) = E[\Psi_A^{0,A}] - E[\Psi_A^{0,AB}] \quad (3.37a)$$

$$\Delta E_{\text{BSSE}}(B) = E[\Psi_B^{0,B}] - E[\Psi_B^{0,AB}] \quad (3.37b)$$

$$\Delta E_{\text{BSSE}} = \Delta E_{\text{BSSE}}(A) + \Delta E_{\text{BSSE}}(B) \quad . \quad (3.37c)$$

Similar approaches are also taken to evaluate the ΔE_{POL} and ΔE_{CT} components of the BLW scheme, instead using the intermediate wavefunction $E[\Psi_{AB}^{\text{BLW}}]$ rather than $E[\Psi_{AB}^{\text{ALMO}}]$. The decomposition of ΔE into these three energy components is shown within Fig. 3.5 and 3.6.

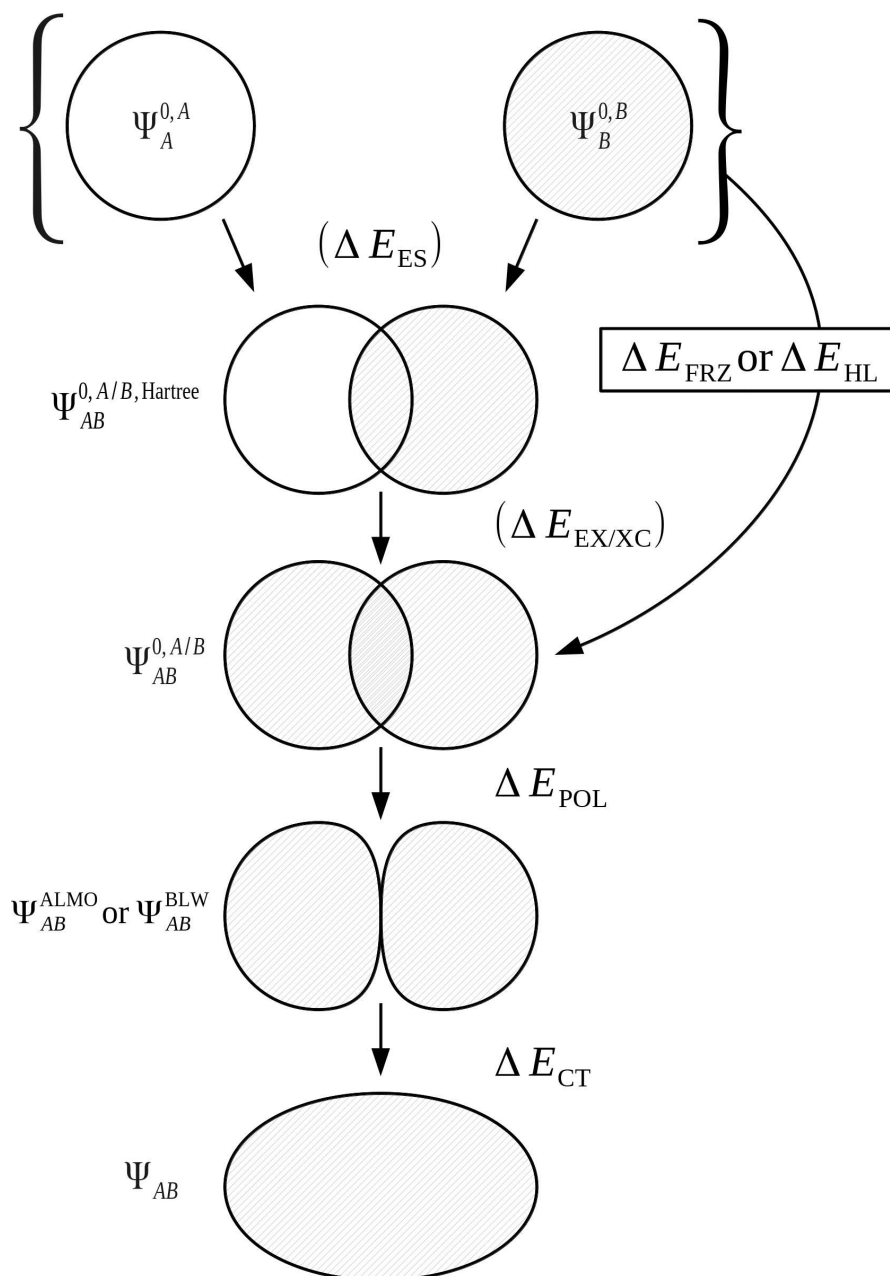


Figure 3.5: The ALMO EDA and BLW EDA scheme for a complex AB .

3.7.3 Assessment

The ALMO EDA scheme relies solely on the use of fully antisymmetrised wavefunctions, therefore obeying the Pauli exclusion principle and avoiding related issues that are observed within the KM EDA and similar schemes. The wavefunction $\Psi_{AB}^{0,A/B,\text{Hartree}}$ adopted within the BLW EDA scheme does not satisfy the Pauli exclusion principle and so the electrostatic and exchange components (which this

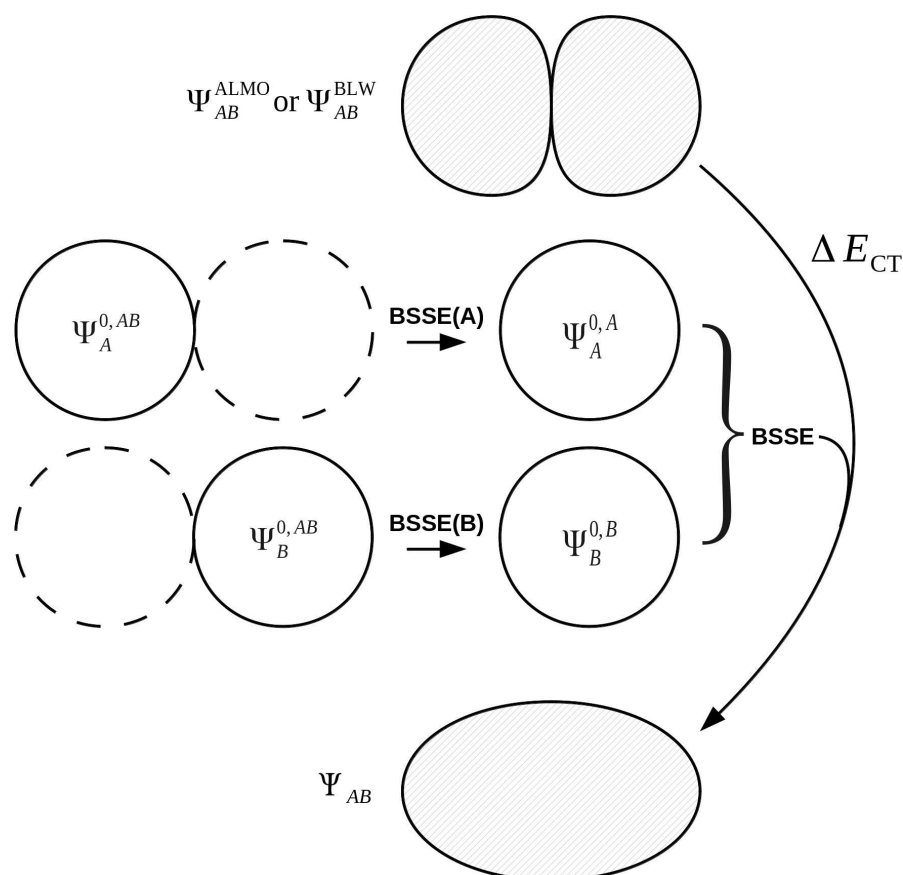


Figure 3.6: The treatment of charge transfer within the ALMO EDA and BLW EDA schemes. The (positive) BSSE is introduced to the charge transfer term because both BSSE and charge transfer are effects resulting from the delocalisation of monomer MOs, caused by including basis functions from the neighbouring fragments.

wavefunction is used to calculate) are often combined to form one single energy component as within the ALMO EDA to avoid its use. It is however noted that the combining of these terms by the ALMO EDA and other schemes may limit the information provided, with schemes that make this separation such as the BLW EDA scheme providing greater partitioning ability at the cost of less well defined electrostatic and exchange energy components.

A relatively recent extension to the ALMO EDA [196] has been developed that allows the isolation of forward and back charge donation quantities using the concept of chemically significant complementary occupied–virtual orbital pairs. The original ALMO EDA scheme also provides a treatment for the charge transfer back and forward donation energies. This involves performing a single non-iterative

Roothaan step correction to estimate charge transfer between the fragments of the system, with a higher order correction included to ensure the fragment charge transfer energies add up to the full ALMO EDA charge transfer energy [15]. Charge transfer has also been quantified in BLW EDA studies by Mulliken, Löwdin and natural population analyses [197–199]. The ability to evaluate charge transfer quantities in addition to energies further enhances the picture of chemical bonding these methods provide.

3.8 Natural EDA

The NBO approach of Weinhold et al. [168; 170] is used as the basis in the NEDA [12; 13; 82; 83] scheme. The use of the NBO basis results in a wavefunction which follows the classic Lewis interpretation of bonds and lone-pairs. Although a number of the components of this scheme are similar to those within the KM EDA scheme, NEDA does not variationally optimise any of its intermediate wavefunctions and this results in a number of artefacts in the values observed when using the NEDA scheme that will be discussed later.

In the following sections, we introduce the concept of the NBO, following which we provide a detailed overview of the NEDA approach. In its latest implementation NEDA takes the form of both a five-term energy decomposition [82] and a three-term energy decomposition [83] by reformulation of the components of the five-term energy decomposition.

3.8.1 The natural bond orbital basis set

The NBO basis of Weinhold et al. [168; 170] adopted within the NEDA scheme [12; 13; 82; 83] describes a set of almost doubly occupied localised orbitals formed by transformation of the full set of MOs. In this way an optimal Lewis description of the electronic wavefunction under study is produced. The vast majority of

total charge density is accounted for by the bonding NBOs, with the remainder described by Rydberg and antibonding NBOs.

Construction of the NBO basis involves the progressive transformation of the atomic orbital basis into localised functions. This begins with the initial transformation of the atomic orbital basis set into natural atomic orbitals (NAOs) of optimised occupancy by occupancy-weighted symmetric orthogonalisation (OWSO) [169; 170; 200]. For a set of atomic orbitals $\{|\phi_i\rangle\}$, a set of NAOs $\{|\phi_i^o\rangle\}$ is constructed as,

$$\{|\phi_i^o\rangle\} = \{|\phi_i\rangle\} C_{\text{OWSO}} \quad (3.38)$$

where C_{OWSO} is a coefficient matrix that orthogonalises the initial basis whilst variationally minimising the square root deviation

$$\sum_i w_i |\phi_i^o - \phi_i|^2 \quad (3.39)$$

between this basis and the orthogonalised basis in an occupancy-weighted manner, where $w_i \geq 0$ is the occupancy of orbital ϕ_i . The process ensures that low occupancy orbitals are able to freely distort in the orthogonalisation transformation whilst high occupancy orbitals maintain their shape [170].

This set of high-occupancy core and valence orbitals and low-occupancy Rydberg orbitals are then linearly combined to form an optimal orthonormal set of natural hybrid orbitals (NHOs) $\{h_X\}$ which are directional and point along chemical bonds,

$$h_X(\mathbf{r}) = \sum_{i \in X} {}^o a_i \phi_i(\mathbf{r}) \quad (3.40)$$

where ${}^o a_i$ are the expansion coefficients of the NAOs and where the expansion spans all NAOs on the atom X .

Linear combination of the NHOs results in construction of a set of 2-centre bonding NBOs,

$$\varphi_{XY}(\mathbf{r}) = a_X h_X(\mathbf{r}) + a_Y h_Y(\mathbf{r}) \quad (3.41)$$

where the polarisation coefficients a_X and a_Y satisfy $a_X^2 + a_Y^2 = 1$. Construction of similar antibonding NBOs to orthogonally complement the bonding NBOs is achieved as,

$$\varphi_{XY*}(\mathbf{r}) = a_X h_X(\mathbf{r}) - a_Y h_Y(\mathbf{r}) \quad . \quad (3.42)$$

The polarisation coefficients describe the polarisation of the NBO, and it is possible for one-centre NBOs to exist where $a_X = 1$ and $a_Y = 0$.

3.8.2 The five-term natural EDA theory

In the five-term NEDA scheme, the decomposition of the interaction energy is of the form,

$$\Delta E = \Delta E_{\text{ES}} + \Delta E_{\text{POL}} + \Delta E_{\text{CT}} + \Delta E_{\text{EX/XC}} + \Delta E_{\text{DEF}} \quad (3.43)$$

where $\Delta E_{\text{EX/XC}}$ is the exchange or exchange-correlation contribution in the HF and DFT cases respectively.

From the common charge densities described earlier, the (CP corrected) interaction energy may be expressed using energy functionals as,

$$\Delta E = E[n_{AB}^{AB}] - E[n_A^{0,AB}] - E[n_B^{0,AB}] \quad (3.44)$$

where $E[n]$ denotes a KS energy functional of charge density $n(\mathbf{r})$ and where $n_A^{0,AB}(\mathbf{r})$ and $n_B^{0,AB}(\mathbf{r})$ represent the charge densities of the unperturbed monomers A and B .

The intermediate charge densities used in the evaluation of the NEDA components are calculated after transforming the KS matrix of the supermolecule to the NBO basis. The charge density associated with the monomer A perturbed in the field of the other monomer B , $n_A^{AB}(\mathbf{r})$, is calculated from the variationally optimised AB supermolecule state and is expressed as,

$$n_A^{AB}(\mathbf{r}) = \sum_{\alpha}^{\text{on } A} Z_{\alpha} \delta(\mathbf{r} - \mathbf{R}_{\alpha}) - 2 \sum_a^{\text{on } A} |\psi_a(\mathbf{r})|^2 \quad (3.45)$$

where summations occur over all nuclei and orbitals comprising monomer A only and where ψ_a are the eigenvectors of the (diagonal) monomer A block of the full NBO KS matrix with these orbitals mutually orthogonal across each of the individual monomers [13; 83]. The equivalent charge density for monomer B , $n_B^{AB}(\mathbf{r})$, is constructed in a similar fashion.

The localised (CT-restricted) charge density $n_{AB}^{\text{loc},AB}(\mathbf{r})$ is calculated from the charge densities associated with the individual perturbed monomers as,

$$n_{AB}^{\text{loc},AB}(\mathbf{r}) = n_A^{AB}(\mathbf{r}) + n_B^{AB}(\mathbf{r}) \quad . \quad (3.46)$$

This differs from the total charge density of the fully interacting state as the AB NBO KS matrix is observed to be block non-diagonal, with the presence of off-diagonal elements representing interfragmental delocalisation interactions (as shown in Fig. 3.7).

From the charge densities described we can define the charge transfer (ΔE_{CT}) and deformation (ΔE_{DEF}) components of the NEDA scheme as,

$$\Delta E_{\text{CT}} = E[n_{AB}^{AB}] - E[n_{AB}^{\text{loc},AB}] \quad (3.47)$$

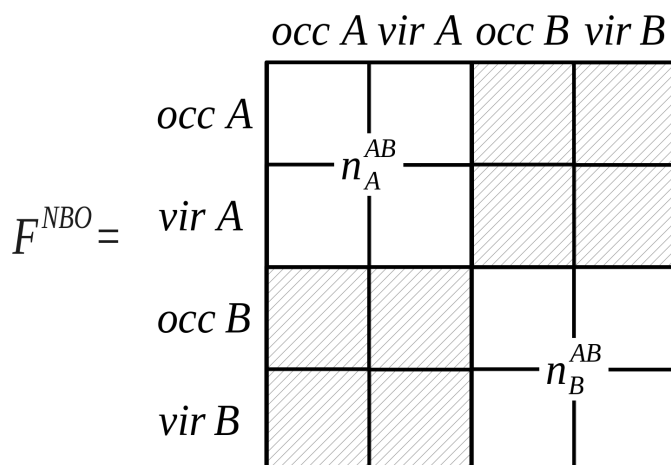


Figure 3.7: The partitioning of the NBO Fock matrix for the AB complex involved in the construction of the $n_{AB}^{\text{loc},AB}(\mathbf{r})$ charge density. Delocalising interactions described by the hashed blocks of the Fock matrix are not included in this charge density construction, where the labels ‘*occ*’ and ‘*vir*’ denote the sets of orbitals that are occupied and virtual on the monomers A and B .

$$\Delta E_{\text{DEF}(A)} = E[n_A^{AB}] - E[n_A^{0,AB}] \quad (3.48a)$$

$$\Delta E_{\text{DEF}(B)} = E[n_B^{AB}] - E[n_B^{0,AB}] \quad (3.48b)$$

$$\Delta E_{\text{DEF}} = \Delta E_{\text{DEF}(A)} + \Delta E_{\text{DEF}(B)} \quad . \quad (3.48c)$$

Whilst the charge transfer and deformation components of the NEDA scheme implemented at the DFT and HF levels of theory are identical, differences exist in the interpretation of the remaining contribution to the interaction energy [13]. The remaining contribution to the interaction energy given by Eq. 3.44 is shown to be that of the interaction of the perturbed monomer charge densities,

$$\Delta E - \Delta E_{\text{CT}} - \Delta E_{\text{DEF}} = E[n_{AB}^{\text{loc},AB}] - (E[n_A^{AB}] + E[n_B^{AB}]) \quad . \quad (3.49)$$

We can consider this to represent both the classical Coulombic interaction of the permanent and induced multipoles of the monomer units (i.e. a combination of the

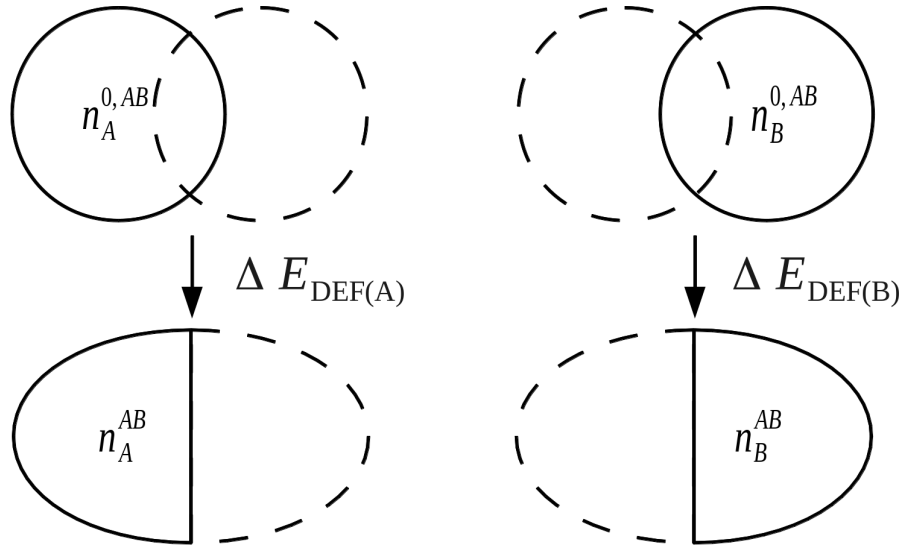


Figure 3.8: The evaluation of ΔE_{DEF} for a complex AB . Non-classical effects of polarisation are captured within the ΔE_{DEF} component along with intrafragmental electrostatic energy effects.

electrostatic (ΔE_{ES}) and polarisation (ΔE_{POL}) contributions), and the quantum exchange-correlation (ΔE_{XC}) contribution,

$$\Delta E - \Delta E_{\text{CT}} - \Delta E_{\text{DEF}} = \Delta E_{\text{ES}} + \Delta E_{\text{POL}} + \Delta E_{\text{XC}} \quad . \quad (3.50)$$

The classical contribution to this remainder of the interaction energy can be expressed simply as,

$$\Delta E_{\text{ES}} + \Delta E_{\text{POL}} = \iint \frac{n_A^{AB}(\mathbf{r})n_B^{AB}(\mathbf{r}')}{|\mathbf{r} - \mathbf{r}'|} d\mathbf{r}d\mathbf{r}' \quad . \quad (3.51)$$

The electrostatic (ΔE_{ES}) contribution is isolated from this contribution as,

$$\Delta E_{\text{ES}} = \iint \frac{n_A^{0,AB}(\mathbf{r})n_B^{0,AB}(\mathbf{r}')}{|\mathbf{r} - \mathbf{r}'|} d\mathbf{r}d\mathbf{r}' \quad (3.52)$$

where ΔE_{ES} describes the interaction of the unperturbed monomer charge densities and therefore the interaction of the permanent multipoles of the monomer units [83]. The ΔE_{POL} contribution may similarly be partitioned and expressed

as,

$$\Delta E_{\text{POL}} = \iint \frac{n_A^{AB}(\mathbf{r})n_B^{AB}(\mathbf{r}')}{|\mathbf{r} - \mathbf{r}'|} d\mathbf{r}d\mathbf{r}' - \iint \frac{n_A^{0,AB}(\mathbf{r})n_B^{0,AB}(\mathbf{r}')}{|\mathbf{r} - \mathbf{r}'|} d\mathbf{r}d\mathbf{r}' \quad . \quad (3.53)$$

where ΔE_{POL} describes the extra electrostatic interaction on polarising the charge densities of the separated fragments in the field of the other fragments when in complex [82]. In this regard, we can consider ΔE_{POL} to be an interfragmental interaction and ΔE_{DEF} to be an intrafragmental interaction. The remaining ΔE_{XC} term accounts for the intermolecular electron exchange–correlation interactions,

$$\Delta E_{\text{XC}} = E_{\text{xc}}[n_{AB}^{\text{loc},AB}] - (E_{\text{xc}}[n_A^{AB}] + E_{\text{xc}}[n_B^{AB}]) \quad (3.54)$$

where within the HF/NEDA scheme this term is substituted with the term ΔE_{EX} of HF exchange origin,

$$\Delta E_{\text{EX}} = -2 \sum_a^{\text{on } A} \sum_b^{\text{on } B} \langle ab|ba \rangle \quad (3.55)$$

which neglects the electron correlation contribution [13; 82].

3.8.3 The self polarisation energy term and the three–term natural EDA

A penalty term associated with the energy cost to polarise the unperturbed monomers to their perturbed charge densities is also included within the NEDA scheme named the self (polarisation) energy, (ΔE_{SE}) [83]. Interpretation of the ΔE_{DEF} component is somewhat problematic as this component includes both the contribution of Pauli repulsions to the interaction energy, as well as the contribution from the self energy penalty. It is sometimes useful to separate these contributions as the isolation of this penalty energy from the ΔE_{DEF} component allows the reduction of the interaction energy expression of Eq. 3.43 into three components: an electrical interaction (ΔE_{EL}), charge transfer (ΔE_{CT}), and core repulsions (ΔE_{CORE}).

The induced monomer charge density on monomer A , $\Delta n_A(\mathbf{r})$, is defined as the difference in the charge densities associated with the perturbed and unperturbed monomer A ,

$$\Delta n_A^{AB}(\mathbf{r}) = n_A^{AB}(\mathbf{r}) - n_A^{0,AB}(\mathbf{r}) \quad . \quad (3.56)$$

From this we define the self energy as the energy cost in forming the induced monomer charge density in the presence of the other monomers, [83]

$$\Delta E_{SE(A)} = -\frac{1}{2} \iint \frac{\Delta n_A^{AB}(\mathbf{r}) n_B^{AB}(\mathbf{r}')}{|\mathbf{r} - \mathbf{r}'|} d\mathbf{r} d\mathbf{r}' \quad (3.57a)$$

$$\Delta E_{SE} = \Delta E_{SE(A)} + \Delta E_{SE(B)} \quad (3.57b)$$

where the self energy for monomer B is evaluated in a complementary manner to that for monomer A . The calculation of this interaction is also shown within Fig. 3.9. The reformulation of the energy decomposition in terms of electrical inter-

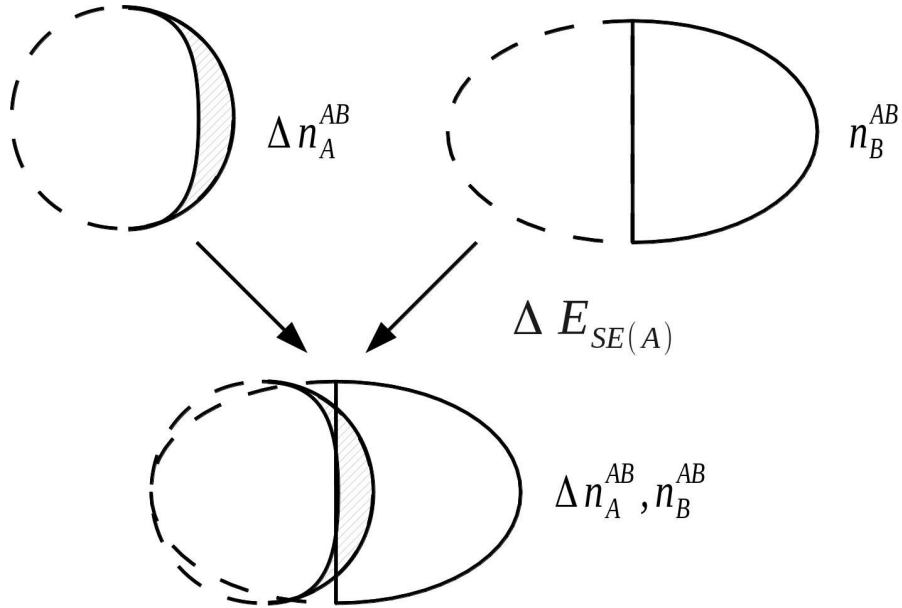


Figure 3.9: The evaluation of self energy component for a monomer A in the field of monomer B . This component is a portion of the deformation component that is electrical in origin, with the remainder of the deformation component resulting from Pauli repulsion contributions.

action (ΔE_{EL}), charge transfer (ΔE_{CT}) and core repulsions (ΔE_{CORE}) is achieved by collection of terms as, [83]

$$\Delta E_{\text{EL}} = \Delta E_{\text{ES}} + \Delta E_{\text{POL}} + \Delta E_{\text{SE}} \quad (3.58\text{a})$$

$$\Delta E_{\text{CORE}} = \Delta E_{\text{DEF}} + \Delta E_{\text{XC}} - \Delta E_{\text{SE}} \quad (3.58\text{b})$$

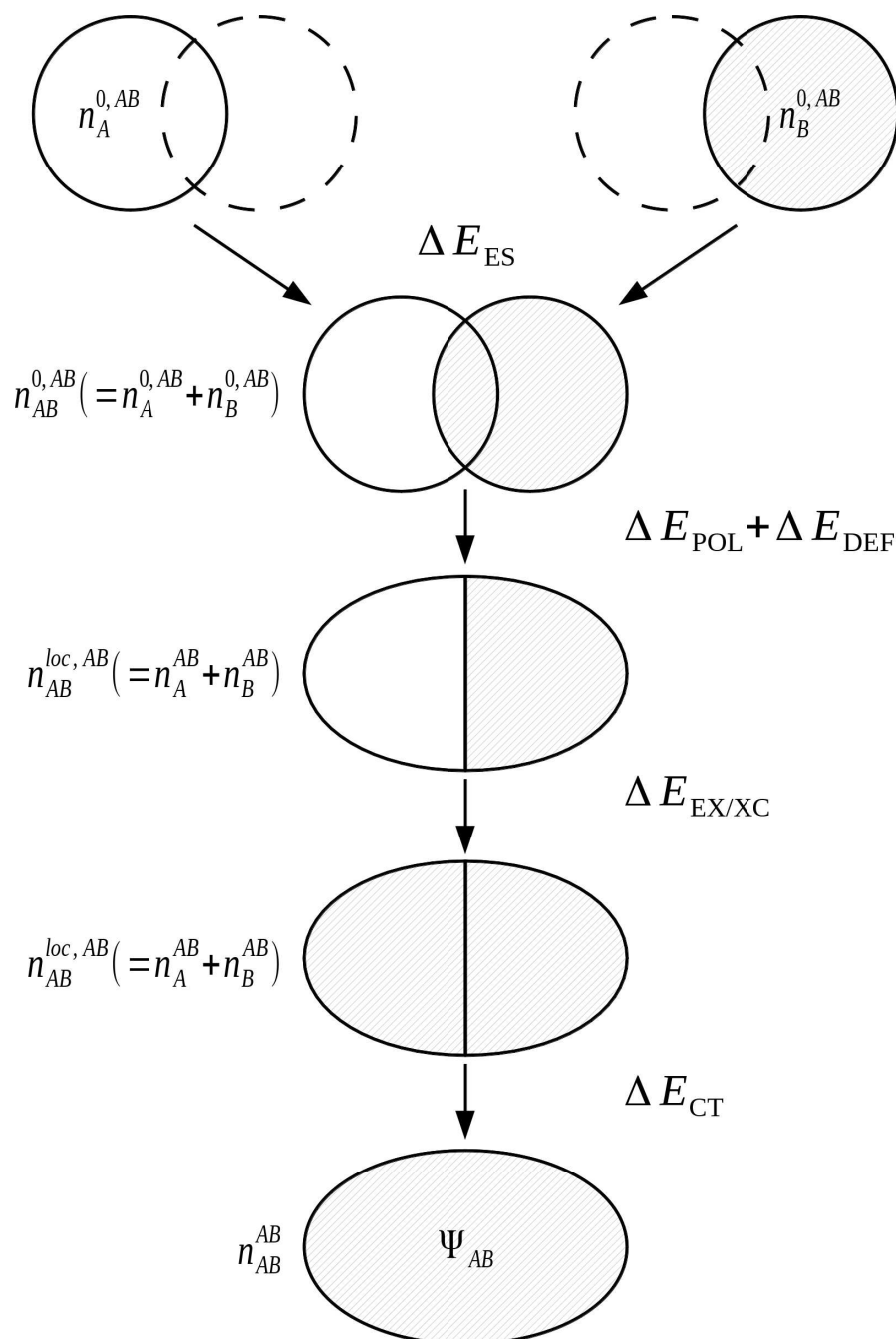
$$\Delta E = \Delta E_{\text{EL}} + \Delta E_{\text{CT}} + \Delta E_{\text{CORE}} \quad . \quad (3.58\text{c})$$

The five-term NEDA scheme can also be described schematically as within Fig. 3.10.

3.8.4 Assessment

A number of notable differences exist between the NEDA and KM derived schemes. One key difference is that the NEDA scheme undertakes the decomposition using only wavefunctions originating from the complex and fragment Fock matrix, avoiding use of variationally optimised intermediate wavefunctions. Lack of variational relaxation of the intermediate wavefunctions leads to a general overestimation of charge transfer values and underestimation of polarisation values [15; 80]: variational optimisation of the equivalent localised state used to evaluate the charge transfer and polarisation terms of the ALMO and BLW EDA schemes avoids this problem for example.

Significantly, the polarisation term of the NEDA scheme is purely electrostatic in origin, while intramolecular electron exchange (or exchange–correlation) effects of polarisation are captured within the deformation component ΔE_{DEF} (Fig. 3.8), and the remaining intermolecular exchange contribution contained within a portion of the exchange component $\Delta E_{\text{EX/XC}}$.

Figure 3.10: The NEDA scheme for a complex AB .

3.9 Symmetry-adapted perturbation theory

3.9.1 SAPT theory

In contrast to the intermediate wavefunction approach of the variational based EDA schemes, symmetry-adapted perturbation theory (SAPT) is presented as

a perturbative expression of the interaction energy in terms of components of chemical interest [17; 18].

The description of SAPT here will focus upon what is usually termed the SAPT(0) approach. The approach assumes the Møller-Plesset fluctuation operators, \hat{W}_A and \hat{W}_B , to not contribute to the interaction energy and provides a concise introductory description of the SAPT formalism.

The SAPT expression for the Hamiltonian of a complex AB is

$$\hat{H} = \hat{H}_A + \hat{H}_B + \xi \hat{W}_A + \eta \hat{W}_B + \zeta \hat{V} \quad (3.59)$$

where the intermolecular Coulomb operator is expressed as

$$\hat{V} = \sum_a^{\text{on } A} \sum_b^{\text{on } B} \frac{1}{|\mathbf{r}_a - \mathbf{r}_b|} + \sum_b^{\text{on } B} \hat{v}_A(b) + \sum_a^{\text{on } A} \hat{v}_B(a) + V_0 \quad (3.60)$$

where,

$$\hat{v}_A(b) = - \sum_{\alpha}^{\text{on } A} \frac{Z_{\alpha}}{|\mathbf{r}_b - \mathbf{R}_{\alpha}|} \quad (3.61a)$$

$$\hat{v}_B(a) = - \sum_{\beta}^{\text{on } B} \frac{Z_{\beta}}{|\mathbf{r}_a - \mathbf{R}_{\beta}|} \quad (3.61b)$$

and where V_0 is the nucleus–nucleus interaction energy between fragments A and B [201].

A symmetrised Rayleigh-Schrödinger (SRS) perturbative expansion with respect to the perturbation parameters ξ , η , and ζ defines the SAPT approach with the interaction energy expressed as

$$\Delta E = \sum_{i=0}^{\infty} \sum_{j=0}^{\infty} (E_{\text{ind}}^{(ij)} + E_{\text{exch}}^{(ij)}) \quad (3.62)$$

where the $E_{\text{ind}}^{(ij)}$ are the polarisation expansion terms and j is the monomer fluctuation potential index and i the intermolecular perturbation index. The SRS

expansion results in each $E_{\text{ind}}^{(ij)}$ term having an associated exchange term, $E_{\text{exch}}^{(ij)}$, to force antisymmetrisation in order to project away Pauli-forbidden components from the interaction energy [18].

Within the SAPT(0) approach, the conditions of $\xi = \eta = 0$ are enforced. This results in an interaction energy SRS expansion of the form

$$\Delta E(\zeta) = \frac{\langle \Psi_0 | \zeta \hat{V} \hat{A}_{AB} | \Psi(\zeta) \rangle}{\langle \Psi_0 | \hat{A}_{AB} | \Psi(\zeta) \rangle} \quad (3.63)$$

where Ψ is the Hartree product of the monomer wavefunctions and Ψ_0 is equal to Ψ evaluated with the restriction $\zeta = 0$. The antisymmetriser \hat{A}_{AB} is introduced to project away the Pauli-forbidden components of the wavefunction Ψ .

The SAPT(0) interaction energy up to the second-order with renaming of terms (cf. Eq. 3.62) may be expressed as

$$\Delta E^{\text{SAPT}(0)} = E_{\text{elst}}^{(1)} + E_{\text{exch}}^{(1)} + E_{\text{pol}}^{(2)} + E_{\text{exch}}^{(2)} \quad (3.64)$$

The second-order energy correction polarisation term, $E_{\text{pol}}^{(2)}$, is formed of an induction and a dispersion contribution

$$E_{\text{pol}}^{(2)} = E_{\text{ind}}^{(2)} + E_{\text{disp}}^{(2)} \quad (3.65)$$

where $E_{\text{ind}}^{(2)}$ is the energy of polarising each monomer in the field of the frozen charge density of the other monomer, and where $E_{\text{disp}}^{(2)}$ is the dispersion correction of the MP2 correlation energy-like form. The induction energy may be expressed as

$$E_{\text{ind}}^{(2)} = E_{\text{ind}}^{(2)}(A \leftarrow B) + E_{\text{ind}}^{(2)}(B \leftarrow A) \quad (3.66)$$

where $A \leftarrow B$ represents polarisation of the charge density of A in the field of the frozen charge density of B and $B \leftarrow A$ represents polarisation of the charge

density of B in the field of the frozen charge density of A [17]. Specifically for the polarisation of A in the field of the frozen charge density of B ,

$$E_{\text{ind}}^{(2)}(A \leftarrow B) = 2 \sum_{ar} t_{ar} (\omega_B)_{ar} \quad (3.67)$$

where,

$$(\omega_B)_{ar} = (\hat{v}_B)_{ar} + \sum_b \langle ab|rb \rangle \quad (3.68a)$$

$$t_{ar} = \frac{(\omega_B)_{ar}}{\epsilon_a - \epsilon_r} \quad (3.68b)$$

The case of the polarisation of B in the field of the frozen charge density of A is of similar but opposite form. The second-order correction for dispersion is given by

$$E_{\text{disp}}^{(2)} = 4 \sum_{ar} \sum_{bs}^{\text{on } A \text{ on } B} \frac{\langle ab|rs \rangle \langle rs|ab \rangle}{\epsilon_a + \epsilon_b - \epsilon_r - \epsilon_s} \quad (3.69)$$

The second-order exchange correction similarly contains dispersion and induction components $E_{\text{exch-ind}}^{(2)}$ and $E_{\text{exch-disp}}^{(2)}$ respectively, and the forms of these may be found in the literature [17; 18].

Substituting the SAPT(0) MOs with KS MOs in the above equations results in a method named SAPT(KS) [202]. The SAPT(KS) approach is noted however as failing to properly reproduce the dispersion energies of the original SAPT scheme [25; 203–205]. This scheme differs from the SAPT(DFT) [25; 203–205] approach in which the dispersion interaction of Eq. 3.69 are obtained from frequency-dependent density susceptibility (FDDS) functions from TD-DFT calculations.

3.9.2 SAPT treatment of polarisation and charge transfer

Normally, the polarisation and charge transfer contributions to the interaction energy are described within the induction energy. These components may be

isolated in an ALMO-like approach that considers the induction energy as representing solely the polarisation contribution when evaluated with the basis set of each fragment limited to its own basis functions [90; 206]. This basis is termed the monomer-centered basis set (MCBS) and the basis with each fragment able to use all basis functions of the full supermolecule is termed the dimer-centered basis set (DCBS). The partitioned charge transfer (E_{ct}) and polarisation¹ (E_{pol}) terms of SAPT are calculated as

$$E_{\text{pol}} = E_{\text{ind,MCBS}}^{(2)} \quad (3.70\text{a})$$

$$E_{\text{ct}} = E_{\text{ind,DCBS}}^{(2)} - E_{\text{ind,MCBS}}^{(2)} \quad (3.70\text{b})$$

where $E_{\text{ind,MCBS}}^{(2)}$ and $E_{\text{ind,DCBS}}^{(2)}$ are the induction energies $E_{\text{ind}}^{(2)}$ calculated in the MCBS and DCBS respectively. Exchange parts of the polarisation and charge transfer terms are calculated in a similar manner from the exchange induction correction $E_{\text{exch-ind}}^{(2)}$ in the MCBS and DCBS also.

3.9.3 Assessment

With recent developments permitting SAPT at the DFT level of theory, this method is becoming a viable alternative to the variational based approaches [203; 204]. As a perturbative treatment of the interaction energy, SAPT inherently differs from the variational approaches in a number of ways. Notably, the SAPT descriptions of polarisation and charge transfer differ from the variational methods we have discussed by implicitly including dispersion contributions within this term [15].

¹ We note that the polarisation term E_{pol} is different to the second-order energy correction term $E_{\text{pol}}^{(2)}$ described earlier.

3.10 Natural bond orbital second-order perturbation theory analysis

A notable asset of the NBO package (of which NEDA belongs) is its ability to calculate second-order perturbation theory energies for a particular donor-acceptor NBO pair [172; 200]. This low-order perturbative correction provides an estimate for the charge transfer contribution of an NBO pair (from a bonding to an anti-bonding NBO) to the total interaction energy. This energy is expressed by the equation,

$$\Delta E_{ij}^{(2)} = \frac{-w_i |F_{ij}|^2}{\varepsilon_j^{(\text{NL})} - \varepsilon_i^{(\text{L})}} \quad (3.71)$$

where w_i is the donor orbital occupancy (approximately 2), F_{ij} is Fock matrix element for the donor-acceptor orbital interaction, and $\varepsilon_i^{(\text{L})}$ and $\varepsilon_j^{(\text{NL})}$ are the energies of the donor and acceptor orbitals respectively. In this manner, the chemist is able to gain useful insight into the non-Lewis interaction of an atom within a molecule with neighbouring functional groups, and therefore allows the study of particular functional groups of chemical interest.

Chapter 4

An evaluation of current biomolecular energy decomposition analysis approaches

A primary focus of the work in this thesis concerns the development of an EDA scheme for the analysis of large-scale biomolecular systems. As such, we begin by investigating the advantages and disadvantages of a number of popular EDA schemes using a series of systems of interest within the field of drug design. We aim to identify the EDA approaches which are most suitable for biomolecular applications by considering a number of criteria. These criteria include the schemes' abilities to describe the interaction energy with chemically useful energy components, physically reasonable energy values, and with minimal basis set dependence.

Specifically, we have calculated the energy components using the Kitaura-Morokuma (KM) EDA, reduced variational space (RVS) EDA, absolutely localised molecular orbital (ALMO) EDA natural EDA (NEDA), and symmetry-adapted perturbation theory (SAPT) schemes applied to 23 small test systems of biomolecular relevance.

As the PIEDA scheme is essentially identical to the KM EDA for molecular fragments, we did not include this in our study. Also, because the NBO second-order perturbation theory is a charge transfer analysis tool and not a full variational or perturbation EDA scheme we have not included results of this approach in our work.

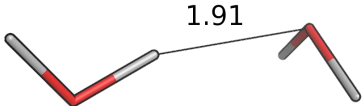
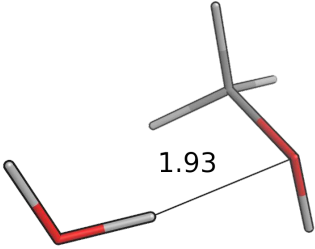
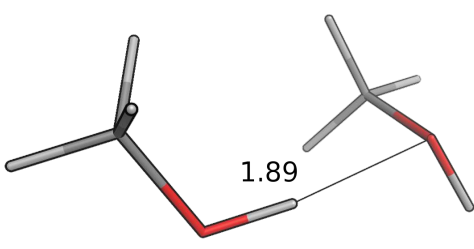
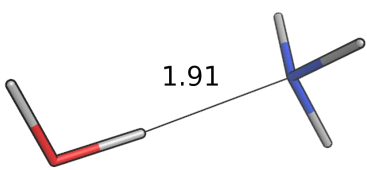
The test systems we have included for study have been selected based on their relevance to biomolecular studies whilst maintaining small size. These model systems express key interactions typically found within ligand–host systems, such as hydrogen bonding, π – π and halogen interactions. These chosen systems are important to understanding trends in the EDA results and to correlate these with chemical common sense. Of key consideration in drug design are effects resulting from hydrogen bonding and dispersion interactions [207; 208]. We have included a number of systems in our work that express these interactions, which we have arranged into 6 congeneric series test sets that are expected to follow key trends in bonding character.

4.1 Calculations

Starting geometries were chosen with the expectation that the test sets would ideally follow a congeneric trend on geometry optimisation. Geometry optimisation was performed at the BLYP-D3/6-311G* level of theory on all structures using the NWChem ab initio package [55]. The –D3 correction for dispersion of Grimme et al. [209] was used in order to properly model the dispersion interactions especially observed in the case of the π – π interacting systems. The BLYP functional was chosen due to its minimal mean absolute deviation (MAD) [209] for the S22 benchmark dataset [210] when using the –D3 correction.

EDA was subsequently performed on the geometry optimised structures at the same BLYP-D3/6-311G* level of theory at which the geometries were optimised for the ALMO EDA, NEDA and SAPT(KS) schemes, and at the HF/6-311G* level

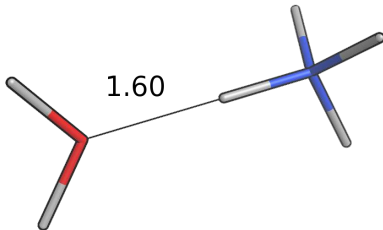
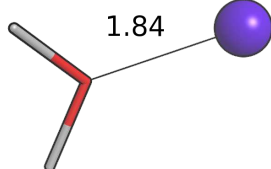
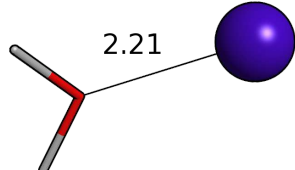
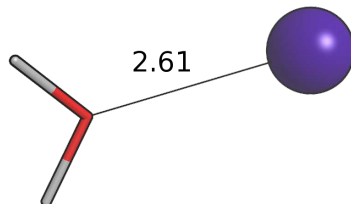
Table 4.1: Test set 1 (hydrogen bonding interactions) BLYP-D3/6-311G* geometry optimised systems for EDA (intermolecular distances are given in Å)

System	Figure
Water – Water	
Water – Methanol	
Methanol – Methanol	
Water – Ammonia	

for the KM EDA and RVS EDA schemes. The KM EDA polarisation component does not obey the Pauli principle and it is possible for valence electrons to collapse into the partner fragment's core orbitals [146–148]. To prevent this and to allow energy convergence, the calculations of the KM EDA and RVS EDA components for the benzene – Li^+ system were performed without d polarisation functions on the lithium atom. The optimised geometries of the systems studied using EDA are shown within Tables 4.1 to 4.6, and further information of preparation of the systems in test set 6 is provided in the footnote¹ below.

¹The systems of test set 6 were obtained in a manner that maintained a geometric trend in the series. These were obtained by finding the BLYP-D3/6-311G* energy minima with regard to intermolecular separation of the frozen monomers when in the T-shaped conformation. The frozen monomer geometries were taken as the monomer structure's geometry optimised in isolation at the BLYP-D3/6-311G* level. The T-shaped conformation is described by the benzene monomer at a 90° angle to the partner halogenated benzene monomer, with the halogen in the axis of the benzene π cloud (i.e. directly centred above the geometric average of the benzene carbon atoms). The benzene – fluorobenzene system is the

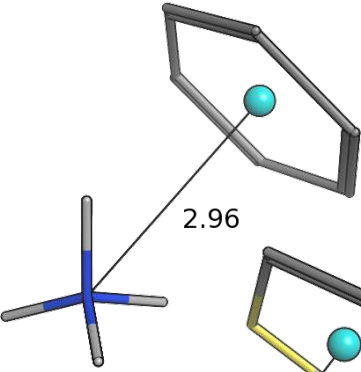
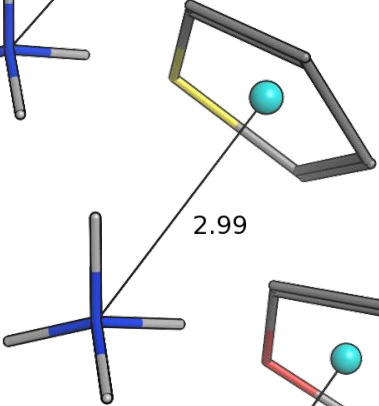
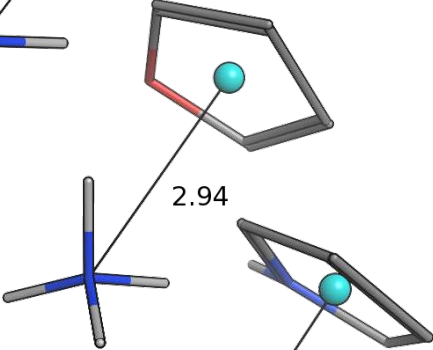
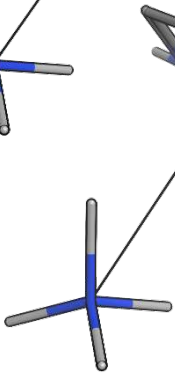
Table 4.2: Test set 2 (water-cations) BLYP-D3/6-311G* geometry optimised systems for EDA (intermolecular distances are given in Å)

System	Figure
Water – Ammonium	
Water – Li ⁺	
Water – Na ⁺	
Water – K ⁺	

NEDA, KM EDA and RVS EDA calculations were performed on the structures using the GAMESS-US [56] ab initio package and ALMO EDA and SAPT(KS) [201; 211] calculations were performed using the Q-CHEM [54] package. The locally projected SCF equations of Gianinetti [189; 190] were used in the ALMO approximation of the ALMO EDA, and partitioning of the charge transfer and polarisation components of the SAPT(KS) approach from the induction energy was achieved using Eqs. 3.70a and 3.70b.

only system of test set 6 not to have a σ hole present on the halogen, and using this approach allows us to compare the effect of the σ hole feature on the EDA components.

Table 4.3: Test set 3 (ammonium- π systems) BLYP-D3/6-311G* geometry optimised systems for EDA (intermolecular distances are given in Å)

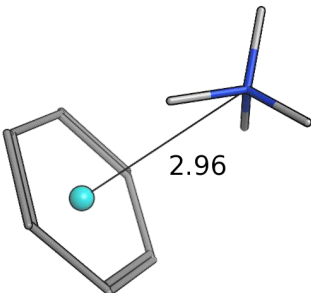
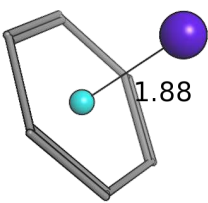
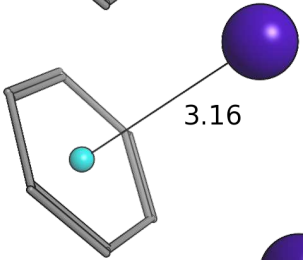
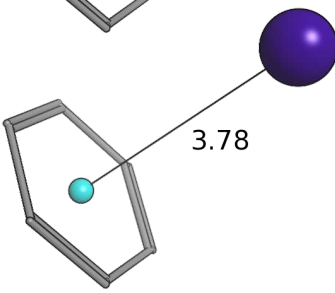
System	Figure
Ammonium – Benzene ^a	
Ammonium – Thiophene	
Ammonium – Furan	
Ammonium – Pyrrole	

^a The benzene – ammonium system of test set 3 is also contained within test set 4.

4.2 Analysis

Within this section, we compare the trends of the various EDA components within each congeneric series. Our goal is to examine the chemical relevance of each EDA method for the different series. An ‘ideal’ EDA would be expected to produce results that agree with chemical intuition in obvious cases and produce sensible

Table 4.4: Test set 4 (π -cations) BLYP-D3/6-311G* geometry optimised systems for EDA (intermolecular distances are given in Å)

System	Figure
Benzene – Ammonium ^a	
Benzene – Li ⁺	
Benzene – Na ⁺	
Benzene – K ⁺	

^a The benzene – ammonium system of test set 3 is also contained within test set 4.

energy components in more difficult cases where chemical intuition is less obvious. Plots of the EDA results for the test sets are given in Fig. 4.1, 4.2 and 4.3, and energy values are provided in Tables A.1 to A.9 of the Appendix.

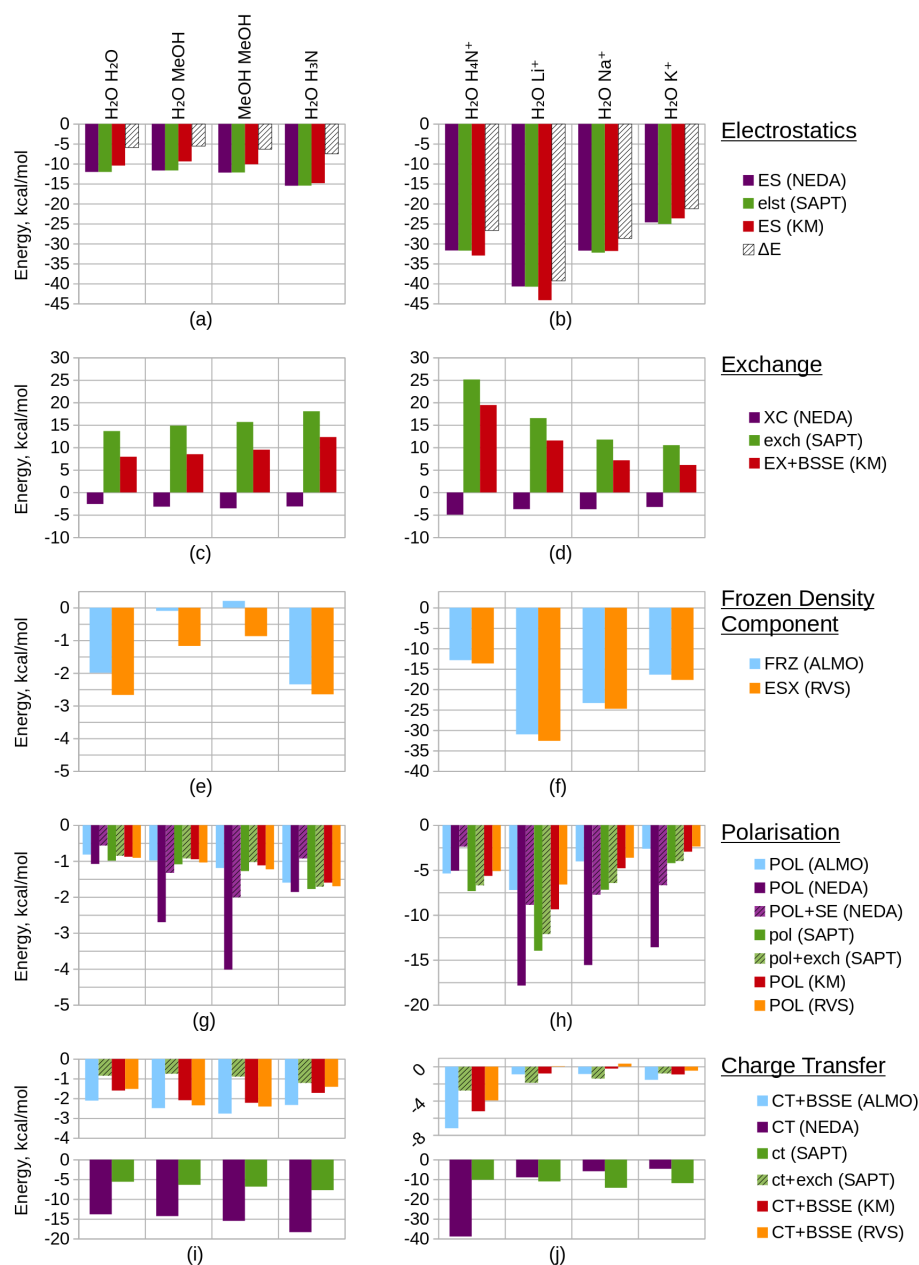


Figure 4.1: Converged EDA component values (in kcal/mol) of the test sets 1 and 2. The results of test set 1 are given by plots (a), (c), (e), (g) and (i), and test set 2 by plots (b), (d), (f), (h) and (j). The EDA results of the electrostatic components are shown within plots (a) and (b), the exchange/exchange–correlation components within plots (c) and (d), the Heitler–London interaction components within plots (e) and (f), the polarisation components within plots (g) and (h), and the charge transfer components within plots (i) and (j). The NEDA polarisation energies corrected with self energy term are given by POL+SE within plots (g) and (h). The green bars of the polarisation and charge transfer plots (g)–(j) represent the SAPT(KS) contributions, where the non–hashed bars represent the electrostatic contribution of this term only and where the hashed bars also include exchange in this term. The full BLYP–D3/6-311G* level interaction energy ΔE is given within plots (a) and (b).

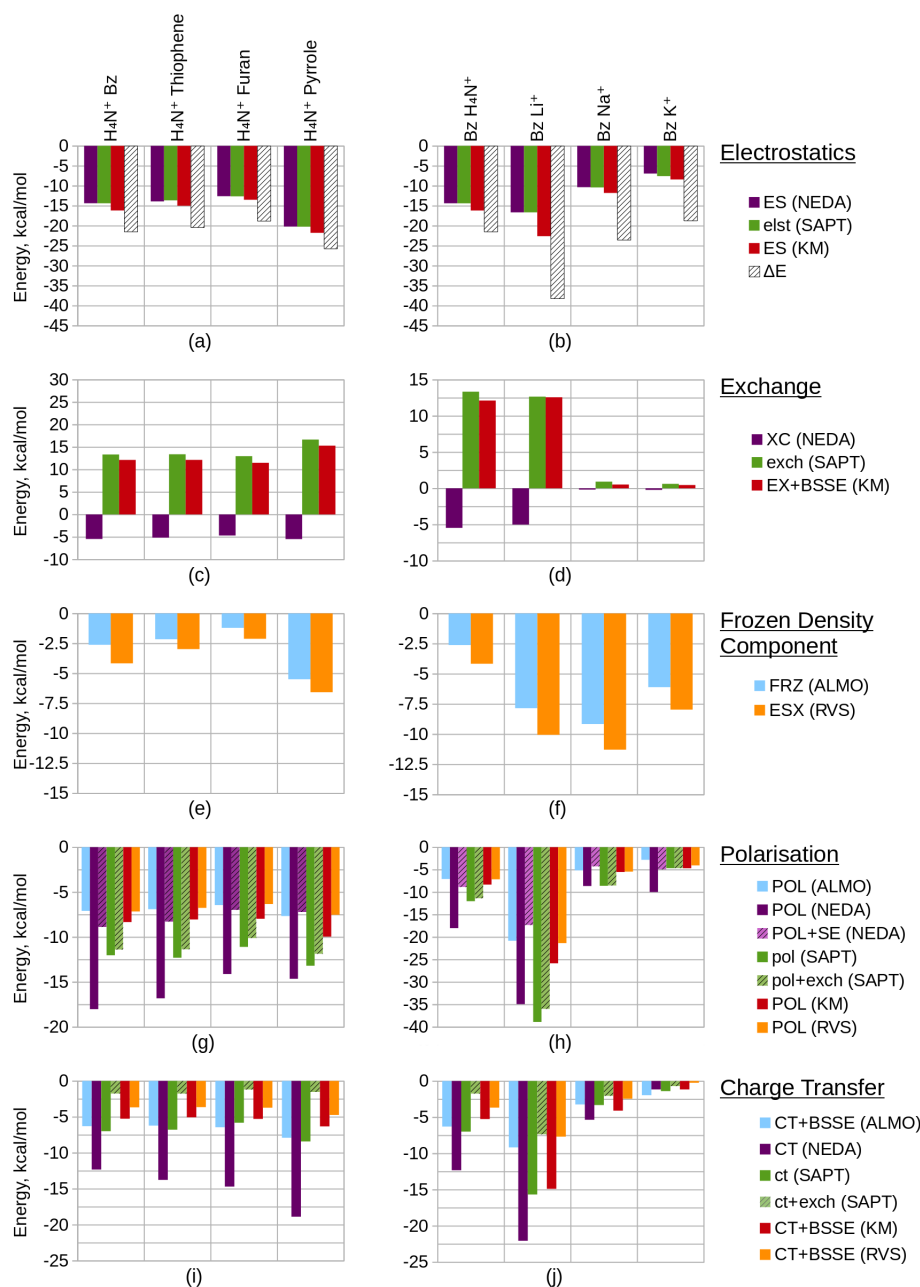


Figure 4.2: Converged EDA component values (in kcal/mol) of the test sets 3 and 4. The results of test set 3 are given by plots (a), (c), (e), (g) and (i), and test set 4 by plots (b), (d), (f), (h) and (j). The EDA results of the electrostatic components are shown within plots (a) and (b), the exchange/exchange–correlation components within plots (c) and (d), the Heitler–London interaction components within plots (e) and (f), the polarisation components within plots (g) and (h), and the charge transfer components within plots (i) and (j). The NEDA polarisation energies corrected with self energy term are given by POL+SE within plots (g) and (h). The green bars of the polarisation and charge transfer plots (g)–(j) represent the SAPT(KS) contributions, where the non–hashed bars represent the electrostatic contribution of this term only and where the hashed bars also include exchange in this term. The full BLYP–D3/6-311G* level interaction energy ΔE is given within plots (a) and (b).

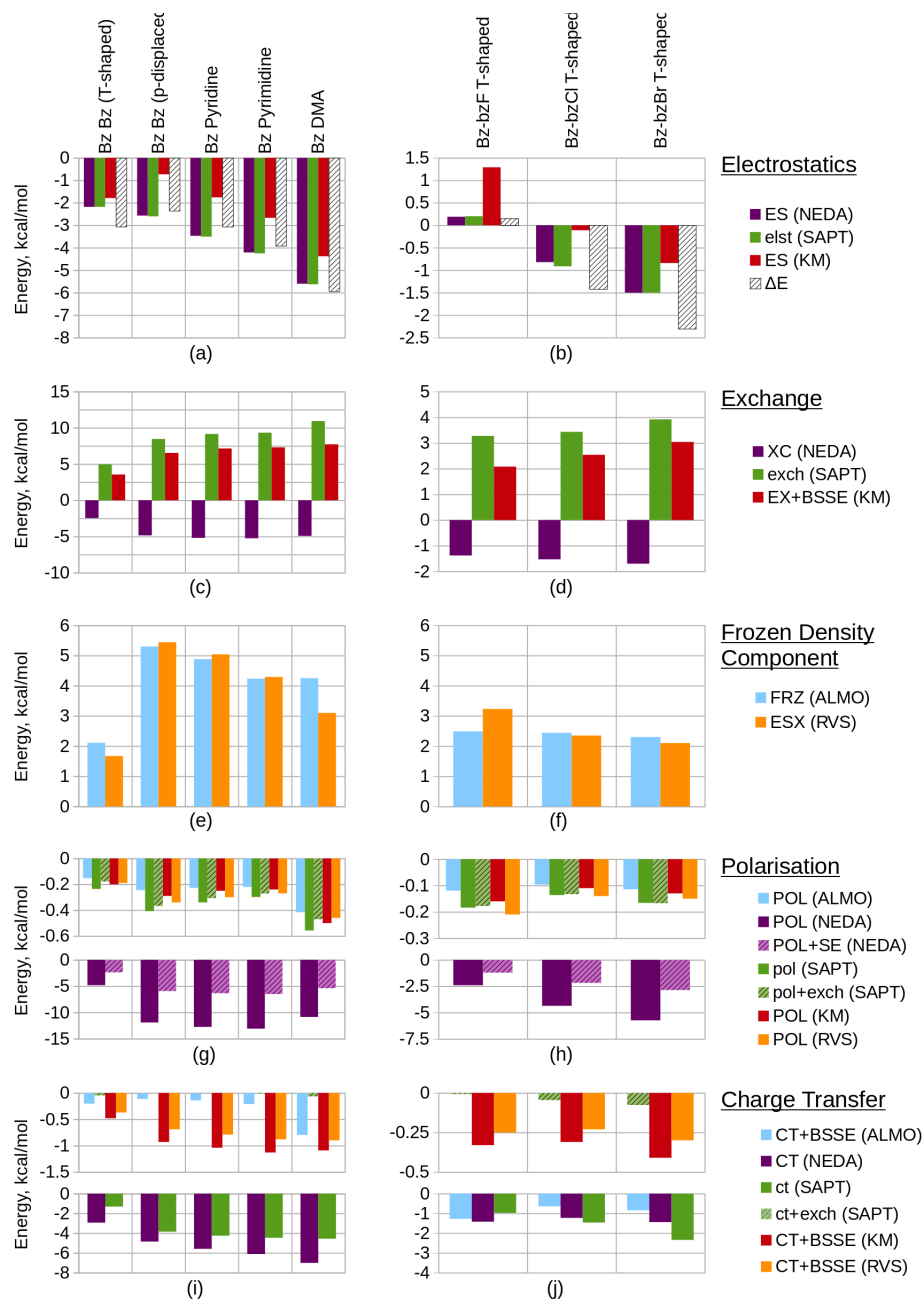
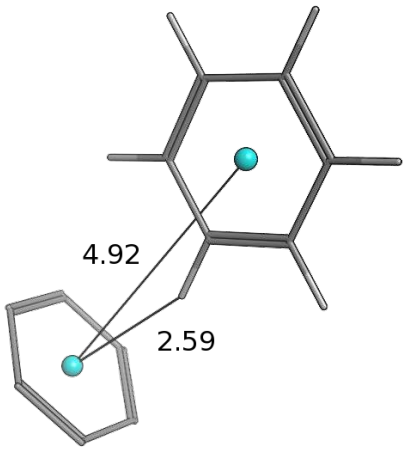

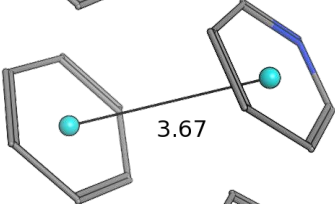
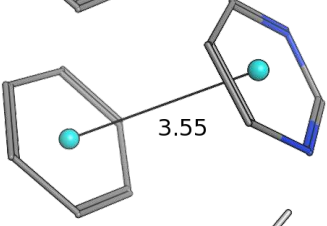
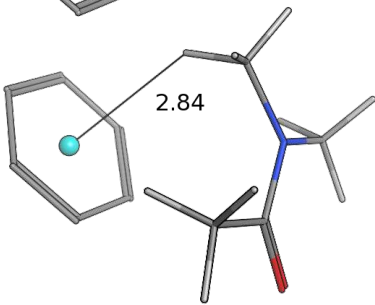


Figure 4.3: Converged EDA component values (in kcal/mol) of the test sets 5 and 6. The results of test set 5 are given by plots (a), (c), (e), (g) and (i), and test set 6 by plots (b), (d), (f), (h) and (j). ‘Bz Bz (p-displaced)’ represents the parallel displaced benzene dimer. The EDA results of the electrostatic components are shown within plots (a) and (b), the exchange/exchange–correlation components within plots (c) and (d), the Heitler–London interaction components within plots (e) and (f), the polarisation components within plots (g) and (h), and the charge transfer components within plots (i) and (j). The NEDA polarisation energies corrected with self energy term are given by POL+SE within plots (g) and (h). The green bars of the polarisation and charge transfer plots (g)–(j) represent the SAPT(KS) contributions, where the non–hashed bars represent the electrostatic contribution of this term only and where the hashed bars also include exchange in this term. The full BLYP–D3/6-311G* level interaction energy ΔE is given within plots (a) and (b).

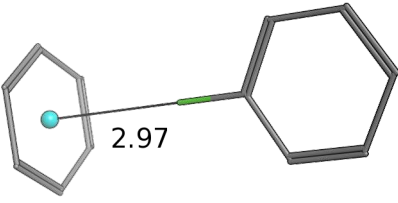
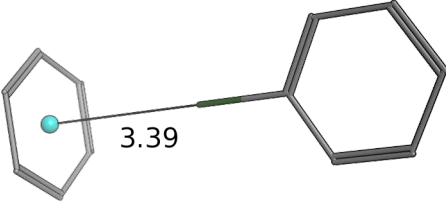
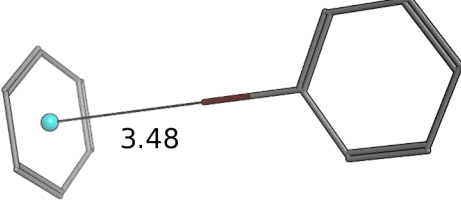
Table 4.5: Test set 5 (π interacting systems) BLYP-D3/6-311G* geometry optimised systems for EDA (intermolecular distances are given in Å)

System	Figure
Benzene – Benzene (T-Shaped)	
Benzene – Benzene (Parallel Displaced)	
Benzene – Pyridine	
Benzene – Pyrimidine	
Benzene – Dimethylacetamide	

4.2.1 Test Set 1: Hydrogen bonding interactions

This test set focusses on the hydrogen bonding interactions of water dimer derived systems, specifically the water dimer, water – methanol, methanol – methanol,

Table 4.6: Test set 6 (halogenated systems) BLYP-D3/6-311G* geometry optimised systems for EDA (intermolecular distances are given in Å)

System	Figure
Benzene – Fluorobenzene	
Benzene – Chlorobenzene	
Benzene – Bromobenzene	

and water – ammonia systems in the geometries shown in Table 4.1. A number of studies concerning the covalency of hydrogen bonding in water have been published [212–219]. EDA allows insight into the covalency of this interaction through the charge transfer component.

In Fig. 4.1(a) we observe that the electrostatics of the water dimer, water – methanol and methanol dimer systems are similar (within 0.52 kcal/mol at the NEDA/SAPT(KS) level and 1.05 kcal/mol at the KM EDA level), and that the water – ammonia system electrostatic energy is more stabilising than the water – methanol system by 3.81 kcal/mol at the NEDA/SAPT(KS) level and 5.44 kcal/mol at the KM EDA level. We would expect that as oxygen is more electronegative than nitrogen this would give rise to a greater dipole moment than for the final nitrogen containing ammonia interacting system and hence a higher electrostatic component for the first three systems. The oxygen containing molecules also possess 2 lone pairs rather than the 1 lone pair found on the nitrogen of ammonia,

and this would also support expectations of a lower electrostatic component for the ammonia interacting system. This trend therefore contradicts our chemical expectations. A similar yet opposite in sign trend is observed for the exchange component of Fig. 4.1(c), with the ΔE_{FRZ} and ΔE_{ESX} terms showing the electrostatic energy to be more dominant than exchange by similar amounts for the water dimer and water – ammonia systems. Polarisation (displayed in Fig. 4.1(g)) is shown to become more stabilising across the set fairly consistently, with a gain observed in stabilisation from the methanol dimer to the water – ammonia system for all but the NEDA (0.41 kcal/mol to 0.68 kcal/mol increase in stabilisation for all other schemes). For the NEDA of these two systems, polarisation (with the self-energy correction) is shown to be less stabilising by 1.08 kcal/mol for the water – ammonia system. This may be seen due to a number of reasons including lack of variational optimisation of the intermediate wavefunctions of NEDA.

We expect charge transfer to be increasingly dominant across the first three systems due to increasing presence of the electron donating methyl substituents. This is shown in Fig. 4.1(i) and is noted to increase consistently and at a slower rate than for the polarisation component across these systems. Charge transfer for the ammonia system is expected to be similar to the water dimer system due to its similar size. Due to the greater electronegativity of oxygen in comparison to nitrogen, we may expect charge transfer to be greater from the ammonia molecule due to its greater ability for electron donation. These features are also observed, with charge transfer indicated as falling for the final water – ammonia system by all schemes but the NEDA and SAPT(KS). For all but the RVS EDA scheme, charge transfer effects are greater for the water – ammonia system than the water dimer system. The NEDA values for charge transfer are also noted as being excessively large (up to -18.35 kcal/mol), almost an order of magnitude larger than the other methods and do not appear chemically credible.

The results suggest electrostatics to be the most dominant driving force of hydrogen bonding, with exchange greatly countering this contribution. Charge transfer remains the next most dominant driving force, except for the SAPT(KS) for

which on including exchange corrections the polarisation component is slightly more dominant across the set (up to 0.49 kcal/mol more dominant). Overall our results therefore suggest the hydrogen bonding interactions of this set to be characterised by dominance of the electrostatic energy component but with significant contribution from the charge transfer component and minimal polarisation contribution. This is a very interesting observation as hydrogen bonds are often described by necessity (e.g. forcefields) as arising only due to electrostatics without involvement of charge transfer effects. Notably, Weinhold and Klein [220] recently characterised a set of hydrogen bonding complexes in which the electrostatic interaction is interpreted as repulsive. Such “anti-electrostatic” hydrogen bonding complexes include interacting fluoride and bicarbonate anions, with the hydrogen bond presence evidenced by near linearity of the FHO unit bond (157.1°), significant vibrational red shift at ν_{OH} , Bader’s QTAIM [98] analysis and natural bond critical point analysis. There exists a significant repulsive penalty in order to form the bond (56.75 kcal/mol at the B3LYP/aug-cc-pVTZ level), with a shallow metastable “hydrogen bond” local minimum $\Delta E = -0.05$ kcal/mol. This is also further supported by our own ALMO EDA calculations at the B3LYP/aug-cc-pVTZ level and using the same geometry as Weinhold and Klein, in which we observe a strongly repulsive frozen density interaction of 64.27 kcal/mol with relatively small polarisation (-8.49 kcal/mol) and charge transfer (-3.81 kcal/mol) contributions. A re-examination of the electrostatic and resonance phenomena of this system by Frenking and Caramori [221] using the ETS EDA [101–103] at the B3LYP-D3/TZ2P+ level gave a deeper energy well (-0.77 kcal/mol) which was interpreted as a stabilising electrostatic interaction. In reply to Frenking and Caramori, Weinhold and Klein [222] argue that their viewpoint is different. This is a clear example that within the chemistry community a variety of EDA interpretations are in use which are not always compatible. This class of systems demonstrates the complex nature of hydrogen bonding (and equally the complex nature of EDA interpretations also), and shows that the presence of stabilising electrostatic interactions may not be necessary for hydrogen bonding between molecules.

4.2.2 Test Set 2: Water–cations

With the presence of charged monomers in the systems, we would expect this set to be dominated by electrostatic interactions. We would additionally expect the contribution of electrostatics to fall with increasing cation mass due to the increased intermolecular distance. This is observed in the EDA results, with the electrostatic energy contributions ranging between -44.14 kcal/mol and -23.66 kcal/mol across the set as displayed in Fig. 4.1(b), where we consider interactions between water and ammonium, lithium, sodium and potassium cations in the geometries shown in Table 4.2.

The trend in exchange (which includes both processes of electron exchange and orbital orthogonalisation, and hence describes a Pauli repulsion–type contribution) shown in Fig. 4.1(d) remains slightly less clear in its origin, as factors of intermolecular distance, electron count and energy costs of orthogonalisation all contribute to the value of this component. Nonetheless, we can rationalise the EDA results as both the energy cost of orthogonalisation and the exchange itself decay with increasing intermolecular distance.

For the alkali metals, we expect polarisation to be most significant for the lithium interacting system due again to the strong electrostatic energy interaction seen for this system as discussed above. The lithium ion is the smallest of the metals and hence is able to approach the water fragment more closely. We would therefore expect this ion to be able to polarise the water molecule charge density more effectively than the remaining metals. This trend is observed within the EDA results as shown in Fig. 4.1(h).

Polarisation is observed to be less stabilising for the ammonium interacting system than for the lithium interacting system, whilst charge transfer is conversely observed to be the most stabilising (excluding SAPT(KS)) for the ammonium interacting system as shown in Fig. 4.1(j). The decrease in polarisation contribution

is possibly a result of the increased $r(\text{O}-\text{N}^{\delta+})$ distance in comparison to the $r(\text{O}-\text{Li}^+)$ distance, and the greater charge transfer contribution of this system may arise through the ability of the ammonium molecule to diffuse its charge over a much larger volume than the alkali cations.

For the charge transfer component of the alkali metals, we again expect the properties of the lithium ion to be significant in determining the trend observed. We would expect the lithium ion to be more effective at withdrawing charge from the partner water molecule, and hence expect the EDA results to display a more stabilising charge transfer component for the lithium ion that decreases down the group 1 metals. This is observed to an extent in Fig. 4.1(j): between the lithium and sodium ion interacting systems the charge transfer contribution falls for all but the SAPT(KS) scheme without the exchange correction. We also note that for the RVS EDA scheme the charge transfer energy is positive and unphysical for these two systems (0.05 kcal/mol and 0.34 kcal/mol for the lithium and sodium ion interacting systems respectively), seemingly through over-correction by the CP correction. Interestingly, we observe charge transfer to increase between the sodium and potassium ion interacting systems for all but the NEDA and SAPT(KS) schemes. It is unclear why this is observed, however through the analysis of the charge transfer BSSE contributions of the schemes that display this unexpected trend it appears that the increase also arises due to an artefact of these schemes' CP corrections.

The charge transfer KM EDA component is indicated as increasing for the final water – potassium system. This observed break from the trend may be due to the known instability of the KM EDA with larger basis sets and smaller intermolecular distances [146–148], whereby a state with occupied orbital occupation number greater than 2 is possible. Whilst the water – cation distance is the greatest for the potassium system, the increase in the extension of the 6-311G* basis with the extra electron shell may be large enough to give rise to this artefact of the KM EDA scheme. This highlights the contradictory observation that using an

incomplete basis set with the KM EDA can give rise to results with more physical relevance.

4.2.3 Test Set 3: Ammonium- π systems

We have considered the interactions of ammonium with benzene, thiophene, furan and pyrrole in the geometries shown in Table 4.3. The results suggest electrostatic effects to be the most dominant interactions for this set followed by exchange, as shown in Fig. 4.2(a) and 4.2(c). Polarisation followed by charge transfer are observed to be the next most dominant interactions as shown in Fig. 4.2(g) and 4.2(i). These observations are supported by a similar EDA analysis of this test set by Aschi et al. [87] using the RVS EDA method. The electrostatics of the benzene and thiophene are observed to be similar in magnitude and lie between the interaction magnitudes of the furan and pyrrole interacting systems, closer to the furan system. In fact the thiophene and benzene interacting systems display similar EDA component profiles across the range of the EDA schemes, evidencing their similar bonding character and possible functional group interchangeability within drug design. The similar components seen for these two systems are expected through the very similar electronegativities of carbon and sulphur and the similar aromatic structures of these systems.

We would chemically expect the vast majority of polarisation to result by effect of the ammonium ion on the aromatic fragment. Aschi et al. [87] support this expectation quantitatively with greater than 98.5% of polarisation contributed by the aromatic fragment and describe the polarisation interaction as “exclusively an ion-induced multipole interaction”. Polarisation is observed to fall slightly (up to 0.59 kcal/mol) between the benzene and thiophene interacting systems, and again between the thiophene and furan interacting systems (up to 1.31 kcal/mol). For the pyrrole interacting system polarisation is observed to increase in stability. The NEDA scheme predicts this stability increase to be small (0.23 kcal/mol) with the contribution of polarisation lying between the thiophene and furan contributions.

However, for the remaining schemes this is suggested to be more significant, with the polarisation contribution of the pyrrole interacting system the greatest for this set.

The magnitude of charge transfer effects is dependent on the electron donating ability of the aromatic system. Based purely on the electronegativities of carbon, sulphur, oxygen and nitrogen (and therefore their electron donating ability into the aromatic ring), we would expect charge transfer to the ammonium to be of the order furan < pyrrole < benzene = thiophene. Our expectations using this model partially confirm this, with the trend supporting similar charge transfer values for the benzene and thiophene interacting systems, and smaller furan charge transfer than for pyrrole. Our model does not account for the less clear effects resulting from the aromatic geometries and constituents however, and this may be the reason for the inaccuracy of our expectations. For the ALMO, KM and RVS EDAs and SAPT(KS), charge transfer is indicated as within a reasonably small range across the set (within 2.60 kcal/mol) but increasing significantly from -12.33 kcal/mol to -18.89 kcal/mol for the NEDA scheme. This large range of NEDA charge transfer energies is unexpected and indicates a lack of stability of this component.

4.2.4 Test Set 4: π -cations

In this set we consider the interactions of benzene with ammonium, lithium, sodium and potassium cations in the geometries shown in Table 4.4. The set is similar to the systems in test set 2 through shared cation molecules, and similar component profiles are observed as a result of this. From a chemical perspective, we would expect similar but less stabilising electrostatic components for the benzene interacting systems of this set than the water interacting systems of test set 2. This is due to a more strongly interacting dipole moment of water in comparison to the quadrupole moment of benzene with the cations. This is confirmed by electrostatic energies between -6.94 kcal/mol to -22.61 kcal/mol across test set 4

compared with electrostatic energies between -23.66 kcal/mol to -44.14 kcal/mol for test set 2.

Exchange effects (Fig. 4.2(d)) are expected to be generally less significant than for test set 2 due to the greater intermolecular distances of the systems of test set 4. This is observed across the set, notably however exchange is not shown to fall in a consistent manner. This observation possibly arises due the comparatively small intermolecular benzene – lithium separation that results in a greater exchange component.

Polarisation within test set 4 (Fig. 4.2(h)) is shown to be approximately twice the magnitude of polarisation within test set 2 (Fig. 4.1(h)). This observation is explained from a chemical perspective by the greater polarisability of benzene ($\alpha = 10.74 \text{ \AA}^3$) in comparison to water ($\alpha = 1.45 \text{ \AA}^3$) [223]. The polarisation component of the lithium interacting system is shown to stabilise the system by more than 400 kcal/mol through the KM EDA using the 6-311G* basis set. Removing d polarisation functions from the lithium basis reduces this component to a more reasonable value (-25.86 kcal/mol). This artefact is believed to originate in the ability of valence electrons to collapse from one fragment into the core orbitals of the other fragment, enabled through the use of intermediate wavefunctions that do not satisfy the Pauli exclusion principle [146–148]. As the completeness of the basis set increases, the polarisation component becomes extreme in magnitude as this process of collapse becomes more significant. We have also included results using the balanced 6-311G basis set in Table A.6 of the Appendix. These results support the use of the modified unbalanced basis as reliable as an approximation to the 6-311G* basis used in the remaining calculations.

Interestingly, charge transfer (Fig. 4.2(j)) does not follow the same trend as within test set 2 (Fig. 4.1(j)) and the ammonium and lithium cations are reversed in their charge transfer contribution trends. This observation is expected, as the hydrogen atom of the ammonium molecule interacting with benzene is directed into the

low electron region of the π cloud whereas for the water – ammonium system an ammonium hydrogen atom is directed towards the oxygen of the water molecule.

Charge transfer within the benzene – lithium system is indicated as highly contributing in comparison to the systems of the other sets. This contribution is possibly due to the cation being able to access the electron-rich π cloud of the benzene by siting itself within this on binding, and due to the charge of the cation interacting with the benzene. A more rapid decrease in charge transfer contribution with increasing cation mass is observed than for the water – cation systems of test set 2. This may be a result of the geometry of the set: the rate of fall in intermolecular distance across the π – cation set (1.90 Å range of r) is greater than across the water – cation set (0.77 Å range of r).

4.2.5 Test Set 5: π interacting systems

In this set we consider a number of systems interacting with the π ring of benzene. Specifically we consider the parallel displaced and T-shaped benzene dimers, and pyridine, pyrimidine and dimethylacetamide (DMA) interacting with benzene in the geometries shown in Table 4.5.

A number of predictions can be made based on the compositions of the structures of study. We would expect the energy components to increase in magnitude when going from the benzene T-shaped to the parallel displaced conformers due to the smaller intermolecular distance between the molecules. Generally this is observed in the results. Notably, however, stabilisation through the KM EDA electrostatic component is shown to fall by over 1 kcal/mol as shown in Fig. 4.3(a). The charge transfer components of the ALMO EDA and SAPT(KS) (with exchange correction) schemes are also observed to fall fractionally between these two systems as shown in Fig. 4.3(i), however these energy changes are so small that they may be considered negligible.

The three π - π interacting parallel displaced systems are structurally very similar and so deducing the expected component trends for these systems is slightly less clear. With an increase in the number of nitrogen constituent atoms on the interacting molecules we observe an increase in charge transfer effects, as also shown in Fig. 4.3(i). This is expected: with increased substitution through benzene, pyridine and pyrimidine the electron withdrawing abilities of these molecules also increase, and so are able to withdraw more charge density from the π cloud of the partner benzene molecule. In considering polarisation effects within these three systems, we would expect a more significant electric moment in the plane of the benzene interacting system with increased substitution to provide a more polarising field for the benzene molecule. Polarisation across these three systems is predicted to be enhanced through this effect. However, the polarisabilities of these molecules themselves are shown to fall across the three systems ($\alpha = 10.74 \text{ \AA}^3$, 9.15 \AA^3 and 8.53 \AA^3 for benzene, pyridine and pyrimidine respectively) [223], and so the final polarisation contribution becomes a balance of these two opposing factors of polarisability and field strength. As shown in Fig. 4.3(g), polarisation falls across the three systems for all but the NEDA scheme, therefore indicating that the effect of falling polarisabilities outweighs the effect of more significant polarising electric fields for the benzene.

For the final DMA interacting system, we observe moderately increased electrostatic and exchange energy contributions as shown in Fig. 4.3(a) and 4.3(c) respectively. This is interesting to note as the DMA molecule to benzene distance is similar to the intermolecular distances seen within the other systems. We may expect a greater polarisation contribution for this system due to the more extended structure of the DMA molecule in comparison to the cyclic structures of the other interacting systems. This is supported by the results shown in Fig. 4.3(g) for all but the NEDA scheme. We expect the proton positioned above the π cloud to act as a means for electron transfer to the DMA molecule, with the oxygen acting as an electron sink stabilised through resonance of the amide bond. As a result of

this, we predict charge transfer to be greater for this system. This is observed for all but the HF level schemes (KM and RVS EDA), as shown in Fig. 4.3(i).

4.2.6 Test Set 6: Halogenated systems

We have considered a selection of halogenated benzene systems interacting with another benzene molecule in test set 6. The halogens we have selected are fluorine, chlorine and bromine and the system geometries are shown in Table 4.6. The systems have been constrained in a T-shaped geometry, with the halogens directly interacting with the π ring through the halogen σ hole [224]. For all our structures the energy minimisation procedure we employed did not use the CP correction. We note that the (BSSE corrected) interaction energy of the benzene – fluorobenzene system is positive as shown in Fig. 4.3(b), with this arising due to the CP correction raising the interaction energy to the point that the interaction becomes repulsive. Natural population analysis of these systems at the BLYP–D3/6-311G* level reveals natural charges on the fluoro–, chloro– and bromobenzene halogens as $-0.326e$, $-0.007e$, $0.061e$ respectively, correlating with the presence of a σ hole on the bromine and chlorine atoms. The σ hole arises due to three unshared electron pairs on the halogen arranging to produce a belt of negative potential around the bond axis on the halogen, leaving a region of positive potential on the halogen opposite to the halogen bond [224]. The presence of the σ holes on the bromine and chlorine atoms is expected to affect the EDA profiles of the systems of test set 6, most significantly through enhanced electrostatics in the systems containing these atoms.

We predict the electrostatic energy to increase from the fluorobenzene interacting system through to the bromobenzene interacting system. This is because going through the series the charge on the halogen becomes more positive, and so the electrostatic interaction of the halogenated benzene molecule with the quadrupole of the benzene will become more favourable. We expect the σ hole on the chlorine and bromine atoms to enhance this effect, as the positive potential on these atoms

is therefore concentrated to a region on the halogen that gives a more favourable electrostatic interaction with the benzene π cloud. In fact, due to lack of a σ hole on the fluorobenzene molecule we may expect the electrostatic interaction in this system to be destabilising. We also expect the increasing intermolecular distances through the series to contribute to a decrease in electrostatic component energy magnitudes. This factor opposes our expectations of increasing electrostatics through the series due to increasing halogen charge. The electrostatic component results are shown in Fig. 4.3(b). It appears that the increase in electrostatics through the series arises due to increasing halogen charge, which more than compensates for any weakening of this component through increased intermolecular distance.

The exchange component is expected to fall through the series due to increased intermolecular separation of the molecules. As halogen electronegativity decreases through the series, we expect the charge on the halogenated benzene molecule to become more localised on the π ring. This is expected to additionally reduce the contribution of exchange, as exchange is distance dependent and the electrons are now further from the partner benzene molecule. We observe a slight fall in exchange that is in agreement with our predictions between the fluorinated and chlorinated systems as shown in Fig. 4.3(d). However, exchange is approximately as strong for the brominated system as the fluorinated system. This arises due to the greater number of electrons on bromobenzene than on fluorobenzene. With more electrons on the bromobenzene available to exchange with the benzene electrons, the exchange interaction for bromobenzene can therefore be stronger despite the greater intermolecular separation for this system.

Whilst polarisation effects are expected to increase through the set as a result of increasing polarisabilities of the halogenated benzene molecules, the increase in intermolecular separations of the systems is also expected to have an impact on this component. The polarisability of fluorobenzene ($\alpha = 10.3 \text{ \AA}^3$) is less than that of chlorobenzene ($\alpha = 14.1 \text{ \AA}^3$) and bromobenzene ($\alpha = 14.7 \text{ \AA}^3$) [223]. However, the benzene π ring to halogen distance is more than 0.42 \AA shorter for the

fluorinated system than for the chlorinated and brominated systems as shown in Table 4.6. The enhancement of polarisation through the smaller benzene – fluorobenzene intermolecular separation could be reasonably similar to the enhancement in the benzene – bromobenzene through the effect of greater bromobenzene polarisability, however we cannot predict by chemical reasoning alone which factor dominates. The intermolecular separations of the chlorinated and brominated systems are reasonably similar, and we expect that polarisation effects will be greater in the brominated system than the chlorinated system solely as a result of differences in molecular polarisabilities. The polarisation results are shown in Fig. 4.3(h). The NEDA results show polarisation to be smallest for the fluorinated system (-1.22 kcal/mol with the self-energy correction), indicating the smaller intermolecular separation within this system to offer little enhancement to polarisation. However, NEDA overestimates polarisation by an order of magnitude compared to the other schemes. More importantly all other schemes show polarisation to be slightly greater for the fluorinated system and therefore instead indicate the smaller intermolecular separation to enhance polarisation to a small degree. Our prediction of increased polarisation from the chlorinated system to the brominated system is in agreement with all the EDA scheme results.

We expect the presence of a σ hole on the chlorine and bromine atoms to enhance charge transfer to a degree in these systems. This is due to the σ holes being located in the high electron region of the benzene π ring. We predict the strongly electron withdrawing nature of the fluorine atom to be more important than the presence of a σ hole in enhancing charge transfer effects. Also, the smaller benzene – halogen separation in the benzene – fluorobenzene system (2.97 Å) is also expected to enhance charge transfer effects in this system. The intermolecular separation is slightly greater within the bromobenzene system than within the chlorobenzene system, and chlorine is more electronegative than bromine. We therefore predict the charge transfer interaction to be weaker for the bromobenzene system than the chlorobenzene system. Our results of charge transfer for this test set are shown in Fig. 4.3(j). The results of the SAPT(KS) scheme shows charge transfer

to increase in strength going through the set from the fluorinated system to the brominated system. This indicates charge transfer to be weakest in the benzene – fluorobenzene system despite this system’s smaller intermolecular separation and the greater electronegativity of the fluorine atom compared to the other halogens, and therefore suggests the presence of a σ hole to be significant in determining charge transfer in these systems. The other schemes generally show similar or greater charge transfer effects for the fluorinated system than for the brominated and chlorinated systems. These schemes therefore instead suggest the presence of a σ hole on the halogen to contribute at least slightly to charge transfer effects in the chlorinated and brominated systems. All schemes show an increase in charge transfer between the chlorinated and brominated systems, confirming our predictions for these two systems.

4.2.7 Dispersion energy treatments

In this section we consider the results of the various treatments of the dispersion energy contribution to the interaction energy. The dispersion component is described as an explicit component of the SAPT(KS) scheme, but as an ad-hoc correction term to the interaction energy of the other EDA schemes provided by the empirical –D3 correction of Grimme [209]. The results of our calculations using these approaches are shown in Fig. 4.4. The form of the –D3 correction is dependent on the choice of density functional used and therefore we note that it is more suitable for the energies of this component to be considered with respect to other –D3 energy values, rather than in direct comparison to the SAPT(KS) dispersion energy values. Overall the SAPT(KS) and –D3 approaches to measuring dispersion are generally in agreement with one another, except in the case of the metallic cation systems of test set 4 shown in Fig. 4.4(d) for which the results differ quite substantially. This inconsistency will be discussed below, in addition to the dispersion component observations for the other test sets.

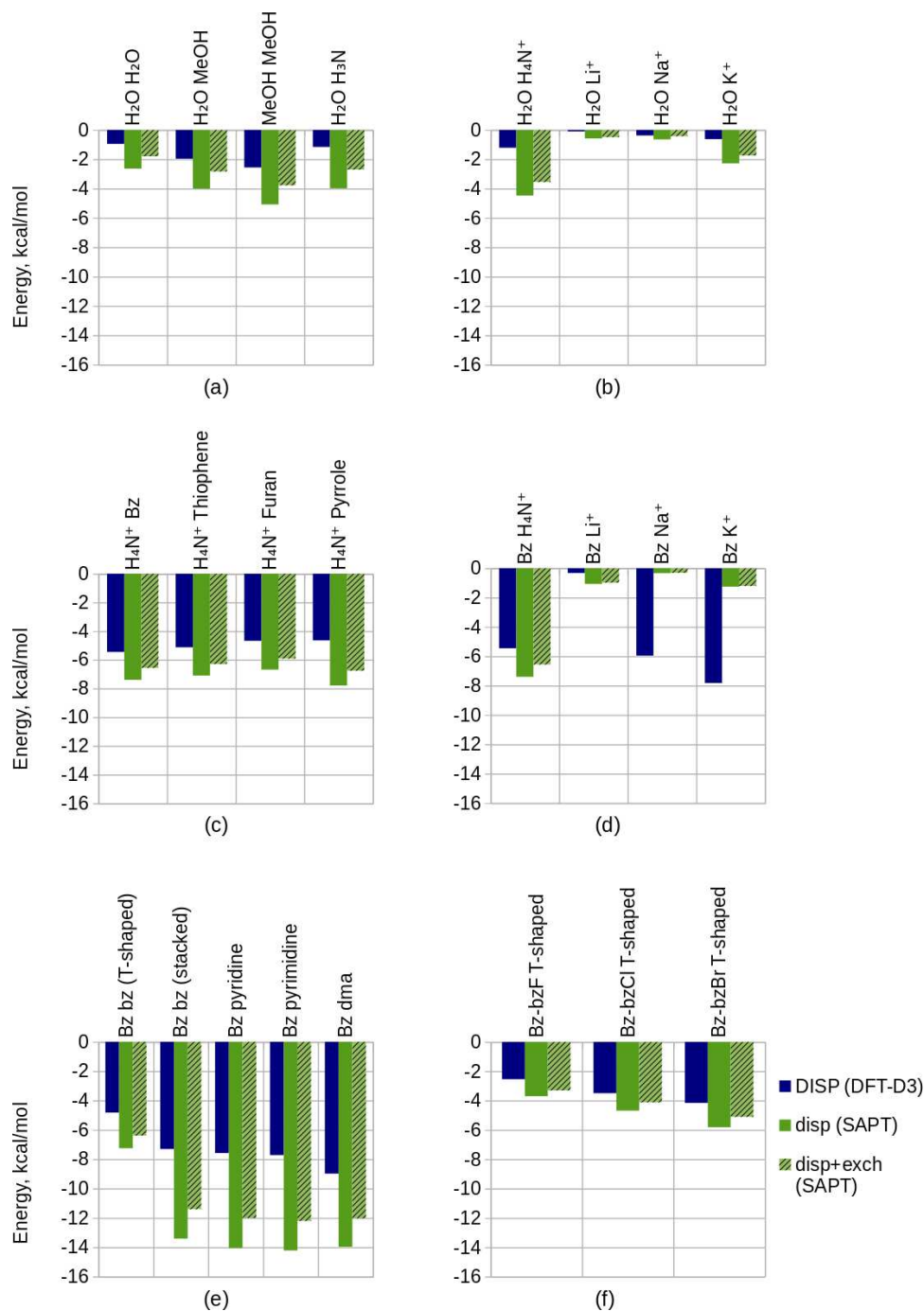


Figure 4.4: The -D3 correction for dispersion (blue), and SAPT(KS) dispersion (green) energy values (in kcal/mol). The energy values for test sets 1–6 are given by plots (a)–(f) respectively. ‘Bz Bz (p-displaced)’ represents the parallel displaced benzene dimer. The non-hashed green bar represents the electrostatic contribution of dispersion only and the hashed bar represents the exchange plus electrostatic contribution of this term.

The dispersion interaction arises as a result of instantaneous polarisation dipoles in the monomers forming and interacting. We would therefore expect greater dispersion contributions for systems where both monomers have high polarisabilities, as this would enable larger instantaneous dipoles to arise. Chemically this component is also highly dependent on the intermolecular separation R , with its magnitude decaying as R^{-6} .

For test set 1, we expect the determining factor of the trends to be the molecular polarisabilities. This is because the intermolecular separations observed in this set are similar, as shown in Table 4.1. The polarisability of methanol ($\alpha = 3.29 \text{ \AA}^3$) [223] is more than twice that of water ($\alpha = 1.45 \text{ \AA}^3$) [223] and therefore an increase in dispersion across the first three systems of this set is expected. The polarisability of methanol is greater than that of ammonia ($\alpha = 2.10 \text{ \AA}^3$) [223] and so we would expect dispersion within the water – methanol system to be greater than within the water – ammonia system. The results of the dispersion component for these systems are shown in Fig. 4.4(a), and our predictions are generally confirmed. We note that our prediction of a greater dispersion component for the water – methanol system than the water – ammonia system is observed in the results of the $-D3$ component, however for the SAPT(KS) scheme dispersion remains nearly constant between these two systems.

We expect the induced electric dipole moment of the ammonium molecules to be greater than for the metal cations for test set 2. This is because despite the presence of more diffuse electrons on the metal cations, the ammonium molecule is much larger and so we expect a larger dipole for this molecule to be able to be induced. The intermolecular separations of the ammonium molecule and metal cations are similar as shown in Table 4.2, and we therefore predict dispersion for the ammonium interacting system to be the strongest. This is confirmed by the results by both dispersion methods as shown in Fig. 4.4(b). In this set the intermolecular distance between the potassium ion and the water molecule is 0.77 \AA greater than for the lithium ion interacting system. As dispersion forces are very close range interactions decaying as R^{-6} , this component would fall to less than $1/8$ th of its

original size if this geometric displacement were applied to the lithium ion. The polarisability of a potassium atom ($\alpha = 43.4 \text{ \AA}^3$) [223] is nearly twice that of lithium ($\alpha = 24.33 \text{ \AA}^3$) [223] and we expect the difference in polarisability of their ions to be similar in size. We would therefore expect that the strong dependence on intermolecular distance for dispersion outweighs the greater polarisability of potassium, resulting in a fall in dispersion across the set. Interestingly, however, the opposite is observed in our results and dispersion instead increases across the set.

As previously stated for our analysis of the remaining energy components of test set 3, we expect the systems of this set to display similar dispersion energy values due to the similar geometries and compositions of the structures. The polarisabilities (α) of benzene [223], thiophene [225], furan [225] and pyrrole [226] are 10.74 \AA^3 , 9.96 \AA^3 , 7.20 \AA^3 , and 8.27 \AA^3 respectively. We therefore expect a slight fall in dispersion contributions from benzene to furan, and for pyrrole to have a dispersion energy value between thiophene and furan. The results for this set shown in Fig. 4.4(c) are in close agreement with our predictions, however for the final pyrrole interacting system we observe a greater than expected contribution by the SAPT(KS) approach and a slightly lesser than expected contribution by the $-D3$ component.

We expect the systems of test set 4 to show similar dispersion component values to the systems of test set 2 because these sets differ only through the interaction of benzene rather than water. Our expectations for test set 2 were of a greater dispersion energy for the ammonium interacting system, and a decrease in dispersion through the metal cation interacting systems due to the significant intermolecular dependence of dispersion. The increase in intermolecular distances through the metal cation interacting systems of test set 4 is much greater than in test set 2, and so we expect an even greater fall in dispersion through these systems in test set 4 than in test set 2. Our prediction of a greater dispersion component for the ammonium interacting system is supported by the results shown in Fig. 4.4(d), however the trends observed for the remaining metal cation interacting systems are

significantly less supportive. In comparison to the results of the metal cation interacting systems of test set 2 (Fig. 4.4(b)), the greater increase in intermolecular distance through test set 4 appears to cause a comparatively weaker contribution of dispersion to the potassium interacting system by the SAPT(KS) scheme. Interestingly the opposite is shown for the $-D3$ component, with this energy unexpectedly increasing significantly across the metal cation interacting systems of test set 4 despite the rapid increase in intermolecular distances.

We note a significant dispersion contribution for the systems of test set 5 as shown in Fig. 4.4(e). This is expected considering the π interacting chemical nature of these systems. For the SAPT(KS) results of the benzene dimer, dispersion for the parallel displaced conformation is almost double than when in the T-shaped conformation. This is rationalised by the fact that the sum of the intermolecular atomic distances for the parallel displaced benzene dimer system is less than in the T-shaped system. It is also noted that the parallel displaced benzene dimer system features close proximity of the π rings of the benzene molecules. This is also expected to contribute to the dispersion interaction. For the three π - π interacting parallel displaced systems our chemical expectations are mixed. Polarisability is noted to fall from benzene to pyrimidine ($\alpha = 10.74 \text{ \AA}^3$ and 8.53 \AA^3 respectively [223]), and so we expect dispersion to fall across these benzene interacting molecules. However, the fall in intermolecular distances across these systems is expected to enhance the contribution of the dispersion energy due to its significant dependence on this parameter. The increase in dispersion across these three systems indicates that the decrease in intermolecular distances is more significant than the fall in polarisabilities of the molecules. For the DMA interacting system, we expect dispersion to be approximately as contributing as in the other systems. However it is difficult to give a precise prediction of this system's relative value due to the many possible chemical factors that affect dispersion. There exists delocalised π systems in all the molecules of this set. In DMA the presence of this feature is in the delocalised amide bond, and for the remaining molecules this is in their aromatic π rings. However, for DMA the amide bond is located further away

from the π ring of benzene and so dispersion resulting from this delocalised feature is expected to be smaller. The structure of DMA is noted to be more extended than the other molecules in this set, and therefore greater dipoles are expected to be able to be induced in this molecules. This factor would be expected to favour a greater dispersion contribution in this system. The intermolecular separations of the systems (excluding the T-shaped benzene dimer system) are similar and therefore the balance of the above two features is difficult to predict. For the -D3 component dispersion is shown to increase moderately, whereas for the SAPT(KS) scheme this component falls by at most only 0.25 kcal/mol.

Within test set 6 we expect dispersion to be most contributing in the fluorinated system, followed by the chlorinated system, and finally the brominated system. The polarisabilities of chlorobenzene ($\alpha = 14.1 \text{ \AA}^3$) and bromobenzene ($\alpha = 14.7 \text{ \AA}^3$) are similar, with the polarisability of fluorobenzene much smaller ($\alpha = 10.3 \text{ \AA}^3$) [223]. However, the intermolecular separation for the fluorinated system (5.69 Å) is also smaller than for the chlorinated (6.50 Å) and brominated systems (6.75 Å), as also shown in Table 4.6. Due to the significant dependence of dispersion on distance we expect dispersion to be relatively strong in the fluorinated system. For the chlorinated and brominated systems, we expect the chlorinated system to show the greater dispersion contribution. The strong dependence of dispersion on intermolecular separation combined with the similar polarisabilities of chlorobenzene and bromobenzene leads us to expect the chlorinated system to show a greater dispersion contribution than the brominated system. Our results shown in Fig. 4.4(f) display opposite trends to our predictions. The -D3 component shows an increase in dispersion from the fluorinated system (-2.54 kcal/mol) to the chlorinated system (-3.50 kcal/mol) and to the brominated system (-4.15 kcal/mol). The SAPT(KS) results show an increase in dispersion from the fluorinated system to the chlorinated system of over 0.8 kcal/mol, and from the chlorinated system to the brominated system of over 1 kcal/mol. It is interesting to note the greater dispersion contribution shown by the EDA results for the benzene – bromobenzene system, and the less than expected dispersion contribution

for the benzene – fluorobenzene system.

4.2.8 Observed EDA scheme advantages and weaknesses

In this section, we compare the features and artefacts of the different EDA schemes studied in this thesis, as emerging by the theory and our tests. An overview of our observations is provided in Table 4.7.

General observations The CP correction is known to overestimate the BSSE [62; 227] and many of the schemes we have included in our investigation apply the CP correction to energy terms. It is important to note that as a result this correction has the potential to give rise to unphysical results, as is observed in the case of the charge transfer energies in the group 1 metal ion interacting systems of test set 2 for example. Over-correction of the RVS EDA charge transfer energies results in a positive and unphysical energy for the lithium and sodium ion interacting systems, as shown in Fig. 4.1(j). Also, on applying the CP correction to the ALMO, KM and RVS EDA scheme charge transfer energy components the trend between the sodium and potassium ion interacting systems reverses. This serves to highlight the possible issues that may arise when applying the CP correction to EDA energy components.

KM EDA. The KM EDA [142; 143] requires an unphysical residual mixing term ΔE_{MIX} to account for the difference between the energy components and the total interaction energy. This is a significant weakness as the mixing component values are at times observed to be of the same magnitude as the chemically meaningful terms. For example when including BSSE corrections, in the case of the metal cation interacting systems of test set 2 the mixing component is greater than the charge transfer term, and for test set 6 this component is greater than the magnitude of the polarisation term. Attempts to reduce this problem have been

Table 4.7: A summary of the EDA approaches investigated

EDA scheme	MO localisation ^a	Additional energy components ^b	Level of theory	Component artefacts and notes
KM EDA	–	ΔE_{MIX}	HF only	Presence of the ΔE_{MIX} energy unascrivable to any particular component. Problems of numerically unstable charge transfer and polarisation energies with large basis sets and at short intermolecular distance [146–148].
RVS EDA	–	ΔE_{MIX}	HF only	Unphysical ΔE_{MIX} present. Typical magnitude is insignificant, but possible for non-negligible magnitudes to be seen.
ALMO	ALMO	–	HF/Correlated	Combined electrostatics and exchange description of the frozen density component may reduce chemical insight.
NEDA	NBO	$\Delta E_{\text{DEF}}, \Delta E_{\text{SE}}$	HF/Correlated	Theoretical overestimation of charge transfer and underestimation of polarisation [15; 80]. Observed to provide unphysical charge transfer values.
PIEDA	FMO	–	HF/Correlated ^c	Shares similar theoretical weaknesses of the KM EDA.
SAPT(KS)	–	$E_{\text{disp}}^{(2)}, E_{\text{exch-disp}}^{(2)}$, ^d	HF/Correlated	Observed overestimation of polarisation and underestimation of charge transfer. SAPT(KS) overestimation of second-order energy components (induction and dispersion) with the B3LYP functional [202].

^a Localisation methods include adopting an alternate basis to the MO basis (the NBO basis), an MO constraining method (ALMO), or a different energy calculation method (FMO).

^b Additional energy components to the electrostatics, exchange, polarisation and charge transfer (or similar) interaction components.

^c The PIEDA scheme is implemented at the HF level (as the basis of this scheme is the KM EDA), with the dispersion component added as an additional term, ΔE_{DI} .

^d SAPT descriptions of polarisation and charge transfer are calculated from the MCBS and DCBS induction energies (see Eqs. 3.70a and 3.70b).

discussed and implemented within the RVS and CSOV schemes, and the problem altogether avoided in other schemes such as the ALMO EDA and NEDA.

Numerical instability problems of the charge transfer and polarisation energies with large basis sets and at short intermolecular distances [146–148] are evidenced in our results. For the benzene – Li⁺ system of test set 4 convergence issues are observed when using the 6-311G* basis set. For this system the intermolecular separation is particularly small (1.88 Å) and gives rise to unphysical polarisation and mixing component energies. This is likely due to valence electrons collapsing from one fragment into the core orbitals of the other fragment [146–148].

RVS EDA. The RVS EDA [10; 84] is similar to the KM EDA, but with modification to the calculations of the polarisation and charge transfer energies to use fully antisymmetric wavefunctions in attempt to remedy the numerical instability problems associated with these components in the KM EDA.

The ΔE_{ESX} component of the RVS EDA scheme (and similar ΔE_{FRZ} component of the ALMO scheme) presents a problem in terms of the analytic information provided. This is because this energy component conceals the magnitudes of its electrostatic and exchange parts. The combined term does however provide useful indication of the dominance of its parts. For example, if this component is highly repulsive this would indicate Pauli repulsions to be significant. Avoiding the use of Hartree product intermediate wavefunctions involved in expressing the separated components may be desired, however, due to it not obeying the Pauli principle.

The RVS EDA scheme shares a component of the KM EDA that describes a residual energy to the interaction energy. In our calculations the magnitude of the RVS mixing component is typically less than 0.1 kcal/mol and therefore much smaller than the KM EDA mixing component. However, for systems containing an ammonium molecule the RVS mixing component is noted to increase significantly, for example the ammonium – pyrrole system of test set 3 has an RVS mixing component of -0.44 kcal/mol. Whilst the magnitude of this term is only a fraction of the

KM EDA mixing term (3.76 kcal/mol with BSSE correction), this does indicate that a notable level of ambiguity can still remain in the origin of a proportion of the interaction energy. Overall, however, the magnitude of the mixing term for any given system is more often than not negligible, and this helps to correct a major weakness of the KM EDA.

In the RVS EDA scheme the BSSE is only partially treated and this may be considered a weakness of the scheme. The interaction energy that is obtained in this scheme omits the exchange BSSE correction of Eqs. 3.13a and 3.13b that is treated in the KM EDA. By adopting the KM EDA BSSE correction for the exchange component, it is possible to remedy this. This is possible because the origin of the exchange component energy of these two schemes are the same, and so the RVS exchange energy is compatible with this BSSE correction and will give the fully BSSE corrected interaction energy.

ALMO EDA. The ALMO EDA scheme [15] used in our calculations provided overall chemically sensible results. There are two possible disadvantages we note of this scheme however. Firstly, as discussed regarding the ΔE_{ESX} component of the RVS EDA scheme above, the ALMO EDA ΔE_{FRZ} component similarly has the potential to be limited in the analytic information it provides. Secondly, it is theoretically possible for the charge transfer contribution to be repulsive on inclusion of the CP BSSE correction. This is because the CP correction has a tendency to overestimate the BSSE [62; 227] as discussed above. As noted by Mo et al. [80], it may be appropriate to consider the ALMO (and BLW) EDA charge transfer energies with and without the BSSE energy correction as the upper and lower bounds of this energy. Our results otherwise show the ALMO EDA scheme to consistently provide results in good agreement with chemical expectations.

NEDA. Our calculations using the NEDA scheme [12; 13; 82; 83] have shown this to give often very large charge transfer and polarisation energy contributions. Theoretically the NEDA scheme is expected to generally overestimate

charge transfer contributions and underestimate polarisation [15; 80]. This is because in NEDA, the polarisation and charge transfer terms are calculated from the monomer and supermolecule charge densities without variational optimisation to an intermediate state. If we consider an alternative scheme such as the ALMO EDA scheme (in which an intermediate state is produced in a constrained optimisation procedure) we can see that the NEDA description of the intermediate state is likely less desirable.

Another key observation of the NEDA scheme is its description of polarisation effects. The polarisation term includes only electrostatic contributions as shown in Eq. 3.53, and the exchange contribution is contained within the deformation component. Furthermore, an electrostatic self energy penalty is also included in the NEDA scheme that describes the energy cost of charge polarisation. This partitioning of polarisation in NEDA may be advantageous or not depending on the situation at hand.

SAPT(KS). The results of the SAPT(KS) scheme [17; 18] are observed to remain in keeping with the trends shown by the other schemes and generally show chemically relevant magnitudes. Polarisation energies of the SAPT(KS) scheme are typically second in magnitude only to the NEDA scheme polarisation energies. The SAPT(KS) is noted as overestimating the second-order energy components (induction and dispersion) with the B3LYP functional [202]. This is suggested to arise due to the poor suitability of DFT canonical virtual orbital energies in the SAPT scheme. The first-order terms (electrostatics and exchange) are not affected by this as their values depend on use of the occupied set of MOs only.

The arrangement of the SAPT energy components is different to within the variational based EDA methods. This organisation is arguably more intuitive than in the other EDA schemes, with the SAPT approach separating the energy terms at the different orders into exchange and electrostatic contributions. Equally, however, the theory of SAPT is also more complicated than the variational based EDA

methods and many energy terms can be involved in describing the interaction energy. For example, Stone et al. [90]. have noted that in some cases exchange uncorrected SAPT(DFT) charge transfer terms are overestimated by up to an order of magnitude. The inclusion of the exchange part corrects and almost cancels the charge transfer term. Indeed, this large correction to charge transfer by the exchange part is observed in many of the results of our SAPT(KS) calculations. For example, in the case of our hydrogen bonding water dimer system, SAPT(KS) charge transfer is -5.60 kcal/mol and the exchange correction is 4.75 kcal/mol giving an overall corrected charge transfer energy of -0.85 kcal/mol. In this case, the additional separation may have the potential to mislead. As discussed above, the lack of consistency of term definitions between the EDA schemes (whether variational or perturbational) can become problematic. For example, one scheme may include exchange contributions in certain energy components while another scheme may not. In SAPT, by partitioning each component into electrostatic and exchange parts, the term descriptions are more clearly described as the terms are explicitly partitioned into their classical and quantum energy contributions.

Whereas the variational EDA approaches we have studied do not include dispersion contributions within the decomposition, the SAPT scheme explicitly includes this energy as $E_{\text{disp}}^{(2)}$. This additional description of dispersion is of merit to this scheme. Our results comparing the SAPT(KS) dispersion energies to the -D3 component energies showed reasonable correlation between the two approaches, as shown in Fig. 4.4.

4.3 Summary

In this section we summarise the findings of our EDA investigation, the theories of which have been described in detail earlier in Chapter 3.

During the past several decades, a wide range of EDA approaches have been developed that decompose the interaction energy into many different chemically

useful forms. Many of these methods have evolved from the early KM EDA of Kitaura and Morokuma [142; 143]. These variational based approaches sometimes share the problems of the KM EDA, such as the RVS EDA retaining a residual unassignable energy as part of the decomposition. However, the problem of energy component instability in the KM EDA has generally been solved in the more recent schemes that build upon the KM EDA. Alternatively, perturbation based approaches such as those of the SAPT family may be used in which the interaction energy is constructed as perturbative corrections to the isolated monomers.

In this chapter we have compared popular currently used EDA schemes of interest to biomolecular application on six congeneric series test sets. The model systems of these test sets were selected to express key interactions typically found within ligand–host systems such as hydrogen bonding, π – π and halogen interactions. In the variational approaches BSSE has been treated very differently between the EDA schemes we have discussed. Whereas the NEDA scheme avoids the issue of BSSE by calculating all energies in the full supermolecule basis set, the KM, RVS, and ALMO EDA schemes treat BSSE by applying a CP correction to the energy components. The KM and RVS EDA schemes both share similar approaches in which partial CP corrections are applied to specific energy components. These corrections are calculated by partitioning the set of ghost orbitals used in the calculation by their occupancies. The ALMO EDA instead applies the full CP correction to the charge transfer component only. These treatments are unique and provide further subtle differences in the definitions of the energy components of the schemes.

One common problem that arises is the issue of energy component consistency. It is often the case that an energy term described by one EDA scheme is significantly different to that of another. Polarisation, for example, can be described as an electrostatic-only effect or as also including exchange within its description. These different descriptions can result in substantially different results. For example, on including the exchange part of the energy components in the SAPT(KS) results, we observe the energy components to often become a fraction of their original

size. In fact, SAPT arguably decomposes the energy components more intuitively in some regards, since each component is split into its electrostatic and exchange constituent. The general inconsistency of term definitions is not necessarily ‘wrong’ as such, but this point highlights the complications that may arise through different descriptions of chemical processes.

Despite the term definitions sometimes lacking consistency, we note a number of meritable features of certain EDA schemes. The KM EDA, despite its theoretical weaknesses, is observed to provide overall reasonably fair energy component values. However, the KM EDA charge transfer energy was extreme and chemically unsound in the case of the benzene – lithium system with the larger 6-311G* basis set. This problem is important to note as it counter-intuitively implies that using more complete basis sets reduces the accuracy of the KM EDA results.

The RVS EDA scheme also performed well, and succeeds the KM EDA by its improved theory that results in better numerical stability of the energy components. Both the RVS and KM EDA schemes are limited to the RHF level of theory. However in systems where correlation effects are important, it may be feasible to perform an additional supermolecular interaction energy calculation at a higher level of theory to evaluate this contribution. Alternatively, the CSOV EDA scheme of Bagus et al. [11; 141] (closely related to the RVS scheme) may provide a useful alternative for treating correlation effects in the energy components as this has been implemented for use with MCSCF wavefunctions [178] and extended to the DFT level [179; 180].

The NBO based NEDA scheme at times displays issues regarding the magnitudes of its energy components: in many cases these are extremely large and chemically unrealistic for our test systems. The approach taken by NEDA to decomposing the interaction energy is somewhat different to the other KM EDA derived schemes. In this, additional energy components of less obvious chemical origin are described such as the deformation and self energy terms. Also the method does not involve intermediate wavefunctions that are variationally optimised. The polarisation and

charge transfer components are therefore calculated directly from the monomer and supermolecular charge densities. The NEDA scheme may perform better in its three component form, decomposing the interaction energy into electrostatic, charge transfer, and core repulsions energy components. As the other schemes we considered did not share equivalent energy components to these three energy components we have not evaluated the NEDA scheme in this form.

SAPT is seen to give chemically sensible results and arguably provides a more intuitive decomposition than the other schemes as stated above. However, relating the theoretical processes of this scheme and their chemical equivalents can at times be more conceptually complicated than for the variational based schemes. It is also noted that a number of more recent SAPT schemes have been developed that may be more preferable than the SAPT(KS) used in this work. These include the SAPT(DFT) [25; 203–205] scheme that also describes the monomers using TD-DFT response functions not present within the SAPT(KS) scheme, and also a new CC treatment of intrafragmental correlation in what has been termed the SAPT(CC) scheme [228–235].

Overall the ALMO EDA scheme is shown to provide the most chemically sensible EDA results for our systems relevant to drug optimisation. This is mostly due to its use of the ALMO description for the charge transfer restricted polarised state. It is noted that the charge transfer BSSE correction may be problematic as it is theoretically possible for ‘repulsive’ charge transfer energies to arise as a result of its use. Also, this scheme combines the electrostatic and exchange energy components to form the frozen density component which may reduce the information provided in the analysis. The related BLW EDA [89] instead separates these terms. However, the wavefunction used in expressing the separated terms is constructed as a Hartree product and avoiding its use may be desired.

Chapter 5

The ONETEP energy decomposition analysis

A primary motivation of the work in this thesis is the development and application of an EDA approach for analysing interaction energies in large biomolecular systems, such as protein-ligand systems, for drug design. EDA studies in literature have typically considered the interactions of smaller systems up to tens of atoms in size, as discussed earlier in Section 3.1. This limit is far below ideal, with biomolecular systems frequently exceeding thousands of atoms in size. For this reason, the implementation of an EDA scheme within a linear-scaling DFT code such as ONETEP that aims to achieve large basis set accuracy in routine calculations is an important capability.

In this chapter we describe the implementation of the linear-scaling ONETEP EDA, which is based on the localised molecular orbital (LMO) EDA [14] and absolutely localised molecular orbital (ALMO) EDA [15] approaches. We decided to implement the ALMO EDA due to the high performance this method showed when applied to our test systems discussed in Chapter 4, and extended this using the LMO EDA to provide notable additional chemical insight at little extra computational cost. This EDA seeks to partition the interaction energy in terms

of six rigorously defined energy terms (electrostatic, exchange, correlation, Pauli repulsion, polarisation, and charge transfer).

In this chapter, we provide examples of calculations using our approach on small model systems which we have used to validate our implementation against the (Gaussian basis set) LMO and ALMO EDA approaches. Here, the stability of the EDA method with respect to basis set size, exchange-correlation functional, and atomic coordinates is also quantified. Overall we found reasonable stability, however basis set dependence was shown to be moderate for the charge transfer and polarisation energy components. A solution to this problem is presented based on the strictly localised property of the NGWFs. Additionally, we present a study of two water trimer systems which we use to demonstrate the high value of the electron density difference (EDD) plots produced by the EDA.

5.1 ONETEP EDA theory

We have implemented within the ONETEP [39] package an EDA approach that combines the ALMO EDA approach [15] and the frozen density component analysis based upon the localised molecular orbital (LMO) EDA theory of Su and Li [14]. Specifically, our prescription includes the electrostatic, exchange, Pauli repulsion and modified correlation terms of the LMO EDA of Su and Li [14] which are contained in the frozen density component of the ALMO EDA. The ALMO EDA polarisation and charge transfer components remain as in their original form. Within this section, we provide detailed descriptions of these approaches as they appear within the ONETEP EDA. We also detail an extension to this approach we have implemented that formally scales linearly with system size.

In order to comprehensively describe the theory of the ONETEP EDA (which we have implemented to allow calculations using arbitrary numbers of fragments, rather than the dimer interaction case as used in our expressions in Chapter 3), we are required to introduce a number of new energy expressions and definitions.

In the following discussion of the theory, we have adopted the Einstein convention of implicit summation over repeated Greek indices only unless otherwise stated. We use the word ‘fragment’ to describe any molecule which is part of a complex held together by intermolecular interactions (i.e. no chemical bonds). All our fragments in the following examples are closed-shell, but it is a straightforward task to extend the implementation to open-shell systems.

5.1.1 The localised and absolutely localised energy decomposition analyses

In order to fully develop the equations used in the EDA approaches, it is necessary to formally express the supermolecule interaction energy for an arbitrary number of fragments. To achieve this, we now¹ use A to refer to any (arbitrary) fragment that compose a supermolecule X . The CP corrected supermolecule interaction energy is therefore given by (c.f. Eq. 3.1),

$$\Delta E = E[\Psi_X] - \sum_{A \in X}^{N_{\text{frag}}} [\Psi_A^{0,A}] + \Delta E_{\text{BSSE}} \quad (5.1)$$

where Ψ represents a variationally optimised wavefunction with the subscripts A and X used to represent the fragments A that compose the supermolecule X . The superscript ‘0’ is used to denote states optimised in isolation from the field of the remaining fragments of the supermolecule and the superscript ‘ A ’ is used to indicate optimisation only in the fragment A basis set. N_{frag} is the number of fragments comprising the supermolecule X , and ΔE_{BSSE} is included as a correction for the total basis set superposition error (BSSE).

5.1.1.1 The absolutely localised energy decomposition analysis

As discussed earlier in Section 3.7.2, the ALMO EDA developed by Head-Gordon et al. [15] decomposes the interaction energy ΔE into the frozen density ΔE_{FRZ} ,

¹In the theory described in Chapter 3, we used the subscripts A and B to refer to two fragments that compose the supermolecule AB

polarisation ΔE_{POL} , and charge transfer ΔE_{CT} interaction terms as,

$$\Delta E = \Delta E_{\text{FRZ}} + \Delta E_{\text{POL}} + \Delta E_{\text{CT}} \quad . \quad (5.2)$$

We now define two key wavefunctions required to describe the EDA theory in terms of systems containing arbitrary numbers of fragments. $\Psi_{\text{X}}^{0,\text{orth}}$ is the properly antisymmetrised wavefunction of the interacting X complex constructed from the nonorthogonal frozen occupied MOs of the fragments. $\Psi_{\text{X}}^{\text{ALMO}}$ is defined as the wavefunction of the polarised state produced by relaxation of the nonorthogonal frozen MOs while still ensuring localisation of the MOs within their corresponding fragments. This localisation is imposed through the constraint that the MOs are only expanded using basis functions on a particular fragment and therefore prevents charge delocalisation between fragments. Each energy component may be described in terms of energy functionals of these intermediate wavefunctions as,

$$\Delta E_{\text{FRZ}} = E[\Psi_{\text{X}}^{0,\text{orth}}] - \sum_{A \in \text{X}}^{N_{\text{frag}}} E[\Psi_A^{0,A}] \quad (5.3)$$

$$\Delta E_{\text{POL}} = E[\Psi_{\text{X}}^{\text{ALMO}}] - E[\Psi_{\text{X}}^{0,\text{orth}}] \quad (5.4)$$

$$\Delta E_{\text{CT}} = E[\Psi_{\text{X}}] - E[\Psi_{\text{X}}^{\text{ALMO}}] + \Delta E_{\text{BSSE}} \quad . \quad (5.5)$$

The geometries of fragments A are defined as found in the (geometry optimised) X complex (i.e. only the electronic density is optimised in this calculation).

The ALMO state, $\Psi_{\text{X}}^{\text{ALMO}}$, that describes a system which is polarised but that has the restriction of no charge transfer between the fragments, is optimised via a procedure termed locally projected SCF for molecular interactions (SCF-MI) [189; 191]. The SCF-MI equations we use are those of Stoll et al. [236] and are described in more detail later.²

²This approach to separating out polarisation and charge transfer effects is the same as that described within the BLW [80; 89] EDA procedure. Specifically, the BLW state that is identical to the ALMO state is optimised either by Jacobi transformation [195] or by the algorithm of Gianinetti and Raimondi et al. [190; 193].

5.1.1.2 The frozen density analysis

In this section we describe a prescription for a frozen density analysis produced via the LMO EDA theory of Su and Li [14], in which ΔE_{FRZ} is further decomposed into individual electrostatic (ΔE_{ES}), exchange (ΔE_{EX}), Pauli–repulsion (ΔE_{REP}) and correlation (ΔE_{CORR}) terms as,

$$\Delta E_{\text{FRZ}} = \Delta E_{\text{ES}} + \Delta E_{\text{EX}} + \Delta E_{\text{REP}} + \Delta E_{\text{CORR}} \quad . \quad (5.6)$$

Combining the classical-like terms of the total Kohn Sham (KS) energy (by excluding the exchange and correlation contributions) as,

$$E_{\text{cl}} = 2 \sum_{i,j}^{N_{\psi(\text{occ})}} h_{ij} \sigma^{ij} + \sum_{i,j,k,l}^{N_{\psi(\text{occ})}} \langle ij|kl \rangle \times \sigma^{ij} \sigma^{kl} + E_{\text{nuc}} \quad (5.7)$$

where E_{nuc} is the nuclei–nuclei electrostatic energy, $N_{\psi(\text{occ})}$ is the number of occupied MOs, kinetic energy effects are included by presence of the full core Hamiltonian matrix h_{ij} , and where the contravariant metric tensor σ^{ij} is the inverse of the MO overlap matrix σ_{ij} ,

$$\sigma_{ij} = \int \psi_i^*(\mathbf{r}) \psi_j(\mathbf{r}) d\mathbf{r} = \langle \psi_i | \psi_j \rangle \quad (5.8)$$

$$\sigma^{ij} \equiv (\sigma^{-1})_{ij} \quad (5.9)$$

the components of the frozen density interaction may be expressed using intermediate wavefunctions as,

$$\Delta E_{\text{ES}} = E_{\text{cl}}[\Psi_{\text{X}}^0] - \sum_{A \in \text{X}}^{N_{\text{frag}}} E_{\text{cl}}[\Psi_A^{0,A}] \quad (5.10)$$

$$\Delta E_{\text{EX}} = E_{\text{X}}[\Psi_{\text{X}}^0] - \sum_{A \in \text{X}}^{N_{\text{frag}}} E_{\text{X}}[\Psi_A^{0,A}] \quad (5.11)$$

$$\begin{aligned} \Delta E_{\text{REP}} = & E_{\text{cl}}[\Psi_{\text{X}}^{0,\text{orth}}] - E_{\text{cl}}[\Psi_{\text{X}}^0] \\ & + E_{\text{X}}[\Psi_{\text{X}}^{0,\text{orth}}] - E_{\text{X}}[\Psi_{\text{X}}^0] \end{aligned} \quad (5.12)$$

$$\begin{aligned} \Delta E_{\text{CORR}} = & E_{\text{C}}[\Psi_{\text{X}}^{0,\text{orth}}] - \sum_{A \in \text{X}}^{N_{\text{frag}}} E_{\text{C}}[\Psi_A^{0,A}] \\ \equiv & \Delta E_{\text{FRZ}} - (\Delta E_{\text{ES}} + \Delta E_{\text{EX}} + \Delta E_{\text{REP}}) \end{aligned} \quad (5.13)$$

where $E_{\text{X}}[n(\mathbf{r})]$ and $E_{\text{C}}[n(\mathbf{r})]$ are the DFT exchange and correlation energy functionals of the electronic density $n(\mathbf{r})$ associated with the wavefunction $\Psi(\mathbf{r})$, and where we note that the kinetic energy contribution to ΔE_{ES} is zero due to the kinetic energy of the fragment states $\Psi_A^{0,A}$ cancelling with the kinetic energy of the frozen supermolecule state Ψ_{X}^0 as σ^{ij} is the identity matrix for $E_{\text{cl}}[\Psi_{\text{X}}^0]$, while it is as in Eqs. 5.8 and 5.9 for $E_{\text{cl}}[\Psi_{\text{X}}^{0,\text{orth}}]$.

The components of this frozen energy decomposition are formally similar to the components described in the LMO EDA [14] but with inclusion of a new component ΔE_{CORR} that isolates the correlation energy change on orthogonalisation contained within the LMO EDA ‘polarisation’ term. It is also noted that the electrostatic term of this decomposition is formally similar to that within the BLW [80; 89] scheme. Additionally, it is important to note that this is not the only approach possible for decomposing (or, in fact, defining) the frozen density interaction. A number of alternative approaches to the above theory have been developed, such as the scheme of Horn et al. [237] that uses fully antisymmetric electronic wavefunctions throughout to calculate contributions to the frozen density interaction, and the density-based energy decomposition analysis (DEDA) of

Wu [238] that calculates the frozen density interaction in a variational manner.

5.1.2 Self-consistent field theory for molecular interactions

In this section, we introduce the self-consistent field for molecular interactions (SCF-MI) approach that is used to obtain a polarised yet charge transfer-restricted state in the EDA. We have adopted the SCF-MI equations of Stoll et al. [236] due to computational considerations regarding memory and matrix multiplication advantages. In addition to the Stoll equations also exist the approaches of Gianinetti et al. [190] and Nagata et al. [191] for solving the SCF-MI problem which are expected to produce equivalent solutions.

5.1.2.1 Overview of the Stoll SCF-MI equations

The SCF-MI approaches involve the construction of locally projected Hamiltonian matrices that cast the whole-system electronic Schrödinger equation for X into a set of problems for the weakly interacting fragments A . Through this partitioning, the MOs on the fragments are expanded only in terms of basis functions local to each fragment and hence remain (fragment) localised MOs. This fragment localisation property, previously expressed for the dimer case in Eq. 3.31, may be expressed by the constrained expansion of the MOs on an arbitrary number of fragments as,

$$|\psi_{Ai}\rangle = |\phi_{A\alpha}\rangle M_{Ai}^{A\alpha} \quad (5.14)$$

where $M_{Ai}^{A\alpha}$ is an expansion coefficient for MO i on fragment A in terms of the basis function (NGWF) α on fragment A , where the constraint of MO localisation is enforced by having $M_{Bi}^{A\alpha} = 0$ for fragments $A \neq B$.

The Stoll et al. equations [236] aim to construct an eigenvalue problem for the polarised MOs of each fragment. To achieve this we need a locally projected

Hamiltonian operator H_S^A constructed as,

$$\hat{H}_S^A \equiv (\hat{1} - \hat{\rho} + \hat{\rho}^{A\dagger}) \hat{H} (\hat{1} - \hat{\rho} + \hat{\rho}^A) \quad (5.15)$$

where $\hat{\rho}$ is the one-particle density operator and $\hat{\rho}^A$ is the fragment density operator. The fragment density operator is given by,

$$\hat{\rho}^A = \sum_i^{N_{\psi(\text{occ},A)}} |\psi^{Ai}\rangle \langle \psi_{Ai}| \quad . \quad (5.16)$$

and the density operator by,

$$\hat{\rho} = \sum_{A \in X}^{N_{\text{frag}}} \sum_i^{N_{\psi(\text{occ},A)}} |\psi^{Ai}\rangle \langle \psi_{Ai}| \quad (5.17)$$

where the indexing of the MOs includes the fragment A in addition to the MO index i , and where the contravariant MOs of fragment A are constructed as,

$$|\psi^{Ai}\rangle = \sum_{B \in X}^{N_{\text{frag}}} \sum_j^{N_{\psi(\text{occ},B)}} |\psi_{Bj}\rangle \sigma^{Bj,Ai} \quad (5.18)$$

where B runs over all fragments of the supermolecule X . Using this modified Hamiltonian, the generalised SCF equation becomes,

$$\hat{H}_S^A |\psi_{Ai}\rangle = |\psi_{Ai}\rangle \epsilon_{Ai} \quad (5.19)$$

where ϵ_{Ai} is the energy of the MO $|\psi_{Ai}\rangle$ on fragment A .

5.1.2.2 Derivation of the Stoll SCF-MI equations

Here we present a derivation of the Stoll et al. equations [236] outlined above. Within this section, Einstein summation convention is used over all repeated indices (including fragment indices) unless otherwise stated in order to facilitate

derivation of the equations. We begin by expressing the gradient of the (electronic) energy with respect to the KS states, given by

$$\frac{\delta E}{\delta \psi_{Ck}^*} = 2 \left[\hat{H} |\psi_{Bj}\rangle \sigma^{Bj,Ck} + \langle \psi_{Ai} | \hat{H} | \psi_{Bj} \rangle \cdot \frac{\delta \sigma^{Bj,Ai}}{\delta \psi_{Ck}^*} \right] . \quad (5.20)$$

Our strategy is to now localise the SCF problem to the fragments to constrain the optimisation as shown in Eq. 5.14. We start by noting the identity

$$\begin{aligned} \sigma^{-1} &= \sigma^{-1} \sigma \sigma^{-1} \\ \therefore \delta \sigma^{-1} &= (\delta \sigma^{-1}) \sigma \sigma^{-1} + \sigma^{-1} (\delta \sigma) \sigma^{-1} + \sigma^{-1} \sigma (\delta \sigma^{-1}) \\ &= 2(\delta \sigma^{-1}) + \sigma^{-1} (\delta \sigma) \sigma^{-1} \\ \therefore \delta \sigma^{-1} &= -\sigma^{-1} (\delta \sigma) \sigma^{-1} . \end{aligned} \quad (5.21)$$

Using this identity with Eq. 5.20 yields

$$\begin{aligned} \frac{\delta E}{\delta \psi_{Ck}^*} &= 2 \left[\hat{H} |\psi_{Bj}\rangle \sigma^{Bj,Ck} + \langle \psi_{Ai} | \hat{H} | \psi_{Bj} \rangle \cdot \left(-\sigma^{Bj,Dl} \frac{\delta \sigma^{Dl, Ef}}{\delta \psi_{Ck}^*} \sigma^{Ef, Ai} \right) \right] \\ &= 2 \left[\hat{H} |\psi_{Bj}\rangle \sigma^{Bj,Ck} - \langle \psi_{Ai} | \hat{H} | \psi_{Bj} \rangle \cdot \left(\sigma^{Bj, Dl} \frac{\langle \delta \psi_{Dl} |}{\delta \psi_{Ck}^*} | \psi_{Ef} \rangle \sigma^{Ef, Ai} \right) \right] \\ &= 2 \left[\hat{H} |\psi_{Bj}\rangle \sigma^{Bj,Ck} - | \psi_{Ef} \rangle \sigma^{Ef, Ai} \langle \psi_{Ai} | \hat{H} | \psi_{Bj} \rangle \sigma^{Bj, Ck} \right] \\ &= 2 \left[\hat{H} |\psi_{Bj}\rangle \sigma^{Bj,Ck} - | \psi^{Ai} \rangle \langle \psi_{Ai} | \hat{H} | \psi_{Bj} \rangle \sigma^{Bj, Ck} \right] . \end{aligned} \quad (5.22)$$

Expressing the (conventional) density operator as

$$\hat{\rho} = | \psi^{Ai} \rangle \langle \psi_{Ai} | \quad (5.23)$$

and substituting into Eq. 5.22,

$$\frac{\delta E}{\delta \psi_{Ck}^*} = 2 \left[(\hat{1} - \hat{\rho}) \hat{H} | \psi_{Bj} \rangle \sigma^{Bj, Ck} \right] . \quad (5.24)$$

We now define a fragment-specific density operator as

$$\hat{\rho}^A = \sum_i^{N_{\psi(\text{occ},A)}} |\psi^{Ai}\rangle \langle \psi_{Ai}| \quad (5.25)$$

where we iterate over only the KS states on fragment A , which has the properties

$$\hat{\rho}^A |\psi^{Bj}\rangle = \delta_{A,B} |\psi^{Bj}\rangle \quad (5.26)$$

and (assuming orthonormality of the KS states on each fragment)

$$\hat{\rho}^A |\psi_{Ai}\rangle = |\psi^{Ai}\rangle \quad . \quad (5.27)$$

Using these properties, it can be shown that

$$\begin{aligned} \hat{H} |\psi^{Bj}\rangle &= \hat{H} |\psi_{Bj}\rangle - \hat{H} |\psi_{Bj}\rangle + \hat{H} |\psi^{Bj}\rangle \\ &= \hat{H} |\psi_{Bj}\rangle - \hat{H} \hat{\rho} |\psi_{Bj}\rangle + \hat{H} \hat{\rho}^B |\psi^{Bj}\rangle \\ &= \hat{H} (\hat{1} - \hat{\rho} + \hat{\rho}^B) |\psi_{Bj}\rangle \quad . \end{aligned} \quad (5.28)$$

Adding and subtracting Eq. 5.25 in Eq. 5.24, we find

$$\begin{aligned} \frac{\delta E}{\delta \psi_{Ck}^*} &= 2 \left[(\hat{1} - \hat{\rho}) \hat{H} |\psi_{Bj}\rangle \sigma^{Bj,Ck} \right] \\ &= 2 \left[(\hat{1} - \hat{\rho} + \hat{\rho}^{C\dagger} - \hat{\rho}^{C\dagger}) \hat{H} |\psi_{Bj}\rangle \sigma^{Bj,Ck} \right] \\ &= 2 \left[(\hat{1} - \hat{\rho} + \hat{\rho}^{C\dagger}) \hat{H} |\psi_{Bj}\rangle \sigma^{Bj,Ck} - \hat{\rho}^{C\dagger} \hat{H} |\psi_{Bj}\rangle \sigma^{Bj,Ck} \right] \\ &= 2 \left[(\hat{1} - \hat{\rho} + \hat{\rho}^{C\dagger}) \hat{H} |\psi_{Bj}\rangle \sigma^{Bj,Ck} - \sum_l^{N_{\psi(\text{occ},C)}} |\psi_{Cl}\rangle \langle \psi^{Cl}| \hat{H} |\psi_{Bj}\rangle \sigma^{Bj,Ck} \right] \\ &= 2 \left[(\hat{1} - \hat{\rho} + \hat{\rho}^{C\dagger}) \hat{H} |\psi_{Bj}\rangle \sigma^{Bj,Ck} - \sum_l^{N_{\psi(\text{occ},C)}} |\psi_{Cl}\rangle \langle \psi^{Cl}| \hat{H} |\psi^{Ck}\rangle \right] \quad . \end{aligned} \quad (5.29)$$

Equating Eq. 5.29 to zero to find the minimum energy of the KS states and using Eq. 5.28, it is seen that

$$\begin{aligned}
\frac{\delta E}{\delta \psi_{Ck}^*} &= 2 \left[(\hat{1} - \hat{\rho} + \hat{\rho}^{C\dagger}) \hat{H} |\psi_{Bj}\rangle \sigma^{Bj,Ck} - \sum_l^{N_{\psi(\text{occ},C)}} |\psi_{Cl}\rangle \langle \psi^{Cl} | \hat{H} | \psi^{Ck} \rangle \right] = 0 \\
\therefore (\hat{1} - \hat{\rho} + \hat{\rho}^{C\dagger}) \hat{H} |\psi^{Ck}\rangle &= \sum_l^{N_{\psi(\text{occ},C)}} |\psi_{Cl}\rangle \langle \psi^{Cl} | \hat{H} | \psi^{Ck} \rangle \\
\therefore (\hat{1} - \hat{\rho} + \hat{\rho}^{C\dagger}) \hat{H} (\hat{1} - \hat{\rho} + \hat{\rho}^C) |\psi_{Ck}\rangle &= \sum_l^{N_{\psi(\text{occ},C)}} |\psi_{Cl}\rangle \langle \psi_{Cl} | (\hat{1} - \hat{\rho} + \hat{\rho}^{C\dagger}) \hat{H} (\hat{1} - \hat{\rho} + \hat{\rho}^C) |\psi_{Ck}\rangle .
\end{aligned} \tag{5.30}$$

Defining the Stoll locally projected Hamiltonian operator \hat{H}_S^C for fragment C as,

$$\hat{H}_S^C = (\hat{1} - \hat{\rho} + \hat{\rho}^{C\dagger}) \hat{H} (\hat{1} - \hat{\rho} + \hat{\rho}^C) \tag{5.31}$$

and by substitution, we find

$$\hat{H}_S^C |\psi_{Ck}\rangle = \sum_l^{N_{\psi(\text{occ},C)}} |\psi_{Cl}\rangle \langle \psi_{Cl} | \hat{H}_S^C | \psi_{Ck} \rangle . \tag{5.32}$$

Assuming $\{|\psi_{Ck}\rangle\}$ are the eigenfunctions of the Hermitian operator \hat{H}_S^C then

$$\begin{aligned}
\langle \psi_{Cl} | \hat{H}_S^C | \psi_{Ck} \rangle &= \langle \psi_{Cl} | \epsilon_{Ck} | \psi_{Ck} \rangle \\
&= \epsilon_{Ck} \langle \psi_{Cl} | \psi_{Ck} \rangle \\
&= \epsilon_{Ck} \delta_{Cl,Ck} .
\end{aligned} \tag{5.33}$$

Therefore by substitution into Eq. 5.32,

$$\begin{aligned}
\hat{H}_S^C |\psi_{Ck}\rangle &= \sum_l^{N_{\psi(\text{occ},C)}} |\psi_{Cl}\rangle \epsilon_{Ck} \delta_{Cl,Ck} \\
\therefore \hat{H}_S^C |\psi_{Ck}\rangle &= \epsilon_{Ck} |\psi_{Ck}\rangle
\end{aligned} \tag{5.34}$$

which are our fragment eigenvalue problems that are solved for each fragment subsystem.

5.1.3 Construction of the frozen density kernels

In the frozen density analysis, we seek expressions of the kernel and set of NGWFs that represent the two intermediate wavefunctions Ψ_X^0 and $\Psi_X^{0,\text{orth}}$. The NGWF set of these wavefunctions, $\{\phi_{A\alpha}(\mathbf{r})\}$, is constructed by superposition of the NGWFs of the isolated fragments A onto the supermolecule X . We now define the two density kernels $K_0^{A\alpha,B\beta}$ and $K_{\text{orth}}^{A\alpha,B\beta}$ that are used to represent Ψ_X^0 and $\Psi_X^{0,\text{orth}}$ in this ‘frozen’ NGWF set.

The density kernel of the frozen state, $K_0^{A\alpha,B\beta}$, is constructed by superposition of the occupied states of the fragments onto the supermolecule. This is constructed from the fragment density kernels $(K_A)^{\alpha\beta}$ as,

$$\begin{aligned} K_0^{A\alpha,A\beta} &= (K_A)^{\alpha\beta} \\ K_0^{A\alpha,B\beta} &= 0|_{A \neq B} \quad . \end{aligned} \quad (5.35)$$

The density kernel $K_{\text{orth}}^{A\alpha,B\beta}$ is the properly antisymmetrised form of $K_0^{A\alpha,B\beta}$. The construction of this kernel requires the coefficients $(M_A)^\alpha_i$ of the isolated fragments. From Eq. 2.54 for the density kernel we can write a generalised eigenvalue problem as,

$$K^{\alpha\beta} S_{\beta\gamma} M^\gamma_i = M^\alpha_i f_i \quad . \quad (5.36)$$

This eigenvalue equation may be expressed for the fragment problems as,

$$(K_A)^{\alpha\beta} (S_A)_{\beta\gamma} (M_A)^\gamma_i = (M_A)^\alpha_i (f_A)_i \quad (5.37)$$

where the subscript A is used to denote a fragment quantity. The vectors of the fragment matrices M_A that are obtained for unoccupied MOs are discarded at this point. This is achieved by ordering the MOs by decreasing orbital occupancy and retaining only $(M_A)_{\beta i}|_{i \leq N_{\psi(\text{occ},A)}}$ where $N_{\psi(\text{occ},A)}$ is the number of occupied MOs on fragment A .

The block-diagonal MO coefficient matrix $M_{Bi}^{A\alpha}$ of the frozen supermolecule is constructed from the fragment coefficient matrices $(M_A)^\alpha_i$ as,

$$\begin{aligned} M_{Ai}^{A\alpha} &= (M_A)^\alpha_i \\ M_{Bi}^{A\alpha} &= 0|_{A \neq B} \quad . \end{aligned} \quad (5.38)$$

Finally, the density kernel $K_{\text{orth}}^{A\alpha,B\beta}$ of the properly antisymmetrised state is expressed using these MO coefficients as,

$$\begin{aligned} K_{\text{orth}}^{A\alpha,B\beta} &= \sum_{C,D \in X}^{N_{\text{frag}}} \sum_i^{N_{\psi(\text{occ},C)}} \sum_j^{N_{\psi(\text{occ},D)}} M_{Ci}^{A\alpha} \sigma^{Ci,Dj} (M^\dagger)_{Dj}^{B\beta} \\ &= \sum_i^{N_{\psi(\text{occ},A)}} \sum_j^{N_{\psi(\text{occ},B)}} M_{Ai}^{A\alpha} \sigma^{Ai,Bj} (M^\dagger)_{Bj}^{B\beta} \end{aligned} \quad (5.39)$$

where we have exploited the block-diagonal structure of M described in Eq. 5.38 and where i and j run over the occupied MOs of the fragments and where the inverse MO overlap matrix $\sigma^{Ai,Bj}$ is constructed from the quantity $\sigma_{Ai,Bj}$,

$$\sigma_{Ai,Bj} = \sum_{C,D \in X}^{N_{\text{frag}}} (M^\dagger)_{Ai}^{C\alpha} S_{C\alpha,D\beta} M_{Bj}^{D\beta} \quad (5.40)$$

where $S_{C\alpha,D\beta}$ is the full NGWF set overlap matrix for the supermolecule. For clarity, the structures of the quantities $M_{Bi}^{A\alpha}$ and $\sigma_{Ai,Bj}$ involved in constructing $K_{\text{orth}}^{A\alpha,B\beta}$ are shown diagrammatically in Fig. 5.1.

The energies of the two intermediate wavefunctions Ψ_X^0 and $\Psi_X^{0,\text{orth}}$ are expressed in terms of energy functionals of the quantities $K_0^{A\alpha,B\beta}$, $K_{\text{orth}}^{A\alpha,B\beta}$ and $\{\phi_{A\alpha}(\mathbf{r})\}$ as,

$$E[\Psi_X^0] \equiv E[\{K_0^{A\alpha,B\beta}\}, \{\phi_{A\alpha}(\mathbf{r})\}] \quad (5.41)$$

$$E[\Psi_X^{0,\text{orth}}] \equiv E[\{K_{\text{orth}}^{A\alpha,B\beta}\}, \{\phi_{A\alpha}(\mathbf{r})\}] \quad . \quad (5.42)$$

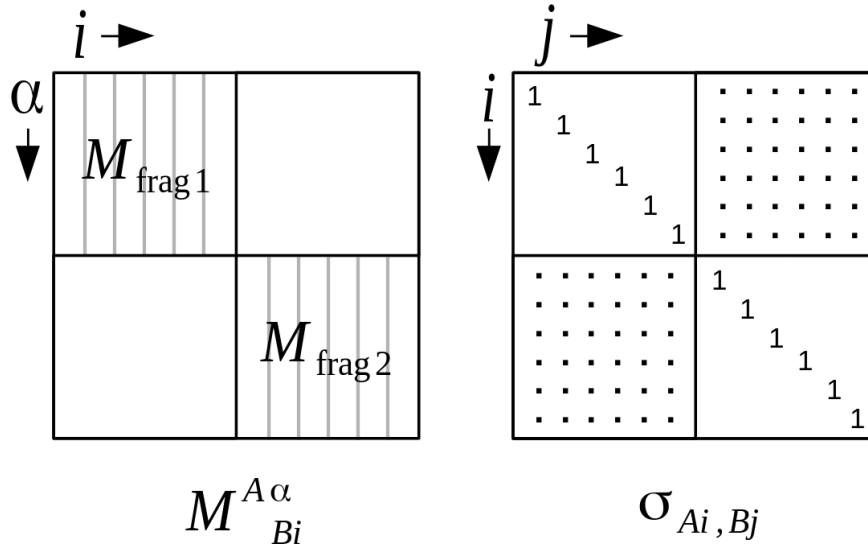


Figure 5.1: A diagrammatic representation of the quantities involved in the construction of the frozen density kernel $K^{A\alpha,B\beta}_{\text{orth}}$ for a system comprising of two fragments ‘frag1’ and ‘frag2’. Empty matrix sub-blocks represent zero blocks, and sub-blocks containing dots represent non-zero blocks. The diagonal intrafragmental MO overlap sub-blocks of $\sigma_{Ai,Bj}$ are identity due to orthonormality of the KS states within fragments, and non-zero for the sub-blocks representing interfragment MO overlaps due to lack of orthonormality.

5.1.4 The polarisation component

5.1.5 Calculation of the polarised density kernel

A brief overview of the ALMO polarisation procedure as implemented within the ONETEP package is now described. As discussed in Section 2.8, the problem of obtaining the ground state of a system in ONETEP involves the optimisation of the NGWFs and the optimisation of the density kernel for each current set of NGWFs. In ONETEP, the Stoll eigenvalue problem is not solved directly by diagonalisation, but the ground state is obtained by a conjugate gradient minimisation of the energy.

The following section describes the Stoll SCF-MI equations [189; 236] in terms of the quantities used in ONETEP. Expanding the Stoll SCF-MI equation in the basis of NGWFs on the fragment A , $\phi_{A\alpha}$, we obtain the set of N_{frag} matrix

equations,

$$[H_S^A]_{AA}[M]_{AA} = [S]_{AA}[M]_{AA}[\epsilon]_{AA} \quad (5.43)$$

where the subscript AA indicates a fragment matrix block where,

$$(H_S^A)_{A\alpha,A\beta} \equiv \langle \phi_{A\alpha} | \hat{H}_S^A | \phi_{A\beta} \rangle \quad (5.44)$$

which must be solved for each fragment block to find the ALMO ground state. The fully expanded form of the projected Hamiltonian matrix for each fragment block AA is given by,

$$\begin{aligned} [H_S^A] = & [H]_{AA} - [HM\sigma^{-1}M^\dagger S]_{AA} \\ & - ([HM\sigma^{-1}M^\dagger S]_{AA})^\dagger \\ & + [SM\sigma^{-1}M^\dagger HM\sigma^{-1}M^\dagger S]_{AA} \\ & + [HM\sigma^{-1}]_{AA}[M^\dagger S]_{AA} \\ & + ([HM\sigma^{-1}]_{AA}[M^\dagger S]_{AA})^\dagger \\ & - [SM\sigma^{-1}M^\dagger HM\sigma^{-1}]_{AA}[M^\dagger S]_{AA} \\ & - ([SM\sigma^{-1}M^\dagger HM\sigma^{-1}]_{AA}[M^\dagger S]_{AA})^\dagger \\ & + [SM]_{AA}[\sigma^{-1}M^\dagger HM\sigma^{-1}]_{AA}[M^\dagger S]_{AA}^\dagger \end{aligned} \quad (5.45)$$

where the quantities within square brackets are full (supermolecule) matrices.

5.1.5.1 Inner loop optimisation: the density kernel

To describe the optimisation of the density kernel in the SCF-MI equations within ONETEP, we begin by introducing the density kernel corresponding to the non-antisymmetrised wavefunction at SCF-MI iteration m as $K_{0(m)}^{A\alpha,B\beta}$. At $m = 0$, this kernel is simply set to the kernel $K_0^{A\alpha,B\beta}$ constructed in the previous frozen density analysis by direct summation of the fragment density kernels. Having obtained this kernel, SCF-MI loops are performed in order to optimise the total energy with

respect to the density kernel. The electronic energy is evaluated at each iteration using the antisymmetrised representation of this kernel, $K_{\text{orth}}^{A\alpha,B\beta}$. This electronic energy is expressed in terms of the quantities used in ONETEP as,

$$\begin{aligned} E_{\text{orth}} &= 2 \sum_{A,B \in X}^{N_{\text{frag}}} \sum_i^{N_{\psi(\text{occ},A)}} \sum_j^{N_{\psi(\text{occ},B)}} \sigma^{Ai,Bj} \langle \psi_{Bj} | \hat{H} | \psi_{Ai} \rangle - E_{\text{DC}} \\ &= 2 \sum_{A,B \in X}^{N_{\text{frag}}} K_{\text{orth}}^{A\alpha,B\beta} H_{B\beta,A\alpha} - E_{\text{DC}} \end{aligned} \quad (5.46)$$

where E_{DC} is the double-counting correction,

$$E_{\text{DC}} = E_{\text{H}}[n(\mathbf{r})] - E_{\text{XC}}[n(\mathbf{r})] + \int \frac{\delta E_{\text{XC}}[n(\mathbf{r})]}{\delta n(\mathbf{r})} n(\mathbf{r}) d\mathbf{r} \quad (5.47)$$

where E_{H} and E_{xc} are the Hartree and exchange and correlation energies, and where,

$$n(\mathbf{r}) = 2 \sum_{A,B \in X}^{N_{\text{frag}}} \phi_{A\alpha}(\mathbf{r}) K_{\text{orth}}^{A\alpha,B\beta} \phi_{B\beta}(\mathbf{r}) \quad . \quad (5.48)$$

A single iteration of the SCF-MI kernel loop contains the following steps:

1. The fragment eigenvalue problems described in Eq. 5.37 are solved to obtain the isolated fragment MO coefficients $(M_A)_{\alpha_i}^{\alpha}$ and subsequently $M_{Bi}^{A\alpha}$.
2. The MO overlap matrix $\sigma_{Ai,Bj}$ is constructed using Eq. 5.40 and inverted to obtain $\sigma^{Ai,Bj}$.
3. The kernel $K_{\text{orth}}^{A\alpha,B\beta}$ is constructed from $M_{Bi}^{A\alpha}$ using Eq. 5.39 and $\sigma^{Ai,Bj}$.
4. The unprojected Hamiltonian $H_{\alpha\beta}$ is calculated and the energy of the ALMOs evaluated as,

$$E_{\text{orth}} = 2 \sum_{A,B \in X}^{N_{\text{frag}}} K_{\text{orth}}^{A\alpha,B\beta} H_{B\beta,A\alpha} - E_{\text{DC}} \quad . \quad (5.49)$$

If variations in the density kernel are less than a specified tolerance then exit.

5. The locally projected Hamiltonian $(H_S^A)_{A\alpha,A\beta}$ is constructed from $H_{A\alpha,B\beta}$, $S_{A\alpha,B\beta}$, $M_{Bi}^{A\alpha}$ and $\sigma^{Ai,Bj}$ using Eq. 5.45.
6. $(H_S^A)_{A\alpha,A\beta}$, $K_{0(m)}^{A\alpha,B\beta}$ are used in a conjugate gradient minimisation of the Stoll locally projected energy of the fragments E_S ,

$$E_S = 2 \sum_{A \in X}^{N_{\text{frag}}} K_{0(m)}^{A\alpha,A\beta} (H_S^A)_{A\beta,A\alpha} - E_{\text{DC}} \quad (5.50)$$

where E_{DC} is evaluated using the associated fragment densities of $K_{0(m)}^{A\alpha,B\beta}$ (Eq. 5.48), to obtain the new density kernel $K_{0(m+1)}^{A\alpha,B\beta}$. The minimisation approach used [78] is the method of Li, Nunes and Vanderbilt [73; 74], wherein the density kernel $K_0^{A\alpha,B\beta}$ is defined in terms of an auxiliary density kernel $L_0^{A\alpha,B\beta}$ by the McWeeny purifying transform [75],

$$K_0^{A\alpha,B\beta} = 3(L_0 S_0 L_0)^{A\alpha,B\beta} - 2(L_0 S_0 L_0 S_0 L_0)^{A\alpha,B\beta} \quad (5.51)$$

where S_0 is the fragment overlap matrix constructed from the fragment overlap matrices S_A as,

$$\begin{aligned} (S_0)_{A\alpha,A\beta} &= (S_A)_{A\alpha,A\beta} \\ (S_0)_{A\alpha,B\beta} &= 0|_{A \neq B} \quad . \end{aligned} \quad (5.52)$$

This purification transformation is iterated as required within the LNV subroutine to yield a fully idempotent $K_0^{A\alpha,B\beta}$, equivalent to orthonormalisation of the KS states within the fragments. The gradient of the total energy with respect to the auxiliary density kernel $L_0^{A\alpha,A\beta}$ is calculated as,

$$\begin{aligned} \frac{\partial E_S}{\partial L_0^{A\alpha,A\beta}} &= 6(S_0 L_0 H_S^A + H_S^A L_0 S_0)_{A\beta,A\alpha} \\ &\quad - 4(S_0 L_0 S_0 L_0 H_S^A + S_0 L_0 H_S^A L_0 S_0 + H_S^A L_0 S_0 L_0 S_0)_{A\beta,A\alpha} \\ \frac{\partial E_S}{\partial L_0^{A\alpha,B\beta}} &= 0|_{A \neq B} \quad . \end{aligned} \quad (5.53)$$

and minimisation of E_S is equivalent to minimisation of E_{orth} with the ALMO constraint.

5.1.5.2 Outer loop optimisation: the NGWFs

Within this section we discuss the minimisation of the energy with respect to the NGWFs $\{\phi_{A\alpha}\}$ on the fragments A . We assume that the idempotent density kernel $K_{\text{orth}}^{A\alpha,B\beta}$ has been fully optimised during the inner loop cycle in this discussion.

In ONETEP, convergence of the NGWFs is achieved by minimising the energy of the NGWFs using a conjugate gradients method. The gradient used in the SCF-MI minimisation is the same as is used in the standard ONETEP orbital optimisation. The expression of the gradient of the energy with respect to the NGWFs is given by,

$$\frac{\delta E_{\text{orth}}}{\delta \phi_{A\alpha}^*(\mathbf{r})} = 2 \left[\sum_{B \in X}^{N_{\text{frag}}} \hat{H} \phi_{B\beta}(\mathbf{r}) K_{\text{orth}}^{B\beta,A\alpha} + \sum_{B \in X}^{N_{\text{frag}}} \phi_{B\beta}(\mathbf{r}) Q^{B\beta,A\alpha} \right] \quad (5.54)$$

where for a converged density kernel,

$$Q^{A\alpha,B\beta} = - \left(\sum_{C,D \in X}^{N_{\text{frag}}} K_{\text{orth}}^{A\alpha,C\gamma} H_{C\gamma,D\eta} S^{D\eta,B\beta} \right) \quad (5.55)$$

and where \hat{H} is the KS Hamiltonian, H is the full Hamiltonian matrix optimised for the current set of NGWFs, and S is the full overlap matrix. This gradient can be equivalently expressed as,

$$\frac{\delta E_{\text{orth}}}{\delta \psi_{Ai}^*(\mathbf{r})} = 2f_{Ai} \left[\hat{H} \psi_{Ai}(\mathbf{r}) - \epsilon_{Ai} \psi_{Ai}(\mathbf{r}) \right] \quad (5.56)$$

using the relationship,

$$\frac{\delta E_{\text{orth}}}{\delta \psi_{Ai}^*(\mathbf{r})} = \sum_{B \in X}^{N_{\text{frag}}} \frac{\delta E_{\text{orth}}}{\delta \phi_{B\beta}^*(\mathbf{r})} M_{B\beta,Ai} \quad (5.57)$$

where f_{Ai} and ϵ_{Ai} are the ALMO occupancies and eigenvalues respectively, and therefore this nested energy minimisation corresponds to solving the KS equations with the SCF-MI constraint.

Once the solution to the minimisation of both the NGWFs and density kernel is found and the final polarised ALMO state energy obtained, the polarisation energy is then calculated using Eq. 5.4.

5.1.6 The charge transfer component

Charge transfer is calculated using Eq. 5.5 but with omission of the ΔE_{BSSE} contribution, i.e.

$$\Delta E_{\text{CT}} = E[\Psi_{\text{X}}] - E[\Psi_{\text{X}}^{\text{ALMO}}] \quad (5.58)$$

where,

$$E[\Psi_{\text{X}}] \equiv E[\{K^{A\alpha, B\beta}\}, \{\phi_{\alpha}(\mathbf{r})\}] \quad (5.59)$$

$$E[\Psi_{\text{X}}^{\text{ALMO}}] \equiv E[\{K_{\text{orth}}^{A\alpha, B\beta}\}, \{(\phi_{\text{ALMO}})_{A\alpha}(\mathbf{r})\}] \quad (5.60)$$

where $\{K^{A\alpha, B\beta}\}$ and $\{\phi_{\alpha}(\mathbf{r})\}$ are respectively the fully optimised density kernel and NGWFs of the supermolecule without ALMO constraint (i.e. the quantities obtained from a standard singlepoint calculation), $\{(\phi_{\text{ALMO}})_{A\alpha}(\mathbf{r})\}$ are the NGWFs determined by the minimisation of Eq. 5.54, and where $\{K_{\text{orth}}^{A\alpha, B\beta}\}$ is the optimised ALMO-constrained kernel (not equal to $\{K_{\text{orth}}^{A\alpha, B\beta}\}$ of Eq. 5.39). The exclusion of ΔE_{BSSE} in the ONETEP implementation is justified as it is zero due to the fact that the psinc basis set is independent of atomic positions.

5.1.7 Parallelisation and numerical eigensolvers

The implementation of the ONETEP EDA described above, referred to as our ‘diagonalisation-dependent’ implementation, contains two separate cubic-scaling

($\mathcal{O}(N^3)$) bottlenecks. The first arises from the requirement of diagonalisation of the density kernel used to obtain the fragment MO eigenvectors. The second arises from the fact that the construction of H_S^A in Eq. 5.45 relies on use of the fragment MO eigenvectors (and related quantities) which are represented using dense matrices. It is therefore important to use high performance mathematical libraries in computing these quantities, as the speed at which these computations are processed will largely determine the overall speed of the EDA calculations³.

Our diagonalisation-dependent EDA implementation adopts use of the LAPACK [239] and SCLAPACK [240] mathematical libraries. These packages consist of optimised routines for computing matrix and vector operations and problems. These differ in their parallelisations: the LAPACK set of routines run in serial, using one central processing unit (CPU) core to solve each problem, whereas the the SCLAPACK set of routines run in parallel, allowing division of the problem over many cores.

To solve the eigenvalue problem described in Eq. 5.37, the DSYGVX eigensolver routine in the LAPACK package is used for serial compilations, and its corresponding parallel routine PDSYGVX in the SCLAPACK package is used for parallel compilations. Notably, the serial routines are necessarily bound by the restrictions of the CPU hardware. This is because the LAPACK routines require each entire matrix to be held in the memory of a single CPU core. The SCLAPACK routines effectively avoid this problem as this package is implemented for distributed memory systems, sharing the matrix data over multiple cores. In principle therefore, allocating sufficient number of cores to solve the problem will relieve the memory limitations.

³The diagonalisation-free EDA implementation described in Chapter 5.1.8 avoids these bottlenecks entirely.

5.1.8 Linear scaling reformulation of the EDA

As discussed above, the original implementation of the EDA in ONETEP requires diagonalisation of the density kernel to obtain the fragment MO eigenvectors used for constructing H_S^A . The computational cost of this procedure scales as $\mathcal{O}(N^3)$. Additionally, the fragment eigenvector matrices produced (as well as their derived quantities) are themselves dense, and therefore the matrix-matrix multiplications required to construct H_S^A in Eq. 5.45 also scale as $\mathcal{O}(N^3)$. By eliminating the diagonalisation bottleneck and using sparse matrix algebra, we present a reformulation of the original implementation that now scales with system size as $\mathcal{O}(N)$.

5.1.8.1 Reformulation of the Stoll SCF-MI

We begin by seeking to re-express the Stoll locally projected Hamiltonian in terms of sparse matrices only. In our diagonalisation-dependent implementation, the dense quantities used are the eigenvectors $M_{Bi}^{A\alpha}$, and the MO overlap matrix $\sigma^{Ai,Bj}$. Here, we present a re-expression of the Stoll locally projected Hamiltonian in which these quantities are substituted using modified representations of the density kernel.

From the definition of the fragment kernel $K_{\text{orth}}^{A\alpha,B\beta}$ of Eq. 5.39, we define a non-Hermitian, modified (fragment) density kernel $K_{\text{orth,col}(A)}^{B\beta,C\gamma}$ as

$$K_{\text{orth,col}(A)}^{B\beta,C\gamma} = \sum_i^{N_{\psi(\text{occ},B)}} \sum_j^{N_{\psi(\text{occ},A)}} M_{Bi}^{B\beta} \sigma^{Bi,Aj} (M^\dagger)_{Aj}^{C\gamma} \quad (5.61)$$

that is present within Eq. 5.45 as the following underlined combination

$$[\cdots \underline{M\sigma^{-1}}]_{AA} [\underline{M^\dagger \cdots}]_{AA} \quad . \quad (5.62)$$

By observing that

$$\begin{aligned}
 K_{\text{orth,col}(A)}^{B\beta,A\alpha} &= \sum_i^{N_{\psi(\text{occ},B)}} \sum_j^{N_{\psi(\text{occ},A)}} M_{Bi}^{B\beta} \sigma^{Bi,Aj} (M^\dagger)_{Aj}^{A\alpha} \\
 &\equiv K_{\text{orth}}^{B\beta,A\alpha} \\
 K_{\text{orth,col}(A)}^{A\alpha,B\beta} &= 0 |_{A \neq B} \\
 K_{\text{orth,col}(A)}^{B\beta,C\gamma} &= 0 |_{A \neq B \neq C}
 \end{aligned} \tag{5.63}$$

due to the block-diagonality of $M_{Bi}^{A\alpha}$ (Eq. 5.38), we note that $K_{\text{orth,col}(A)}^{B\beta,C\gamma}$ is constructed simply from the fragment A columns of $K_{\text{orth}}^{A\alpha,B\beta}$. This is shown visually for an example system in Fig. 5.2.

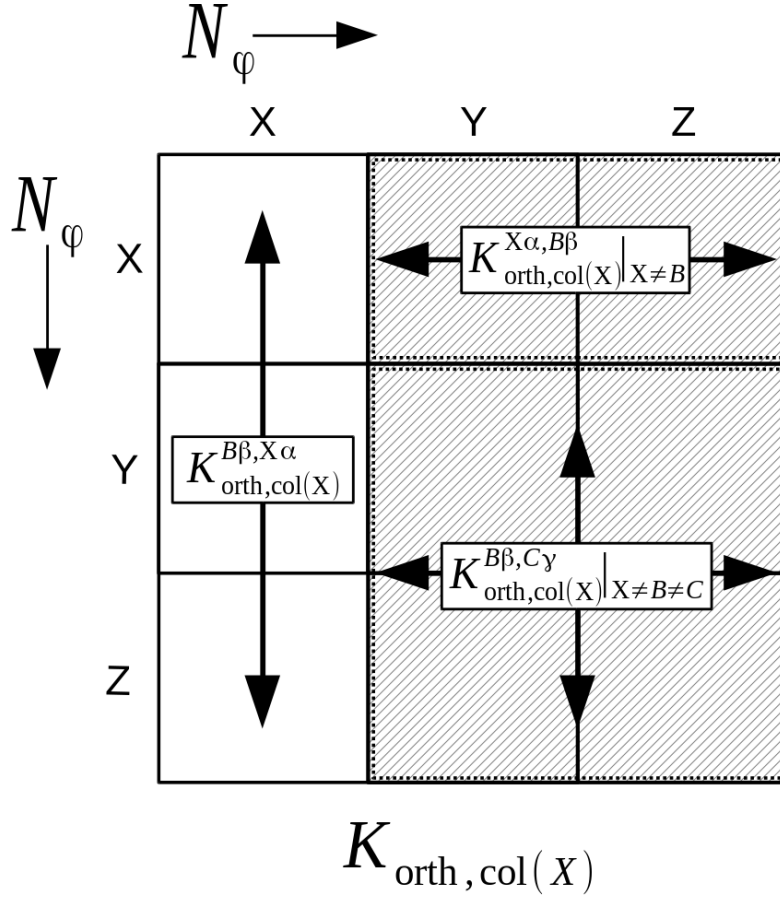


Figure 5.2: The modified kernel of a system comprising three fragments $\{X,Y,Z\}$, where the index A of $K_{\text{orth,col}(A)}^{B\beta,C\gamma}$ is set to fragment X . The shaded blocks are set to zero, with the non-shaded blocks equal to the relevant blocks of the (full supermolecule, orthogonalised MO) kernel $K_{\text{orth}}^{B\beta,A\alpha}$.

Substituting Eq. 5.39 and Eq. 5.61 into Eq. 5.45, we obtain an expression for the Stoll locally projected Hamiltonian,

$$\begin{aligned}
[H_S^A] = & [H]_{AA} - [HK_{\text{orth}}S]_{AA} \\
& - ([HK_{\text{orth}}S]_{AA})^\dagger \\
& + [SK_{\text{orth}}HK_{\text{orth}}S]_{AA} \\
& + [HK_{\text{orth,col}(A)}S]_{AA} \\
& + ([HK_{\text{orth,col}(A)}S]_{AA})^\dagger \\
& - [SK_{\text{orth}}HK_{\text{orth,col}(A)}S]_{AA} \\
& - ([SK_{\text{orth}}HK_{\text{orth,col}(A)}S]_{AA})^\dagger \\
& + [SK_{\text{orth,col}(A)}^\dagger HK_{\text{orth,col}(A)}S]_{AA}^\dagger
\end{aligned} \tag{5.64}$$

that avoids explicit calculation of the coefficients $M_{Bi}^{A\alpha}$ and where all the quantities involved can be represented using sparse matrices.

5.1.8.2 The adaptive McWeeny purification transformation

Having re-expressed the Stoll locally projected Hamiltonian in terms of eigenvector-free sparse matrices, our strategy now lies in solving the problem of orthogonalising the MO states of $K_{\text{orth}}^{A\alpha,B\beta}$ in a linear-scaling fashion.

In our original EDA implementation, orthogonality of the MO states was imposed by diagonalising the fragment density kernels $(K_A)^{\alpha\beta}$ as in Eq. 5.37 to obtain the fragment MO eigenvectors, which were in turn used with the quantity $\sigma^{Ai,Bj}$ to construct the (orthogonal) density kernel $K_{\text{orth}}^{A\alpha,B\beta}$ using Eq. 5.39. In our new approach, we instead adaptively purify the (non-orthogonal) frozen density kernel $K_0^{A\alpha,B\beta}$ to produce $K_{\text{orth}}^{A\alpha,B\beta}$. Our implementation is a prescription of the McWeeny purification functional [75] that purifies at such a rate that orbital occupancy instabilities are avoided.

For a given nearly idempotent ‘auxiliary’ density kernel L , the McWeeny transformation may be applied iteratively to impose idempotency as,

$$K = 3LSL - 2LSLSL \quad . \quad (5.65)$$

The McWeeny purification transformation remains stable so long as the MO occupation numbers are in the interval $\left[\frac{1-\sqrt{5}}{2}, \frac{1+\sqrt{5}}{2}\right]$ [241]. However, there exists the risk of orbital occupancies ‘flipping’ unless the occupancies are in the interval $\left[\frac{1-\sqrt{3}}{2}, \frac{1+\sqrt{3}}{2}\right]$. An illustration of this purification and the bounds of occupancy flipping is given in Fig. 5.3.

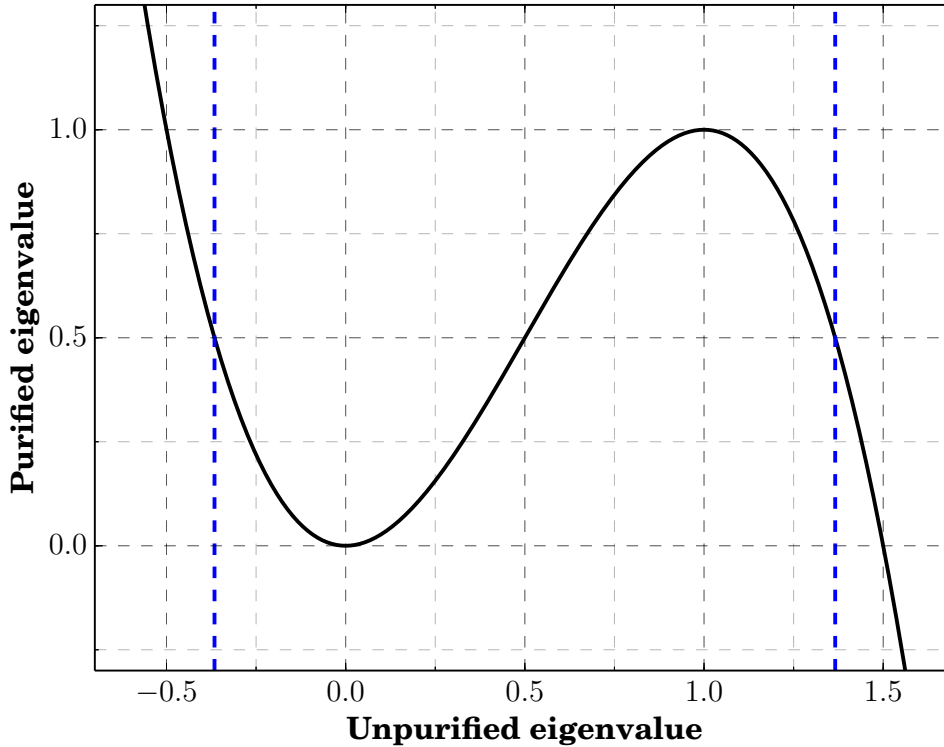


Figure 5.3: The standard McWeeny purification transformation mapping of the unpurified to purified eigenvalues of the density kernel (orbital occupancies). The lower and upper orbital occupancy bounds $\left(\frac{1-\sqrt{3}}{2}, \frac{1+\sqrt{3}}{2}\right)$ that ensure stability of the transformation with respect to flipping is shown by the blue vertical lines.

The construction of $K_{\text{orth}}^{A\alpha, B\beta}$ entails orthogonalisation of the fragment MOs in the presence of newly introduced fragment-fragment blocks of the overlap matrix. In

cases, purifying using the McWeeny purification transformation (rather than via diagonalisation) will fail as the unpurified occupancies of the initial MOs will lie outside of the stable occupancy interval. Our strategy is to modify the standard McWeeny transformation to be adaptive and therefore ensure stability for any range of initial orbital occupancies.

The McWeeny purification transformation of Eq. 5.65 can be equivalently expressed in the form of a steepest descent search problem as,

$$K = L - \lambda(4LSLSL - 6LSL + 2L) \quad . \quad (5.66)$$

where in the standard purification transformation $\lambda = 0.5$. In the adaptive purification approach, we purify using an optimised λ value that prevents orbital occupancy instabilities. The minimum and maximum occupancies f_{\min} and f_{\max} are calculated in $\mathcal{O}(N)$ operations by extremising (using an iterative conjugate gradients method) the generalised Rayleigh quotient [78],

$$R(K, S^{-1}, M) = \frac{M^\dagger K M}{M^\dagger S^{-1} M} \quad . \quad (5.67)$$

where S^{-1} is the inverse of the full supermolecule overlap matrix, and where extremising this Rayleigh quotient results in obtaining the extremal occupancy eigenvalues of the eigenvalue problem,

$$KM = fS^{-1}M \quad . \quad (5.68)$$

If these occupancies lie outside of the interval $\left[\frac{1-\sqrt{3}}{2}, \frac{1+\sqrt{3}}{2}\right]$ that preserves the initial occupancy numbers, then λ is explicitly calculated as,

$$\lambda = \min[\lambda_f(f_{\min}), \lambda_f(f_{\max})] - \delta \quad (5.69)$$

where $\lambda_f(f)$ is a function of λ that gives the step length that bounds occupancy flipping,

$$\lambda_f(f) = \frac{1}{4(f-1)f} \quad (5.70)$$

and where δ is introduced to force the step to be lower than this bound of occupancy flipping (in practice, δ is set to 0.001).

If the occupancies lie in the occupancy-preserving interval, then λ is set to 0.5, which results in the steepest descent search simplifying to the standard McWeeny transformation of Eq. 5.65. The calculation of λ is displayed in Fig. 5.4.

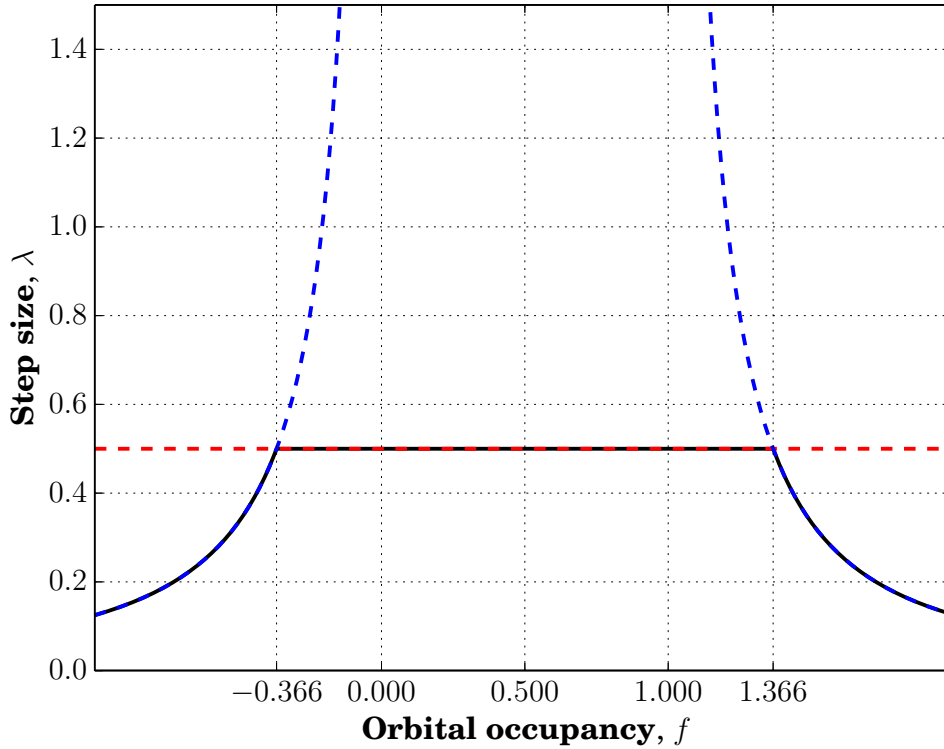


Figure 5.4: The steepest descent step length λ for various extremal orbital occupancies f . The step length is set to 0.5 (red) when in the occupancy interval that guarantees preservation of occupancy number $(\left[\frac{1-\sqrt{3}}{2}\right], \left[\frac{1+\sqrt{3}}{2}\right])$. When outside of this interval, the step length is determined analytically (blue) using Eq. 5.69. The overall value of λ is given by the solid black line.

Having obtained the value of λ , the kernel is iteratively purified using Eq. 5.66 until convergence. Convergence is defined using the root mean squared error (RMSE)

of idempotency as,

$$\text{RMSE}(KSK - K) \leq 1.0E - 8 \quad . \quad (5.71)$$

By combining our EDA method with the reformulated Stoll locally projected Hamiltonian, the adaptive purification transformation and the ONETEP sparse matrix algebra engine, we present a linear-scaling, diagonalisation-free implementation of our EDA approach.

5.1.8.3 The lambda function

Here, we derive the function $\lambda_f(f)$ that provides the stepsize λ that bounds orbital occupancy instability for a given orbital occupancy f . We begin by expressing the steepest descent formulation of the McWeeny purification transformation as,

$$f_1 = f_0 - \lambda(4f_0^3 - 6f_0^2 + 2f_0) \quad (5.72)$$

where f_0 represents the unpurified occupancy number and f_1 represents the purified occupancy number.

We first note that the bound of occupancy flipping of f_0 occurs when the purified occupancy mapped onto by Eq. 5.72 is $f_1 = 0.5$. To find the maximum possible step size ($\lambda > 0$) that bounds occupancy flipping, we seek to find the value of λ that purifies f_0 to $f_1 = 0.5$,

$$0.5 = f_0 - \lambda(4f_0^3 - 6f_0^2 + 2f_0) \quad (5.73)$$

$$\therefore \lambda(4f_0^3 - 6f_0^2 + 2f_0) = f_0 - 0.5 \quad (5.74)$$

$$\begin{aligned} \therefore \lambda &= \frac{f_0 - 0.5}{4f_0^3 - 6f_0^2 + 2f_0} \\ &= \frac{f_0 - 0.5}{4f_0(f_0 - 0.5)(f_0 - 1)} \\ &= \frac{1}{4(f_0 - 1)f_0} \quad . \end{aligned} \quad (5.75)$$

This expression of λ therefore provides the bound to stability of purified occupancy number for a given unpurified occupancy f_0 , i.e.

$$\lambda_f(f) = \frac{1}{4(f-1)f} \quad (5.76)$$

where f is an unpurified occupancy number.

5.2 Electron density difference plots

Electron density difference (EDD) plots display the change in electron density that result from EDA processes, and are useful as a means to identify key regions of systems that are involved in binding. Specifically, these plots are associated with the polarisation and charge transfer energy components of the EDA. The EDD plot quantities are given by,

$$\begin{aligned} n_{\text{EDD(POL)}}(\mathbf{r}) &= n_{\text{POL}}(\mathbf{r}) - n_{\text{FRZ}}(\mathbf{r}) \\ n_{\text{EDD(CT)}}(\mathbf{r}) &= n_0(\mathbf{r}) - n_{\text{POL}}(\mathbf{r}) \end{aligned} \quad (5.77)$$

where $n_{\text{FRZ}}(\mathbf{r})$, $n_{\text{POL}}(\mathbf{r})$, and $n_0(\mathbf{r})$ are the frozen (idempotent), polarised, and fully relaxed electron densities respectively, which are calculated during the EDA calculation.

5.3 Results and discussion

5.3.1 Validation

We have applied our EDA to a number of small test systems which model interactions relevant within the field of drug design in order to validate the accuracy of the ONETEP EDA against its ALMO and LMO EDA counterparts in the

Q-CHEM [54] and GAMESS-US [56] ab initio packages respectively. These systems have been selected as they provide examples of important interactions such as hydrogen bonding, π - π , and dispersion [207; 208].

5.3.1.1 Calculations

Geometry optimisation was performed at the PBE-D2/aug-cc-pVTZ level of theory [44; 242] on all structures using the Q-CHEM ab initio package [54]. The -D2 correction for dispersion of Grimme [242] was used in order to properly model the dispersion interactions especially observed in the case of the π - π interacting systems. The optimised geometries of the systems studied are shown within Tables 5.1 and 5.2.

Table 5.1: Test set 1 of PBE-D2/aug-cc-pVTZ geometry optimised systems for EDA (intermolecular distances are given in Å)

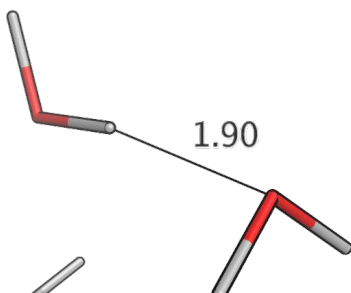
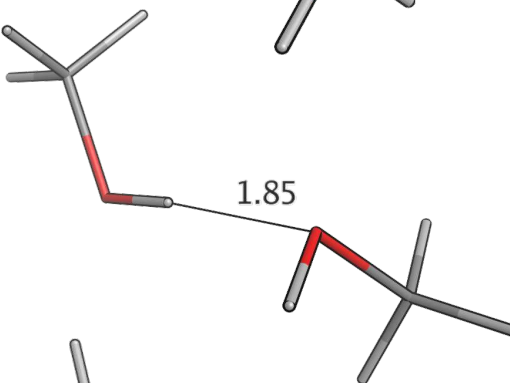
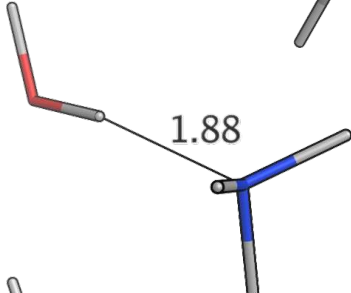
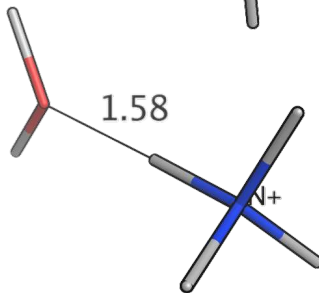
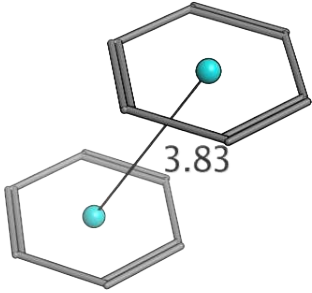
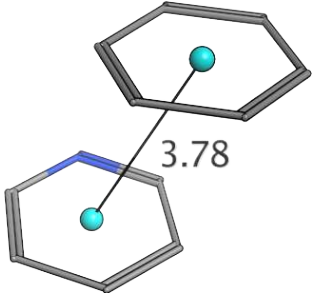
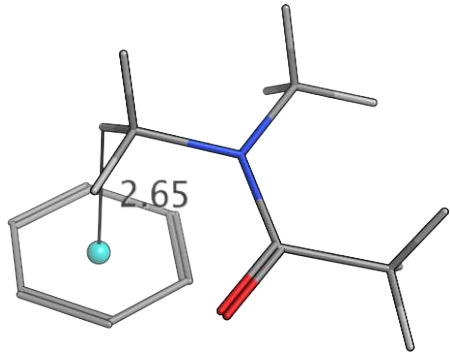
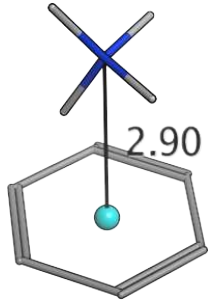
System	Figure
Water – Water	 A diagram showing two water molecules. Each molecule consists of a red oxygen atom and two white hydrogen atoms. A line connects the oxygen atom of one molecule to a hydrogen atom of the other molecule, with the value '1.90' written next to it.
Methanol – Methanol	 A diagram showing two methanol molecules. Each molecule consists of a red oxygen atom, a grey carbon atom, and four white hydrogen atoms. A line connects the oxygen atom of one molecule to a hydrogen atom of the other molecule, with the value '1.85' written next to it.
Water – Ammonia	 A diagram showing a water molecule (red oxygen, two white hydrogens) and an ammonia molecule (blue nitrogen, three white hydrogens). A line connects the oxygen atom of the water molecule to a hydrogen atom of the ammonia molecule, with the value '1.88' written next to it.
Water – Ammonium	 A diagram showing a water molecule (red oxygen, two white hydrogens) and an ammonium ion (blue nitrogen with a '+' sign, four grey hydrogens). A line connects the oxygen atom of the water molecule to a hydrogen atom of the ammonium ion, with the value '1.58' written next to it.

Table 5.2: Test set 2 of PBE-D2/aug-cc-pVTZ geometry optimised systems for EDA (intermolecular distances are given in Å)

System	Figure
Benzene – Benzene (Parallel Displaced)	
Benzene – Pyridine	
Benzene – Dimethylacetamide	
Benzene – Ammonium	

EDA was performed on the geometry optimised structures at the PBE-D2/aug-cc-pVTZ level of theory⁴ in the case of the LMO and ALMO EDAs, and at the PBE-D2 level with a 1200 eV psinc basis set cutoff energy and 8 Bohr NGWF radii in the case of the ONETEP EDA.⁵ Additionally, the Martyna-Tuckerman approach was used [243; 244] in the ONETEP calculations to prevent interactions with periodic system images. Evidence of convergence of the calculations with respect to psinc basis set kinetic energy cutoff (and the EDA energy values referred to in this section) are provided in Tables B.1 and B.2 of the Appendix.

5.3.1.2 Analysis

Test set 1: hydrogen-bonding interactions In this test set, we assess the bonding components of important hydrogen bonded systems such as the water dimer, methanol – methanol, water – ammonia and water – ammonium (geometries are shown in Table 5.1). Studies were published that investigate the covalency of hydrogen-bonding in water [212–219], and this covalency may be further analysed by considering the strength of the charge transfer component through EDA.

The ALMO EDA frozen density component ΔE_{FRZ} , further partitioned into its constituent electrostatic, exchange and Pauli-repulsion parts, is shown in Fig. 5.5. These constituent components follow the same definitions as in the LMO EDA and are in good agreement throughout the set. Additionally included in the ONETEP EDA is the correlation component that is required to form ΔE_{FRZ} as shown in Eq. 5.6.

We observe that the net effect of these frozen density components is almost negligible for all systems excluding the ammonium interacting case as shown by the small magnitudes of the ΔE_{FRZ} component values ($0.1 \text{ kcal/mol} > \Delta E_{\text{FRZ}} >$

⁴Grimme -D3 correction results are also included for comparison in Tables B.1 and B.2 of the Appendix. The -D3 contributions were calculated using the DFT-D3 program as only the -D2 correction is currently implemented in ONETEP.

⁵ For all calculations excluding the benzene – ammonium system the polarisation stage NGWFs were initialised to the converged fragment NGWFs. For the benzene – ammonium system, re-initialisation to guess NGWFs at the polarisation stage was required in order to prevent under-convergence of the polarisation energy component.

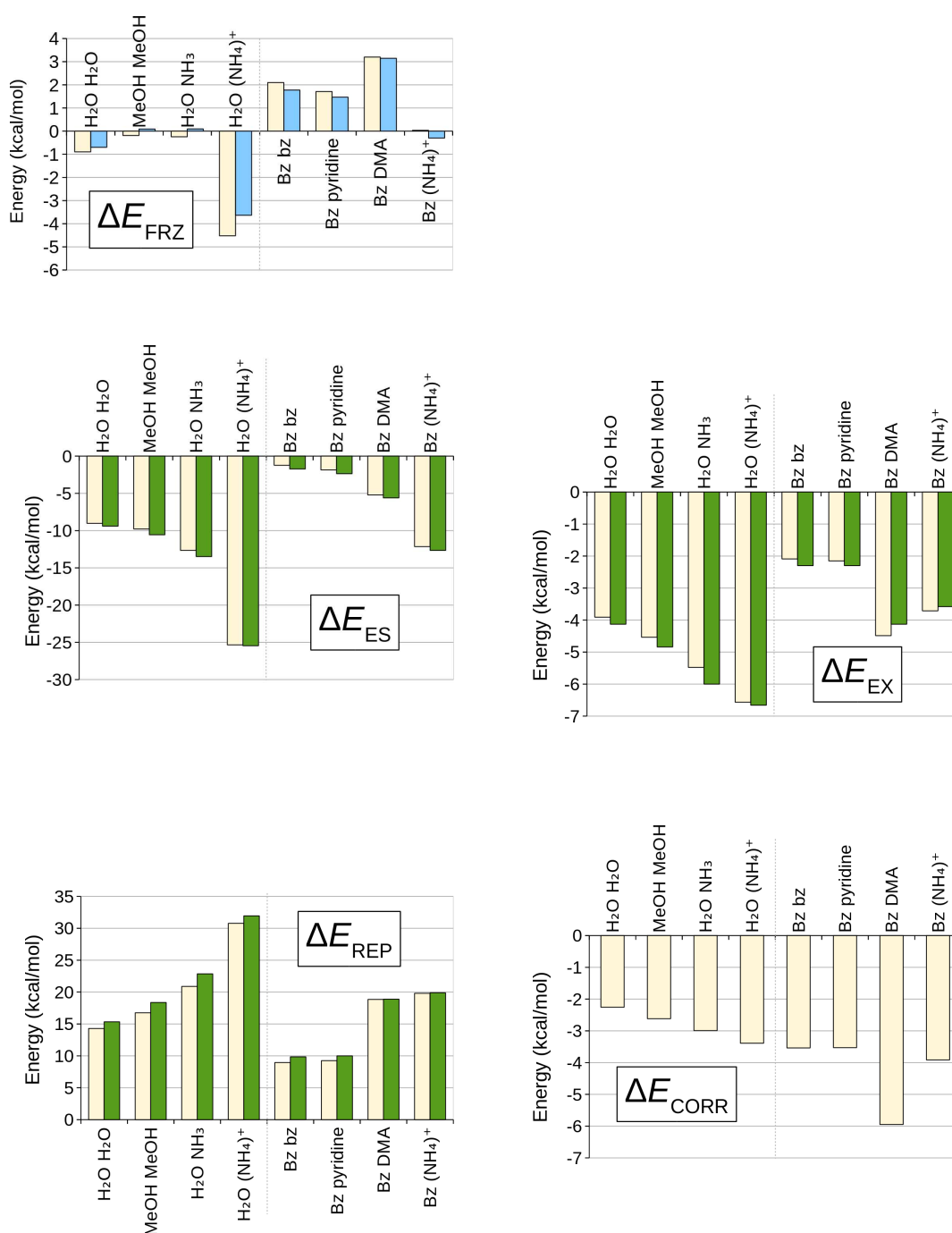


Figure 5.5: Frozen density analysis energy components for test sets 1 and 2. EDA component values are given in kcal/mol and were calculated with the PBE-D2 functional. ONETEP EDA calculations (yellow) were performed with a psinc basis set with a kinetic energy cutoff of 1200 eV. Q-CHEM ALMO EDA calculations (blue) and GAMESS-US LMO EDA calculations (green) were performed with an aug-cc-pVTZ Gaussian basis set. The ALMO frozen density component is the sum of the electrostatic, exchange, Pauli-repulsion and correlation energy components as shown in Eq. 5.6

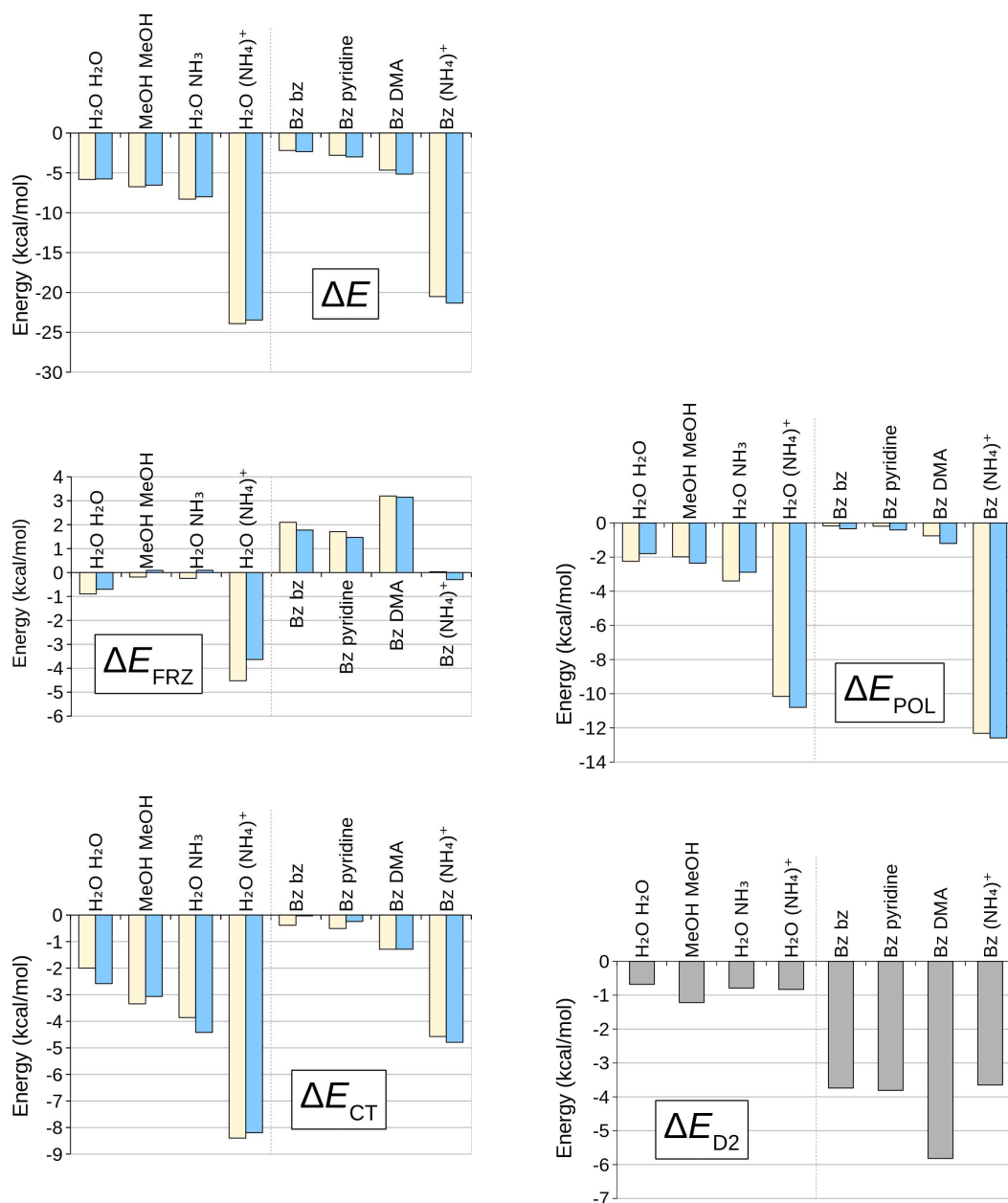


Figure 5.6: EDA energy components for test sets 1 and 2. EDA component values are given in kcal/mol and were calculated with the PBE-D2 functional. ONETEP EDA calculations (yellow) were performed with a psinc basis set with a kinetic energy cutoff of 1200 eV. Q-CHEM ALMO EDA calculations (blue) were performed with an aug-cc-pVTZ Gaussian basis set. Values of Grimme's -D2 correction for dispersion are also provided (grey).

-0.9 kcal/mol). Intuitively, a more favourable ΔE_{FRZ} component is expected for the water – ammonium system due to the strong electrostatic interaction of the charged ammonium molecule with the dipole of the water molecule. Our expectations are confirmed by assessment of the electrostatic energy: for this system we observe electrostatic contributions of -25.3 kcal/mol and -25.5 kcal/mol through the ONETEP and LMO EDAs respectively, whereas in the case of the uncharged systems we observe $\Delta E_{\text{ES}} \leq -13.5$ kcal/mol. The increased effect of electrostatics in the water – ammonium system is also moderated significantly by a 9.9 kcal/mol (ONETEP) and 9.1 kcal/mol (LMO) increase in the Pauli-repulsion term compared to the water – ammonia system.

Exchange in the ONETEP EDA is observed to increase through the test set from -3.9 kcal/mol for the water dimer to -6.6 kcal/mol for the ammonium interacting system, in good agreement with the LMO EDA results. The correlation term is also observed to increase in magnitude through the test set from -2.3 kcal/mol for the water dimer to -3.4 kcal/mol for the ammonium interacting system. This observation is rationalised through the increasing electron counts of the systems through the set and decreasing intermolecular separations.

Polarisation and charge transfer energies obtained through the ALMO and ONETEP EDAs are shown in Fig. 5.6. The LMO EDA does not attempt to distinguish polarisation from charge transfer effects and instead simply describes both as an inter- and intramolecular polarisation term. Again, the ALMO and ONETEP schemes show generally good agreement of the polarisation term, with the strength of polarisation increasing through the set to the ammonium interacting system (-10.2 kcal/mol (ONETEP) and -10.8 kcal/mol (ALMO)). Polarisation is shown to be similar in magnitude to the charge transfer contribution in the ONETEP EDA of the water dimer system, with a polarisation energy of -2.2 kcal/mol and a charge transfer energy of -2.0 kcal/mol. In the case of the ALMO EDA, charge transfer is observed to be much more significant (-2.6 kcal/mol) than polarisation effects (-1.8 kcal/mol). Despite these differences which are expected due to

the different basis sets used in the ONETEP and ALMO EDAs, the values observed and inferences drawn for these components are generally in good agreement between the schemes.

Test set 2: π -bonding systems In this test set, we assess the energy components of a number of molecules interacting with the π -electron cloud of a benzene molecule. Specifically, we have investigated the interactions of benzene, pyridine, dimethylacetamide (DMA) and ammonium with benzene (geometries shown in Table 5.2).

We note overall good agreement between the ONETEP and LMO EDAs through the electrostatic, exchange and Pauli-repulsion energy components as displayed in Fig. 5.5. We also observe good agreement for the ALMO EDA frozen density component that is partially constructed from these terms. Through the set, the contributions of electrostatics (-1.2 kcal/mol to -12.1 kcal/mol (ONETEP)), Pauli-repulsion (9.0 kcal/mol to 19.8 kcal/mol (ONETEP)), polarisation (-0.2 kcal/mol to -12.3 kcal/mol (ONETEP)) and charge transfer (-0.4 kcal/mol to -4.6 kcal/mol (ONETEP)) generally increase as expected with decreasing intermolecular separation and the presence of charged or larger molecules.

The largest correlation effects are observed for the benzene – DMA system (-5.9 kcal/mol). This compares to correlation energies of -3.5 kcal/mol for the benzene – benzene and benzene – pyridine systems, and -3.9 kcal/mol for the benzene – ammonium interacting system. This difference likely arises due to the small intermolecular separation (2.65\AA) of the DMA molecule compared to the other systems within the set (2.90\AA to 3.83\AA), and the larger number of interacting atoms. A similar trend is observed in the contribution of exchange and this can also be rationalised through similar considerations.

ALMO and ONETEP polarisation and charge transfer contributions for test set 2 are shown in Fig. 5.6 and also display good agreement. The ability of DMA to delocalise charge through its structure appears to enhance polarisation to a

degree, as shown by a polarisation energy of -0.8 kcal/mol for the ONETEP EDA and -1.2 kcal/mol for the ALMO EDA. Interestingly, polarisation is observed to increase markedly to -12.3 kcal/mol (ONETEP) and -12.6 kcal/mol (ALMO) in the case of the ammonium interacting system. This is likely the result of the placement of a positively charged molecule directly within the polarisable π -cloud of the partner benzene molecule.

Charge transfer is most significant in the DMA (-1.3 kcal/mol (ONETEP and ALMO)) and ammonium (-4.6 kcal/mol (ONETEP) and -4.8 kcal/mol (ALMO)) interacting systems. This is expected due to the ability of the DMA molecule to delocalise and stabilise incumbent charge, and due to the high favourability of the positively charged ammonium molecule to accept electron density. Charge transfer is especially strong in the ammonium interacting system, reflecting the consequence of placement of a charged molecule directly within the π -cloud of the partner benzene molecule as was also observed in the case of polarisation.

5.3.2 Basis set dependence

A notable weakness of using the SCF-MI approach to separate polarisation and charge transfer effects is its significant basis set dependency. As the basis set size increases, the polarised state increasingly becomes described using basis functions that extend into the space of the partner fragment and therefore this component increasingly includes charge transfer contributions. This ill-definition of the energy components is similar to the sensitivity [245; 246] of Mulliken charges [177] to basis set size. Rigorous separation of the polarisation and charge transfer terms is of key importance for obtaining an accurate chemical description, and the presence of this ill-definition presents an issue. In this section, we aim to quantify the extent to which this effect affects the accuracy of the EDA results.

5.3.2.1 Calculations

Structures of water – water, methanol – methanol, and benzene – ammonium systems were geometry optimised at the PBE-D2/aug-cc-pVTZ level⁶ using the Q-CHEM [54] DFT package. The optimised geometries of these systems are shown within Tables 5.1 and 5.2.

ONETEP and ALMO EDA calculations were performed using ONETEP and Q-CHEM [54] using the PBE-D2 functional using basis sets of increasing completeness. For the ONETEP EDA, calculations were performed using 6, 7, 8 and 9 Bohr NGWF radii with a 1200 eV kinetic energy cutoff. The Martyna-Tuckerman approach was used [243; 244] in the ONETEP calculations to prevent interactions with periodic system images. In the case of the ALMO EDA, the basis sets used were the aug-cc-pVDZ, aug-cc-pVTZ, aug-cc-pVQZ and aug-cc-pV5Z basis sets.

5.3.2.2 Analysis

Plots demonstrating the basis set dependence of the frozen density, polarisation, and charge transfer components are provided in Fig. 5.7.

The effect of polarisation and charge transfer ambiguity may be countered and chemically accurate contributions obtained by adopting a consistent basis set choice of carefully considered spatial extension. In previous work the use of the aug-cc-pVTZ basis set for ALMO EDA calculations has been shown to offer a fair balance between accuracy and stability of terms [219; 247]. Fig. 5.7 shows that adopting between 7.5 Bohr to 8.5 Bohr NGWF radii is approximately equal to using the aug-cc-pVTZ basis set in the Gaussian code ALMO EDA. We suggest the use of 8.0 Bohr NGWF radii NGWFs in order to fairly balance the accuracy of ΔE with accuracy in partitioning polarisation and charge transfer effects.

Ascribing polarisation and charge transfer contributions using approaches based on the ALMO methodology is not without challenge. Methods that seek to avoid

⁶These structure are identical to those of Section 5.3.1.

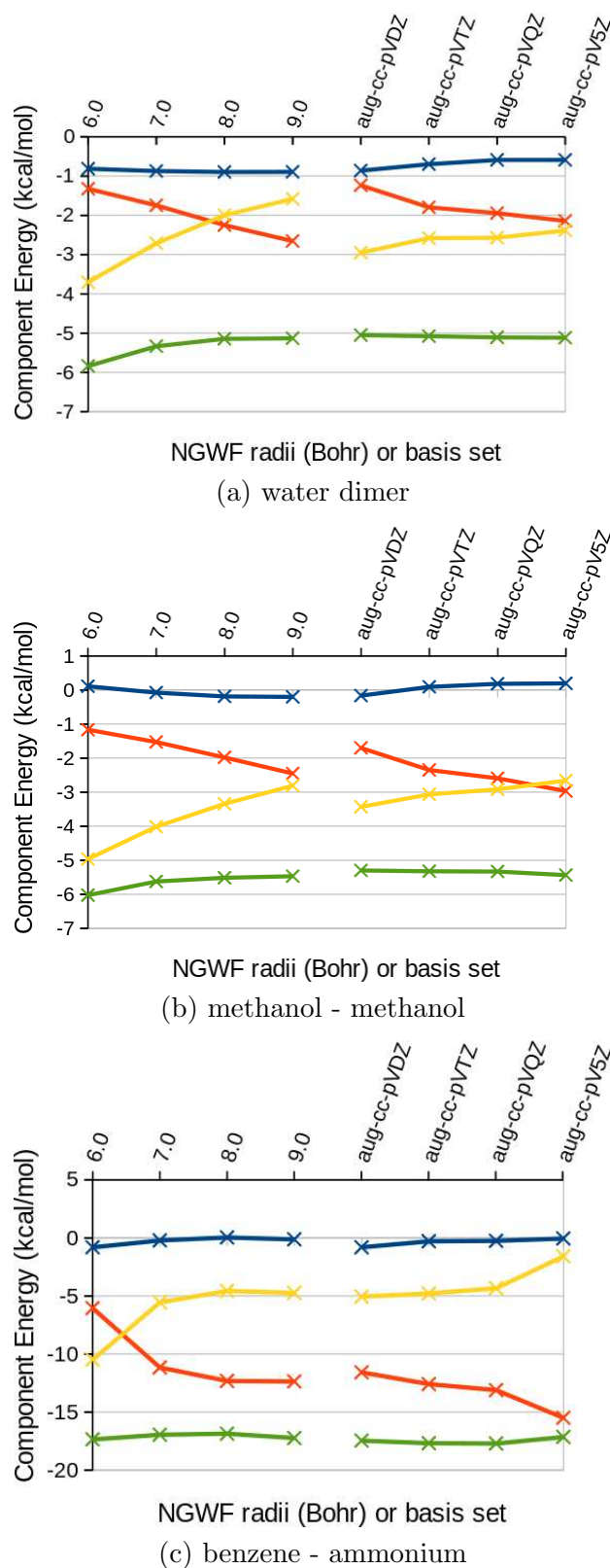


Figure 5.7: The ONETEP (6 Bohr to 9 Bohr NGWF radii) and ALMO (aug-cc-pVDZ to aug-cc-pV5Z) EDA of PBE-D2/aug-cc-pVTZ geometry optimised (a) water dimer, (b) methanol - methanol, and (c) benzene - ammonium systems. The PBE/1200 eV level ΔE (green) is partitioned into the frozen density (blue), polarisation (red), and charge transfer (yellow) energy components as described in Eq. 5.2. The -D2 correction for dispersion of Grimme is independent of basis set size and so was not included for clarity.

this ambiguity include the constrained DFT (CDFT) approach of Wu that exploit population analysis calculations to partition polarisation and charge transfer by real space definitions [16], and also the recent fragment electric-field response functions (FERF) approach of Horn and Head-Gordon [248] that adopts the use of fragment polarisation subspaces for variationally defining the polarisation contribution. These approaches have shown success in isolating energy contributions with minimal basis set dependence, presenting the opportunity for the development of new EDA schemes with ever more chemically relatable energy components.

5.3.3 Exchange-correlation functional dependence

The choice of exchange-correlation functional is important within DFT calculations as this will often determine the accuracy of the results obtained. Functionals often have specific strengths and weaknesses, and so their choice should be thoughtfully considered. For example, Handy et al. [249] showed the BLYP functional to generally overestimate bond lengths, and LDA to significantly overestimate binding energies. Additionally, the LDA and GGA families of functionals are known to generally underestimate the band gaps of semiconductors [250] and so would be unfavourable for use in such applications. Due to the importance of functional choice in DFT calculations, we seek to measure the dependence of the EDA method with respect to exchange-correlation functional in this section.

5.3.3.1 Calculations

Structures of water – ammonium and benzene – dimethylacetamide (DMA) systems were geometry optimised at the PBE-D2/aug-cc-pVTZ level⁷ using the Q-CHEM [54] DFT package. The optimised geometries of these systems are shown within Tables 5.1 and 5.2.

⁷These structure are identical to those of Section 5.3.1.

We have compared the results of these systems using the PBE [44] and BLYP [48; 49] GGA exchange-correlation functionals and LDA (with VWN correlation [41]) functional using ONETEP with a 1200eV basis set kinetic energy cutoff. As Grimme’s correction for dispersion depends upon the choice of exchange-correlation functional by a simple applied scaling factor, we have omitted this correction from our discussion. The Martyna-Tuckerman approach was used [243; 244] to prevent interactions with periodic system images.

5.3.3.2 Analysis

Table 5.3: The water - ammonium ONETEP EDA energy components using a 1200eV basis set kinetic energy cutoff.

Energy term (kcal/mol)	Exchange-correlation functional		
	PBE	BLYP	LDA (VWN)
FRZ ⁸	-4.5	-3.4	-8.3
ES	-25.3	-25.7	-25.7
EX	-6.6	-4.9	-12.9
REP	30.8	31.4	32.4
CORR	-3.4	-4.2	-2.1
POL	-10.2	-10.2	-10.4
CT	-8.4	-8.0	-8.6
ΔE	-23.1	-21.5	-27.4

Table 5.4: The benzene - dimethylacetamide (DMA) ONETEP EDA energy components using a 1200eV basis set kinetic energy cutoff.

Energy term (kcal/mol)	Exchange-correlation functional		
	PBE	BLYP	LDA (VWN)
FRZ ⁸	3.2	6.8	-3.0
ES	-5.2	-5.4	-5.5
EX	-4.5	-0.6	-15.6
REP	18.9	19.2	21.2
CORR	-5.9	-6.5	-3.1
POL	-0.8	-0.9	-0.8
CT	-1.3	-1.3	-1.8
ΔE	1.2	4.7	-5.6

The results of this functional comparison are displayed in Tables 5.3 and 5.4. As we may expect, the LDA results display generally poor agreement of ΔE values

⁸ONETEP EDA components contained within the ΔE_{FRZ} energy component are right-adjusted for clarity in the data tables provided in this thesis.

with the GGA functionals. Analysing the EDA components, we observe that this is primarily due to differences in the exchange components, for example this component is 11.1 kcal/mol lower for the LDA functional than the PBE functional in the case of the benzene – DMA system. This disagreement is partially cancelled by the Pauli repulsions and correlation components, giving a ΔE_{FRZ} component energy 6.2 kcal/mol lower for the LDA functional with this system. Polarisation and charge transfer effects are captured with surprising accuracy by the LDA functional for the two systems studied, with polarisation within 0.2 kcal/mol of the GGA functionals' values and charge transfer within 0.6 kcal/mol.

There is good agreement between the GGA results, indicating that energy components within this class of functionals could be expected to be comparable. As with the LDA functional, differences using the PBE and BLYP functionals are apparent within the ΔE_{FRZ} components, with the ΔE_{FRZ} term 1.1 kcal/mol lower for PBE than BLYP in the case of the water – ammonium system and 3.6 kcal/mol lower in the case of the benzene – DMA system. Polarisation and charge transfer are in good agreement (0.4 kcal/mol) between the GGA functionals.

5.3.4 Atomic coordinate dependence

When preparing biomolecular systems for calculation, the initial structures (such as those downloaded from the Protein Data Bank [251]) typically have an error attributed to the quality of the atomic coordinates. This quality is determined by the crystallographic resolution, which relates to the scattering of X-rays during the diffraction process. For example a high-resolution structure could be considered any structure with a resolution of 1 Å or below. Additional error is also introduced during protonation of the structures as we must model the placement of these hydrogen atoms within the structure.

In this section, we seek to quantify the sensitivity of the EDA method with respect to changes in atomic coordinates. Here, we perform EDA calculations on a number of model protein-ligand structures that differ only in their atomic coordinates.

Ideally, the EDA approach should exhibit minimal sensitivity to these changes as excessive sensitivity would indicate lesser accuracy. Nonetheless, a degree of variability should be expected, as the systems that we are studying are necessarily different. The variability in the value of ΔE for the systems is considered a fair benchmark for the variability in the EDA components.

5.3.4.1 Calculations

In order to assess the dependence of the EDA on atomic coordinates, we prepared a set of three systems prepared from the structure of thrombin interacting with the T87 inhibitor (pdb:1G30 [252]), each produced using different atomic tether forces during their geometry optimisation.

The following protocol was used to prepare the 1G30 protein structures for EDA. The missing 7-loop⁹ of the initial thrombin-inhibitor crystal structure was built using MOE homology modelling suite. The structure was then capped using COCH₃ and NHCH₃ groups, and protonated using the Protonate3d software [253]. Three structures were then produced by energy minimisation using the MMFF94x force-field with the generalised Born implicit solvent (GBIS) model using tethering force constants of $(3/2)kT/\sigma^2$ ($\sigma = 0.25, 0.50$, and 1.00 \AA) for all atoms during the minimisation. A larger σ value produces a weaker force constant. These structures were then truncated to remove residues beyond 5 \AA of the ligand, and further truncated to ensure consensus of the protein residues across all of the systems. Finally, the cleaved backbone of the structures were capped using hydrogens. The superposition of the structures are shown in Fig. 5.8. ONETEP EDA was performed on the resulting systems using a 800 eV psinc basis set cutoff energy and 8 Bohr NGWF radii at the PBE-D2 level of theory. Dispersion corrections were also calculated using the -D3 correction of Grimme et al. [209] for comparison.

⁹The 7-loop refers to the missing residues Trp147A, Thr147B, Ala147C, Asn147D, Val147E, Gly147F, and Lys147G.

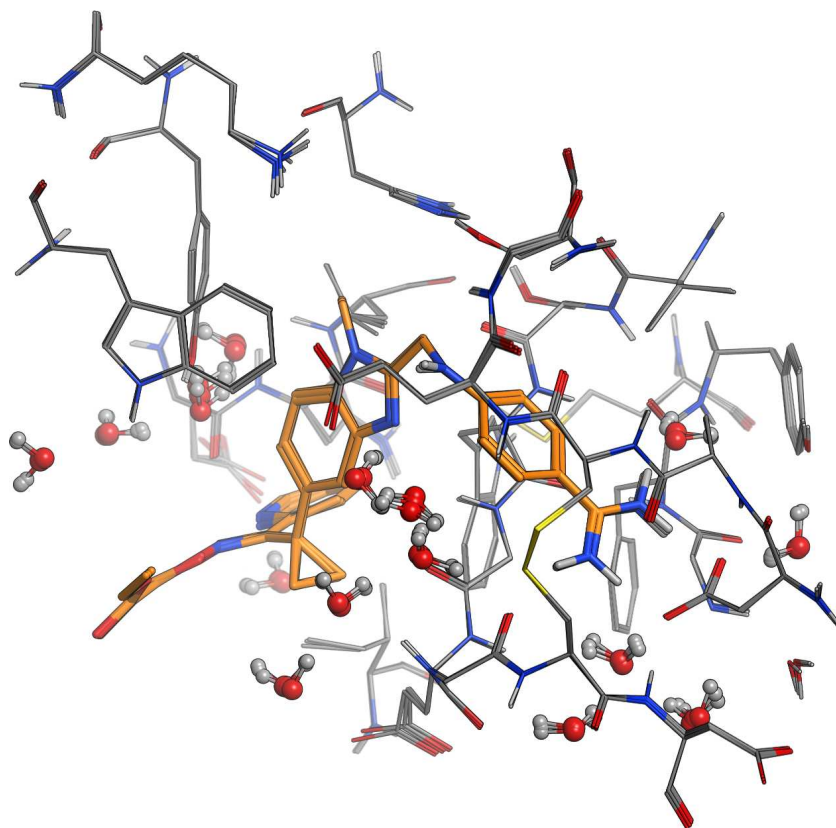


Figure 5.8: Superposition of the optimised 1G30 systems used to quantify atomic coordinate sensitivity.

5.3.4.2 Analysis

The results of the three EDA calculations are shown in Table 5.5, with EDA component errors and root-mean-square deviation (RMSD) values of the atomic coordinates calculated with respect to the $\sigma = 0.25\text{\AA}$ system. This $\sigma = 0.25\text{\AA}$ system is the system which most closely resembles the original 1G30 pdb crystal structure. The mean absolute errors (MAEs) of the core¹⁰ EDA components are 2.1 kcal/mol and 2.9 kcal/mol for the $\sigma = 0.50\text{\AA}$ and $\sigma = 1.00\text{\AA}$ systems respectively.

¹⁰This refers to the electrostatic, exchange, Pauli repulsion, correlation, polarisation, charge transfer and -D2 correction components.

Table 5.5: The PBE-D2/800eV ONETEP EDA energy components and errors for the 1G30 optimised systems used to quantify atomic coordinate sensitivity.

Optimisation tether deviation, σ (Å)	0.25		0.50		1.00	
RMSD ^a (Å)	0.00		0.04		0.11	
ONETEP EDA (kcal/mol)	Value	Error ^a	Value	Error ^a	Value	Error ^a
FRZ	-20.5	0.0	-18.7	1.9	-17.7	2.9
ES	-135.6	0.0	-138.7	-3.1	-139.0	-3.4
EX	-52.7	0.0	-53.6	-0.9	-53.3	-0.6
REP	229.9	0.0	235.3	5.4	233.8	3.9
CORR	-62.2	0.0	-61.6	0.6	-59.2	3.0
POL	-30.9	0.0	-32.5	-1.6	-33.6	-2.7
CT	-32.6	0.0	-34.5	-1.9	-35.4	-2.7
ΔE (PBE/800eV)	-84.0	0.0	-85.6	-1.6	-86.6	-2.6
-D2 Correction	-75.1	0.0	-74.0	1.1	-71.1	4.0
-D3 Correction ^b	-78.0	0.0	-77.6	0.4	-75.9	2.1
ΔE (PBE-D2/800eV)	-159.2	0.0	-159.7	-0.5	-157.8	1.4

^a RMSD and EDA component error calculated with respect to $\sigma = 0.25$ Å geometry.

^b Grimme -D3 correction results are included for comparison.

We begin our analysis by noting that the geometric displacements occur most significantly in the freely mobile water molecules of the system which are located in relatively close proximity to the ligand as shown in Fig. 5.8. For this reason, the geometric RMSD values should be considered in relative terms only, as these values do not reflect the fact that much of the system remains rigid during the different optimisations.

With weaker tethering force constant (i.e. the $\sigma = 1.00$ Å system), the forcefield model has greater dominance over the final optimised system conformation. The EDA component profile changes smoothly with weakening of the force constant, with polarisation and charge transfer both increasing in strength, and the frozen density component and dispersion falling. Overall, the dispersion contributions are observed to cancel the error in ΔE to a large degree. For example, in the $\sigma = 1.00$ Å system the absolute ΔE error is 2.6 kcal/mol without the -D2 correction, but on including the -D2 correction the error falls to 1.4 kcal/mol. This cancellation is even more pronounced using the -D3 correction.

The empirical dispersion corrections show errors similar in magnitude to the DFT-derived EDA component errors. For example in the $\sigma = 1.00\text{\AA}$ system, the average of the -D2 and -D3 corrections errors is 3.1 kcal/mol, comparable to the frozen density component (2.9 kcal/mol), polarisation (-2.7 kcal/mol) and charge transfer (-2.7 kcal/mol) errors. This is interesting to note as this indicates that the DFT-derived energy components are comparable in sensitivity to those derived from pair-potential models.

Overall, the results show mild sensitivity of the EDA components to changes in atomic coordinates, comparable to the sensitivity of ΔE itself. This can be seen through the MAE values for the EDA components and the absolute errors in ΔE . For the $\sigma = 0.50\text{\AA}$ and $\sigma = 1.00\text{\AA}$ systems, the MAE values of the core EDA components (2.1 kcal/mol and 2.9 kcal/mol) are slightly greater than the absolute errors in ΔE without -D2 correction (1.6 kcal/mol and 2.6 kcal/mol), and notably greater than the absolute errors in ΔE with -D2 correction (0.5 kcal/mol and 1.4 kcal/mol). As discussed above, however, the dispersion correction leads to a cancellation of error and may be considered to artificially lower the error in ΔE . Accounting for this effect, these results therefore indicate reasonable stability of the EDA method.

5.3.5 Electron density difference water trimer test example

In this section, we demonstrate the value of electron density difference (EDD) plots which are provided alongside the EDA results. EDD plots show the redistributions of charge that occur during polarisation and charge transfer, and are able to provide indication of important regions of chemical significance within systems. For our test, we used the water trimer. This relatively simple system is useful for demonstrating the redistributions of charge that occur through the processes involved in bonding, and also serves to show application of the EDA to a three-fragment system. Although simple in structure, this additionally provides a physical example investigating hydrogen bonding networks within solvent.

5.3.5.1 Calculations

Two water trimer geometries were prepared for our calculations. The first system was prepared directly from the (C_3 symmetry) 3-UUU water isomer of Temelso et al. [254] which we refer to as the UUU geometry. This system was optimised using the resolution-of-the-identity MP2 (RI-MP2) method [255; 256] with the aug-cc-pVDZ basis set. The second system was prepared by manually rotating a single water molecule around its centre to break the hydrogen bonding network, which we refer to as the UUU_{rot} geometry. These systems are displayed in Fig. 5.9. ONETEP EDA and EDD calculations were performed using a 800 eV psinc basis set cutoff energy and 8 Bohr NGWF radii using the PBE exchange-correlation functional.

5.3.5.2 Analysis

Table 5.6: The water trimer ONETEP EDA energy components using a 800eV basis set kinetic energy cutoff.

Energy term (kcal/mol)	Conformation	
	UUU	UUU_{rot}
FRZ	-2.3	4.1
ES	-23.9	-14.0
EX	-9.9	-8.7
REP	37.9	32.6
CORR	-6.4	-5.7
POL	-7.1	-4.4
CT	-6.3	-4.2
ΔE	-15.7	-4.5

EDD plots of the UUU and UUU_{rot} systems are displayed in Fig. 5.10 (polarisation) and Fig. 5.11 (charge transfer). The results of the EDA are displayed in Table 5.6.

The polarisation EDD plots show clearly symmetrical polarisation of electron density for the UUU system, and the restricted polarisation of the UUU_{rot} system. Generally, we observe that electron density is redistributed from the oxygen atom of each water molecule to the hydrogen involved in hydrogen bonding with the neighbouring water molecule during polarisation. Polarisation in the UUU_{rot}

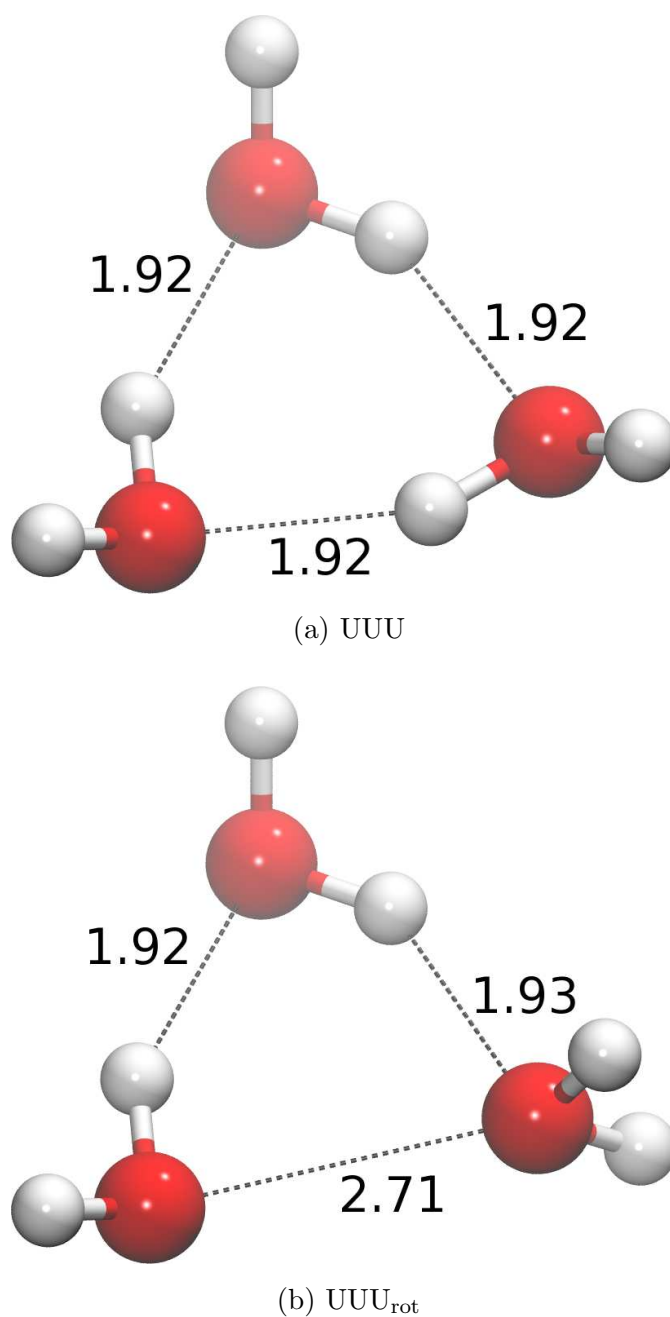


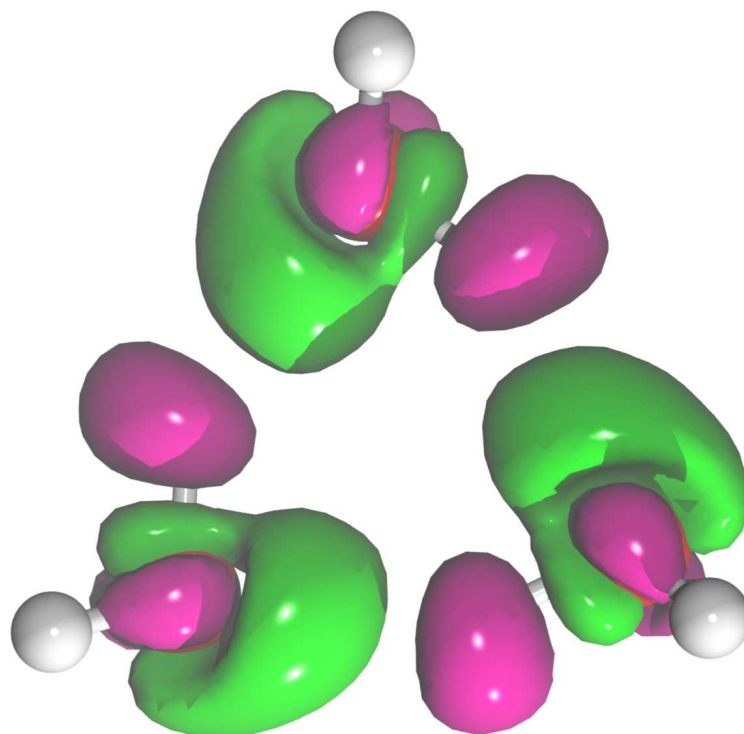
Figure 5.9: The (a) UUU and (b) UUU_{rot} water trimer test systems. Hydrogen bonding extends throughout the system in the case of the UUU system, but is broken between the lower water molecules in the case of the UUU_{rot} system.

system is limited by the unfavourable angle of the (lower right) rotated water molecule: polarisation of this rotated water is restricted to electron flows through the oxygen rather than the full molecule. This is not the case in the UUU system, in which electron density is able to migrate from the hydrogen atom in the direction of the O–H···O hydrogen bond. This observation is supported by the EDA

values, as we observe a much lower polarisation energy of -4.4 kcal/mol for the UUU_{rot} conformation compared with -7.1 kcal/mol for the UUU conformation.

Similarly, the charge transfer EDD plots display symmetrical charge transfer delocalisations for the UUU system, and limited delocalisations for the UUU_{rot} system. Three hydrogen bonds are clearly formed in the UUU system as shown by the presence of green isosurfaces in the region between the hydrogen and oxygen molecules of the neighbouring water molecules. In the UUU_{rot} system a hydrogen bond is not present between the lower two water molecules. This observation reflects the fact that the rotation of the lower right water molecule has broken the hydrogen bond. Bond formation between these molecules is unfavourable, as such a bond would effectively involve electron density redistributing between two δ^- oxygen atoms. Support of this observation is provided by the EDA values, in which we note a much lower charge transfer energy of -4.2 kcal/mol for the UUU_{rot} conformation, which corresponds to $2/3$ of the charge transfer energy (-6.3 kcal/mol) of the UUU conformation.

These EDD plots are useful for understanding the electron redistributions occurring through polarisation and charge transfer effects. Importantly, however, we also see notable differences in the frozen density analysis EDA values for which no EDD is computed. Here, we observe a 9.9 kcal/mol decrease in electrostatic stabilisation within the UUU_{rot} conformation which results in an overall repulsive frozen density component for this system (4.1 kcal/mol) compared to the UUU conformation. This is expected, as forming the UUU_{rot} conformation from its separated molecules involves an unfavourable dipole-dipole interaction between the lower two waters of this system. Additionally, we observe a decrease in Pauli repulsions for the UUU_{rot} conformation due to rotation of the hydrogen atom away from the intermolecular bonding region of the lower two water molecules. Despite the lack of an EDD plot analogue for the frozen density analysis, the EDD plots nonetheless show significant value for analysing the mechanisms driving bond formation.



(a) UUU

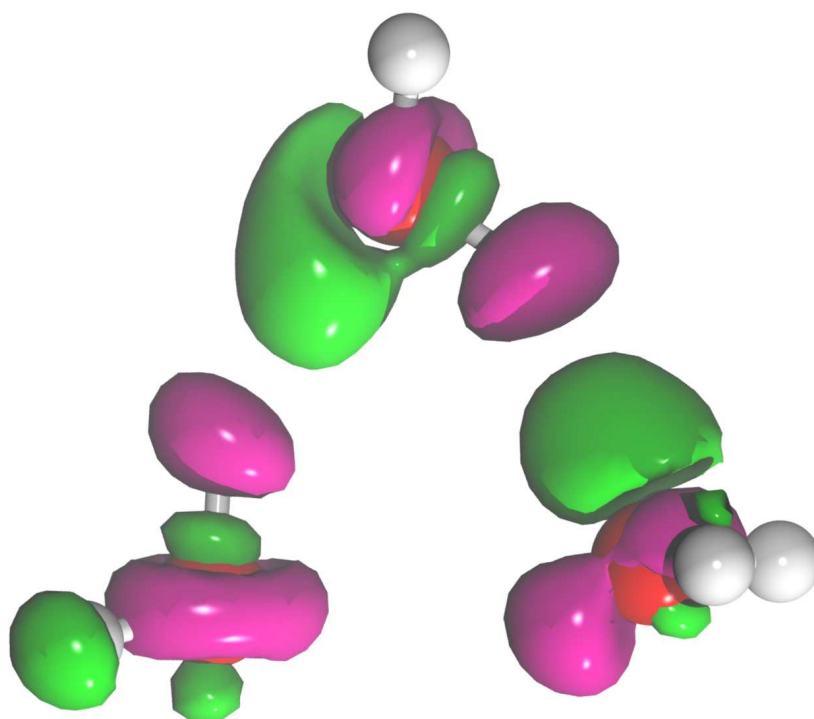
(b) UUU_{rot}

Figure 5.10: Polarisation EDD plots of the (a) UUU and (b) UUU_{rot} water trimer test systems calculated using the PBE exchange-correlation functional with an 800 eV psinc basis set cutoff energy and 8 Bohr NGWF radii. The isosurface contour levels are displayed at 0.01 electrons per cubic Angstrom with green surfaces representing electron gain and magenta surfaces representing electron loss

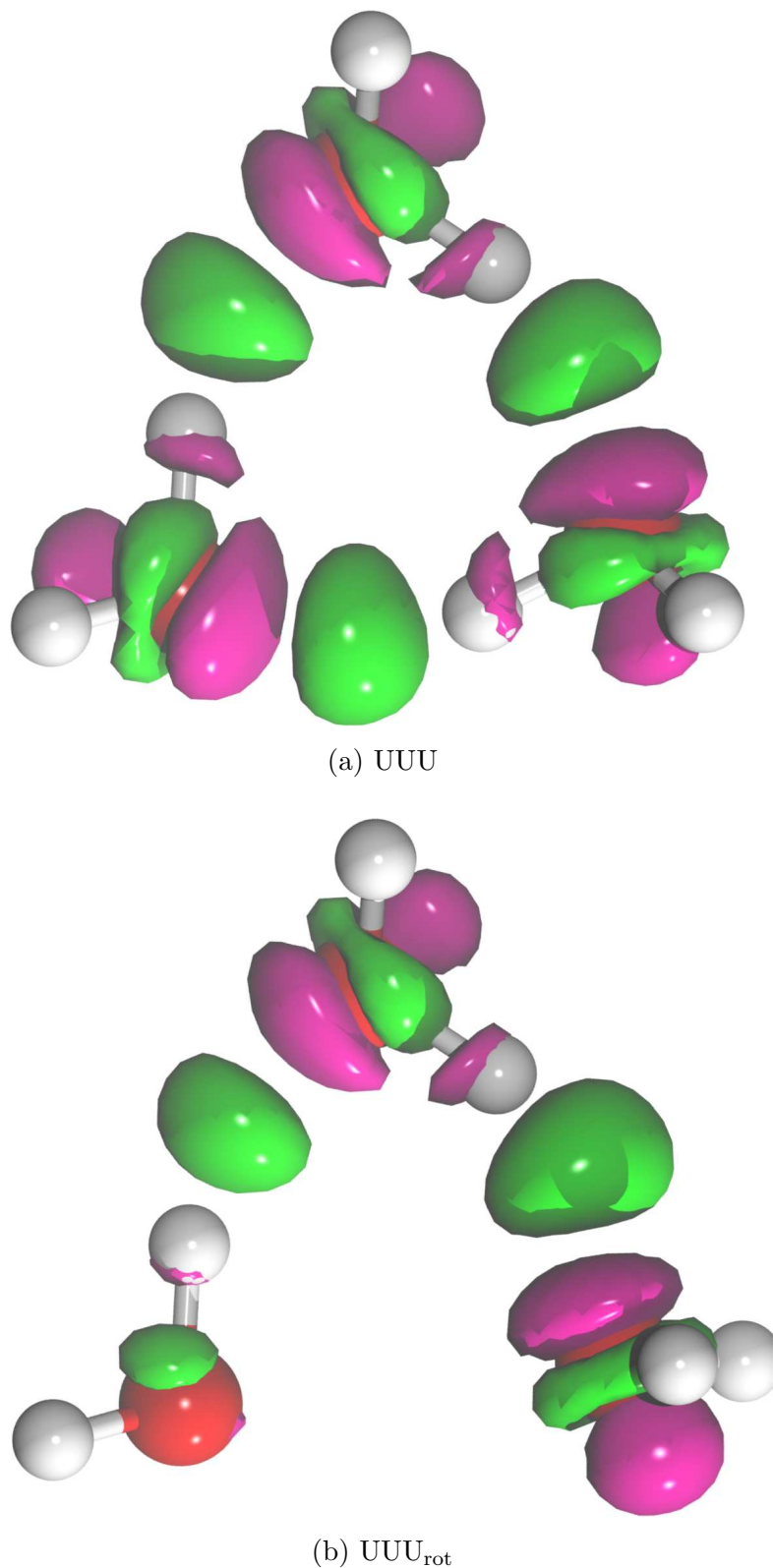


Figure 5.11: Polarisation EDD plots of the (a) UUU and (b) UUU_{rot} water trimer test systems calculated using the PBE exchange-correlation functional with an 800 eV psinc basis set cutoff energy and 8 Bohr NGWF radii. The isosurface contour levels are displayed at 0.01 electrons per cubic Angstrom with green surfaces representing electron gain and magenta surfaces representing electron loss

Chapter 6

Applications of the ONETEP energy decomposition analysis

In this chapter, we present a series of protein-ligand studies with the aim of demonstrating the high value of the information provided by the EDA method we have developed. In particular, we are interested in the success of the EDA in aiding understanding of the origins of the interaction energy both energetically and spatially.

Thrombin is a serine protease which plays a central role in the blood coagulation cascade [257]. The blood coagulation cascade refers to the series of reactions that result in the formation of insoluble fibrin by the action of thrombin on fibrinogen [258]



The inhibition of thrombin is therefore a key target in the treatment and prevention of thrombosis by delaying coagulation. We have applied the ONETEP EDA to the thrombin protein, which contains an active site consisting of three well-shaped pockets: S1, S2, and S3/4 [258].

In this chapter, we begin by demonstrating the EDA on the thrombin protein interacting with the C24 ligand, measuring the effect of protein truncation on the

EDA. We present EDD plots which show the key electron density redistributions involved in the polarisation and charge transfer effects to investigate the important regions of binding.

Following this, we identify the enthalpic contributions of specific protein-ligand regions to binding by partitioning a selection of thrombin ligands into fragments and calculating their EDA components. In this work, we also quantify an additivity error that measures the error due to ligand fragmentation. This is an important measure that provides an indication of the effect of our fragmentation approximation on the EDA results.

Lastly, we present a study of the interactions of small binders with the thrombin S1 pocket. The small binders studied are all less than 30 atoms in size and share many structural features. By selecting highly comparable binders for EDA, we are able to gain clear insight into the relative importance of specific features on the interaction energies we observe. We also combine this knowledge with our understanding of the key electron redistributions by EDD plot analysis.

6.1 Thrombin - C24

6.1.1 Calculations

We have analysed the bonding components of thrombin-inhibitor complex models using the ONETEP EDA, with varying degrees of protein truncation applied in order to enable measurement of EDA component convergence with protein model size. A brief description of these systems' preparation follows.

Four model systems at various truncation radii were prepared from the structure of the ligand C24 (shown in Fig. 6.1) bound to thrombin (pdb:1KTS) [251; 259]. The initial thrombin-inhibitor crystal structure was capped using COCH₃ and NHCH₃ groups ¹ and protonated using the Protonate3d software [253]. The protein side

¹Caps were placed at the Glu1C, Tyr14J, Thr147, Gly150 and Leu264 residues.

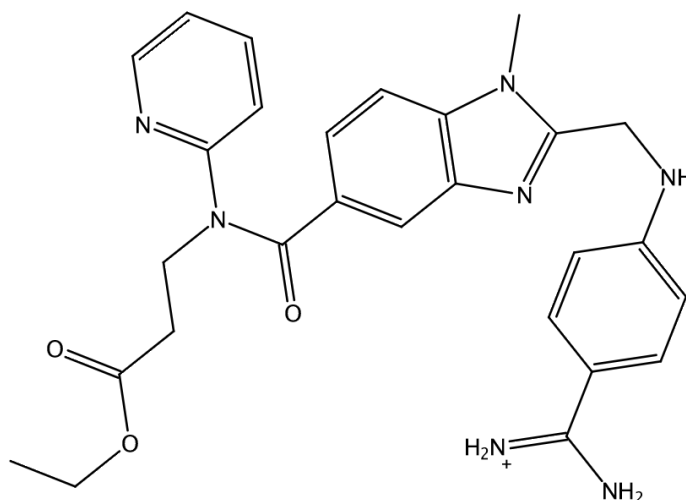


Figure 6.1: The C24 ligand (pdb:1KTS).

chains, caps and hydrogens were then optimised using the MMFF94x forcefield with the generalised Born implicit solvent (GBIS) model. The hirudin and its waters were subsequently removed from the system. This structure (referred to as the untruncated system) was then truncated to remove residues beyond various distances (3\AA , 9\AA , 15\AA) from the ligand. Caps (COCH_3 and NHCH_3 groups) were then added to the resulting protein fragments. The structures were then reprotonated and any bond clashes introduced by capping removed by further geometry optimisation (MMFF94x, GBIS) of the caps and the hydrogens. ONETEP EDA was performed on the resulting thrombin-C24 systems using a 800 eV psinc basis set cutoff energy and 8 Bohr NGWF radii at the PBE-D2 level of theory. A summary of the protein models and EDA fragment definitions is given in Table 6.1 and visualisation of the protein binding pocket in Fig. 6.2.

Table 6.1: A summary of the fragments of the thrombin-C24 complexes used in the ONETEP EDA, where ‘ ∞ ’ refers to the full, untruncated protein (charges given in parenthesis).

Protein Truncation	Fragment atom count		
	Protein and solvent	Ligand	Supermolecule
3\AA	374 (-1)	67 (+1)	441 (0)
9\AA	1328 (-1)	67 (+1)	1395 (0)
15\AA	2621 (+1)	67 (+1)	2688 (+2)
∞	4908 (+2)	67 (+1)	4975 (+3)

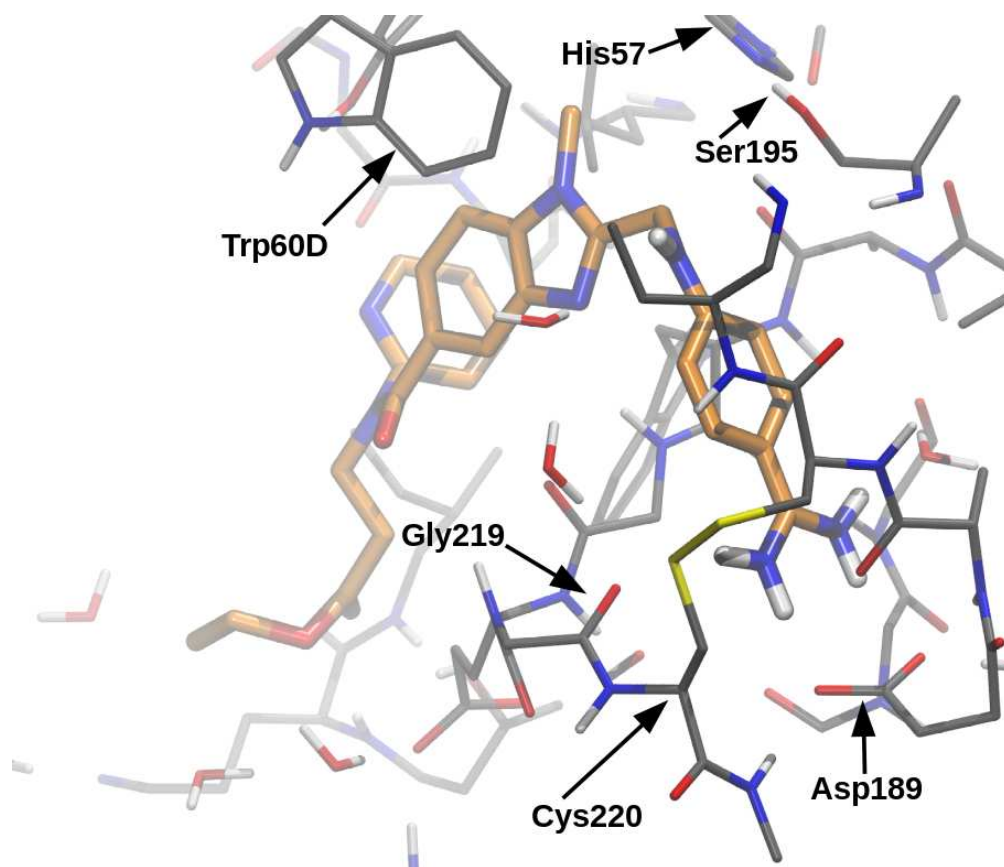


Figure 6.2: The binding pocket of the untruncated (4975 atom) protein system. The C24 ligand has been highlighted in orange.

6.1.2 Analysis

Values of the ONETEP EDA components and their convergence with respect to the untruncated protein system are shown in Fig. 6.3 and Fig. 6.4 (energy values are provided in Table C.1 of the Appendix). The EDA components show a significant electrostatic contribution (-150.3 kcal/mol) to ΔE , reflecting the strong influence of the charged Asp189 residue interacting with the positively charged amidine of the ligand. The total contribution of exchange (-53.7 kcal/mol) and correlation (-63.6 kcal/mol) is shown to provide almost as much stability to binding as electrostatics. Stabilisation from electrostatics, exchange and correlation is however largely countered by steric Pauli-repulsion effects (228.7 kcal/mol). Polarisation (-33.1 kcal/mol) is of similar magnitude to charge transfer (-31.2 kcal/mol), reflecting the balanced contribution of these effects to binding. A significant contribution to binding is provided by Grimme's -D2 correction for dispersion

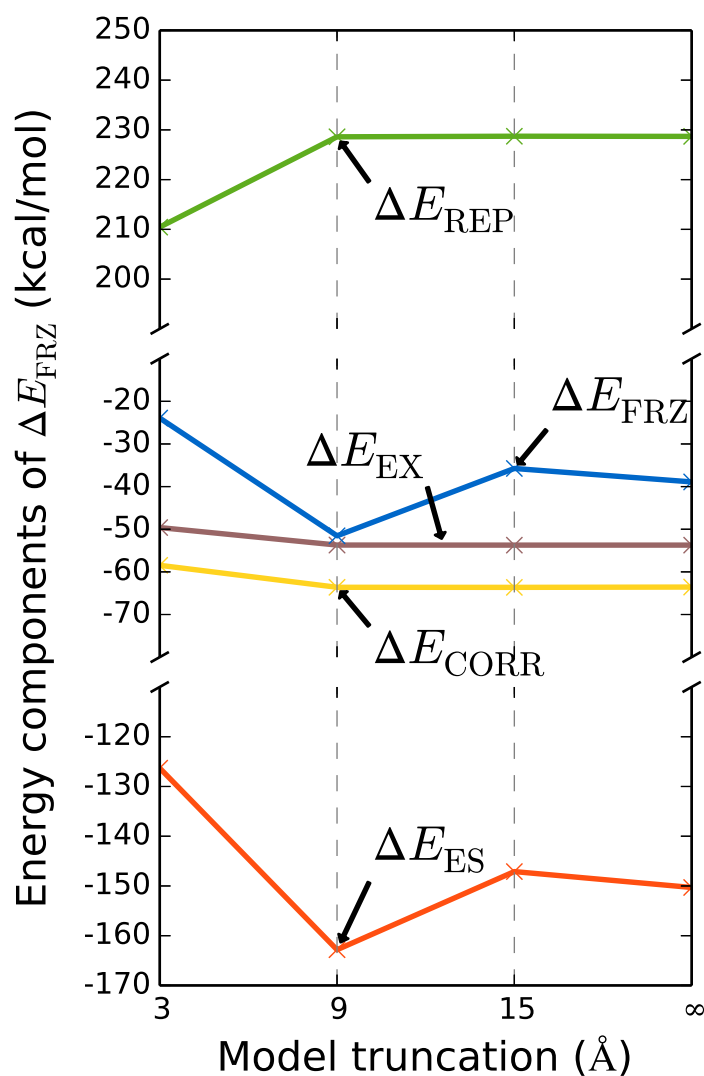


Figure 6.3: Frozen density analysis of the thrombin-C24 complexes calculated at the PBE-D2/800 eV level of theory (component values are given in kcal/mol). Error of the energy components is shown with respect to the full, untruncated (4975 atom) protein system. The frozen density component is formally equivalent to adding the electrostatic, exchange, Pauli-repulsion and correlation energy components as shown in Eq. 5.6

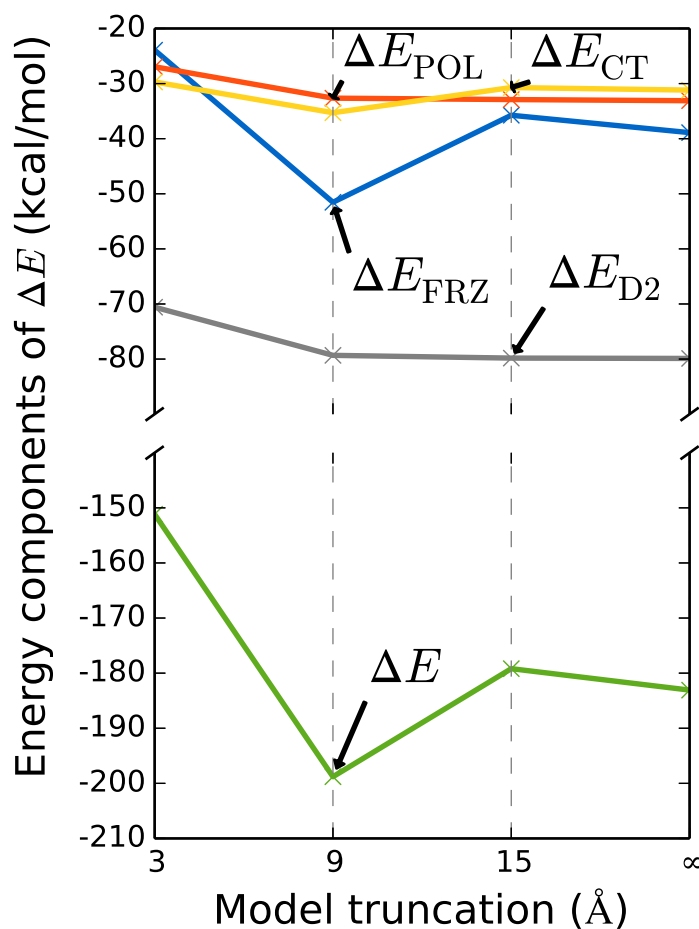


Figure 6.4: EDA components of the thrombin-C24 complexes calculated at the PBE-D2/800 eV level of theory (component values are given in kcal/mol). Error of the energy components is shown with respect to the full, untruncated (4975 atom) protein system. The full interaction energy ΔE is equivalent to adding the frozen density component, polarisation, charge transfer, and Grimme -D2 dispersion energy components.

(-79.9 kcal/mol) which arises due to the many long-range contributions over the large number of atoms in the protein.

Convergence of the exchange, Pauli-repulsion and correlation components is reached between 3\AA and 9\AA truncation, with full convergence of electrostatics observed between 15\AA truncation and the full protein. The large truncation radius required for convergence of electrostatics is likely due to differences in the charge distributions within the truncated proteins and the long-range nature of electrostatics, and is interesting to observe as in molecular mechanics descriptions electrostatics are often truncated at around $9\text{-}10\text{\AA}$ [260; 261]. Polarisation and dispersion are shown to converge smoothly with reduced protein truncation, with charge transfer displaying a similar convergence profile to the frozen density component and electrostatics. Again, the similar convergence profile of charge transfer may be an indication of differences in the protein charge distributions at the different truncation levels. Overall, our results indicate heavy protein truncation to have the potential to adversely affect the outcome of the EDA values. Minimal truncation of protein models is therefore shown to be necessary to ensure convergence of the EDA components.

Qualitative descriptions of intra- and inter-fragment delocalisations are provided by electron density difference (EDD) plots [89] (Fig. 6.5 and 6.6). EDD plots are constructed as electron density differences between intermediate states of the EDA procedure. The polarisation EDD is calculated by subtracting the electron density corresponding to the frozen density state from the polarised state electron density. Similarly, the charge transfer EDD is calculated by subtracting the electron density corresponding to the polarised state from that of the fully (electronically) relaxed state. Earlier work has demonstrated the high value of these plots in drug design, for example by application to HIV-1 protease inhibitors by Hensen et al. [262] and to δ -opioid models by Mo et al. [263] using the BLW EDA.

The EDD plots of the 3\AA truncated and untruncated systems both display the

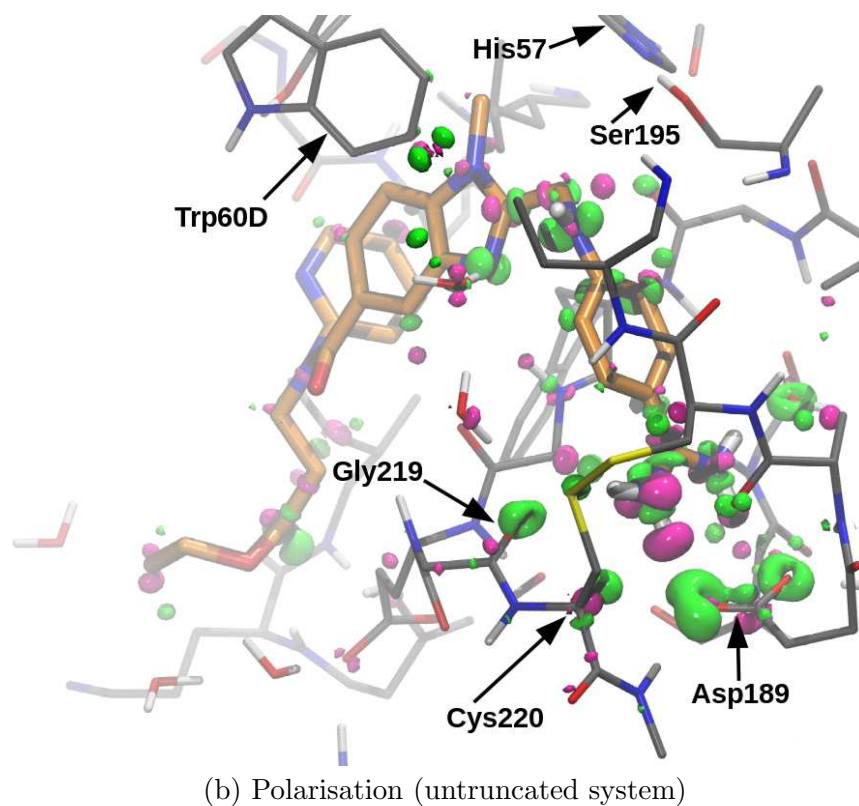
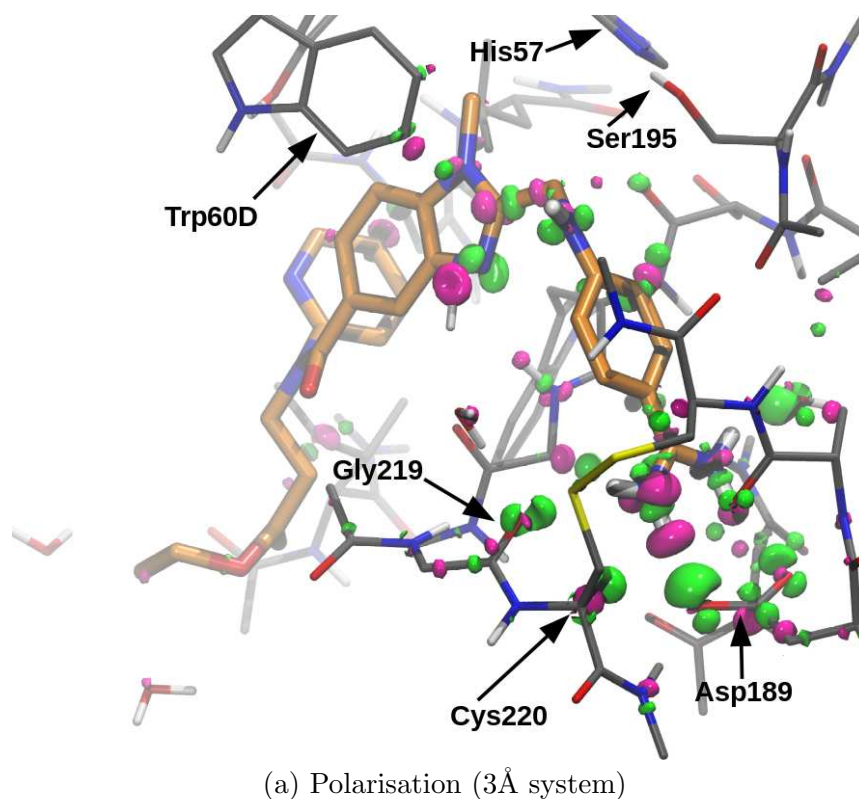
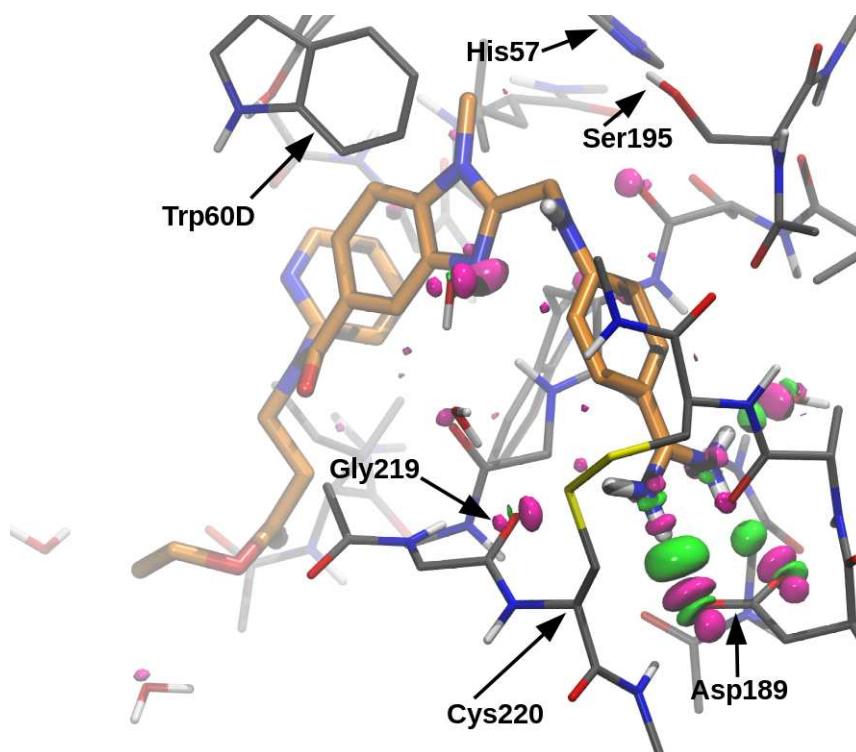
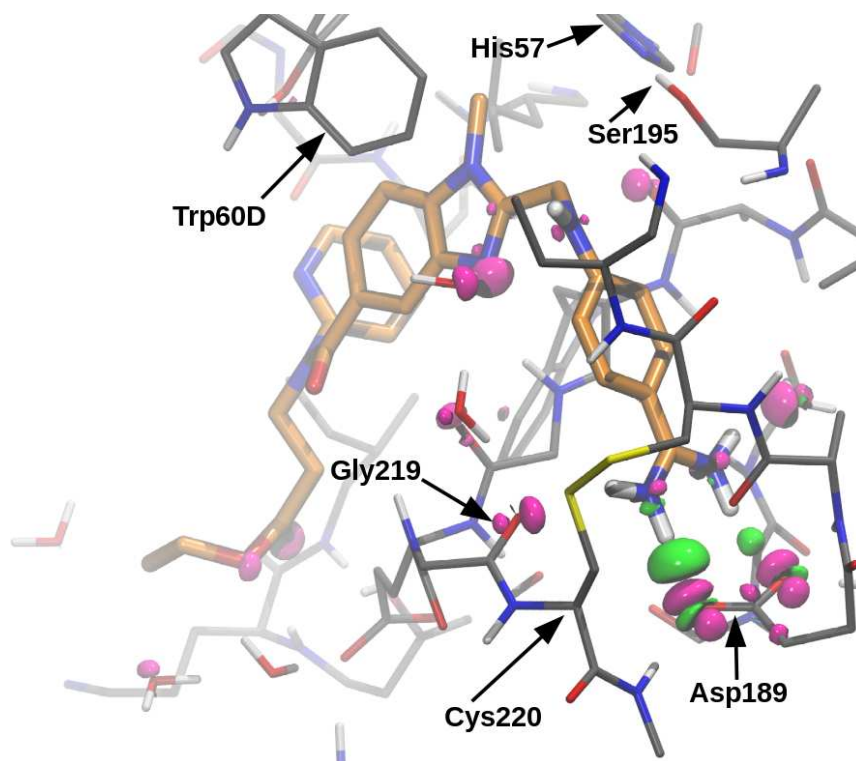


Figure 6.5: EDD plots of polarisation for the (a) 3 Å system and (b) untruncated system. The isosurface contour levels are displayed at 0.0175 electrons per cubic Angstrom with green surfaces representing electron gain and magenta surfaces representing electron loss. The C24 ligand has been highlighted in orange. The EDD plots show the contributions of functional groups to polarisation and charge transfer.



(a) Charge transfer (3Å system)



(b) Charge transfer (untruncated system)

Figure 6.6: EDD plots of charge transfer for the (a) 3Å system, and (b) untruncated system. The isosurface contour levels are displayed at 0.0175 electrons per cubic Angstrom with green surfaces representing electron gain and magenta surfaces representing electron loss. The C24 ligand has been highlighted in orange. The EDD plots show the contributions of functional groups to polarisation and charge transfer.

key polarisation and charge transfer interactions. Overall, polarisation is demonstrated as an important effect with charge transfer interactions involved in the formation of the many hydrogen bonds observed. Electron density is observed to gather in the carboxylate of Asp189 through polarisation effects, with bond formation to the amidine group of the C24 ligand being observed in the charge transfer EDD plot. The Gly219 and Cys220 residues of the protein are also shown to interact with the amidine group of the ligand. For these two residues minor differences are observed between the 3Å truncated and untruncated systems in the nature of the charge redistributions through polarisation effects. In addition to interactions of the protein with the ligand, notable interactions involving water molecules are also observed, specifically with the ligand's amidine and 1-methylbenzimidazole functional groups. These interactions highlight the importance of solvent participation in ligand-protein binding. Overall, the 3Å and infinite cutoff EDD plots (for both polarisation and charge transfer) appear qualitatively very similar. Thus the 3Å description is sufficient for qualitative and visual interpretations. For accurate energy components however, the 15Å description is needed as we saw in the previous section.

EDD plots are shown to be an important tool for visualising the key interactions that are responsible for the polarisation and charge transfer energies and allow us to associate these energies with particular functional groups. For example it can be seen that during the polarisation stage charge is redistributed in Asp189. Then during charge transfer, charge delocalises to the amidine group of the ligand, clearly showing the formation of bonding in this ion pair. Thus the value of such plots can be very high for assisting in the fine-tuning of drug-protein interactions.

6.2 Thrombin - small fragmented binders

In this section, we investigate the important enthalpic contributions to protein binding provided by key regions of ligands of pharmaceutical interest using small fragment binder molecules and the ONETEP EDA method. Our fragment based study is arranged in two subsections, with all structures prepared using similar protocols.

In the first subsection, we partition a selection of thrombin ligands into small fragments and analyse the chemical information provided by their energy components. Our motivation for this study is to measure the reproducibility of the ligand binding components when fragmented into specific subregions, and to understand the usefulness of the information provided by these fragments' energy components. Here, we quantify the error associated with the fragmentation process. This is achieved by calculating an 'additivity error' that is the energetic difference between the total fragment contributions (to a particular EDA component) and the full, unfragmented ligand contribution.

In the second subsection, we seek to investigate the usefulness of EDA for identifying important functional group interactions in drug binding. Here, we apply our EDA approach to a series of small fragments that bind to the S1 pocket of thrombin that contains a number of key interactions. By considering simple fragment binders that have the potential to be used as building blocks of larger ligands, we aim to be able to more easily rationalise and understand the interaction driving forces involved in the larger ligands themselves.

6.2.1 Calculations

The ability to observe differences in structural features of ligands is of key importance within this work. For this reason, thrombin-inhibitor binders were taken from the literature of Rühmann [258] and Baum [264] based on their high suitability for structural comparison (i.e. the ligands are structurally different, but

not so dissimilar as to prevent comparison). The pdb codes of the structures selected for fragmentation were 4UDW [258], 2ZGX [264], and 5AFZ [258], and the pdb codes of the structures selected for the S1 pocket analysis were 4UD9 [258], 5AFY [258], 5AHG [258], 5AF9 [258], 4UEH [258], and 4UE7 [258] (downloaded from the Protein Data Bank [251]).

The following protocol was used to prepare the protein structures for EDA. The missing 7-loop² of each of the initial thrombin-inhibitor crystal structures was built using MOE homology modelling suite. Each structure was then capped using COCH₃ and NHCH₃ groups, and protonated using the Protonate3d software [253]. The structures were energy minimised using the MMFF94x forcefield with the generalised Born implicit solvent (GBIS) model using a tethering force constant of $(3/2)kT/\sigma^2$ ($\sigma = 0.5\text{\AA}$) for all atoms during the minimisation. The hirudin and all waters (excluding the water molecules³ involved in the S1 pocket salt bridge interaction) were subsequently removed from the systems. These structures were then truncated to remove residues beyond 15Å of the ligand, and further truncated to ensure consensus of the protein residues across all of the systems. Further capping of the cleaved backbone of the structures was performed using COCH₃ and NHCH₃ groups. In this work, the systems produced from this protocol are referred to as the reference structures, and their ligands are referred to as the reference ligands.

In the ligand fragmentation study (4UDW, 2ZGX, and 5AFZ complexes), the reference ligands were further partitioned into fragments that interact with particular regions of the thrombin active site. Specifically, we have selected fragments with index F1 to interact with the S1 pocket, F2 with the S2 pocket, and F3 to interact with the S3/4 pocket. Details of the ligand fragmentation positions are shown in Fig. 6.7. To partition the ligands into fragments, the selected bonds were cleaved and the missing bonding atom(s) replaced with hydrogen atom(s). ONETEP

²The 7-loop refers to the missing residues Trp147A, Thr147B, Ala147C, Asn147D, Val147E, Gly147F, and Lys147G.

³Water molecules involved in the Asp189 salt bridge interaction were retained in the 2ZGX, 5AFZ, 4UE7, and 4UEH systems.

EDA was performed on the resulting thrombin-fragment and thrombin-reference ligand systems using a 800 eV psinc basis set cutoff energy and 8 Bohr NGWF radii at the PBE-D2 level of theory. Additionally, desolvation energies ΔE_{desolv} were calculated for the ligands at the same level of theory using the ONETEP solvation model [265]. This is a fully self-consistent model based on direct solution of the non-homogeneous Poisson equation. The ligand desolvation energies were added to ΔE to attempt to capture the cost of the ligand leaving the water environment to bind to the receptor pocket.

To quantify the error introduced through fragmentation of the ligands, an ‘additivity’ error is defined for each of the reference ligands’ energy components. This quantity is expressed as

$$\Delta E_{\text{err},Y}(X) = \Delta E_Y(X) - \sum_{A \in X}^{N_{\text{frag}}} \Delta E_Y(A) \quad (6.2)$$

where $\Delta E_Y(X)$ is the value of the EDA energy component Y for the reference ligand X protein interaction, and $\Delta E_Y(A)$ is the value of the EDA energy component Y for the fragment A protein interaction (where fragment A is a constituent of the reference ligand X).

6.2.2 Analysis: ligand fragmentations

In this section, we analyse the binding of the 4UDW, 2ZGX, and 5AFZ reference ligands and their fragments with thrombin. The structures of these ligands are shown in Fig. 6.7. Plots of the EDA components are displayed in Fig. 6.8 and Fig. 6.9, and EDD plots are shown in Figs. 6.11–6.13. Energy component values are also provided in Table D.1 of the Appendix.

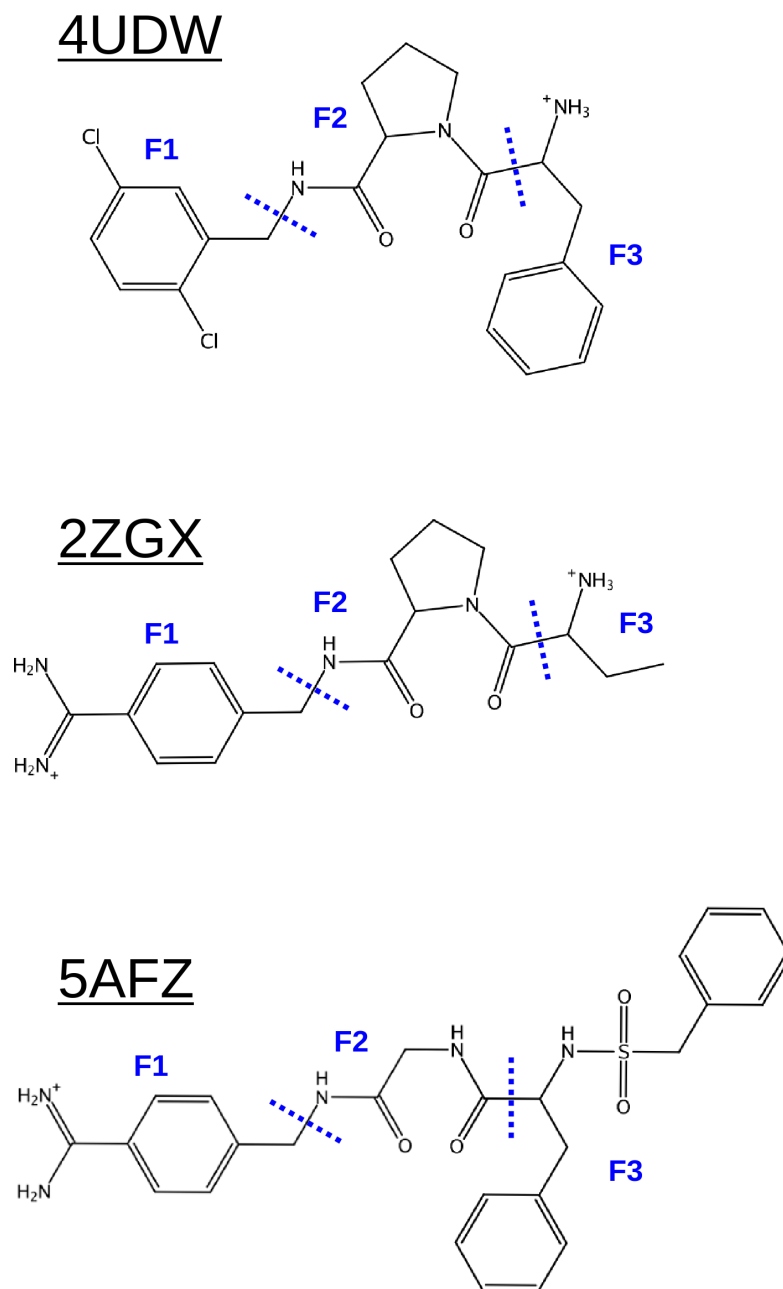


Figure 6.7: The ligand fragmentation scheme for the 4UDW, 2ZGX, and 5AFZ ligands. The bond partitions of the ligands are shown by the dashed blue lines, with each fragment produced capped with a hydrogen atom. The F1, F2, and F3 ligands refer to the fragment indexes 1, 2, and 3.

6.2.2.1 Frozen density component

We begin our discussion by noting the important role of electrostatics, and in particular those arising from the fragment charges, as a factor in determining the overall ΔE . Electrostatics were observed to play a key role in the interaction of

C24 with thrombin discussed earlier (Section 6.1). In this system, the positively charged amidine moiety interacts strongly with the negatively charged Asp189 residue of the protein, giving rise to a significant electrostatic interaction energy. The stability provided through this interaction is expected to have provided a significant proportion of the electrostatic contribution (-150.3 kcal/mol). In the F1 fragments of the 2ZGX and 5AFZ systems considered here, a similar amidine-Asp189 interaction is observed. Importantly, here we are able to determine the individual contributions of ligand functional groups to binding, and can quantify the contribution of the amidine-Asp189 interaction. Here we observe total electrostatic components of -208.3 kcal/mol (2ZGX) and -169.7 kcal/mol (5AFZ) for the full reference ligand, with the F1 fragments each contributing -129.2 kcal/mol and -135.7 kcal/mol respectively to these values (Fig. 6.8). From this, we are able to conclude that this salt bridge interaction contributes well over half of electrostatics in these systems.

It is important, however, to consider the accuracy of the fragmentation process that underlies this conclusion. Notably, we observe a 6.5 kcal/mol difference in electrostatics for the F1 fragments of the 2ZGX and 5AFZ systems despite these fragments sharing identical chemical structures. Errors in the electrostatic component due to fragmentation (calculated using Eq. 6.2) are < 1 kcal/mol and are therefore unlikely to be significant factors in this difference. Therefore this difference, representing a $\pm 2.5\%$ error from the mean, arises from variances in the structural geometries. Specifically, the negatively charged Glu192 residue is much closer to the benzene ring in the 5AFZ when compared to the 2ZGX system. As well as minor difference in the EDA components of the F1 fragments of the 2ZGX and 5AFZ systems attributable to geometric differences, we also observe differences in the energy components for the F2 fragments of the 2ZGX and 4UDW structures. This is also initially surprising as these fragments are structurally identical (the superposition of these fragments is shown in Fig. 6.10). On closer inspection, however, we see that this difference also likely arises due to similar differences in the Gly192 geometry. These observations demonstrate that care must be taken

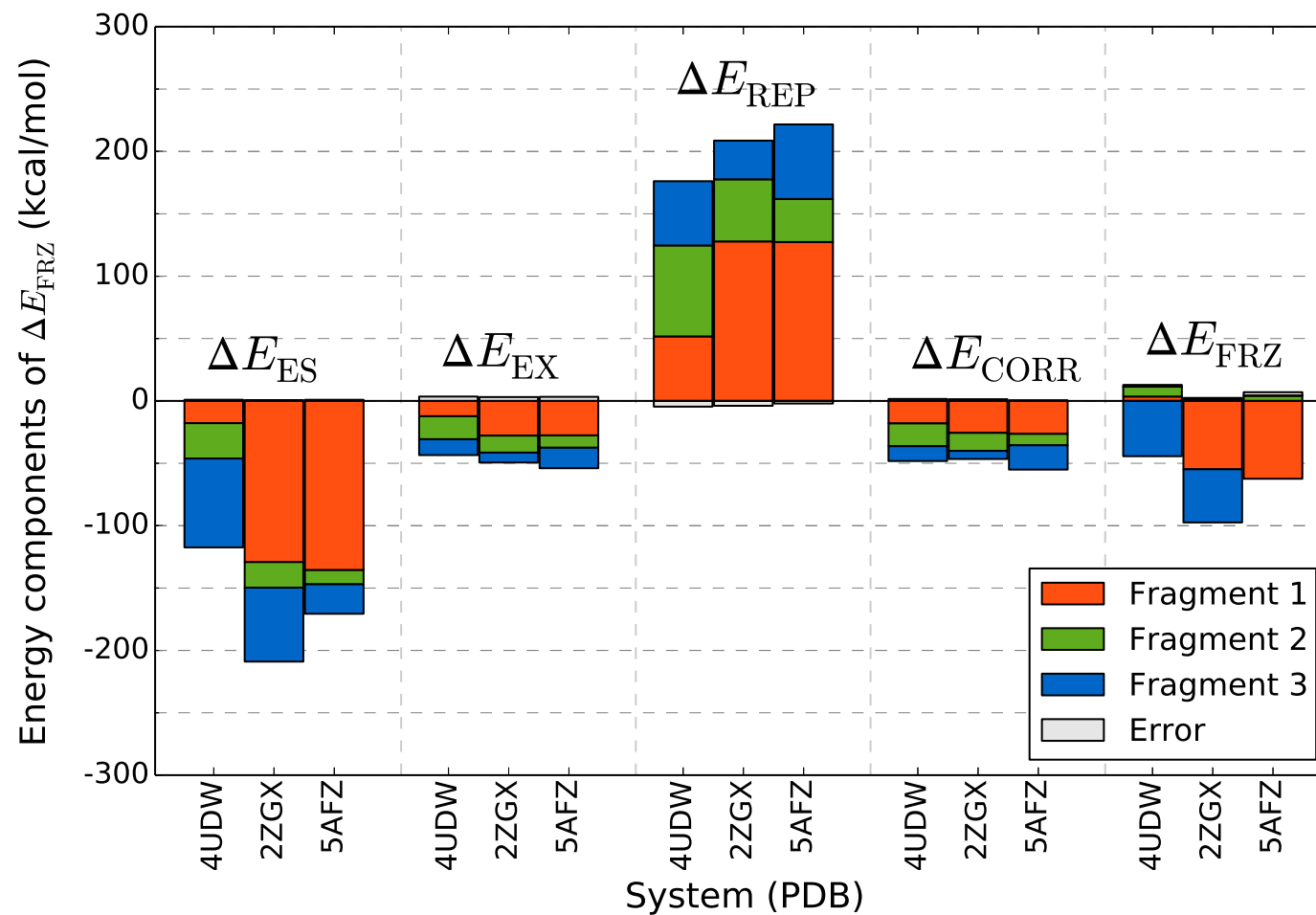


Figure 6.8: Frozen density analysis of the fragmented 4UDW, 2ZGX, and 5AFZ complexes calculated at the PBE-D2/800 eV level of theory (component values are given in kcal/mol). F1, F2, and F3 refer to the fragments that compose the full reference ligand. For each energy component, the fragmentation error equals the sum of the fragment contributions subtracted from the contribution of the full reference ligand (Eq. 6.2).

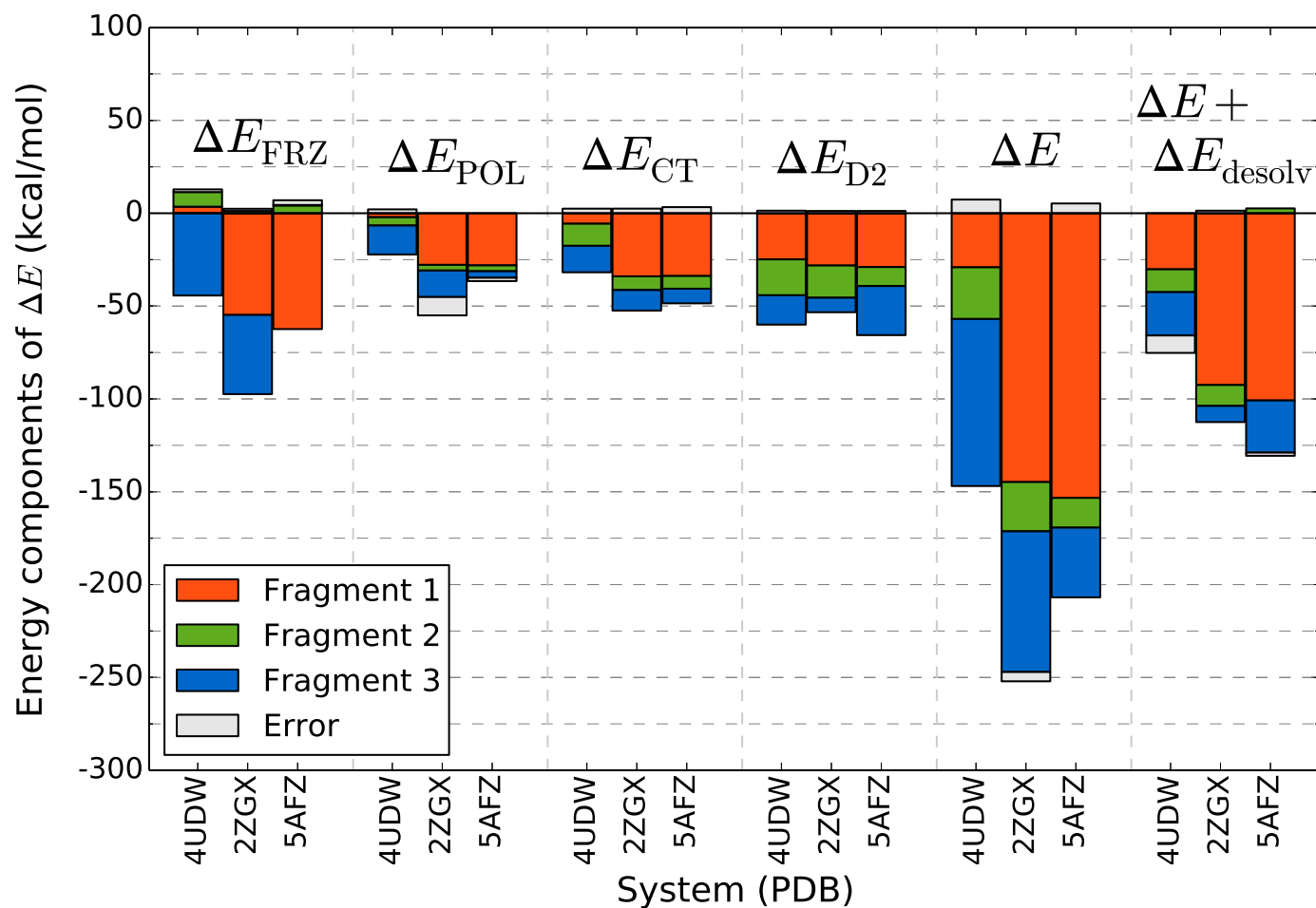


Figure 6.9: EDA components of the fragmented 4UDW, 2ZGX, and 5AFZ complexes calculated at the PBE-D2/800 eV level of theory (component values are given in kcal/mol). D2 refers to the dispersion energy correction of Grimme. F1, F2, and F3 refer to the fragments that compose the full reference ligand. For each energy component, the fragmentation error equals the sum of the fragment contributions subtracted from the contribution of the full reference ligand (Eq. 6.2). The total ΔE in combination with the cost of ligand desolvation ΔE_{desolv} is also shown.

drawing conclusions from EDA results using a single structure. It is expected that improvements in the accuracy of EDA results would be made by computing averages of EDA component values using snapshots taken from molecular dynamics simulations.

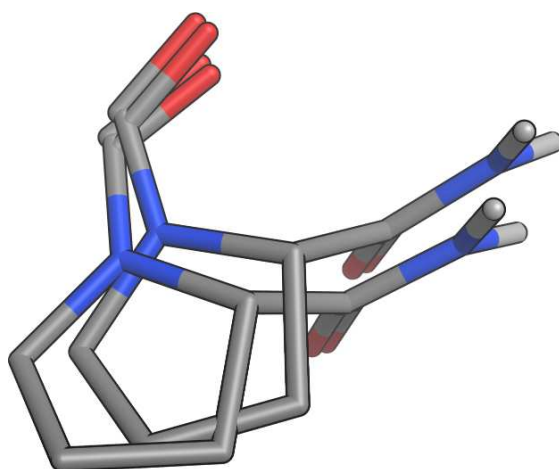


Figure 6.10: Superposition of the 4UDW and 2ZGX F2 fragments.

We also note the importance of electrostatics in the F3 fragments of 4UDW and 2ZGX. These fragments are also charged, and we expect that important stabilising contributions arise through interaction of the charged amine group with the Gly216 oxygen. Evidence of the importance of this $\delta^+\text{NH}\cdots\text{OC}$ interaction in stabilising polarisation and charge transfer is also shown in Figs. 6.11 and 6.12. The stability provided to these fragments by electrostatics is -71.2 kcal/mol (4UDW) and -59.3 kcal (2ZGX). The additional 11.9 kcal/mol stability gain in 4UDW is due to the presence of benzene in this fragment (see Fig. 6.7). This additional benzene, relatively isolated from charged residues, enhances electrostatics and dispersion significantly more than the polarisation or charge transfer interactions. This is reflective of the fact that the electrostatic and dispersion interactions occur over much longer ranges than charge transfer and polarisation effects.

Overall, the fragment charge is observed to play a significant role in determining the frozen density component. For 4UDW and 5AFZ, each containing one charged fragment, the frozen density component is stabilised significantly by its charged fragment (-44.3 kcal/mol by F1 of 4UDW, and -62.4 kcal/mol by F1 of 5AFZ).

For 2ZGX, containing two charged fragments, the frozen density component is stabilised by similar amounts through each of its charged fragments (-54.8 kcal/mol by F1 and -42.6 kcal/mol by F3). The 2ZGX and 5AFZ F1 fragments gain significant electrostatic stabilisation through salt bridge formation with the Asp189 residue, but at the cost of high Pauli repulsions. The 4UDW F1 fragment is unable to form this interaction, and instead the interaction with the protein occurs primarily through long range dispersion effects as shown by the EDA components. For this reason, electrostatics in the 2ZGX and 5AFZ fragments are approximately 114.7 kcal/mol more stabilising than in the 4UDW fragment. In fact, this electrostatic stabilisation provided by the 2ZGX and 5AFZ fragments is greater than the total electrostatic stabilisation provided by the whole of the 4UDW ligand. A high Pauli repulsions penalty is paid (approximately 75.9 kcal/mol) to enable this high electrostatic stabilisation (and additionally the short range polarisation and charge transfer stabilisations). This observation highlights the importance of sterics when suggesting modifications for drug design.

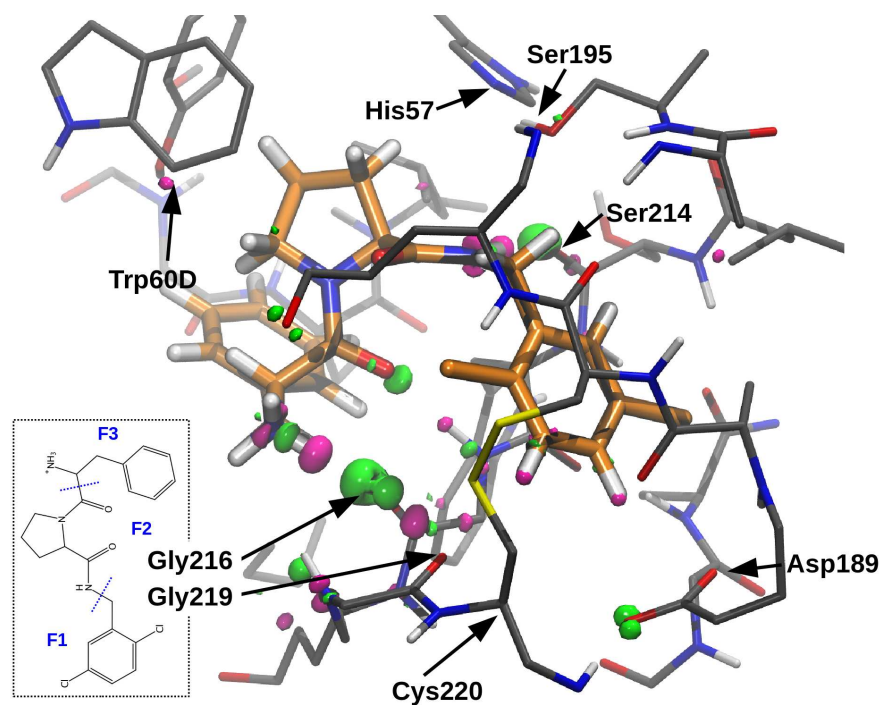
The fragment exchange and correlation contributions to ΔE are largely determined by the fragment sizes and proximity to the protein. For example, exchange and correlation are shown to respectively contribute -7.9 kcal/mol and -6.5 kcal/mol stability to ΔE in the F3 fragment of the 2ZGX system. As we would expect, in the larger and more closely interacting F3 fragment of 4UDW exchange and correlation are also greater (-12.7 kcal/mol and -11.9 kcal/mol respectively). For the full reference ligand, the contributions of exchange and correlation (up to -50.7 kcal/mol and -54.6 kcal/mol respectively) are comparable to the contributions of polarisation (up to -55.0 kcal/mol) and charge transfer (up to -50.0 kcal/mol). These effects therefore contribute important driving forces to binding. However, the range of these values is relatively small for exchange (10.8 kcal/mol) and correlation (8.0 kcal/mol) when compared with the ranges for polarisation (34.9 kcal/mol), and charge transfer (20.7 kcal/mol). Additionally, the fragmentation error associated with exchange is consistently positive (3.1 kcal/mol to 3.5 kcal/mol), indicating that the fragment contributions slightly overestimate the stabilisation

provided through exchange. This error is also moderately large when considering that this represents a 6.5-8.8% exchange contribution unattributable to any particular fragment. Overall, differences in the exchange and correlation contributions are therefore less distinct and the origins of these components less easily attributable than the other energy components. Nonetheless, it is possible to identify certain useful key observations. For example, we observe a slightly larger correlation energy for the F1 fragment of 4UDW (-18.0 kcal/mol) than might be expected when compared to the other systems. This is due to the presence of chlorine atoms in this fragment, which through their more diffuse and larger electron clouds enhance the overall fragment contribution to correlation. This argument may also be used to rationalise the enhanced dispersion contribution seen for this fragment.

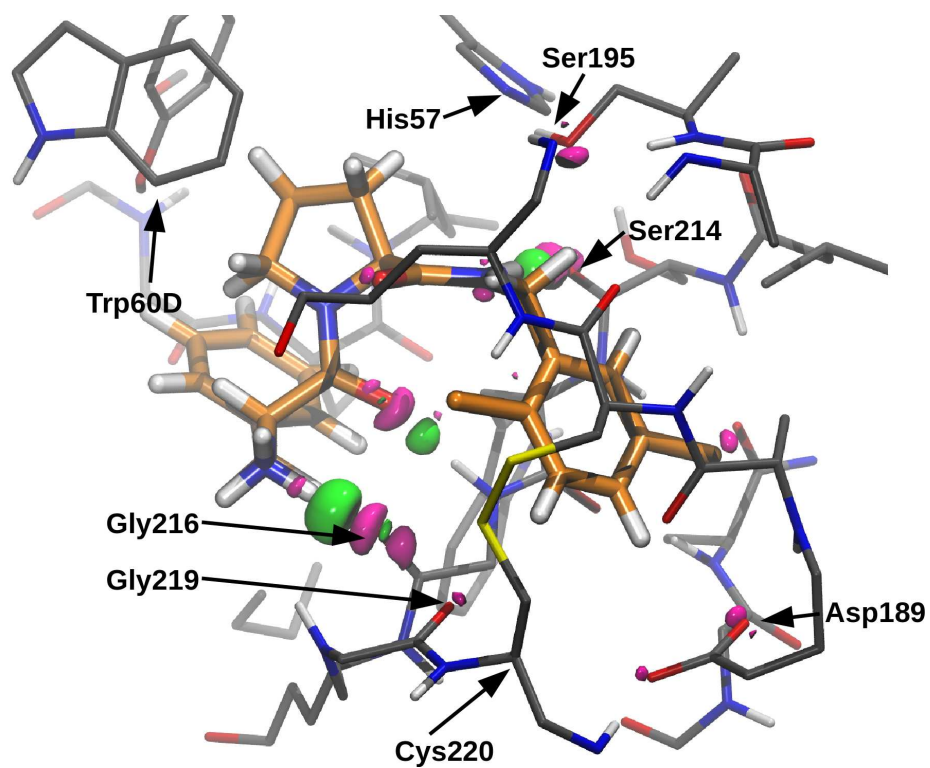
6.2.2.2 Polarisation, charge transfer and dispersion

Here we consider the polarisation and charge transfer EDA components for the fragmented systems through their values and EDD plots shown in Figs. 6.11 to 6.13.

We begin by noting the significant contributions by the F1 fragments of 2ZGX and 5AFZ to ΔE through polarisation and charge transfer. These fragments contribute a total polarisation and charge transfer ($\Delta E_{\text{POL}} + \Delta E_{\text{CT}}$) of -61.8 kcal/mol and -61.9 kcal/mol respectively. This strong interaction is due to the salt bridge interaction with Asp189, with contributions also observed from Gly219 and Cys220 and the water molecule in this pocket. In these plots, charge is seen to gather at the Asp189 oxygens by attraction of the positively charged amidine group of the ligand. Simultaneously, charge density is repelled away from the amidine group hydrogen atoms in the direction of the benzene ring. Two hydrogen bonds are subsequently formed by proton donation from the amidine group to the Asp189 residue, as shown in the charge transfer EDD plot (Fig. 6.13). The interactions

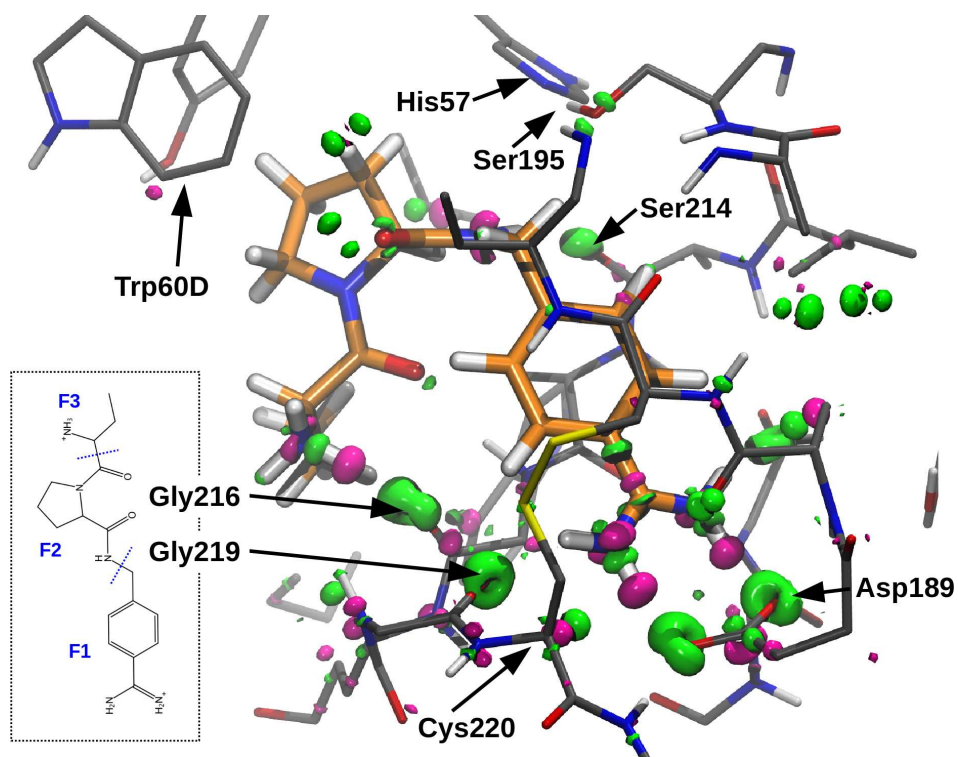


(a) Polarisation

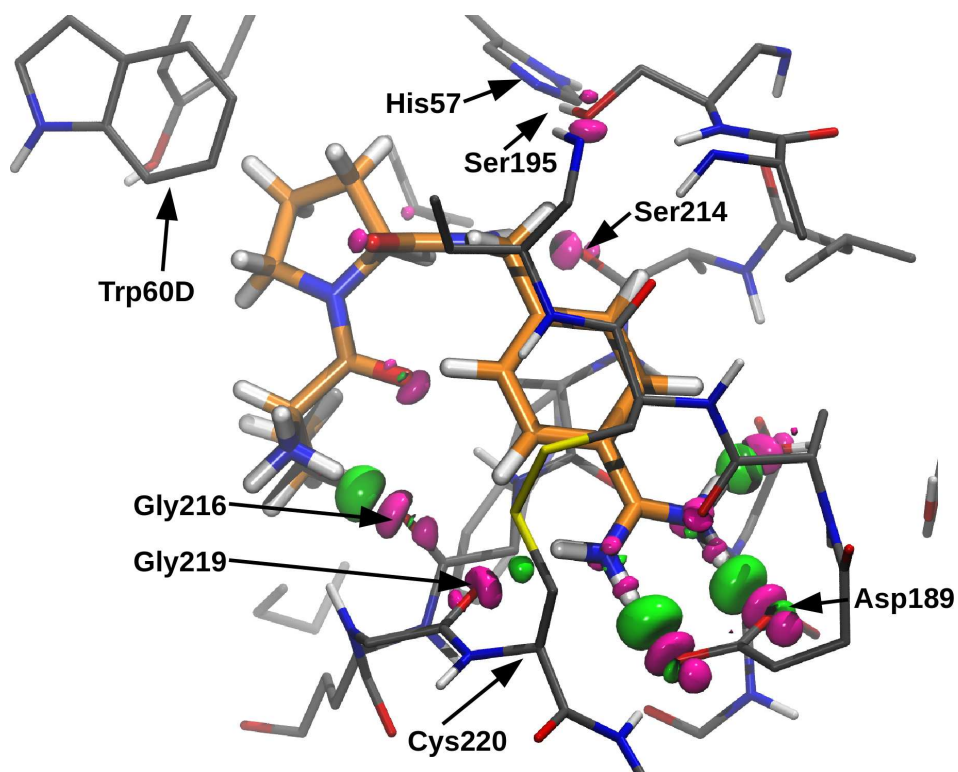


(b) Charge transfer

Figure 6.11: EDD plots of (a) polarisation and (b) charge transfer for the 4UDW system. The isosurface contour levels are displayed at 0.025 electrons per cubic Angstrom with green surfaces representing electron gain and magenta surfaces representing electron loss. The ligand of the 4UDW system has been highlighted in orange.

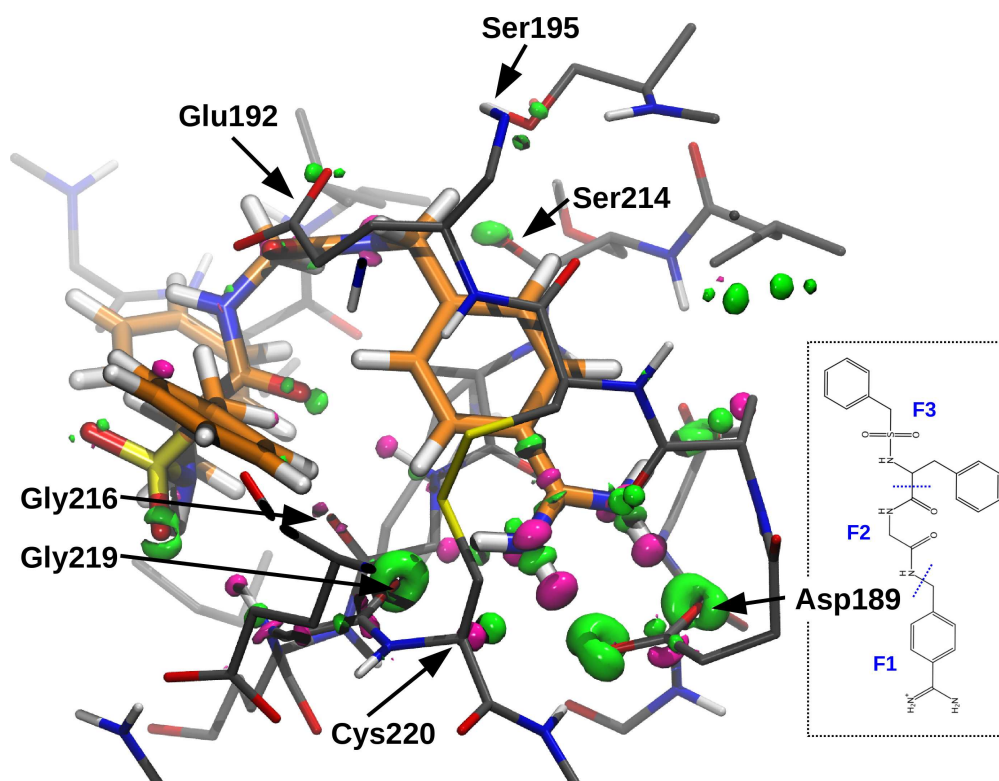


(a) Polarisation

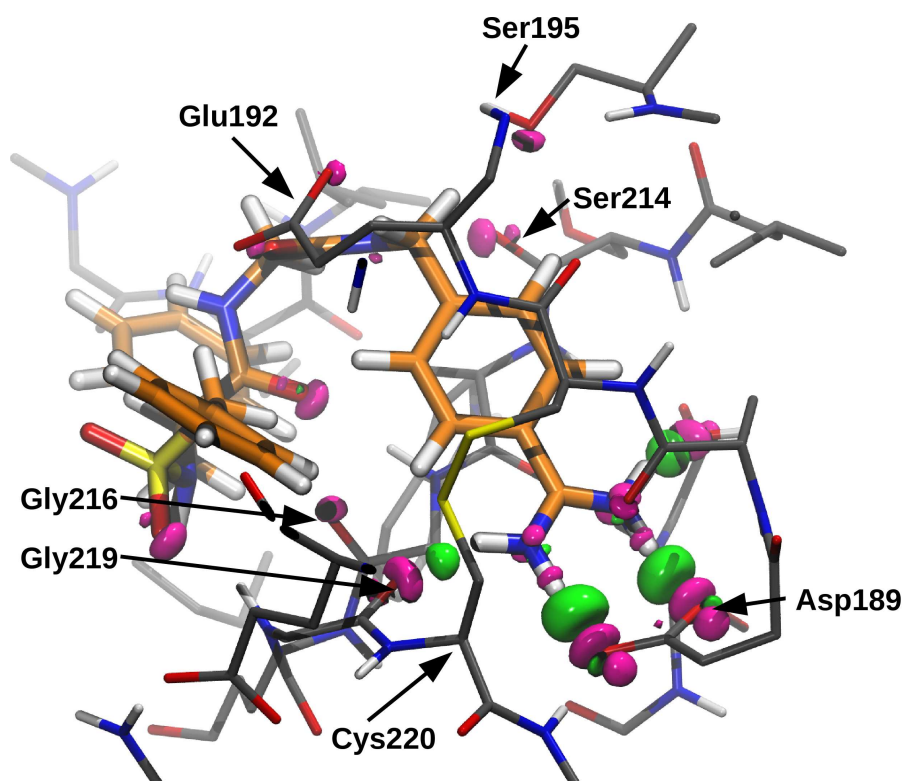


(b) Charge transfer

Figure 6.12: EDD plots of (a) polarisation and (b) charge transfer for the 2ZGX system. The isosurface contour levels are displayed at 0.025 electrons per cubic Angstrom with green surfaces representing electron gain and magenta surfaces representing electron loss. The ligand of the 2ZGX system has been highlighted in orange.



(a) Polarisation



(b) Charge transfer

Figure 6.13: EDD plots of (a) polarisation and (b) charge transfer for the 5AFZ system. The isosurface contour levels are displayed at 0.025 electrons per cubic Angstrom with green surfaces representing electron gain and magenta surfaces representing electron loss. The ligand of the 5AFZ system has been highlighted in orange.

observed in this region are very similar to the C24 - thrombin interaction discussed in Section 6.1.

The EDD plots show a number of other protein and ligand regions involved in key interactions. The Ser214 residue is shown to be involved in interactions with the F2 fragments of every ligand of this study. For example, in the 4UDW system, charge is seen to gather on the oxygen of Ser214 through polarisation and form a bond with a nitrogen of the ligand prolinamide group. The overall interaction of the protein with the 4UDW F2 fragment is moderately strong and likely stabilised greatly by this specific interaction: polarisation is -4.5 kcal/mol and charge transfer is -11.9 kcal/mol. This interaction is shown for 4UDW in Fig. 6.14.

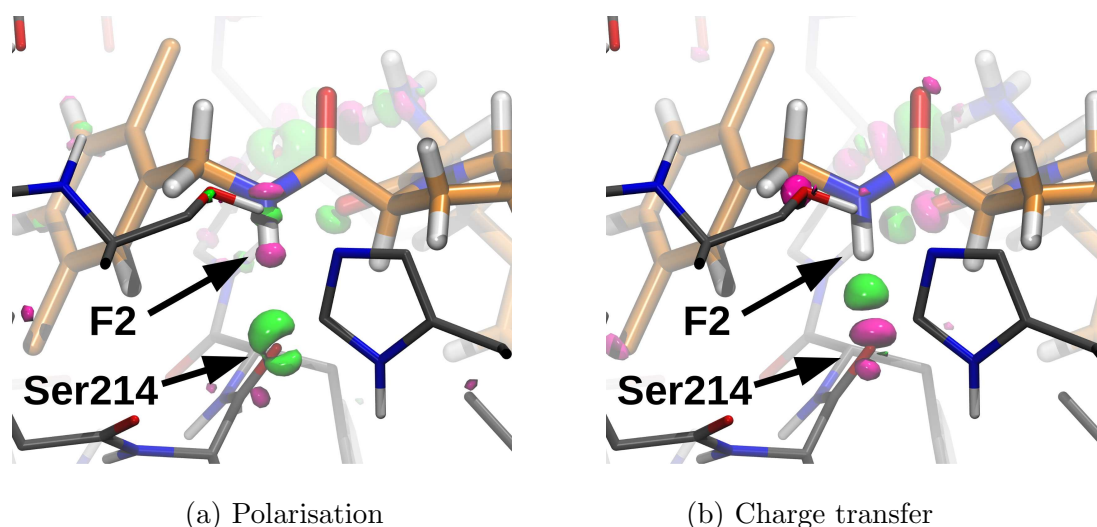


Figure 6.14: EDD plots of (a) polarisation and (b) charge transfer for the F2 fragment region of 4UDW with Ser214. The isosurface contour levels are displayed at 0.025 electrons per cubic Angstrom with green surfaces representing electron gain and magenta surfaces representing electron loss. The ligand of the 4UDW system has been highlighted in orange.

In the 4UDW and 2ZGX F3 fragments, notable stabilising contributions are also observed through polarisation and charge transfer. These arise through interaction of the charged amine group with the Gly216 oxygen through formation of a $\delta^+\text{NH}\cdots\text{OC}$ bond. This interaction is clearly shown in the EDD plots of Figs. 6.11 and 6.12. In the case of 5AFZ, the F3 fragment has a lesser interaction with the Gly216 oxygen atom due to the fact that this fragment is uncharged. However, this fragment is more extended than the F3 fragments of 4UDW and 2ZGX and

therefore has opportunity for interaction with other protein residues. Specifically, interactions of this fragment are seen with the Gly216, Gly219, and Ser214 protein residues. EDD plots of these specific interactions are shown in Fig. 6.15, using a smaller isosurface value of 0.015 electrons per cubic Angstrom in order to precipitate the interactions for visualisation. The weaker stabilisation provided through these interactions is reflected by a > 10 kcal/mol decrease in polarisation compared to the F3 fragments of 4UDW and 2ZGX, and a > 3 kcal/mol decrease in charge transfer.

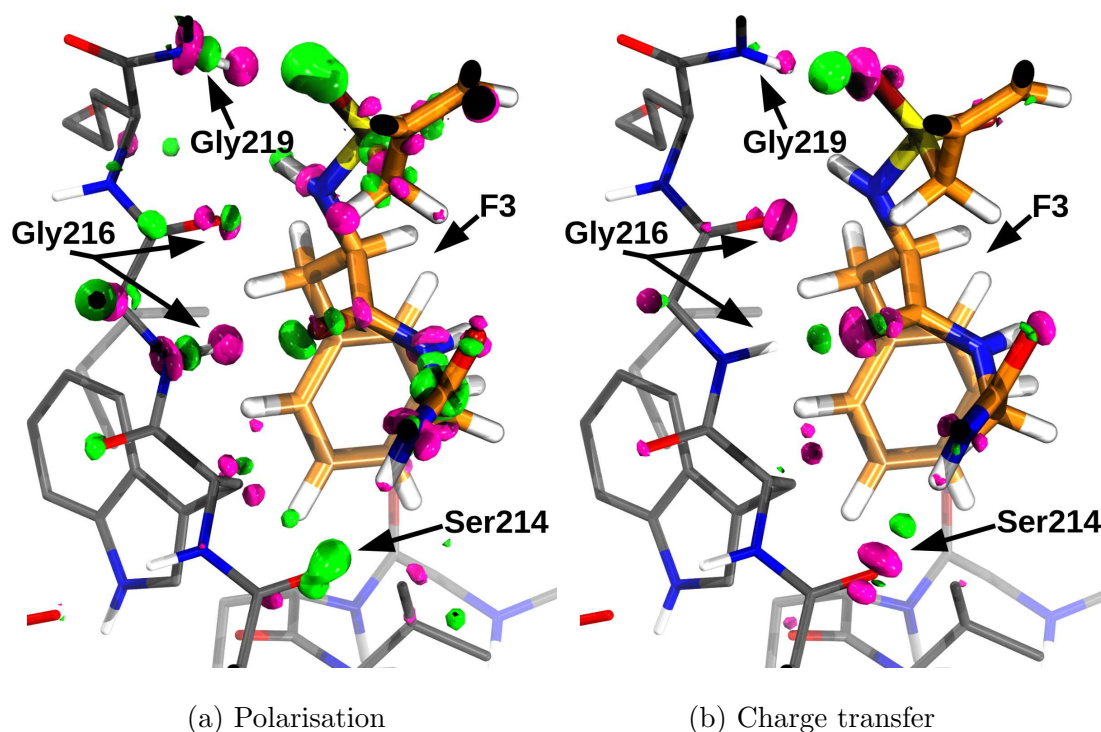


Figure 6.15: EDD plots of (a) polarisation and (b) charge transfer for the 5AFZ system F3 fragment interaction with thrombin. The isosurface contour levels are displayed at 0.015 electrons per cubic Angstrom with green surfaces representing electron gain and magenta surfaces representing electron loss. The ligand of the 5AFZ system has been highlighted in orange.

In considering the EDA components, we note a significant fragmentation error for the polarisation component of the 2ZGX system. This error is -9.9 kcal/mol, and therefore 18% of the polarisation is not attributable to any particular fragment. This is possibly the result of the fragmentation scheme we have adopted for this system, as it may be the case that the total polarisation through the full ligand is impeded by bond partitioning and that the polarisation interaction is not properly

reproduced after fragmentation. Related to this idea, it is possible that giving the F3 fragment of 2ZGX a +1 integer charge is physically unjustifiable. This may be the case as this fragment is relatively small and may potentially stabilise its electron deficiency by withdrawing charge from its neighbouring fragment (F2). This is evidenced by population analysis of the full ligand (performed at the same level of theory as the EDA) in which the fragment atoms are observed to have a net charge of +0.91 e (Mulliken population) and +0.89 e (natural population), notably different to a +1 integer charge. This observation shows that care must be taken when partitioning bonds, especially in the case of small, charged fragments which should ideally be avoided.

We also show ΔE including the ligand desolvation cost (ΔE_{desolv}) in Fig. 6.9. This is included to capture the cost of ligand desolvation when binding within the pocket. It is important to note that this is an approximate measure, as this assumes the cavity to be entirely devoid of water molecules, and also does not account for desolvation within the binding pocket itself. Nonetheless, this provides useful indication of the importance of solvation effects in the enthalpic contribution to binding.

The desolvation energy cost significantly lowers the stability provided through the charged fragments. This is most notably observed for the F3 fragment of 2ZGX in which the ΔE of -75.8 kcal/mol is nearly cancelled by the ligand desolvation cost of 67.1 kcal/mol. In fact, the $\Delta E + \Delta E_{\text{desolv}}$ value for this charged F3 fragment (-11.3 kcal/mol) is lower than even the neutrally charged F2 fragment of 2ZGX (-8.7 kcal/mol), although it should again be reiterated that the ΔE_{desolv} value provides an approximate indication of solvation effect importance in our study. This high ligand desolvation cost is expected, as cationic species will commonly be stabilised more strongly than neutral molecules in solvent. Despite this high cost, the charged fragments still typically display stronger or comparable $\Delta E + \Delta E_{\text{desolv}}$ energies than the uncharged fragments.

The fragmentation error is moderate for ΔE_{desolv} . Generally this error cancels

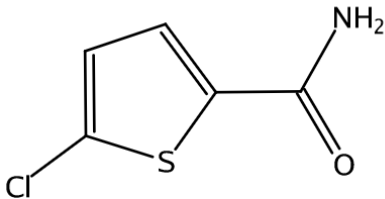
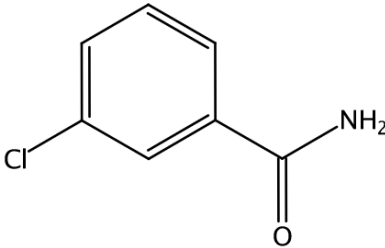
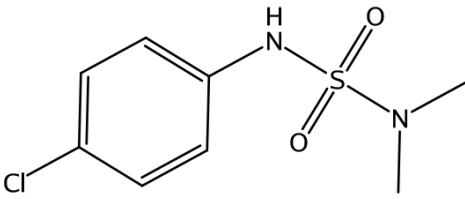
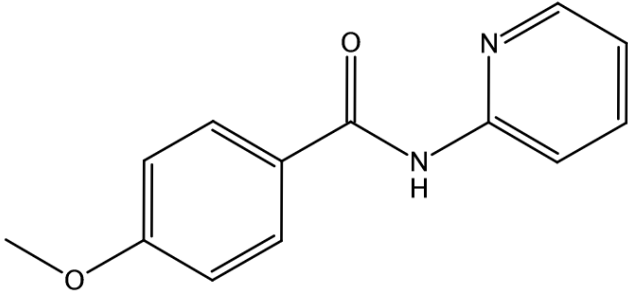
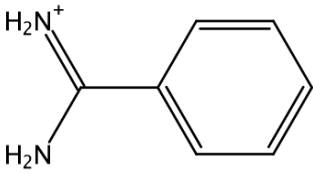
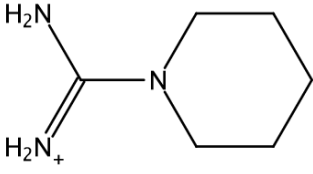
with the error of ΔE to give an overall low error for $\Delta E + \Delta E_{\text{desolv}}$. For example, in the 2ZGX system the fragmentation error of ΔE is -5.0 kcal/mol, and the fragmentation error of ΔE_{desolv} is 6.4 kcal/mol, cancelling to give a fragmentation error for $\Delta E + \Delta E_{\text{desolv}}$ of only 1.4 kcal/mol. This is misleading as this suggests the ΔE_{desolv} -corrected interaction energy to be more accurately decomposable into its fragment contributions than without correction. This observation further supports the view that the ligand desolvation energies used here provide qualitatively correct, but not necessarily quantitatively correct, indications of solvent effect importance.

6.2.3 Analysis: S1 pocket binders

In this section, we analyse the binding of the 4UD9, 5AFY, 5AHG, 5AF9, 4UEH, and 4UE7 reference ligands with the thrombin S1 pocket. The structures of these ligands are shown Table 6.2, and plots of the EDA components are displayed in Fig. 6.16 and Fig. 6.17. Energy component values of the S1 binders are also provided in Table D.2 of the Appendix.

We begin by noting an overall trend in the frozen energy components' magnitudes, and to a lesser extent also in the polarisation, charge transfer and dispersion energy components. For example, 5AFY generally displays the smallest individual energy contributions of the ligands, and the charged ligands generally show the largest energy contributions. Subtle differences are observed in these components however. These differences arise from structural and conformational differences both in the ligand and in the protein. For this reason, in our discussion that follows we consider the binding components of ligand pairs on a case-by-case basis, allowing us to properly consider the differences in the ligand and protein structures and conformations.

Table 6.2: Small fragment binders of the thrombin S1 pocket for EDA.

System	Figure
4UD9	
5AFY	
5AHG	
5AF9	
4UEH	
4UE7	

6.2.3.1 5AFY and 5AHG

We begin our discussion by considering the interactions of the 5AFY and 5AHG ligands which both share a similar chlorobenzene functional group. Despite key differences in the chlorobenzene substitutions, these ligands display significant overlap when superposed within the binding pocket. Slight differences are, however, observed in the protein conformations for these systems. These differences in the protein conformations are expected to directly affect the binding modes of the ligands and therefore the EDA results.

As the chlorobenzene moieties of the ligands are almost identically positioned within the pocket, these are assumed to make almost identical contributions to the EDA components. The different amide and sulfonamide functional groups of the ligands are therefore expected to be the primary origin of differences seen in the EDA values. Importantly, the meta- and para-substitution of these ligands is observed to result in interactions with alternate sides of the binding pocket. Through the EDD plots shown in Figs. 6.18 and 6.19, we observe that the meta-substituted 5AFY ligand favours interaction with the Ser195 residue alone, whereas the para-substituted 5AHG ligand favours interaction with the Gly219 residue (and to a lesser degree the Ser214 residue).

The magnitudes of the individual components of the frozen density interaction are much larger in the 5AHG system than the 5AFY system, and importantly Pauli repulsions are 13.1 kcal/mol more repulsive in the 5AHG interaction. This observation is explained by the greater size of the 5AHG ligand than the 5AFY ligand, and also the close interaction (1.7 Å separation) of this ligand with the Ser195 hydrogen. Overall, the greater magnitudes of the interactions for the 5AHG ligand balance to give overall frozen density components of 2.8 kcal/mol and 2.1 kcal/mol for 5AFY and 5AHG. Dispersion is also significantly stronger in 5AHG (−32.0 kcal/mol) than 5AFY (−25.2 kcal/mol). As with the frozen density components, this observation can be understood to originate from the larger size of 5AHG.

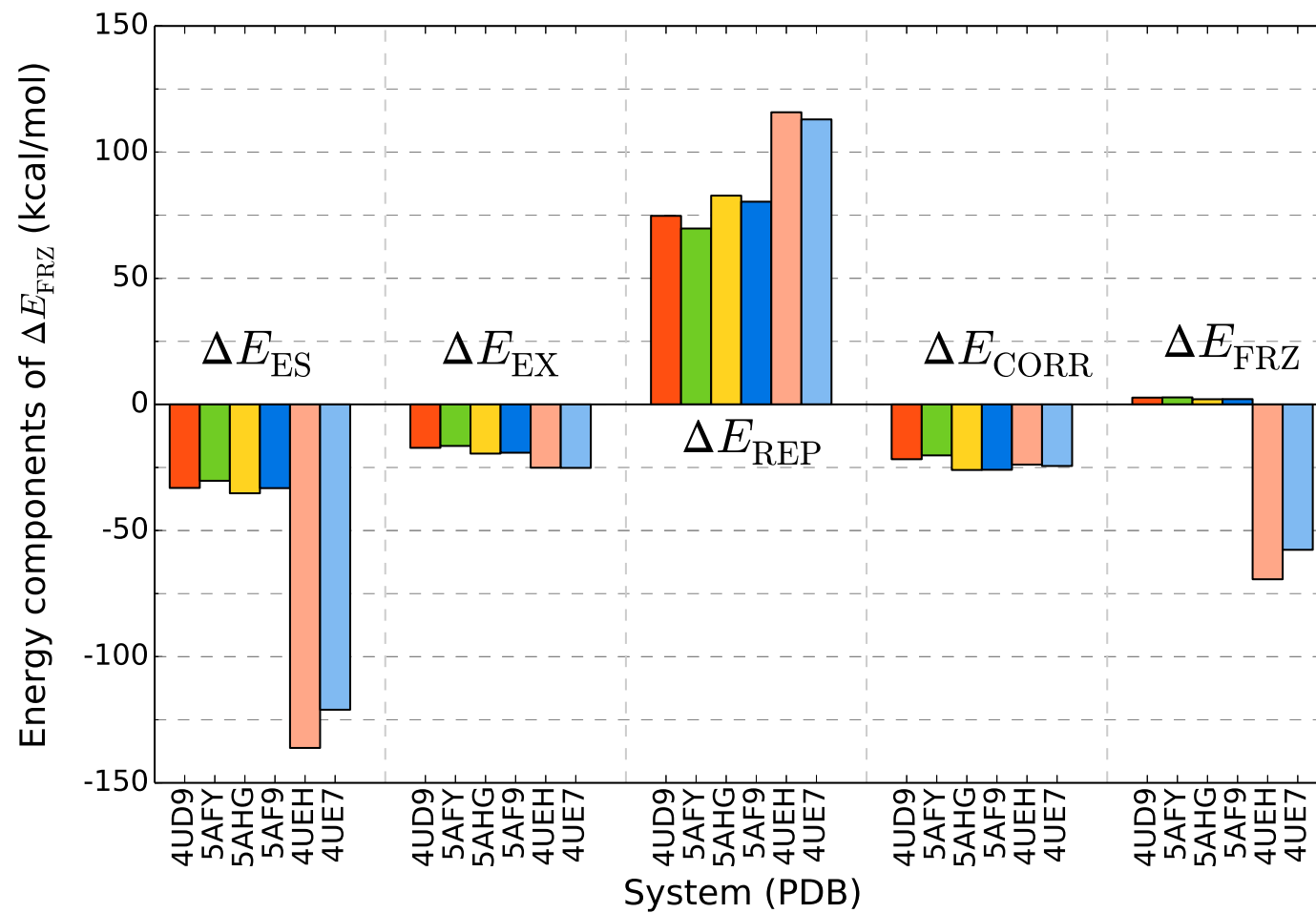


Figure 6.16: Frozen density analysis of the fragmented thrombin S1 pocket complexes calculated at the PBE-D2/800 eV level of theory (component values are given in kcal/mol).

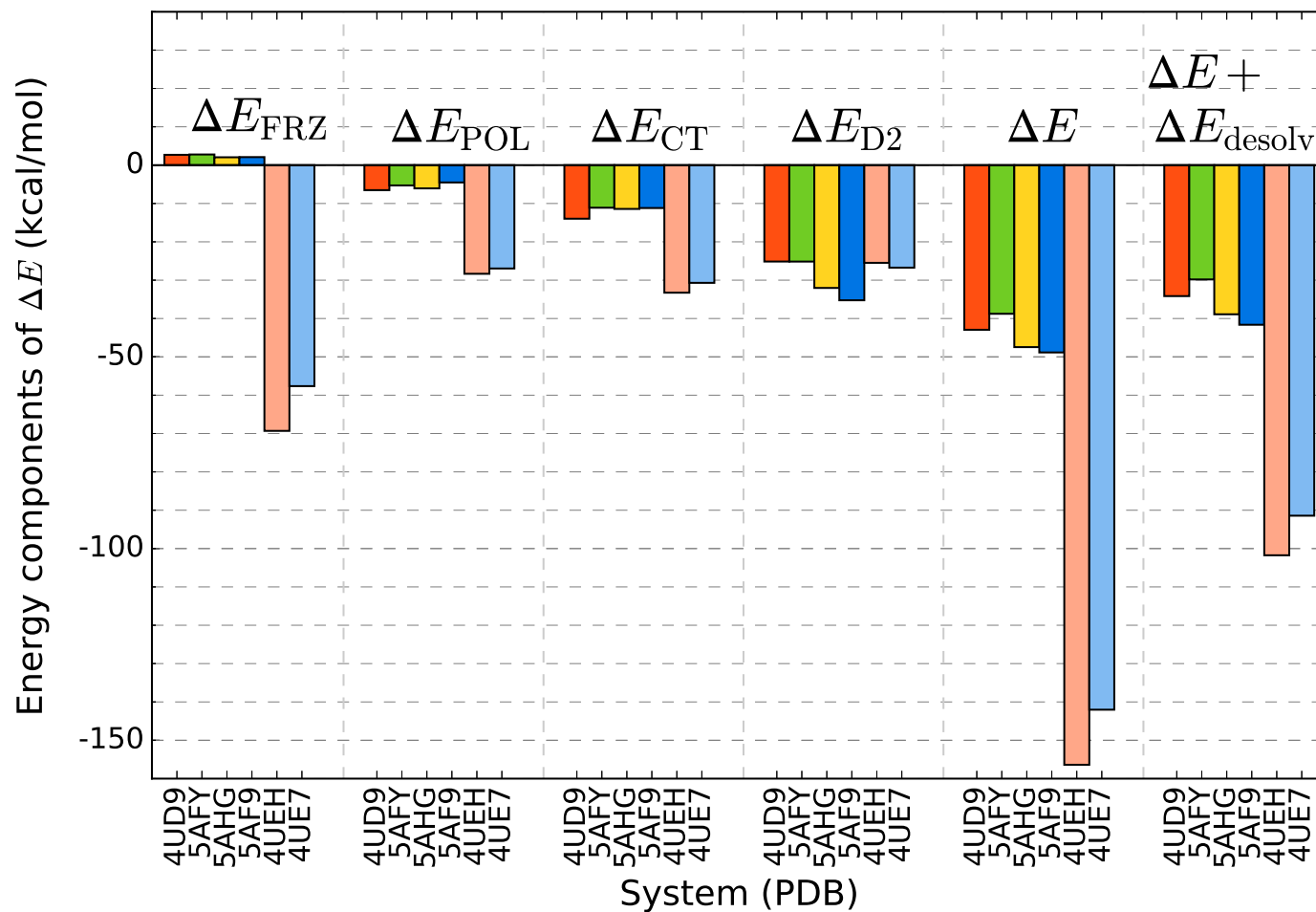


Figure 6.17: EDA components of the fragmented thrombin S1 pocket complexes calculated at the PBE-D2/800 eV level of theory (component values are given in kcal/mol). D2 refers to the dispersion energy correction of Grimme. The total ΔE in combination with the cost of ligand desolvation ΔE_{desolv} is also shown.

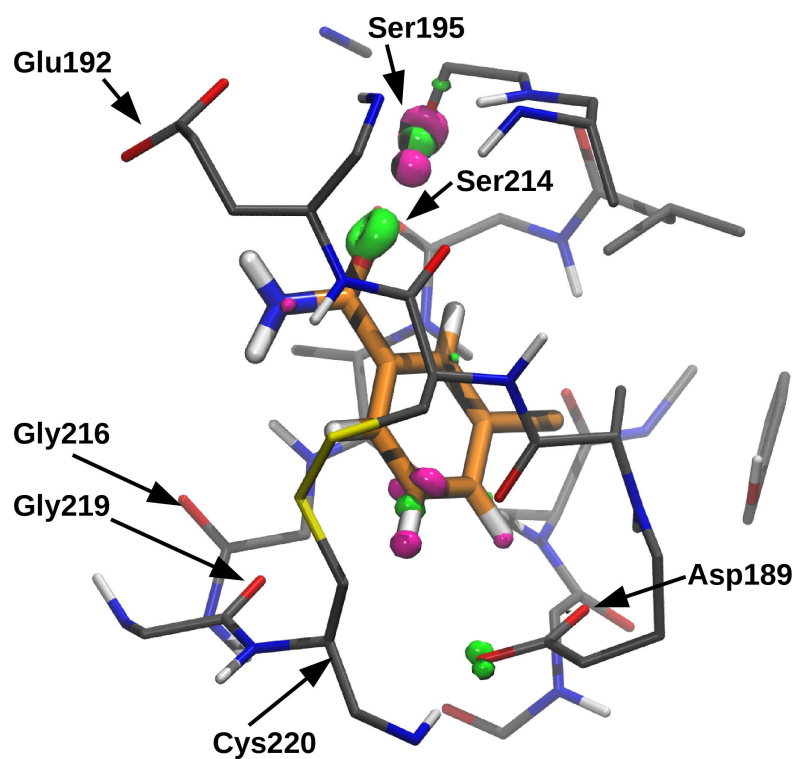
Polarisation (-5.3 kcal/mol and -6.1 kcal/mol) and charge transfer (-11.1 kcal/mol and -11.4 kcal/mol) are comparable for the 5AFY and 5AHG ligands, with 5AHG displaying slightly stronger interactions. The 0.8 kcal/mol greater polarisation in 5AHG is explained by the larger size of this ligand: this greater size increases the opportunity for stabilisation through intramolecular charge redistributions during binding. These differences are small when compared to the differences in the other energy components. Therefore, we can consider there to exist approximate energetic equivalence of the 5AFY ligand polarisation and charge transfer interactions with the Ser195 residue and the 5AHG ligand with the Gly219 and Ser214 residues.

Plots of ΔE with the ligand desolvation cost ΔE_{desolv} are shown in Fig. 6.17, which attempt to quantify the cost of ligand desolvation when binding within the pocket. As discussed in Section 6.2.2.2 above, this is an approximate measure due to the assumptions used in this calculation. Overall, ligand desolvation effects are similar for the ligands, differing by only 0.4 kcal/mol. This correction therefore contributes negligibly to the differences in the results we observe.

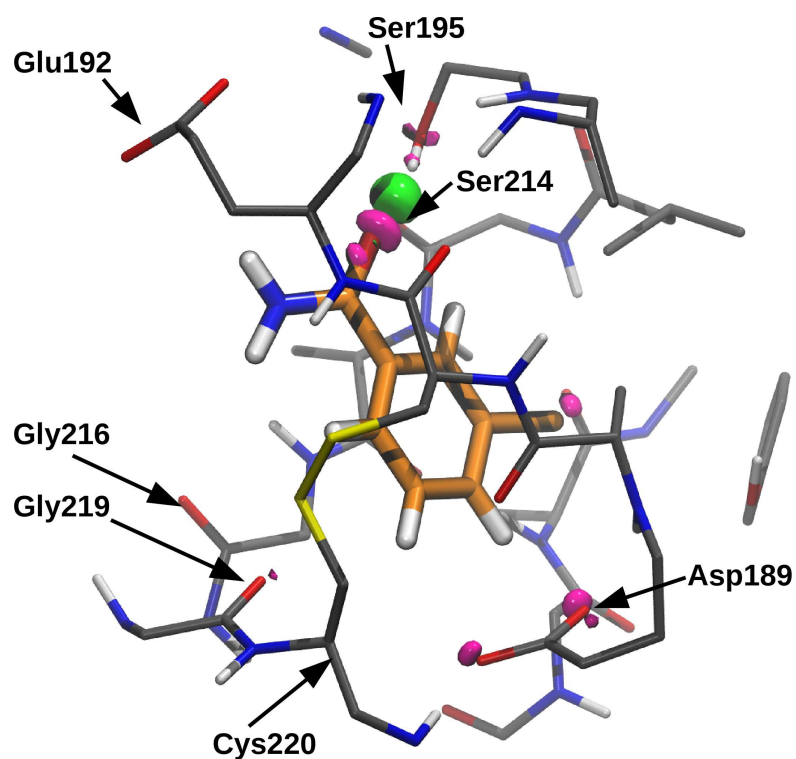
In conclusion, the differences in the frozen density, polarisation and charge transfer energy components are overall relatively small, with the dispersion component remaining as the primary driving force behind the greater interaction energy of 5AHG (-38.9 kcal/mol) than 5AFY (-29.8 kcal/mol).

6.2.3.2 4UD9 and 5AFY

The 4UD9 and 5AFY ligands differ only by their aromatic ring constituent. Considering the ligand structures alone, the asymmetrical polar thiophene ring of 4UD9 would be expected to enhance electrostatic, polarisation and charge transfer effects compared to the symmetrical benzene ring of 5AFY. Indeed, the interaction components of 4UD9 are all greater than 5AFY, for example electrostatics

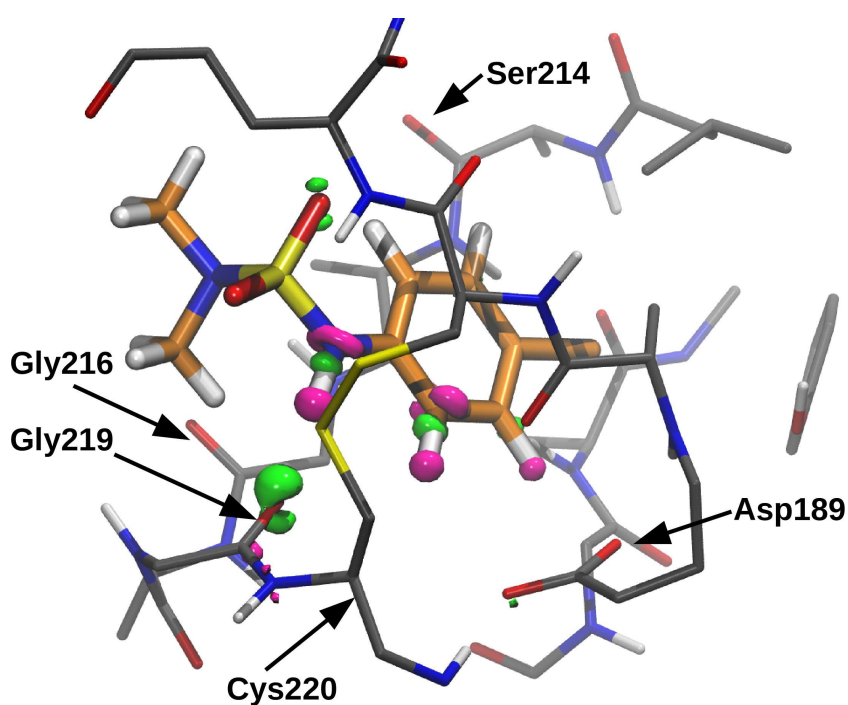


(a) Polarisation

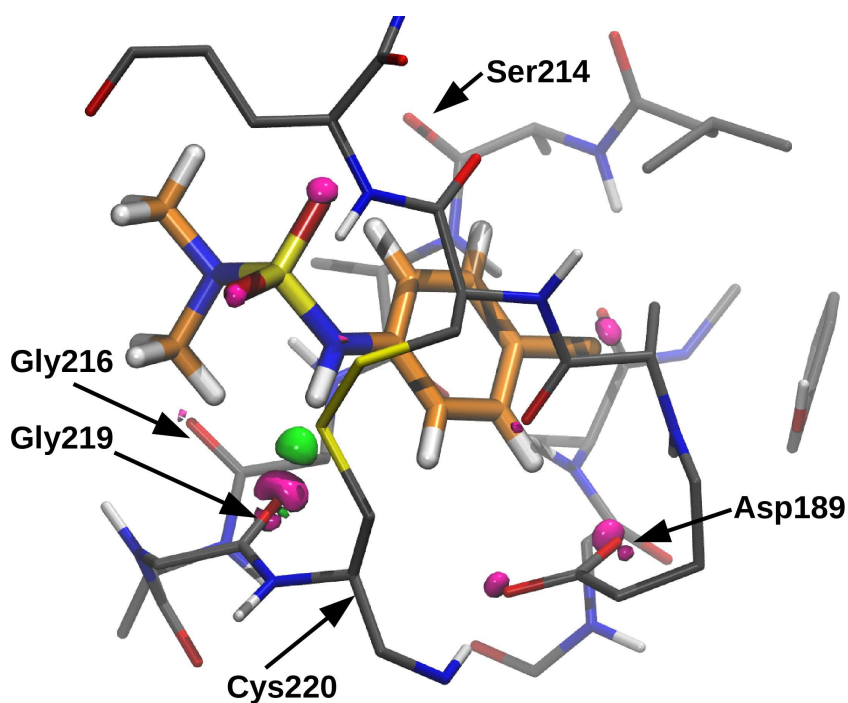


(b) Charge transfer

Figure 6.18: EDD plots of (a) polarisation and (b) charge transfer for the 5AFY system. The isosurface contour levels are displayed at 0.025 electrons per cubic Angstrom with green surfaces representing electron gain and magenta surfaces representing electron loss. The ligand of the 5AFY system has been highlighted in orange.



(a) Polarisation



(b) Charge transfer

Figure 6.19: EDD plots of (a) polarisation and (b) charge transfer for the 5AHG system. The isosurface contour levels are displayed at 0.025 electrons per cubic Angstrom with green surfaces representing electron gain and magenta surfaces representing electron loss. The ligand of the 5AHG system has been highlighted in orange.

(-33.1 kcal/mol), polarisation (-6.5 kcal/mol), and charge transfer (-14.0 kcal/mol) in 4UD9 compared with 5AFY (-30.3 kcal/mol, -5.3 kcal/mol, and -11.1 kcal/mol respectively).

Notably however, the interactions of 4UD9 and 5AFY differ significantly in the hydrogen bonds they form. The 4UD9 ligand forms three notable hydrogen bonds with the Gly219 and Glu192 residues, whereas 5AFY forms a notable hydrogen bond with Ser195. These interactions are shown clearly in Figs. 6.20 and 6.18. Additionally, the benzene of 5AFY favours a conformation with two hydrogens interacting with the Asp189 residue, whereas the 4UD9 conformation primarily involves one hydrogen interacting with the Asp189 residue and another with the Cys220 backbone. Overall therefore, these structurally similar binders display very dissimilar interactions with the protein pocket, and therefore the difference in the EDA components is not explained by the aromatic ring substituent alone.

Nonetheless, by analysis of the EDD plots we may still expect the bonding of 4UD9 to be stronger than 5AFY. Specifically, the EDD plots suggest greater quantities of charge to be redistributed during polarisation and charge transfer for the 4UD9 ligand than for the 5AFY ligand, and we expect these quantities to correlate with the strengths of the bonds formed. Overall, we therefore conclude that the 4UD9 ligand shows stronger interactions not only due to the favourable interactions of its aromatic ring, but also due to the stronger bonds that it forms.

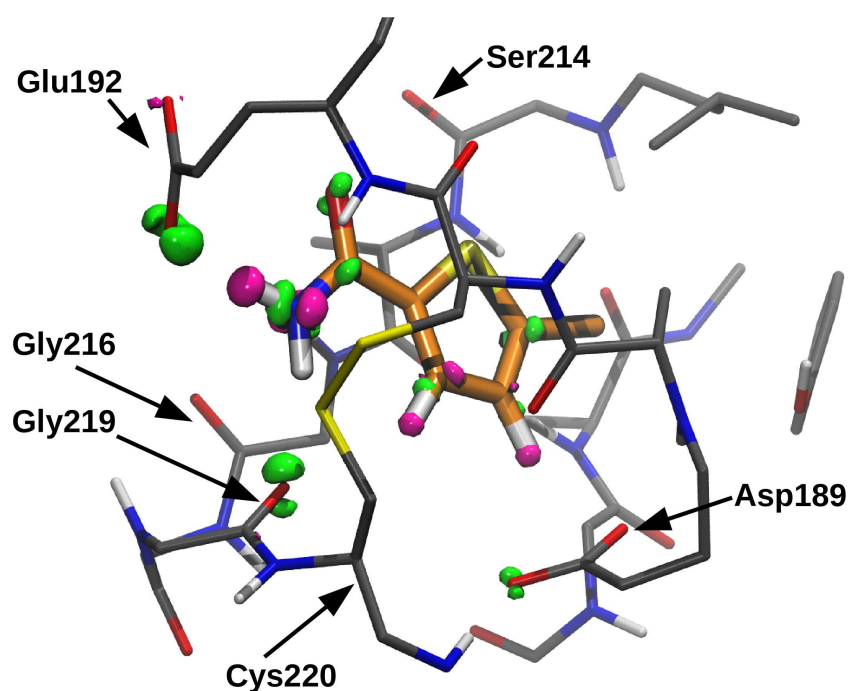
It is also important to consider the frozen density component of the 4UD9 and 5AFY interactions. These display a small difference of 0.1 kcal/mol, largely due to cancellation of the individual components that contribute to the frozen density interaction. The greater electrostatics, exchange and correlation in 4UD9 (5.0 kcal/mol) almost exactly cancels with the greater Pauli repulsions cost (5.0 kcal/mol). Differences in these individual contributions are reconciled through a number of considerations. Similar to the arguments concerning the polarisation and charge transfer contributions presented above, we expect electrostatics in 4UD9 to be

more stabilising than in 5AFY due the presence of a dipole moment in the thiophene ring of 4UD9, and due the closer interactions of this ligand with the protein. Additionally, the thiophene ring has a slightly greater electron count than benzene which we expect to enhance exchange and correlation effects in the 4UD9 interaction. Finally, whilst the 5AFY ligand is larger than the 4UD9 ligand, the 4UD9 ligand is observed to interact more strongly with the Glu192 residue, and so overall Pauli repulsions are greater for 4UD9. Ligand desolvation is very similar for these ligands (8.8 kcal/mol for 4UD9, and 9.0 kcal/mol for 5AFY), and overall the difference in the interaction energy for these ligands is concluded to be primarily of charge transfer origin.

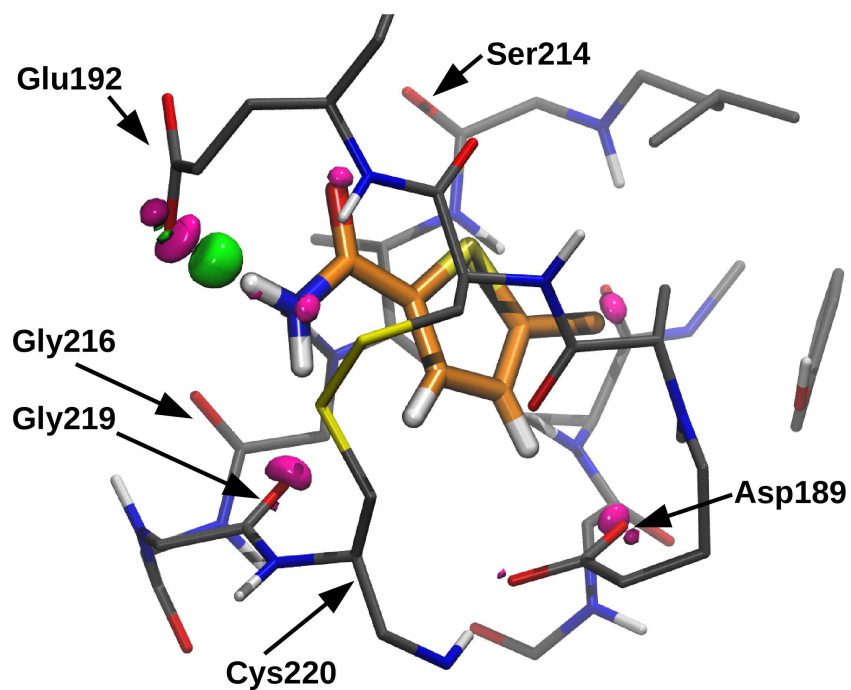
6.2.3.3 4UD9 and 5AF9

We now consider the interactions of the 4UD9 and 5AF9 ligands. Despite the much smaller size of the 4UD9 ligand compared to the 5AF9 ligand, we observe similar electrostatics of 4UD9 (-33.1 kcal/mol) and 5AF9 (-33.2 kcal/mol). All the other contributions to the frozen density component remain larger in magnitude for the 5AF9 ligand, as expected considering the larger size of this ligand. To understand this observation, we begin by noting that the 5AF9 and 4UD9 ligands and their protein conformations overlap closely when superposed yet the Glu192 residue positions differ significantly. This is shown in Figs 6.20 and 6.21, where we observe the Glu192 residue actively participating in binding to the 4UD9 ligand. This interaction with the charged Glu192 residue provides additional stability to the 4UD9 ligand through electrostatics, increasing the total electrostatics up to the level of the larger 5AF9 ligand.

Overall, the frozen density contribution is slightly more repulsive for 4UD9 (2.7 kcal/mol) than 5AF9 (2.1 kcal/mol). This greater repulsion is due to the presence of additional short range stabilisations for the 4UD9 ligand that reduce the intermolecular separation and increase Pauli repulsions. Specifically, polarisation (-6.5 kcal/mol) and charge transfer (-14.0 kcal/mol) interactions are also seen

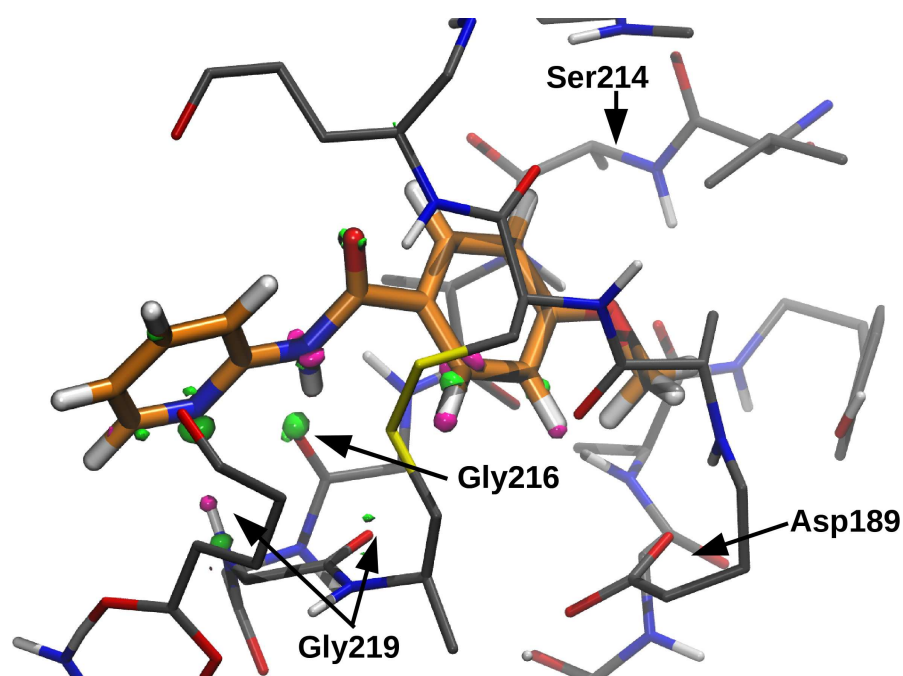


(a) Polarisation

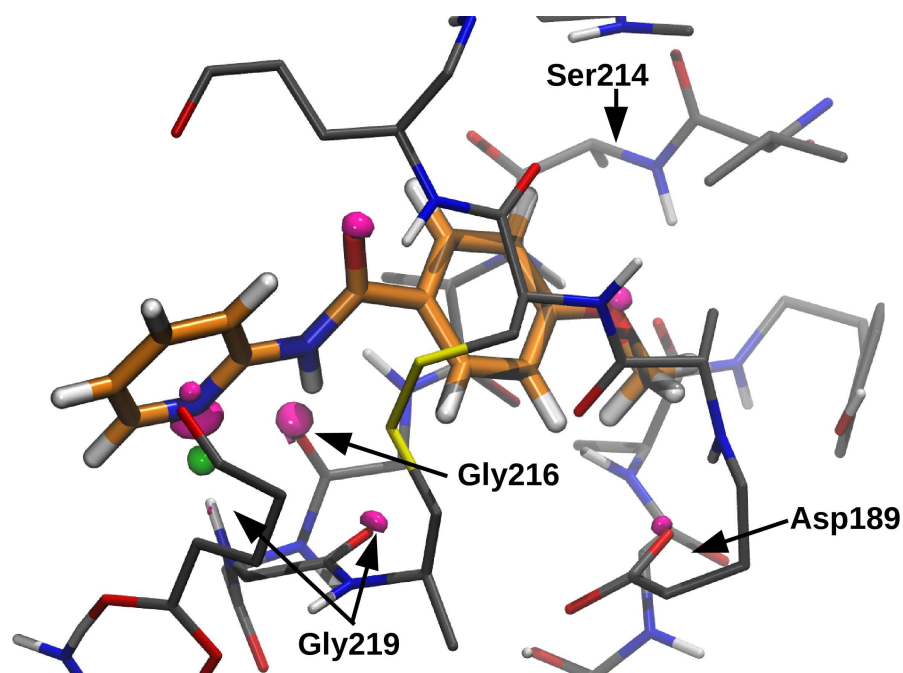


(b) Charge transfer

Figure 6.20: EDD plots of (a) polarisation and (b) charge transfer for the 4UD9 system. The isosurface contour levels are displayed at 0.025 electrons per cubic Angstrom with green surfaces representing electron gain and magenta surfaces representing electron loss. The ligand of the 4UD9 system has been highlighted in orange.



(a) Polarisation



(b) Charge transfer

Figure 6.21: EDD plots of (a) polarisation and (b) charge transfer for the 5AF9 system. The isosurface contour levels are displayed at 0.025 electrons per cubic Angstrom with green surfaces representing electron gain and magenta surfaces representing electron loss. The ligand of the 5AF9 system has been highlighted in orange.

with the negatively charged Glu192 residue (in addition to the electrostatic interaction discussed above). These interactions favour paying the Pauli repulsions cost (74.7 kcal/mol) of an overall closer intermolecular separation, which in turn results in a more repulsive frozen density component for 4UD9.

For these ligands, the ligand desolvation energy cost is greater for 4UD9 (8.8 kcal/mol) than 5AF9 (7.2 kcal/mol). This is likely a result of a number of factors. For example, the bulkier size of 5AF9 results in a 3.6 kcal/mol greater solvent cavitation energy cost during solvation than for 4UD9. This energy is released during ligand desolvation, lowering the desolvation energy cost for 5AF9. Additionally, the presence of the chlorine substituted thiophene ring is expected to increase the polarity of the 4UD9 ligand, and in turn increase stabilisation when solvated in water. This will increase the ligand desolvation energy cost of 4UD9 as a result.

Overall, dispersion effects for 5AF9 (−35.2 kcal/mol) are seen to be significantly greater than for 4UD9 (−25.1 kcal/mol). This is the primary driving force behind the greater interaction energy of 5AF9 than 4UD9 with thrombin. It is interesting to observe the relatively high strength of dispersion in 5AF9 when compared with the other energy components of this ligand. This is likely due to the presence of two aromatic rings in 5AF9 which we would expect to interact notably through dispersion effects with thrombin.

6.2.3.4 4UEH and 4UE7

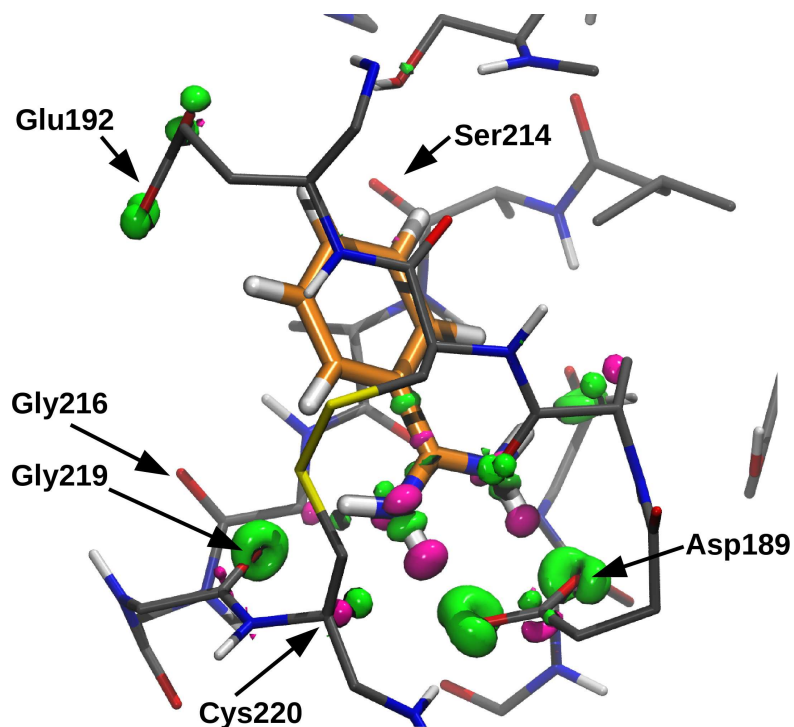
Here, we consider the interactions of the two charged ligands of our study, 4UEH and 4UE7. We begin our discussion by considering the important overall differences between these two ligands' interactions and those of the remaining uncharged ligands. The charged ligands show the largest energy component magnitudes for all but correlation and dispersion. This observation is explained by considering the structures of the ligands in addition to their charges. The 4UEH and 4UE7 ligands are smaller than the remaining uncharged ligands, and therefore we expect the correlation and exchange contributions (which depend on electron count) of

4UEH and 4UE7 to be weakened by this. On the other hand, these two ligands are positively charged and so favour closer interaction with the protein pocket. A particularly strong interaction with the negatively charged Asp189 residue is observed, as shown in Figs 6.22 and 6.23. This closer interaction significantly increases Pauli repulsions (115.8 kcal/mol for 4UEH and 113.0 kcal/mol for 4UE7) above even the large 5AF9 ligand (80.4 kcal/mol). At the same time, this interaction enhances electrostatics (-136.2 kcal/mol for 4UEH and -121.0 kcal/mol for 4UE7) as we would expect from this interaction of positively and negatively charged functional groups. Exchange is enhanced by this closer interaction such that 4UEH and 4UE7 are the ligands that are most stabilised through this energy component (-25.1 kcal/mol and -25.2 kcal/mol respectively). However, correlation (-23.8 kcal/mol and -24.4 kcal/mol) is not enhanced enough to be above that seen in the 5AHG and 5AF9 systems (-26.0 kcal/mol and -25.9 kcal/mol). This may be reconciled as the 5AHG and 5AF9 ligands contain notable delocalised functional groups with high electron counts which are well suited to correlation interactions with the protein. A similar argument also applies to the dispersion component, for which we also observe the strongest dispersion interactions for the 5AHG and 5AF9 ligands.

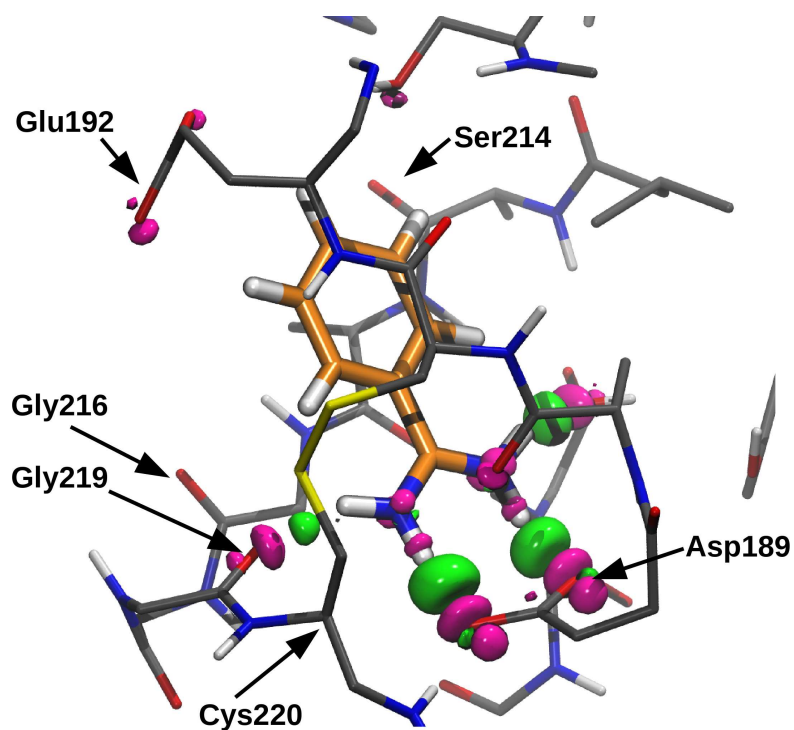
The desolvation energy costs for these two charged ligands are notably greater than for the uncharged ligands. In the uncharged systems, the range of the desolvation energy cost is between 7.2 kcal/mol and 9.0 kcal/mol, whereas in the 4UEH system the cost is 54.6 kcal/mol and 50.6 kcal/mol in the 4UE7 system. This is explained by considering the effect of the ligand charge: the negatively charged fragments will bind more favourably with the solvent than the uncharged molecules and so show a greater energy cost to leave the solvent environment. Whilst correcting the interaction energy using the ligand desolvation energy (as $\Delta E + \Delta E_{\text{desolv}}$) helps to normalise the charged and uncharged ligand interaction values to a closer range as seen in Fig. 6.17, the difference between the values for the charged and uncharged ligands is still large. This observation suggests that the approximations used in our correction may be overly limiting, as we would expect the charged and uncharged

fragments to display much closer interaction energies after correcting for solvation effects.

Having discussed the important differences between the charged and uncharged ligand interactions, we now consider the interaction energy driving forces of the 4UEH and 4UE7 ligands. As these ligands are structurally very similar, the differences in the energy components are relatively simple to reconcile. Electrostatics, polarisation and charge transfer are greater in 4UEH than in 4UE7 by 15.1 kcal/mol, 1.4 kcal/mol and 2.6 kcal/mol respectively. This is likely a direct result of the additional interaction of 4UEH with the charged Glu192 residue as seen in Fig. 6.22. Due to this additional interaction, Pauli repulsions are greater in 4UEH (115.8 kcal/mol) than in 4UE7 (113.0 kcal/mol), despite the greater number of protons present in 4UE7 which would be expected to increase steric pressure. Correlation is slightly greater in 4UE7 (-24.4 kcal/mol) than in 4UEH (-23.8 kcal/mol), which is explained by the greater electron count of the 4UE7 ligand. Overall, the greater strength of the 4UEH interaction is seen to originate from its stronger electrostatics, which is moderated by a 4.0 kcal/mol greater ligand desolvation cost above 4UE7.

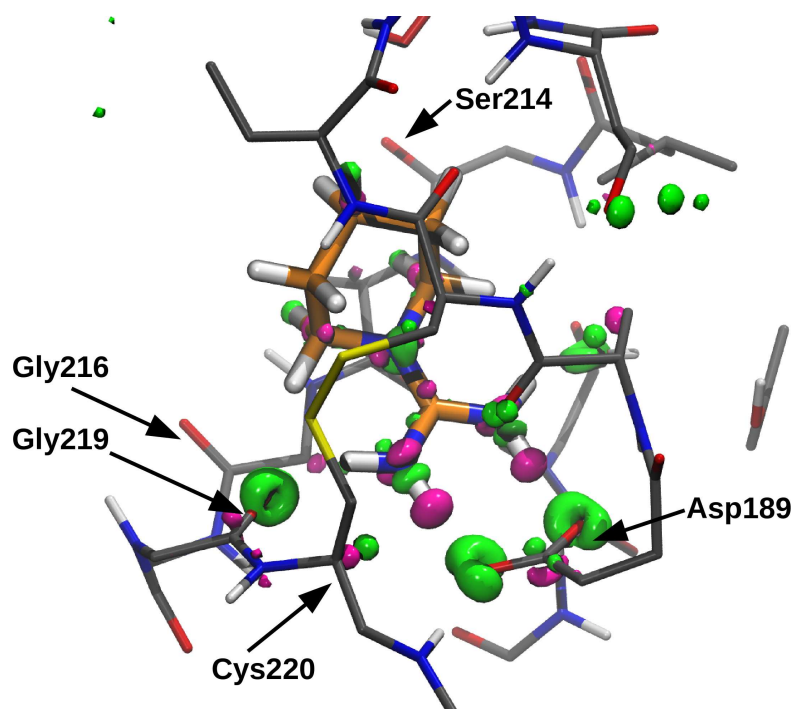


(a) Polarisation

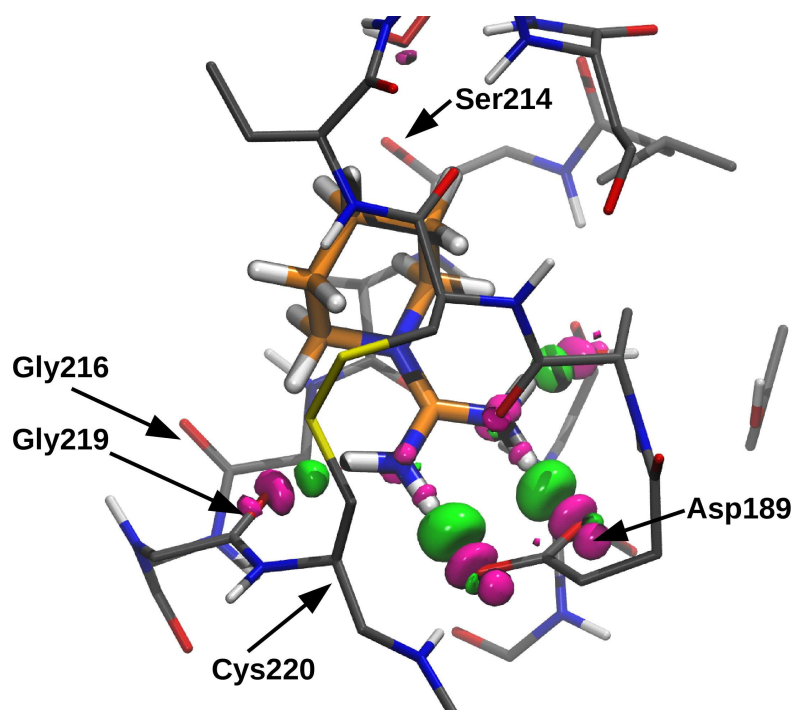


(b) Charge transfer

Figure 6.22: EDD plots of (a) polarisation and (b) charge transfer for the 4UEH system. The isosurface contour levels are displayed at 0.025 electrons per cubic Angstrom with green surfaces representing electron gain and magenta surfaces representing electron loss. The ligand of the 4UEH system has been highlighted in orange.



(a) Polarisation



(b) Charge transfer

Figure 6.23: EDD plots of (a) polarisation and (b) charge transfer for the 4UE7 system. The isosurface contour levels are displayed at 0.025 electrons per cubic Angstrom with green surfaces representing electron gain and magenta surfaces representing electron loss. The ligand of the 4UE7 system has been highlighted in orange.

Chapter 7

Conclusions

This thesis has sought to develop and apply a new density functional theory (DFT) based energy decomposition analysis (EDA) method for the analysis of intermolecular bonding in large biomolecular systems. This new scheme, referred to as the ONETEP EDA, has a computational cost that scales linearly with system size. In this work, we have used our approach to investigate the driving forces of binding in systems up to 4975 atoms in size.

In Chapters 1 and 2, we introduced the approximations of quantum mechanics that are used to formulate computational methods for solving the Schrödinger equation. Here, we introduced Hartree-Fock theory and DFT. We also detailed the theory of the ONETEP package, which is a linear-scaling DFT method that seeks to minimise the energy directly with respect to the density matrix (kernel) and NGWFs.

In Chapters 3 and 4, we investigated the current EDA approaches with focus on their application to biomolecular studies and drug design. Here, we described the EDA theory in a unified manner that allowed for simple comparison of the EDA approaches. Through our studies, we found the absolutely localised molecular orbital (ALMO) EDA scheme to be well suited to identifying the key driving forces of binding within biomolecular systems. This was due to the properties of the ALMO state used to calculate the polarisation energy component, specifically

that this state is properly antisymmetrised and variationally optimised. This scheme decomposes the interaction energy into three separate energy components: the frozen density component, polarisation, and charge transfer terms.

In Chapter 5, we showed that through making minor modifications to the energy components of the localised molecular orbital (LMO) EDA scheme, the frozen density component of the ALMO EDA may be further decomposed into four energy components (electrostatics, exchange, Pauli-repulsions, and correlation) at very little extra computational cost. We implemented a version of this ALMO-LMO hybrid approach in the ONETEP package, using the Stoll equations to construct the intermediate polarised ALMO state. Additionally, by revising the equations of the EDA we were able to remove the diagonalisation bottleneck of our approach and produce a linear-scaling formulation. Our aim implementing this scheme was to enable EDA calculations to be readily performed on systems of very large size, and in particular biomolecular systems. Our EDA was validated against the Gaussian basis set implementations of the ALMO and LMO EDA approaches using a set of small interacting test systems. Additionally, we tested the dependence of our EDA method with respect to basis set size, exchange-correlation functional, and atomic coordinates. Here, a solution for the problem of polarisation and charge transfer basis set dependence was proposed that exploits the strictly localised property of the ONETEP orbitals. We also demonstrated the usefulness of information provided by the polarisation and charge transfer electron density difference (EDD) plots which are provided as part of the EDA method for a model water trimer test system. These plots are valuable as they provide indication of the key regions involved in polarisation and charge transfer interactions in the system.

An investigation of the binding driving forces in the thrombin-C24 inhibitor complex was presented in Chapter 6, using our EDA method (alongside EDD plots) on systems up to 4975 atoms in size. Here, we observed the effect of protein residues to play a significant role in the binding components, for example the position of the charged Glu192 residue was shown to notably affect the overall contribution

of electrostatics in these systems. The effect of protein truncation was also quantified using the thrombin-C24 system, where we showed full convergence of the energy components at approximately 15Å truncation radius of the ligand. Having demonstrated the use of the EDA for investigating ligand interactions within large protein systems, we applied the EDA in a fragment based study. The interactions of small binders with the S1 pocket were also considered in this chapter, which we showed to be readily understood through the combined use of the EDA and EDD plots. In this, we showed that the fragmentation process must be performed with care and that small charged fragments should be avoided. This is due to the necessary approximation that must be made in our EDA that the fragments must each have integer charge, which presents a problem for small charged fragments because the true charge is more likely to be fractional as a result of delocalisations. Here, we also attempted to capture desolvation effects of the ligand during binding using QM techniques.

7.1 Future work

There are a number of directions future work suggested by our observations may take, which we now discuss.

Ideally, the ALMO state used in our EDA should guarantee charge localisation to the fragments without any fragment-fragment delocalisation effects. In Section 5.3.2 we demonstrated the notable basis set dependence of this state, with larger basis sets resulting in a larger polarisation contributions. This observation originates from the fact that as the basis set becomes larger, the basis set increasingly extends into the space of the neighbouring molecule, and so the ALMO state (and therefore polarisation) increasingly includes charge transfer effects. Our proposed solution to this problem exploits the strictly localised property of the NGWFs. Here, we showed use of between 7.5 Bohr to 8.5 Bohr NGWF radii approximately equals use of the aug-cc-pVTZ basis set in the Gaussian ALMO EDA. Therefore, one may choose to consider polarisation and charge transfer as

relative quantities by using a consistent NGWF radii (e.g. 8.0 Bohr) in all EDA calculations. This is not a perfect solution, however, as this fails to fully solve the problem of rigorously defining and preventing fragment-fragment delocalisation during polarisation. As we also discussed in this section, the CDFT approach of Wu [16] and FERF approach of Horn and Head-Gordon [248] that seek to avoid this ambiguity may be used to reduce this sensitivity. Future work may involve integrating similar approaches into our EDA scheme to fully resolve this issue.

In our EDA studies, desolvation effects were only partially captured in an approximate manner. Future work may target this shortcoming and attempt to capture solvation effects as an explicit energy component of the ONETEP EDA. This has been achieved in a number of EDA schemes in literature, for example the LMO [266] and PIEDA [184] based polarisable continuum model (PCM) [267–269] EDA schemes. The ONETEP solvation model [265], based on direct solution of the non-homogeneous Poisson equation, may be directly interfaced with the EDA to yield a solvation energy component construction.

Additionally, the important contribution of entropy was not considered in our calculations. This is an essential contribution to the total free energy of binding, and it would be valuable for quantitative understanding to capture this. This could, for example, take the form of a decomposition scheme for entropy, in which entropy contributions are calculated for the protein and ligand. Unfortunately, the calculation of entropy is a much more complicated problem than the enthalpy problem, and so this remains a goal outside the scope of the current work.

Accuracy of the results are also hindered by the fact that our studies considered only energy minimised structures at a temperature of 0K. Typically, drug binding is a transient process occurring in biomolecular assemblies at temperatures much greater than 0K. To remedy this, the calculation protocol may be adjusted by taking snapshots from molecular dynamics (MD) simulations and calculating average EDA component values for these samples.

Insight into the weaknesses of forcefields can be obtained by comparing the energy terms of a given EDA approach with the molecular mechanics potential [270]. For example, Tafipolsky and Ansorg [23] used the SAPT scheme to investigate hydrogen bond directionality, proposing a number of modifications to the design of forcefields to improve the description of non-bonded interactions. The ONETEP EDA would also be applicable to forcefield analysis, potentially able to identify specific atoms in large systems with ill-suited forcefield parameters. Importantly, EDA has the potential for use in automated forcefield parameterisation. Our scheme has the benefit of being able to calculate energy components of very large systems, and so may be applicable to the tailored parameterisation of next-generation forcefields for large systems, for example proteins.

Appendices

Appendix A

EDA benchmarking tests

Table A.1: The BLYP/6-311G* level ALMO EDA and NEDA results performed on the BLYP-D3/6-311G* optimised geometries of test sets 1 and 2.

Energy Term (kcal/mol)	H ₂ O H ₂ O	H ₂ O MeOH	MeOH MeOH	H ₂ O H ₃ N	H ₂ O H ₄ N ⁺	H ₂ O Li ⁺	H ₂ O Na ⁺	H ₂ O K ⁺
<u>ALMO EDA</u>								
FRZ (ALMO)	-1.99	-0.10	0.21	-2.35	-12.84	-31.01	-23.34	-16.39
POL (ALMO)	-0.82	-0.98	-1.19	-1.60	-5.38	-7.22	-4.04	-2.63
CT (ALMO)	-5.93	-7.45	-7.10	-5.62	-10.02	-5.74	-4.48	-4.28
CT+BSSE (ALMO)	-2.11	-2.49	-2.77	-2.33	-7.20	-0.91	-0.87	-1.55
ΔE (BLYP)	-4.92	-3.57	-3.75	-6.28	-25.43	-39.14	-28.24	-20.56
DISP ^a	-0.95	-1.96	-2.56	-1.16	-1.21	-0.10	-0.38	-0.63
ΔE (BLYP-D3)	-5.87	-5.53	-6.31	-7.44	-26.64	-39.23	-28.62	-21.19
<u>NEDA</u>								
ES (NEDA)	-12.04	-11.68	-12.20	-15.49	-31.70	-40.71	-31.74	-24.66
XC (NEDA)	-2.58	-3.17	-3.55	-3.12	-4.95	-3.73	-3.75	-3.24
POL (NEDA)	-1.08	-2.70	-4.02	-1.86	-5.07	-17.85	-15.57	-13.59
DEF (NEDA)	24.62	28.26	31.49	32.51	55.20	32.22	28.97	25.66
CT (NEDA)	-13.84	-14.29	-15.49	-18.35	-38.90	-8.97	-5.89	-4.67
ΔE	-4.92	-3.58	-3.76	-6.30	-25.43	-39.04	-28.00	-20.51
POL + SE ^b	-0.57	-1.33	-2.01	-0.93	-2.40	-8.88	-7.75	-6.70
CORE (DEF + XC - SE ^b)	21.53	23.72	25.93	28.46	47.58	19.52	17.40	15.53
EL (ES + POL + SE ^b)	-12.61	-13.01	-14.21	-16.42	-34.10	-49.59	-39.49	-31.36

^a The dispersion component DISP has been calculated as the Grimme D3 correction to the interaction energy.

^b The self-energy component of NEDA does not contribute to ΔE .

Table A.2: The BLYP/6-311G* level DCBS and MCBS SAPT(KS) results performed on the BLYP-D3/6-311G* optimised geometries of test sets 1 and 2.

Energy Term (kcal/mol)	H ₂ O H ₂ O	H ₂ O MeOH	MeOH MeOH	H ₂ O H ₃ N	H ₂ O H ₄ N ⁺	H ₂ O Li ⁺	H ₂ O Na ⁺	H ₂ O K ⁺
<u>SAPT(KS) DCBS</u>								
E1(elst)	-12.04	-11.67	-12.18	-15.46	-31.74	-40.76	-32.25	-25.07
E1(exch)	13.65	14.87	15.68	18.06	25.13	16.53	11.76	10.51
E2(ind)	-6.59	-7.47	-8.12	-9.50	-17.53	-25.02	-21.47	-16.13
E2(exch-ind)	4.88	5.79	6.18	6.57	8.01	10.99	13.59	11.31
E2(disp)	-2.64	-4.01	-5.08	-3.98	-4.47	-0.58	-0.64	-2.28
E2(exch-disp)	0.84	1.16	1.30	1.27	0.91	0.09	0.21	0.53
E1 corrections	1.60	3.20	3.50	2.59	-6.61	-24.23	-20.49	-14.55
E2 corrections	-3.51	-4.52	-5.71	-5.65	-13.09	-14.52	-8.31	-6.57
SAPT(0) ΔE	-1.90	-1.32	-2.22	-3.05	-19.70	-38.75	-28.80	-21.12
<u>SAPT(KS) MCBS</u>								
E2(ind) ^a	-0.99	-1.09	-1.28	-1.78	-7.34	-13.98	-7.19	-4.23
E2(exch-ind) ^a	0.13	0.16	0.25	0.06	0.63	1.84	0.74	0.23
POL+EXCH ^a	-0.85	-0.93	-1.03	-1.71	-6.72	-12.13	-6.45	-4.00
CT ^a	-5.60	-6.38	-6.84	-7.73	-10.19	-11.04	-14.27	-11.90
CT EXCH ^a	4.75	5.63	5.94	6.50	7.38	9.14	12.85	11.08
CT+EXCH ^a	-0.85	-0.75	-0.90	-1.22	-2.81	-1.90	-1.42	-0.82

^a The MCBS calculation of the ‘E2(ind)’ component is used as the SAPT polarisation component, and the MCBS ‘E2(exch-ind)’ component is used as the SAPT exchange correction for polarisation. The charge transfer component is calculated using these MCBS values and the equivalent DCBS values of these SAPT terms.

Table A.3: The HF/6-311G* level KM EDA and RVS EDA results performed on the BLYP-D3/6-311G* optimised geometries of test sets 1 and 2.

Energy Term (kcal/mol)	H ₂ O H ₂ O	H ₂ O MeOH	MeOH MeOH	H ₂ O H ₃ N	H ₂ O H ₄ N ⁺	H ₂ O Li ⁺	H ₂ O Na ⁺	H ₂ O K ⁺
<u>KM EDA</u>								
ES (KM)	-10.45	-9.40	-10.11	-14.84	-32.97	-44.14	-31.83	-23.66
EX (KM)	7.78	8.22	9.25	12.19	19.33	11.55	7.10	5.97
EX+BSSE (KM)	7.94	8.50	9.51	12.32	19.44	11.55	7.15	6.10
POL (KM)	-0.88	-0.95	-1.12	-1.60	-5.65	-9.37	-4.80	-2.96
CT (KM)	-2.59	-2.99	-3.06	-3.03	-6.52	-3.40	-2.06	-2.02
CT+BSSE (KM)	-1.60	-2.09	-2.22	-1.72	-5.22	-0.81	-0.24	-0.92
MIX (KM)	-0.08	-0.56	-0.52	0.15	1.38	3.29	1.52	0.83
MIX+BSSE (KM)	0.82	0.94	0.84	0.63	1.65	3.66	1.93	1.14
<u>RVS EDA</u>								
CEX (RVS)	-2.67	-1.17	-0.87	-2.65	-13.64	-32.59	-24.73	-17.68
POL (RVS)	-0.91	-1.04	-1.23	-1.70	-5.11	-6.61	-3.63	-2.38
CT+BSSE (RVS) ^a	-1.52	-2.35	-2.41	-1.41	-3.95	0.05	0.34	-0.48
MIX (RVS)	-0.02	-0.10	-0.11	-0.03	-0.33	-0.02	-0.03	-0.10
$\Delta E(\text{RVS/KM})$	-6.21	-5.68	-5.56	-7.13	-24.43	-42.07	-30.07	-21.84
$\Delta E(\text{RVS})+\text{BSSE}(\text{RVS})$	-5.12	-4.66	-4.62	-5.79	-23.03	-39.17	-28.05	-20.64
$\Delta E(\text{KM})+\text{BSSE}(\text{KM})$	-4.17	-3.01	-3.10	-5.21	-22.76	-39.12	-27.79	-20.30

^a In the RVS EDA theory the charge transfer component includes a BSSE contribution implicitly. We have labelled this component ‘CT+BSSE’ to clarify this.

Table A.4: The BLYP/6-311G* level ALMO EDA and NEDA results performed on the BLYP-D3/6-311G* optimised geometries of test sets 3 and 4.

Energy Term (kcal/mol)	H ₄ N ⁺ – Benzene	H ₄ N ⁺ – Thiophene	H ₄ N ⁺ – Furan	H ₄ N ⁺ – Pyrrole	Benzene – H ₄ N ⁺	Benzene – Li ⁺	Benzene – Na ⁺	Benzene – K ⁺
<u>ALMO EDA</u>								
FRZ (ALMO)	-2.62	-2.16	-1.21	-5.49	-2.62	-7.85	-9.16	-6.11
POL (ALMO)	-7.09	-6.91	-6.45	-7.67	-7.09	-20.84	-5.18	-2.83
CT (ALMO)	-6.92	-7.03	-7.21	-8.66	-6.92	-10.66	-4.13	-2.41
CT+BSSE (ALMO)	-6.30	-6.22	-6.45	-7.91	-6.30	-9.17	-3.24	-1.97
ΔE (BLYP)	-16.01	-15.28	-14.11	-21.07	-16.01	-37.87	-17.59	-10.90
DISP ^a	-5.45	-5.12	-4.67	-4.64	-5.45	-0.32	-5.95	-7.82
ΔE (BLYP-D3)	-21.46	-20.41	-18.78	-25.72	-21.46	-38.19	-23.54	-18.72
<u>NEDA</u>								
ES (NEDA)	-14.38	-13.91	-12.62	-20.21	-14.38	-16.65	-10.35	-6.94
XC (NEDA)	-5.47	-5.18	-4.69	-5.49	-5.47	-5.01	-0.18	-0.22
POL (NEDA)	-18.03	-16.82	-14.12	-14.65	-18.03	-34.94	-8.65	-10.00
DEF (NEDA)	34.01	34.03	31.89	38.01	34.01	40.55	6.85	7.34
(SE (NEDA) ^b)	9.14	8.52	7.13	7.43	9.14	17.58	4.34	5.03
CT (NEDA)	-12.33	-13.77	-14.70	-18.89	-12.33	-22.07	-5.36	-1.17
ΔE (BLYP)	-16.20	-15.64	-14.24	-21.22	-16.20	-38.12	-17.69	-10.98
POL + SE ^b	-8.89	-8.30	-6.99	-7.22	-8.89	-17.36	-4.31	-4.97
CORE (DEF + XC - SE ^b)	19.40	20.33	20.07	25.09	19.40	17.96	2.33	2.09
EL (ES + POL + SE ^b)	-23.27	-22.21	-19.61	-27.43	-23.27	-34.01	-14.66	-11.91

^a The dispersion component DISP has been calculated as the Grimme D3 correction to the interaction energy.

^b The self-energy component of NEDA does not contribute to ΔE .

Table A.5: The BLYP/6-311G* level DCBS and MCBS SAPT(KS) results performed on the BLYP-D3/6-311G* optimised geometries of test sets 3 and 4.

Energy Term (kcal/mol)	H ₄ N ⁺ – Benzene	H ₄ N ⁺ – Thiophene	H ₄ N ⁺ – Furan	H ₄ N ⁺ – Pyrrole	Benzene – H ₄ N ⁺	Benzene – Li ⁺	Benzene – Na ⁺	Benzene – K ⁺
SAPT(KS) DCBS								
E1(elst)	-14.39	-13.66	-12.65	-20.24	-14.39	-16.65	-10.41	-7.58
E1(exch)	13.34	13.38	12.96	16.66	13.34	12.66	0.91	0.61
E2(ind)	-19.03	-19.09	-16.92	-21.62	-19.03	-54.58	-11.93	-6.09
E2(exch-ind)	5.86	5.93	5.58	8.20	5.86	11.16	1.30	0.68
E2(displ)	-7.39	-7.09	-6.68	-7.79	-7.39	-1.06	-0.33	-1.25
E2(exch-displ)	0.83	0.80	0.75	1.03	0.83	0.08	0.02	0.04
E1 corrections	-1.05	-0.28	0.31	-3.58	-1.05	-3.99	-9.49	-6.97
E2 corrections	-19.73	-19.45	-17.27	-20.18	-19.73	-44.40	-10.95	-6.62
SAPT(0) ΔE	-20.78	-19.72	-16.96	-23.77	-20.78	-48.39	-20.44	-13.59
SAPT(KS) MCBS								
E2(ind) ^a	-12.03	-12.30	-11.10	-13.20	-12.03	-38.90	-8.60	-4.69
E2(exch-ind) ^a	0.62	0.93	0.98	1.32	0.62	2.87	0.04	0.00
POL+EXCH ^a	-11.41	-11.38	-10.12	-11.88	-11.41	-36.03	-8.57	-4.69
CT ^a	-7.00	-6.79	-5.82	-8.42	-7.00	-15.68	-3.33	-1.40
CT EXCH ^a	5.24	5.01	4.60	6.88	5.24	8.29	1.26	0.68
CT+EXCH ^a	-1.76	-1.78	-1.22	-1.54	-1.76	-7.39	-2.07	-0.72

^a The MCBS calculation of the ‘E2(ind)’ component is used as the SAPT polarisation component, and the MCBS ‘E2(exch-ind)’ component is used as the SAPT exchange correction for polarisation. The charge transfer component is calculated using these MCBS values and the equivalent DCBS values of these SAPT terms.

Table A.6: The HF/6-311G* level KM EDA and RVS EDA results performed on the BLYP-D3/6-311G* optimised geometries of test sets 3 and 4.

Energy Term (kcal/mol)	H ₄ N ⁺ – Benzene	H ₄ N ⁺ – Thiophene	H ₄ N ⁺ – Furan	H ₄ N ⁺ – Pyrrole	Benzene – H ₄ N ⁺	Benzene – Li ⁺			Benzene – Na ⁺	Benzene – K ⁺
	6-311G*	6-311G*	6-311G*	6-311G*	6-311G*	BS1 ^(a,b)	6-311G ^a	6-311G* ^a	6-311G*	6-311G*
<u>KM EDA</u>										
ES (KM)	-16.19	-15.00	-13.51	-21.78	-16.19	-22.61	-20.13	-22.61	-11.80	-8.41
EX (KM)	12.02	12.01	11.39	15.20	12.02	12.55	12.43	12.55	0.51	0.44
EX+BSSE (KM)	12.12	12.13	11.48	15.30	12.12	12.57	12.45	12.57	0.52	0.45
POL (KM)	-8.34	-8.05	-7.97	-9.96	-8.34	-25.86	-22.56	-410.54	-5.53	-4.70
CT (KM)	-5.57	-5.40	-5.66	-6.67	-5.57	-15.39	-15.34	-18.47	-4.59	-1.21
CT+BSSE (KM)	-5.26	-5.07	-5.29	-6.33	-5.26	-14.90	-14.86	-17.80	-4.10	-1.17
MIX (KM)	2.42	2.40	2.91	3.53	2.42	11.51	9.86	397.97	1.64	1.47
MIX+BSSE (KM)	2.62	2.68	3.13	3.76	2.62	11.79	10.23	398.24	1.80	1.51
<u>RVS EDA</u>										
CEX (RVS)	-4.17	-2.98	-2.12	-6.58	-4.17	-10.06	-7.70	-10.06	-11.29	-7.97
POL (RVS)	-7.16	-6.76	-6.33	-7.53	-7.16	-21.36	-18.33	-21.36	-5.45	-4.07
CT+BSSE (RVS) ^c	-3.68	-3.65	-3.73	-4.74	-3.68	-7.69	-9.02	-8.81	-2.45	-0.25
MIX (RVS)	-0.32	-0.29	-0.26	-0.44	-0.32	-0.01	0.00	-0.02	-0.01	-0.07
ΔE (RVS/KM)	-15.67	-14.04	-12.85	-19.67	-15.67	-39.80	-35.74	-41.09	-19.76	-12.40
ΔE (RVS) +BSSE(RVS)	-15.33	-13.68	-12.44	-19.29	-15.33	-39.12	-35.05	-40.25	-19.20	-12.36
ΔE (KM) +BSSE(KM)	-15.05	-13.32	-12.16	-19.01	-15.05	-39.01	-34.86	-40.15	-19.11	-12.32

^a The geometry used for this calculation was obtained at the BLYP-D3/6-311G* level.

^b The basis set BS1 is the 6-311G* basis set excluding d polarisation function augmentation on lithium.

^c In the RVS EDA theory the charge transfer component includes a BSSE contribution implicitly. We have labelled this component ‘CT+BSSE’ to clarify this.

Table A.7: The BLYP/6-311G* level ALMO EDA and NEDA results performed on the BLYP-D3/6-311G* optimised geometries of test sets 5 and 6.

Energy Term (kcal/mol)	Benzene – T-shaped	Benzene – Parallel displaced	Benzene – Pyridine	Benzene – Pyrimidine	Benzene – DMA ^a	Benzene – F-benzene ^a	Benzene – Cl-benzene ^a	Benzene – Br-benzene ^a
<u>ALMO EDA</u>								
FRZ (ALMO)	2.11	5.30	4.88	4.23	4.25	2.49	2.44	2.30
POL (ALMO)	-0.15	-0.24	-0.23	-0.22	-0.42	-0.12	-0.10	-0.11
CT (ALMO)	-1.09	-1.44	-1.69	-1.87	-2.53	-1.27	-0.64	-0.85
CT+BSSE (ALMO)	-0.20	-0.11	-0.14	-0.21	-0.80	0.33	-0.27	-0.34
ΔE (BLYP)	1.76	4.94	4.51	3.80	3.04	2.70	2.08	1.85
DISP ^b	-4.82	-7.30	-7.58	-7.72	-8.98	-2.54	-3.50	-4.15
ΔE (BLYP-D3)	-3.06	-2.36	-3.07	-3.91	-5.94	0.15	-1.42	-2.30
<u>NEDA</u>								
ES (NEDA)	-2.18	-2.57	-3.47	-4.21	-5.60	0.19	-0.82	-1.50
XC (NEDA)	-2.46	-4.85	-5.19	-5.25	-4.92	-1.38	-1.53	-1.70
POL (NEDA)	-4.82	-11.91	-12.75	-13.08	-10.86	-2.41	-4.36	-5.74
DEF (NEDA)	14.13	29.12	31.52	32.47	31.44	7.69	10.02	12.23
(SE (NEDA) ^c)	2.43	5.96	6.39	6.56	5.45	1.19	2.17	2.87
CT (NEDA)	-2.93	-4.85	-5.59	-6.11	-7.01	-1.42	-1.23	-1.44
ΔE (BLYP)	1.74	4.94	4.51	3.81	3.05	2.66	2.08	1.85
POL + SE ^c	-2.39	-5.95	-6.36	-6.52	-5.41	-1.22	-2.19	-2.87
CORE (DEF + XC - SE ^c)	9.24	18.31	19.94	20.66	21.07	5.12	6.32	7.66
EL (ES + POL + SE ^c)	-4.57	-8.52	-9.83	-10.73	-11.01	-1.03	-3.01	-4.37

^a DMA, F-benzene, Cl-benzene, and Br-benzene refer to dimethylacetamide, fluorobenzene, chlorobenzene, and bromobenzene respectively.

^b The dispersion component DISP has been calculated as the Grimme D3 correction to the interaction energy.

^c The self-energy component of NEDA does not contribute to ΔE .

Table A.8: The BLYP/6-311G* level DCBS and MCBS SAPT(KS) results performed on the BLYP-D3/6-311G* optimised geometries of test sets 5 and 6.

Energy Term (kcal/mol)	Benzene – T-shaped	Benzene – Parallel displaced	Benzene – Pyridine	Benzene – Pyrimidine	Benzene – DMA ^a	Benzene – F-benzene ^a	Benzene – Cl-benzene ^a	Benzene – Br-benzene ^a
SAPT(KS) DCBS								
E1(elst)	-2.18	-2.60	-3.51	-4.25	-5.63	0.20	-0.91	-1.50
E1(exch)	4.96	8.46	9.15	9.33	10.94	3.28	3.43	3.92
E2(ind)	-1.55	-4.26	-4.59	-4.77	-5.12	-1.16	-1.60	-2.51
E2(exch-ind)	1.32	3.90	4.29	4.48	4.58	0.97	1.42	2.26
E2(displ)	-7.25	-13.41	-14.06	-14.22	-13.97	-3.70	-4.69	-5.81
E2(exch-displ)	0.86	2.00	2.05	2.01	1.93	0.39	0.56	0.69
E1 corrections	2.78	5.86	5.65	5.08	5.32	3.48	2.52	2.42
E2 corrections	-6.62	-11.78	-12.31	-12.49	-12.57	-3.49	-4.31	-5.36
SAPT(0) ΔE	-3.84	-5.92	-6.66	-7.41	-7.26	-0.02	-1.79	-2.94
SAPT(KS) MCBS								
E2(ind) ^b	-0.24	-0.41	-0.34	-0.30	-0.56	-0.18	-0.14	-0.17
E2(exch-ind) ^b	0.06	0.04	0.03	0.03	0.09	0.01	0.00	0.00
POL+EXCH ^b	-0.18	-0.37	-0.31	-0.27	-0.47	-0.18	-0.13	-0.17
CT ^b	-1.31	-3.85	-4.25	-4.47	-4.56	-0.97	-1.46	-2.34
CT EXCH ^b	1.26	3.86	4.25	4.45	4.50	0.97	1.42	2.26
CT+EXCH ^b	-0.05	0.01	0.00	-0.01	-0.07	-0.01	-0.05	-0.08

^a DMA, F-benzene, Cl-benzene, and Br-benzene refer to dimethylacetamide, fluorobenzene, chlorobenzene, and bromobenzene respectively.

^b The MCBS calculation of the ‘E2(ind)’ component is used as the SAPT polarisation component, and the MCBS ‘E2(exch-ind)’ component is used as the SAPT exchange correction for polarisation. The charge transfer component is calculated using these MCBS values and the equivalent DCBS values of these SAPT terms.

Table A.9: The HF/6-311G* level KM EDA and RVS EDA results performed on the BLYP-D3/6-311G* optimised geometries of test sets 5 and 6.

Energy Term (kcal/mol)	Benzene – T-shaped	Benzene – Parallel displaced	Benzene – Pyridine	Benzene – Pyrimidine	Benzene – DMA ^a	Benzene – F-benzene ^a	Benzene – Cl-benzene ^a	Benzene – Br-benzene ^a
<u>KM EDA</u>								
ES (KM)	-1.79	-0.73	-1.76	-2.67	-4.38	1.29	-0.11	-0.84
EX (KM)	3.46	6.17	6.79	6.96	7.49	1.94	2.45	2.94
EX+BSSE (KM)	3.56	6.53	7.15	7.30	7.73	2.08	2.54	3.04
POL (KM)	-0.20	-0.29	-0.25	-0.24	-0.50	-0.16	-0.11	-0.13
CT (KM)	-0.73	-1.40	-1.56	-1.67	-1.68	-0.80	-0.46	-0.54
CT+BSSE (KM)	-0.48	-0.93	-1.04	-1.13	-1.09	-0.33	-0.31	-0.41
MIX (KM)	0.07	0.17	0.15	0.16	0.09	0.03	0.04	0.08
MIX+BSSE (KM)	0.31	0.58	0.57	0.59	0.61	0.40	0.20	0.23
<u>RVS EDA</u>								
CEX (RVS)	1.67	5.44	5.04	4.29	3.10	3.23	2.35	2.10
POL (RVS)	-0.19	-0.34	-0.30	-0.27	-0.46	-0.21	-0.14	-0.15
CT+BSSE (RVS) ^b	-0.37	-0.69	-0.79	-0.88	-0.90	-0.25	-0.23	-0.30
MIX (RVS)	-0.02	0.02	-0.01	-0.02	-0.06	0.02	0.01	0.01
$\Delta E(\text{RVS/KM})$	0.81	3.93	3.38	2.53	1.01	2.31	1.82	1.51
$\Delta E(\text{RVS})$ +BSSE(RVS)	1.09	4.43	3.94	3.12	1.68	2.79	1.99	1.66
$\Delta E(\text{KM})$ +BSSE(KM)	1.40	5.17	4.67	3.86	2.38	3.29	2.21	1.88

^a DMA, F-benzene, Cl-benzene, and Br-benzene refer to dimethylacetamide, fluorobenzene, chlorobenzene, and bromobenzene respectively.

^b In the RVS EDA theory the charge transfer component includes a BSSE contribution implicitly. We have labelled this component ‘CT+BSSE’ to clarify this.

Appendix B

EDA validation tests

Table B.1: The ALMO, LMO and ONETEP EDA energy components for the PBE-D2/aug-cc-pVTZ optimised systems of Test Set 1.

Energy Term (kcal/mol)	System			
	Water - Water	Methanol - Methanol	Water - Ammonia	Water - Ammonium
<u>ALMO EDA^a</u>				
FRZ	-0.7	0.1	0.1	-3.6
POL	-1.8	-2.4	-2.9	-10.8
CT	-2.6	-3.2	-4.5	-8.3
CT+BSSE	-2.6	-3.1	-4.4	-8.2
$\Delta E(\text{PBE}/\text{ACCT})$	-5.1	-5.3	-7.2	-22.6
$\Delta E(\text{PBE-D2}/\text{ACCT})$	-5.8	-6.5	-8.0	-23.5
<u>LMO EDA^a</u>				
ES	-9.4	-10.6	-13.5	-25.5
EX	-4.1	-4.8	-6.0	-6.7
REP	15.3	18.4	22.9	32.0
POL	-4.4	-5.4	-7.2	-17.8
DISP	-2.5	-2.9	-3.4	-4.8
$\Delta E(\text{PBE}/\text{ACCT})$	-5.1	-5.3	-7.2	-22.7
$\Delta E(\text{PBE-D2}/\text{ACCT})$	-5.8	-6.5	-8.0	-23.5
<u>ONETEP EDA^b</u>				
FRZ	-0.9 (-0.9)	-0.2 (-0.2)	-0.2 (-0.3)	-4.5 (-4.6)
ES	-9.0 (-9.1)	-9.8 (-9.8)	-12.7 (-12.7)	-25.3 (-25.5)
EX	-3.9 (-3.9)	-4.5 (-4.6)	-5.5 (-5.5)	-6.6 (-6.6)
REP	14.3 (14.3)	16.8 (16.8)	20.9 (21.0)	30.8 (30.8)
CORR	-2.3 (-2.3)	-2.6 (-2.6)	-3.0 (-3.0)	-3.4 (-3.4)
POL	-2.2 (-2.3)	-2.0 (-2.1)	-3.4 (-3.5)	-10.2 (-10.2)
CT	-2.0 (-2.0)	-3.3 (-3.2)	-3.9 (-3.8)	-8.4 (-8.3)
$\Delta E(\text{PBE})$	-5.1 (-5.2)	-5.5 (-5.5)	-7.5 (-7.5)	-23.1 (-23.1)
$\Delta E(\text{PBE-D2})$	-5.8 (-5.9)	-6.7 (-6.8)	-8.3 (-8.3)	-23.9 (-23.9)
<u>Grimme -D Correction</u>				
-D2 Correction	-0.7	-1.2	-0.8	-0.8
-D3 Correction ^c	-0.5	-1.0	-0.6	-0.6

^a Results were obtained at the PBE/aug-cc-pVTZ level of theory for the Gaussian basis set codes.

^b Results using a 1200eV psinc basis set cutoff are provided for the ONETEP code, with 800eV basis set cutoff results also provided in parenthesis to evidence convergence with respect to psinc basis set cutoff.

^c Grimme -D3 correction results are included for comparison.

Table B.2: The ALMO, LMO and ONETEP EDA energy components for the PBE-D2/aug-cc-pVTZ optimised systems of Test Set 2.

Energy Term (kcal/mol)	System			
	Benzene - Benzene	Benzene - Pyridine	Benzene - DMA	Benzene - Ammonium ^a
<u>ALMO EDA^b</u>				
FRZ	1.8	1.5	3.1	-0.3
POL	-0.3	-0.4	-1.2	-12.6
CT	-0.7	-0.8	-1.7	-5.0
CT+BSSE	0.0	-0.2	-1.3	-4.8
$\Delta E(\text{PBE/ACCT})$	1.4	0.8	0.7	-17.7
$\Delta E(\text{PBE-D2/ACCT})$	-2.3	-3.0	-5.2	-21.3
<u>LMO EDA^b</u>				
ES	-1.7	-2.4	-5.6	-12.7
EX	-2.3	-2.3	-4.1	-3.6
REP	9.9	10.0	18.9	19.9
POL	-1.6	-1.6	-2.9	-14.6
DISP	-2.9	-3.0	-5.7	-6.8
$\Delta E(\text{PBE/ACCT})$	1.3	0.8	0.6	-17.7
$\Delta E(\text{PBE-D2/ACCT})$	-2.4	-3.1	-5.2	-21.4
<u>ONETEP EDA^c</u>				
FRZ	2.1 (2.1)	1.7 (1.7)	3.2 (3.2)	0.0 (0.0)
ES	-1.2 (-1.2)	-1.9 (-1.9)	-5.2 (-5.2)	-12.1 (-12.2)
EX	-2.1 (-2.1)	-2.2 (-2.1)	-4.5 (-4.5)	-3.7 (-3.7)
REP	9.0 (9.0)	9.2 (9.3)	18.9 (18.8)	19.8 (19.8)
CORR	-3.5 (-3.5)	-3.5 (-3.5)	-5.9 (-5.9)	-3.9 (-3.9)
POL	-0.2 (-0.2)	-0.2 (-0.2)	-0.8 (-0.8)	-12.3 (-12.4)
CT	-0.4 (-0.4)	-0.5 (-0.5)	-1.3 (-1.4)	-4.6 (-4.6)
$\Delta E(\text{PBE})$	1.5 (1.5)	1.0 (1.0)	1.2 (1.1)	-16.9 (-17.0)
$\Delta E(\text{PBE-D2})$	-2.2 (-2.2)	-2.8 (-2.8)	-4.7 (-4.7)	-20.5 (-20.6)
<u>Grimme -D Correction</u>				
-D2 Correction	-3.7	-3.8	-5.8	-3.7
-D3 Correction ^d	-3.9	-3.9	-4.9	-2.7

^a The initial state of the benzene-ammonium polarisation stage was constructed using initial guess NGWFs. In all other calculations, this state was constructed using the converged fragment NGWFs.

^b Results were obtained at the PBE/aug-cc-pVTZ level of theory for the Gaussian basis set codes.

^c Results using a 1200eV psinc basis set cutoff are provided for the ONETEP code, with 800eV basis set cutoff results also provided in parenthesis to evidence convergence with respect to psinc basis set cutoff.

^d Grimme -D3 correction results are included for comparison.

Appendix C

Thrombin - C24 ligand EDA

Table C.1: The PBE-D2/800eV ONETEP EDA energy components of the thrombin-C24 systems.

ONETEP EDA (kcal/mol)	Truncation, Å			
	3.0	9.0	15.0	∞
FRZ	-23.9	-51.5	-35.7	-38.9
ES	-126.3	-162.8	-147.1	-150.3
EX	-49.6	-53.7	-53.7	-53.7
REP	210.5	228.6	228.7	228.7
CORR	-58.5	-63.6	-63.6	-63.6
POL	-26.9	-32.6	-32.9	-33.1
CT	-29.7	-35.3	-30.7	-31.2
$\Delta E(\text{PBE}/800\text{eV})$	-80.6	-119.5	-99.4	-103.2
-D2 Correction	-70.6	-79.3	-79.8	-79.9
-D3 Correction ^a	-72.6	-81.5	-82.1	-82.2
$\Delta E(\text{PBE-D2}/800\text{eV})$	-151.2	-198.8	-179.2	-183.1

^a Grimme -D3 correction results are included for comparison.

Appendix D

Thrombin - fragment binder EDA

Table D.1: The PBE-D2/800eV ONETEP EDA energy components of the full and fragmented thrombin-ligand systems 4UDW, 2ZGX and 5AFZ.

ONETEP EDA (kcal/mol)	4UDW					2ZGX					5AFZ				
	Full	F1	F2	F3	Error	Full	F1	F2	F3	Error	Full	F1	F2	F3	Error
FRZ	-31.5	3.5	7.9	-44.3	1.4	-95.0	-54.8	1.2	-42.6	1.2	-55.4	-62.4	4.2	0.3	2.6
ES	-116.5	-17.8	-28.4	-71.2	0.9	-208.3	-129.2	-20.5	-59.3	0.6	-169.7	-135.7	-11.4	-23.6	0.9
EX	-39.9	-12.3	-18.4	-12.7	3.5	-46.3	-27.8	-13.6	-7.9	3.1	-50.7	-27.7	-9.9	-16.4	3.3
REP	171.5	51.7	72.9	51.5	-4.6	204.7	127.8	49.8	31.0	-3.9	219.6	127.3	34.5	59.8	-2.1
CORR	-46.6	-18.0	-18.3	-11.9	1.6	-45.2	-25.6	-14.4	-6.5	1.4	-54.6	-26.4	-9.1	-19.5	0.5
POL	-20.1	-2.2	-4.5	-15.6	2.1	-55.0	-27.8	-3.0	-14.3	-9.9	-36.5	-28.1	-3.1	-3.5	-1.8
CT	-29.3	-5.6	-11.9	-14.2	2.5	-50.0	-34.0	-7.4	-11.1	2.5	-45.2	-33.8	-6.9	-7.9	3.3
$\Delta E(\text{PBE}/800\text{eV})$	-80.9	-4.3	-8.5	-74.1	6.0	-200.0	-116.6	-9.2	-68.0	-6.2	-137.2	-124.3	-5.8	-11.1	4.0
-D2 Correction	-58.6	-24.9	-19.3	-15.8	1.4	-52.1	-28.2	-17.3	-7.8	1.2	-64.4	-29.0	-10.2	-26.4	1.2
-D3 Correction ^a	-64.3	-28.5	-20.1	-17.7	2.1	-55.6	-30.4	-18.5	-8.6	1.9	-71.1	-31.3	-11.5	-30.2	1.9
$\Delta E(\text{PBE-D2}/800\text{eV})$	-139.5	-29.1	-27.8	-90.0	7.4	-252.1	-144.8	-26.5	-75.8	-5.0	-201.6	-153.3	-16.0	-37.6	5.3
ΔE_{desolv}	64.3	-1.1	15.5	66.6	-16.8	141.0	52.3	15.3	67.1	6.4	73.6	52.5	18.6	9.5	-7.0
$\Delta E(\text{PBE-D2}/800\text{eV})$ + ΔE_{desolv}	-75.2	-30.2	-12.3	-23.3	-9.4	-111.1	-92.5	-11.3	-8.7	1.4	-128.0	-100.8	2.6	-28.1	-1.7

^a Grimme -D3 correction results are included for comparison.

Table D.2: The PBE-D2/800eV ONETEP EDA energy components of the thrombin S1 pocket binder systems 4UD9, 5AFY, 5AHG, 5AF9, 4UEH, and 4UE7.

ONETEP EDA (kcal/mol)	4UD9	5AFY	5AHG	5AF9	4UEH	4UE7
FRZ	2.7	2.8	2.1	2.1	-69.3	-57.6
ES	-33.1	-30.3	-35.2	-33.2	-136.2	-121.0
EX	-17.2	-16.5	-19.5	-19.1	-25.1	-25.2
REP	74.7	69.7	82.8	80.4	115.8	113.0
CORR	-21.7	-20.2	-26.0	-25.9	-23.8	-24.4
POL	-6.5	-5.3	-6.1	-4.5	-28.3	-27.0
CT	-14.0	-11.1	-11.4	-11.2	-33.3	-30.7
$\Delta E(\text{PBE}/800\text{eV})$	-17.8	-13.6	-15.4	-13.6	-130.9	-115.3
-D2 Correction	-25.1	-25.2	-32.0	-35.2	-25.5	-26.7
-D3 Correction ^a	-28.7	-28.6	-35.9	-38.5	-27.8	-28.0
$\Delta E(\text{PBE-D2}/800\text{eV})$	-42.9	-38.8	-47.5	-48.9	-156.4	-142.0
ΔE_{desolv}	8.8	9.0	8.6	7.2	54.6	50.6
$\Delta E(\text{PBE-D2}/800\text{eV})$ + ΔE_{desolv}	-34.2	-29.8	-38.9	-41.6	-101.8	-91.4

^a Grimme -D3 correction results are included for comparison.

References

- [1] N. Schwierz, C. V. Frost, P. L. Geissler, and M. Zacharias, *J. Am. Chem. Soc.* **138**, 527 (2016).
- [2] C. Acquah, M. Cagnetta, L. E. K. Achenie, S. L. Suib, and A. T. Karunanithi, *Ind. Eng. Chem. Res.* **54**, 12108 (2015).
- [3] A. Barik, N. C, S. P. Pilla, and R. P. Bahadur, *J. Biomol. Struct. Dyn.* **33**, 2738 (2015).
- [4] E. Wu, Y. Qi, S. Park, S. Mallajosyula, A. MacKerell Jr., J. Klauda, and W. Im, *Biophys. J.* **109**, 2090 (2015).
- [5] R.-P. Ye, J.-X. Yang, X. Zhang, L. Zhang, and Y.-G. Yao, *J. Mol. Struct.* **1106**, 192 (2016).
- [6] X. Liu, H. Dong, D. Hu, H. Shen, B. Zheng, B. Ling, and J. Bi, *Mol. Cryst. Liq. Cryst.* **623**, 319 (2015).
- [7] S. S. Tafreshi, A. Roldan, and N. H. de Leeuw, *Surf. Sci.* **637-638**, 140 (2015).
- [8] P. V. Jasen, G. Brizuela, Z. Padin, E. A. Gonzalez, and A. Juan, *Appl. Surf. Sci.* **236**, 394 (2004).
- [9] K. Morokuma, *J. Chem. Phys.* **55**, 1236 (1971).
- [10] W. J. Stevens and W. H. Fink, *Chem. Phys. Lett.* **139**, 15 (1987).
- [11] P. S. Bagus, K. Hermann, and C. W. Bauschlicher, *J. Chem. Phys.* **80**, 4378 (1984).

- [12] E. D. Glendening and A. Streitwieser, J. Chem. Phys. **100**, 2900 (1994).
- [13] E. D. Glendening, J. Phys. Chem. A. **109**, 11936 (2005).
- [14] P. Su and H. Li, J. Chem. Phys. **131**, 014102 (2009).
- [15] R. Z. Khaliullin, E. A. Cobar, R. C. Lochan, A. T. Bell, and M. Head-Gordon, J. Phys. Chem. A **111**, 8753 (2007).
- [16] Q. Wu, P. W. Ayers, and Y. Zhang, J. Chem. Phys. **131**, 164112 (2009).
- [17] B. Jeziorski, R. Moszynski, A. Ratkiewicz, S. Rybak, K. Szalewicz, and H. L. Williams, *Methods and Techniques in Computational Chemistry: METECC-94*, volume B, chapter 13, pages 79–129, STEF, Cagliari, 1993.
- [18] B. Jeziorski, R. Moszynski, and K. Szalewicz, Chem. Rev. **94**, 1887 (1994).
- [19] M. P. Mitoraj, A. Michalak, and T. Ziegler, J. Chem. Theory Comput. **5**, 962 (2009).
- [20] T. A. N. Nguyen and G. Frenking, Chem. Eur. J. **18**, 12733 (2012).
- [21] S. Ndambuki and T. Ziegler, Inorg. Chem. **51**, 7794 (2012).
- [22] M. P. Mitoraj and A. Michalak, J. Mol. Model. **19**, 4681 (2013).
- [23] M. Tafipolsky and K. Ansorg, J. Chem. Theory Comp. **12**, 1267 (2016).
- [24] J. G. McDaniel and J. Schmidt, Annu. Rev. Phys. Chem. **67**, 467 (2016).
- [25] A. J. Misquitta, R. Podeszwa, B. Jeziorski, and K. Szalewicz, J. Chem. Phys. **123**, 214103 (2005).
- [26] A. Szabo and N. S. Ostlund, *Modern Quantum Chemistry*, Dover Publishing, New York, 1996.
- [27] M. Born and R. Oppenheimer, Ann. Phys. **389**, 457 (1927).
- [28] W. Pauli, Z. Physik **31**, 765 (1925).
- [29] D. A. Hartree, Proc. Camb. Phil. Soc. **24**, 89 (1928).

- [30] V. Fock, Z. Phys. **61**, 126 (1930).
- [31] C. Møller and M. S. Plesset, Phys. Rev. **46**, 618 (1934).
- [32] J. Čížek, J. Chem. Phys. **45**, 4256 (1966).
- [33] B. Roos, Chem. Phys. Lett. **15**, 153 (1972).
- [34] B. O. Roos, P. R. Taylor, and P. E. Siegbahn, Chem. Phys. **48**, 157 (1980).
- [35] L. H. Thomas, Proc. Camb. Phil. Soc. **23**, 542 (1927).
- [36] E. Fermi, Z. Physik **48**, 73 (1928).
- [37] P. A. M. Dirac, Math. Proc. Camb. Phil. Soc. **26**, 376 (1930).
- [38] P. Hohenberg and W. Kohn, Phys. Rev. **136**, B864 (1964).
- [39] C.-K. Skylaris, P. D. Haynes, A. A. Mostofi, and M. C. Payne, J. Chem. Phys. **122**, 084119 (2005).
- [40] W. Kohn and L. J. Sham, Phys. Rev. **140**, A1133 (1965).
- [41] S. H. Vosko, L. Wilk, and M. Nusair, Can. J. Phys. **58**, 1200 (1980).
- [42] J. P. Perdew and Y. Wang, Phys. Rev. B **45**, 13244 (1992).
- [43] J. P. Perdew, *Electronic Structure of Solids '91*, page 11, Akademie Verlag, Berlin, 1991.
- [44] J. P. Perdew, K. Burke, and M. Ernzerhof, Phys. Rev. Lett. **77**, 3865 (1996).
- [45] J. P. Perdew, S. Kurth, A. Zupan, and P. Blaha, Phys. Rev. Lett. **82**, 2544 (1999).
- [46] M. Filatov and W. Thiel, Phys. Rev. A **57**, 189 (1998).
- [47] A. D. Becke, J. Chem. Phys. **98**, 5648 (1993).
- [48] A. D. Becke, Phys. Rev. A **38**, 3098 (1988).
- [49] C. Lee, W. Yang, and R. G. Parr, Phys. Rev. B **37**, 785 (1988).

- [50] P. J. Stephens, F. J. Devlin, C. F. Chabalowski, and M. J. Frisch, *J. Chem. Phys.* **98**, 11623 (1994).
- [51] J. C. Slater, *Phys. Rev.* **36**, 57 (1930).
- [52] E. R. Davidson and D. Feller, *Chem. Rev.* **86**, 681 (1986).
- [53] S. F. Boys, *Proc. R. Soc. Lond. A* **200**, 542 (1950).
- [54] Y. Shao, L. F. Molnar, Y. Jung, J. Kussmann, C. Ochsenfeld, S. T. Brown, A. T. Gilbert, L. V. Slipchenko, S. V. Levchenko, D. P. O'Neill, R. A. DiStasio Jr, R. C. Lochan, T. Wang, G. J. Beran, N. A. Besley, J. M. Herbert, C. Yeh Lin, T. Van Voorhis, S. Hung Chien, A. Sodt, R. P. Steele, V. A. Rassolov, P. E. Maslen, P. P. Korambath, R. D. Adamson, B. Austin, J. Baker, E. F. C. Byrd, H. Dachsel, R. J. Doerksen, A. Dreuw, B. D. Dunietz, A. D. Dutoi, T. R. Furlani, S. R. Gwaltney, A. Heyden, S. Hirata, C.-P. Hsu, G. Kedziora, R. Z. Khalliulin, P. Klunzinger, A. M. Lee, M. S. Lee, W. Liang, I. Lotan, N. Nair, B. Peters, E. I. Proynov, P. A. Pieniazek, Y. Min Rhee, J. Ritchie, E. Rosta, C. David Sherrill, A. C. Simmonett, J. E. Subotnik, H. Lee Woodcock III, W. Zhang, A. T. Bell, A. K. Chakraborty, D. M. Chipman, F. J. Keil, A. Warshel, W. J. Hehre, H. F. Schaefer III, J. Kong, A. I. Krylov, P. M. W. Gill, and M. Head-Gordon, *Phys. Chem. Chem. Phys.* **8**, 3172 (2006).
- [55] M. Valiev, E. J. Bylaska, N. Govind, K. Kowalski, T. P. Straatsma, H. J. J. van Dam, D. Wang, J. Nieplocha, E. Apra, T. L. Windus, and W. A. de Jong, *Comput. Phys. Commun.* **181**, 1477 (2010).
- [56] M. W. Schmidt, K. K. Baldridge, J. A. Boatz, S. T. Elbert, M. S. Gordon, J. H. Jensen, S. Koseki, N. Matsunaga, K. A. Nguyen, S. Su, T. L. Windus, M. Dupuis, and J. A. Montgomery, *J. Comput. Chem.* **14**, 1347 (1993).
- [57] S. J. Clark, M. D. Segall, C. J. Pickard, P. J. Hasnip, M. J. Probert, K. Refson, and M. C. Payne, *Z. Kristallogr.* **220**, 567 (2005).

-
- [58] P. Giannozzi, S. Baroni, N. Bonini, M. Calandra, R. Car, C. Cavazzoni, D. Ceresoli, G. L. Chiarotti, M. Cococcioni, I. Dabo, A. D. Corso, S. de Gironcoli, S. Fabris, G. Fratesi, R. Gebauer, U. Gerstmann, C. Gougoussis, A. Kokalj, M. Lazzeri, L. Martin-Samos, N. Marzari, F. Mauri, R. Mazzarello, S. Paolini, A. Pasquarello, L. Paulatto, C. Sbraccia, S. Scandolo, G. Sclauzero, A. P. Seitsonen, A. Smogunov, P. Umari, and R. M. Wentzcovitch, *J. Phys.: Condens. Matter* **21**, 395502 (2009).
- [59] C.-K. Skylaris, A. A. Mostofi, P. D. Haynes, O. Diéguez, and M. C. Payne, *Phys. Rev. B* **66**, 035119 (2002).
- [60] F. B. van Duijneveldt, J. G. C. M. van Duijneveldt-van de Rijdt, and J. H. van Lenthe, *Chem. Rev.* **94**, 1873 (1994).
- [61] S. F. Boys and F. Bernardi, *Mol. Phys.* **19**, 553 (1970).
- [62] A. Johansson, P. Kollman, and S. Rothenberg, **29**, 167 (1973).
- [63] D. R. Hamann, M. Schlüter, and C. Chiang, *Phys. Rev. Lett.* **43**, 1494 (1979).
- [64] L. Kleinman and D. M. Bylander, *Phys. Rev. Lett.* **48**, 1425 (1982).
- [65] T. V. Russo, R. L. Martin, and P. J. Hay, *J. Phys. Chem.* **99**, 17085 (1995).
- [66] D. Vanderbilt, *Phys. Rev. B* **41**, 7892 (1990).
- [67] P. E. Blöchl, *Phys. Rev. B* **50**, 17953 (1994).
- [68] S. Goedecker, *Rev. Mod. Phys.* **71**, 1085 (1999).
- [69] D. R. Bowler and T. Miyazaki, *Rep. Prog. Phys.* **75**, 036503 (2012).
- [70] W. Kohn, *Phys. Rev. Lett.* **76**, 3168 (1996).
- [71] E. Prodan and W. Kohn, *Proc. Natl. Acad. Sci. U.S.A.* **102**, 11635 (2005).
- [72] S. Ismail-Beigi and T. A. Arias, *Phys. Rev. Lett.* **82**, 2127 (1999).
- [73] X.-P. Li, R. W. Nunes, and D. Vanderbilt, *Phys. Rev. B* **47**, 10891 (1993).

- [74] R. W. Nunes and D. Vanderbilt, Phys. Rev. B **50**, 17611 (1994).
- [75] R. McWeeny, Rev. Mod. Phys. **32**, 335 (1960).
- [76] A. A. Mostofi, C.-K. Skylaris, P. D. Haynes, and M. C. Payne, Comput. Phys. Commun. **147**, 788 (2002).
- [77] A. A. Mostofi, P. D. Haynes, C.-K. Skylaris, and M. C. Payne, J. Chem. Phys. **119**, 8842 (2003).
- [78] P. D. Haynes, C.-K. Skylaris, A. A. Mostofi, and M. C. Payne, J. Phys.: Condens. Matter **20**, 294207 (2008).
- [79] A. A. Mostofi, *On linear-scaling methods for quantum mechanical first-principles calculations*, PhD thesis, University of Cambridge, 2003.
- [80] Y. Mo, J. Gao, and S. D. Peyerimhoff, J. Chem. Phys. **112**, 5530 (2000).
- [81] H. Umeyama and K. Morokuma, J. Am. Chem. Soc. **99**, 1316 (1977).
- [82] E. D. Glendening, J. Am. Chem. Soc. **118**, 2473 (1996).
- [83] G. K. Schenter and E. D. Glendening, J. Phys. Chem. **100**, 17152 (1996).
- [84] W. Chen and M. S. Gordon, J. Phys. Chem. **100**, 14316 (1996).
- [85] M. v. Hopffgarten and G. Frenking, WIREs Comput. Mol. Sci. **2**, 43 (2012).
- [86] C. S. Brauer, M. B. Craddock, J. Kilian, E. M. Grumstrup, M. C. Orilall, Y. Mo, J. Gao, and K. R. Leopold, J. Phys. Chem. A **110**, 10025 (2006).
- [87] M. Aschi, F. Mazza, and A. D. Nola, J. Mol. Struct. (Theochem) **587**, 177 (2002).
- [88] S. N. Steinmann, C. Corminboeuf, W. Wu, and Y. Mo, J. Phys. Chem. A **115**, 5467 (2011).
- [89] Y. Mo, P. Bao, and J. Gao, Phys. Chem. Chem. Phys. **13**, 6760 (2011).
- [90] A. J. Stone and A. J. Misquitta, Chem. Phys. Lett. **473**, 201 (2009).

- [91] Q. Ban, R. Li, Q. Li, W. Li, and J. Cheng, *Comput. Theor. Chem.* **991**, 88 (2012).
- [92] K. Ansorg, M. Tafipolsky, and B. Engels, *J. Phys. Chem. B* **117**, 10093 (2013).
- [93] C. D. Sherrill, *Acc. Chem. Res.* **46**, 1020 (2013).
- [94] H. Hirao, *J. Phys. Chem. B* **115**, 11278 (2011).
- [95] H. Hirao, *Chem. Lett.* **40**, 1179 (2011).
- [96] D. G. Fedorov and K. Kitaura, *J. Comput. Chem.* **28**, 222 (2007).
- [97] M. D. Esrafil and H. Behzadi, *Mol. Simul.* **39**, 629 (2013).
- [98] R. Bader, *Atoms in Molecules: A Quantum Theory*, Oxford University Press, New York, 1994.
- [99] J. Church, S. Pezeshki, C. Davis, and H. Lin, *J. Phys. Chem. B* **117**, 16029 (2013).
- [100] N. Thellamurege and H. Hirao, *Molecules* **18**, 6782 (2013).
- [101] T. Ziegler and A. Rauk, *Theor. Chem. Acc.* **46**, 1 (1977).
- [102] T. Ziegler and A. Rauk, *Inorg. Chem.* **18**, 1558 (1979).
- [103] T. Ziegler and A. Rauk, *Inorg. Chem.* **18**, 1755 (1979).
- [104] T. Nakano, T. Kaminuma, T. Sato, Y. Akiyama, M. Uebayasi, and K. Kitaura, *Chem. Phys. Lett.* **318**, 614 (2000).
- [105] K. Kitaura, E. Ikeo, T. Asada, T. Nakano, and M. Uebayashi, *Chem. Phys. Lett.* **313**, 701 (1999).
- [106] D. G. Fedorov and K. Kitaura, *Modern Methods for Theoretical Physical Chemistry and Biopolymers*, pages 3–38, Elsevier, Amsterdam, 2006.
- [107] D. G. Fedorov and K. Kitaura, *J. Phys. Chem. A* **111**, 6904 (2007).

- [108] T. Ishikawa, Y. Mochizuki, S. Amari, T. Nakano, H. Tokiwa, S. Tanaka, and K. Tanaka, *Theor. Chem. Acc.* **118**, 937 (2007).
- [109] T. Ishikawa, Y. Mochizuki, S. Amari, T. Nakano, S. Tanaka, and K. Tanaka, *Chem. Phys. Lett.* **463**, 189 (2008).
- [110] Y. Koyama, K. Ueno-Noto, and K. Takano, *Chem. Phys. Lett.* **578**, 144 (2013).
- [111] Y. Koyama, K. Ueno-Noto, and K. Takano, *Comput. Biol. Chem.* **49**, 36 (2014).
- [112] Y. Mochizuki, K. Yamashita, T. Murase, T. Nakano, K. Fukuzawa, K. Takematsu, H. Watanabe, and S. Tanaka, *Chem. Phys. Lett.* **457**, 396 (2008).
- [113] T. Iwata, K. Fukuzawa, K. Nakajima, S. Aida-Hyugaji, Y. Mochizuki, H. Watanabe, and S. Tanaka, *Comput. Biol. Chem.* **32**, 198 (2008).
- [114] K. Takematsu, K. Fukuzawa, K. Omagari, S. Nakajima, K. Nakajima, Y. Mochizuki, T. Nakano, H. Watanabe, and S. Tanaka, *J. Phys. Chem. B* **113**, 4991 (2009).
- [115] Y. Mochizuki, K. Yamashita, K. Fukuzawa, K. Takematsu, H. Watanabe, N. Taguchi, Y. Okiyama, M. Tsuboi, T. Nakano, and S. Tanaka, *Chem. Phys. Lett.* **493**, 346 (2010).
- [116] T. Sawada, T. Hashimoto, H. Nakano, T. Suzuki, H. Ishida, and M. Kiso, *Biochem. Biophys. Res. Comm.* **351**, 40 (2006).
- [117] T. Sawada, T. Hashimoto, H. Nakano, T. Suzuki, Y. Suzuki, Y. Kawaoka, H. Ishida, and M. Kiso, *Biochem. Biophys. Res. Comm.* **355**, 6 (2007).
- [118] T. Sawada, T. Hashimoto, H. Tokiwa, T. Suzuki, H. Nakano, H. Ishida, M. Kiso, and Y. Suzuki, *Glycoconj. J.* **25**, 805 (2008).
- [119] T. Sawada, T. Hashimoto, H. Tokiwa, T. Suzuki, H. Nakano, H. Ishida, M. Kiso, and Y. Suzuki, *J. Mol. Genet. Med.* **3**, 133 (2009).

- [120] T. Sawada, D. G. Fedorov, and K. Kitaura, *J. Phys. Chem. B* **114**, 15700 (2010).
- [121] A. Yoshioka, K. Fukuzawa, Y. Mochizuki, K. Yamashita, T. Nakano, Y. Okiyama, E. Nobusawa, K. Nakajima, and S. Tanaka, *J. Mol. Graphics Modell.* **30**, 110 (2011).
- [122] A. Yoshioka, K. Takematsu, I. Kurisaki, K. Fukuzawa, Y. Mochizuki, T. Nakano, E. Nobusawa, K. Nakajima, and S. Tanaka, *Theor. Chem. Acc.* **130**, 1197 (2011).
- [123] T. Ishikawa, T. Ishikura, and K. Kuwata, *J. Comput. Chem.* **30**, 2594 (2009).
- [124] T. Ishikawa and K. Kuwata, *J. Chem. Theory Comp.* **6**, 538 (2010).
- [125] K. Hasegawa, S. Mohri, and T. Yokoyama, *Prion* **7**, 185 (2013).
- [126] K. Fukuzawa, K. Kitaura, M. Uebayasi, K. Nakata, T. Kaminuma, and T. Nakano, *J. Comput. Chem.* **26**, 1 (2005).
- [127] K. Fukuzawa, Y. Mochizuki, S. Tanaka, K. Kitaura, and T. Nakano, *J. Phys. Chem. B* **110**, 16102 (2006).
- [128] T. Watanabe, Y. Inadomi, K. Fukuzawa, T. Nakano, S. Tanaka, L. Nilsson, and U. Nagashima, *J. Phys. Chem. B* **111**, 9621 (2007).
- [129] K. Yamagishi, K. Yamamoto, S. Yamada, and H. Tokiwa, *Chem. Phys. Lett.* **420**, 465 (2006).
- [130] K. Yamamoto, D. Abe, N. Yoshimoto, M. Choi, K. Yamagishi, H. Tokiwa, M. Shimizu, M. Makishima, and S. Yamada, *J. Med. Chem.* **49**, 1313 (2006).
- [131] S. Motoyoshi, K. Yamagishi, S. Yamada, and H. Tokiwa, *J. Steroid Biochem. Mol. Biol.* **121**, 56 (2010), Proceedings of the 14th Vitamin D Workshop.
- [132] K. Yamagishi, H. Tokiwa, M. Makishima, and S. Yamada, *J. Steroid Biochem. Mol. Biol.* **121**, 63 (2010), Proceedings of the 14th Vitamin D Workshop.

- [133] M. Ito, K. Fukuzawa, Y. Mochizuki, T. Nakano, and S. Tanaka, *J. Phys. Chem. B* **111**, 3525 (2007).
- [134] M. Ito, K. Fukuzawa, Y. Mochizuki, T. Nakano, and S. Tanaka, *J. Phys. Chem. A* **112**, 1986 (2008).
- [135] M. Ito, K. Fukuzawa, T. Ishikawa, Y. Mochizuki, T. Nakano, and S. Tanaka, *J. Phys. Chem. B* **112**, 12081 (2008).
- [136] W. H. James III, E. G. Buchanan, C. W. Müller, J. C. Dean, D. Kosenkov, L. V. Slipchenko, L. Guo, A. G. Reidenbach, S. H. Gellman, and T. S. Zwier, *J. Phys. Chem. A* **115**, 13783 (2011).
- [137] H. Mori and K. Ueno-Noto, *J. Phys. Chem. B* **115**, 4774 (2011).
- [138] M. Bayat, M. von Hopffgarten, S. Salehzadeh, and G. Frenking, *J. Organomet. Chem.* **696**, 2976 (2011).
- [139] M. Bayat, S. Salehzadeh, and G. Frenking, *J. Organomet. Chem.* **697**, 74 (2012).
- [140] A. Marjolin, C. Gourlaouen, C. Clavagura, J.-P. Dognon, and J.-P. Piquemal, *Chem. Phys. Lett.* **563**, 25 (2013).
- [141] P. S. Bagus and F. Illas, *J. Chem. Phys.* **96**, 8962 (1992).
- [142] K. Kitaura and K. Morokuma, *Int. J. Quantum Chem.* **10**, 325 (1976).
- [143] K. Morokuma, *Acc. Chem. Res.* **10**, 294 (1977).
- [144] P. O. Löwdin, *J. Chem. Phys.* **18**, 365 (1950).
- [145] R. Cammi, R. Bonaccorsi, and J. Tomasi, *Theo. Chim. Acta* **68**, 271 (1985).
- [146] M. Gutowski and L. Piela, *Mol. Phys.* **64**, 337 (1988).
- [147] R. F. Frey and E. R. Davidson, *J. Chem. Phys.* **90**, 5555 (1989).
- [148] S. M. Cybulski and S. Scheiner, *Chem. Phys. Lett.* **166**, 57 (1990).

- [149] S. Scheiner, *Hydrogen Bonding: A Theoretical Perspective*, Oxford University Press, Oxford, 1997.
- [150] K. Morokuma and K. Kitaura, *Chemical Applications of Atomic and Molecular Electrostatic Potentials*, page 215, Plenum, New York, 1981.
- [151] A. Michalak, M. Mitoraj, and T. Ziegler, *J. Phys. Chem. A* **112**, 1933 (2008).
- [152] M. Mitoraj and A. Michalak, *Organometallics* **26**, 6576 (2007).
- [153] M. Mitoraj and A. Michalak, *J. Mol. Model.* **13**, 347 (2007).
- [154] M. Mitoraj and A. Michalak, *J. Mol. Model.* **14**, 681 (2008).
- [155] M. P. Mitoraj, A. Michalak, and T. Ziegler, *Organometallics* **28**, 3727 (2009).
- [156] S. Ndambuki and T. Ziegler, *Int. J. Quantum Chem.* **113**, 753 (2013).
- [157] I. Cukrowski, J. H. de Lange, and M. Mitoraj, *J. Phys. Chem. A* **118**, 623 (2014).
- [158] M. P. Mitoraj, *J. Phys. Chem. A* **115**, 14708 (2011).
- [159] M. P. Mitoraj and A. Michalak, *Inorg. Chem.* **50**, 2168 (2011).
- [160] M. A. Celik, C. Dash, V. A. K. Adiraju, A. Das, M. Yousufuddin, G. Frenking, and H. V. R. Dias, *Inorg. Chem.* **52**, 729 (2013).
- [161] A. Das, C. Dash, M. A. Celik, M. Yousufuddin, G. Frenking, and H. V. R. Dias, *Organometallics* **32**, 3135 (2013).
- [162] D. Cappel, S. Tüllmann, A. Krapp, and G. Frenking, *Angew. Chem. Int. Ed.* **44**, 3617 (2005).
- [163] I. Fernandez and G. Frenking, *Chem. Eur. J.* **13**, 5873 (2007).
- [164] I. Fernandez and G. Frenking, *Faraday Discuss.* **135**, 403 (2007).
- [165] G. Frenking, K. Wichmann, N. Fröhlich, C. Loschen, M. Lein, J. Frunzke, and V. M. Rayón, *Coord. Chem. Rev.* **238–239**, 55 (2003), *Theoretical and Computational Chemistry*.

- [166] M. Lein, A. Szabo, A. Kovacs, and G. Frenking, *Faraday Discuss.* **124**, 365 (2003).
- [167] I. Fernandez and G. Frenking, *Open Org. Chem. J.* **5**, 79 (2011).
- [168] J. P. Foster and F. Weinhold, *J. Am. Chem. Soc.* **102**, 7211 (1980).
- [169] A. E. Reed and F. Weinhold, *J. Chem. Phys.* **78**, 4066 (1983).
- [170] A. E. Reed, R. B. Weinstock, and F. Weinhold, *J. Chem. Phys.* **83**, 735 (1985).
- [171] A. E. Reed, F. Weinhold, L. A. Curtiss, and D. J. Pochatko, *J. Chem. Phys.* **84**, 5687 (1986).
- [172] A. E. Reed, L. A. Curtiss, and F. Weinhold, *Chem. Rev.* **88**, 899 (1988).
- [173] E. Francisco, A. Martn Pends, and M. A. Blanco, *J. Chem. Theory Comp.* **2**, 90 (2006).
- [174] A. D. Becke and K. E. Edgecombe, *J. Chem. Phys.* **92**, 5397 (1990).
- [175] A. Savin, R. Nesper, S. Wengert, and T. F. Fässler, *Angew. Chem. Int. Ed. Engl.* **36**, 1808 (1997).
- [176] F. Hirshfeld, *Theor. Chim. Acta* **44**, 129 (1977).
- [177] R. S. Mulliken, *J. Chem. Phys.* **23**, 1833 (1955).
- [178] C. W. Bauschlicher, P. S. Bagus, C. J. Nelin, and B. O. Roos, *J. Chem. Phys.* **85**, 354 (1986).
- [179] K. M. Neyman, P. Strodel, S. P. Ruzankin, N. Schlensog, H. Knözinger, and N. Rösch, *Catal. Lett.* **31**, 273 (1995).
- [180] K. Albert, K. M. Neyman, V. A. Nasluzov, S. P. Ruzankin, C. Yeretian, and N. Rösch, *Chem. Phys. Lett.* **245**, 671 (1995).
- [181] M. S. Gordon, D. G. Fedorov, S. R. Pruitt, and L. V. Slipchenko, *Chem. Rev.* **112**, 632 (2012).

- [182] D. G. Fedorov and K. Kitaura, *The Fragment Molecular Orbital Method: Practical Applications to Large Molecular Systems*, chapter 2, pages 5–36, CRC, Boca Rotan, FL, 2009.
- [183] D. G. Fedorov, J. H. Jensen, R. C. Deka, and K. Kitaura, *J. Phys. Chem. A* **112**, 11808 (2008).
- [184] D. G. Fedorov and K. Kitaura, *J. Phys. Chem. A* **116**, 704 (2012).
- [185] D. G. Fedorov, T. Nagata, and K. Kitaura, *Phys. Chem. Chem. Phys.* **14**, 7562 (2012).
- [186] T. Ishikawa, Y. Mochizuki, T. Nakano, S. Amari, H. Mori, H. Honda, T. Fujita, H. Tokiwa, S. Tanaka, Y. Komeiji, K. Fukuzawa, K. Tanaka, and E. Miyoshi, *Chem. Phys. Lett.* **427**, 159 (2006).
- [187] Y. Okiyama, K. Fukuzawa, H. Yamada, Y. Mochizuki, T. Nakano, and S. Tanaka, *Chem. Phys. Lett.* **509**, 67 (2011).
- [188] J. C. Faver, Z. Zheng, and K. M. Merz, *J. Chem. Phys.* **135**, 144110 (2011).
- [189] R. Z. Khaliullin, M. Head-Gordon, and A. T. Bell, *J. Chem. Phys.* **124**, 204105 (2006).
- [190] E. Gianinetti, M. Raimondi, and E. Tornaghi, *Int. J. Quantum Chem.* **60**, 157 (1996).
- [191] T. Nagata, O. Takahashi, K. Saito, and S. Iwata, *J. Chem. Phys.* **115**, 3553 (2001).
- [192] A. Famulari, E. Gianinetti, M. Raimondi, and M. Sironi, *Int. J. Quantum Chem.* **69**, 151 (1998).
- [193] E. Gianinetti, I. Vandoni, A. Famulari, and M. Raimondi, *Adv. Quantum Chem.* **31**, 251 (1998).
- [194] A. Famulari, R. Specchio, E. Gianinetti, and M. Raimondi, *Valence Bond Theory*, volume 10, page 313, Elsevier, Amsterdam, 2002.

- [195] Y. Mo and S. D. Peyerimhoff, J. Chem. Phys. **109**, 1687 (1998).
- [196] R. Z. Khaliullin, A. T. Bell, and M. Head-Gordon, J. Chem. Phys. **128**, 184112 (2008).
- [197] Y. Mo, L. Song, W. Wu, and Q. Zhang, J. Am. Chem. Soc. **126**, 3974 (2004).
- [198] Y. Mo and J. Gao, J. Phys. Chem. B **110**, 2976 (2006).
- [199] Y. Mo, L. Song, and Y. Lin, J. Phys. Chem. A **111**, 8291 (2007).
- [200] F. Weinhold and C. R. Landis, *Discovering Chemistry With Natural Bond Orbitals*, Wiley, New Jersey, 2012.
- [201] L. D. Jacobson and J. M. Herbert, J. Chem. Phys. **134**, 094118 (2011).
- [202] H. L. Williams and C. F. Chabalowski, J. Phys. Chem. A **105**, 646 (2001).
- [203] A. J. Misquitta, B. Jeziorski, and K. Szalewicz, Phys. Rev. Lett. **91**, 033201 (2003).
- [204] A. Heßelmann and G. Jansen, Chem. Phys. Lett. **367**, 778 (2003).
- [205] A. Heßelmann, G. Jansen, and M. Schütz, J. Chem. Phys. **122**, 014103 (2005).
- [206] A. J. Stone, Chem. Phys. Lett. **211**, 101 (1993).
- [207] H.-J. Gabius, Pharm. Res. **15**, 23 (1998).
- [208] J. Řezáč and P. Hobza, J. Chem. Theory Comp. **8**, 141 (2012).
- [209] S. Grimme, J. Antony, S. Ehrlich, and H. Krieg, J. Chem. Phys. **132**, 154104 (2010).
- [210] P. Jurecka, J. Sponer, J. Cerny, and P. Hobza, Phys. Chem. Chem. Phys. **8**, 1985 (2006).
- [211] J. M. Herbert, L. D. Jacobson, K. Un Lao, and M. A. Rohrdanz, Phys. Chem. Chem. Phys. **14**, 7679 (2012).

- [212] E. D. Isaacs, A. Shukla, P. M. Platzman, D. R. Hamann, B. Barbiellini, and C. A. Tulk, *Phys. Rev. Lett.* **82**, 600 (1999).
- [213] A. Hellemans, *Science* **283**, 614 (1999).
- [214] T. W. Martin and Z. S. Derewenda, *Nat. Struct. Mol. Biol.* **6**, 403 (1999).
- [215] T. K. Ghanty, V. N. Staroverov, P. R. Koren, and E. R. Davidson, *J. Am. Chem. Soc.* **122**, 1210 (2000).
- [216] A. Rashin, I. Topol, G. Tawa, and S. Burt, *Chem. Phys. Lett.* **335**, 327 (2001).
- [217] B. Barbiellini and A. Shukla, *Phys. Rev. B* **66**, 235101 (2002).
- [218] J. F. Beck and Y. Mo, *J. Comput. Chem.* **28**, 455 (2007).
- [219] R. Khaliullin, A. Bell, and M. Head-Gordon, *Chem. Eur. J.* **15**, 851 (2009).
- [220] F. Weinhold and R. A. Klein, *Angew. Chem. Int. Ed.* **53**, 11214 (2014).
- [221] G. Frenking and G. F. Caramori, *Angew. Chem. Int. Ed.* **54**, 2596 (2015).
- [222] F. Weinhold and R. A. Klein, *Angew. Chem. Int. Ed.* **54**, 2600 (2015).
- [223] D. P. Lide, editor, *CRC Handbook of Chemistry and Physics*, pages 10–193 – 10–202, CRC Press, Boca Raton, 90 edition, 2003.
- [224] T. Clark, M. Hennemann, J. Murray, and P. Politzer, *J. Mol. Model.* **13**, 291 (2007).
- [225] K. Kamada, M. Ueda, H. Nagao, K. Tawa, T. Sugino, Y. Shmizu, and K. Ohta, *J. Phys. Chem. A* **104**, 4723 (2000).
- [226] K. E. Calder, R. L. Calvert, P. B. Lukins, and G. L. D. Ritchie, *Aust. J. Chem.* **34**, 1835 (1981).
- [227] F. J. Olivares del Valle, S. Tolosa, J. J. Esperilla, E. A. Ojalvo, and A. Requena, *J. Chem. Phys.* **84**, 5077 (1986).

- [228] T. Korona, B. Jeziorski, and R. Moszynski, *Mol. Phys.* **100**, 1723 (2002).
- [229] T. Korona, B. Jeziorski, and R. Moszynski, *J. Chem. Phys.* **125**, 184109 (2006).
- [230] T. Korona, *Phys. Chem. Chem. Phys.* **9**, 6004 (2007).
- [231] T. Korona and B. Jeziorski, *J. Chem. Phys.* **128**, 144107 (2008).
- [232] T. Korona, *J. Chem. Phys.* **122**, 224104 (2008).
- [233] T. Korona, *Phys. Chem. Chem. Phys.* **10**, 5698 (2008).
- [234] T. Korona, *Phys. Chem. Chem. Phys.* **10**, 6509 (2008).
- [235] T. Korona, *Recent Progress in Coupled Cluster Methods*, chapter Coupled cluster treatment of intramonomer correlation effects in intermolecular interactions, page 267, Springer-Verlag, 2010.
- [236] H. Stoll, G. Wagenblast, and H. Preuß, *Theor. Chim. Acta* **57**, 169 (1980).
- [237] P. R. Horn, Y. Mao, and M. Head-Gordon, *J. Chem. Phys.* **144**, 114107 (2016).
- [238] Q. Wu, *J. Chem. Phys.* **140**, 244109 (2014).
- [239] E. Anderson, Z. Bai, C. Bischof, S. Blackford, J. Demmel, J. Dongarra, J. Du Croz, A. Greenbaum, S. Hammarling, A. McKenney, and D. Sorensen, *LAPACK Users' Guide*, Society for Industrial and Applied Mathematics, Philadelphia, PA, third edition, 1999.
- [240] L. S. Blackford, J. Choi, A. Cleary, E. D'Azevedo, J. Demmel, I. Dhillon, J. Dongarra, S. Hammarling, G. Henry, A. Petitet, K. Stanley, D. Walker, and R. C. Whaley, *ScaLAPACK Users' Guide*, Society for Industrial and Applied Mathematics, Philadelphia, PA, 1997.
- [241] C. A. White, P. Maslen, M. S. Lee, and M. Head-Gordon, *Chem. Phys. Lett.* **276**, 133 (1997).

- [242] S. Grimme, *J. Comput. Chem* **27**, 1787 (2006).
- [243] G. J. Martyna and M. E. Tuckerman, *J. Chem. Phys.* **110**, 2810 (1999).
- [244] N. D. M. Hine, J. Dziedzic, P. D. Haynes, and C.-K. Skylaris, *J. Chem. Phys.* **135**, 204103 (2011).
- [245] P.-O. Åstrand, K. Ruud, K. V. Mikkelsen, and T. Helgaker, *J. Phys. Chem. A* **102**, 7686 (1998).
- [246] J. Cioslowski, *J. Am. Chem. Soc.* **111**, 8333 (1989).
- [247] R. J. Azar, P. R. Horn, E. J. Sundstrom, and M. Head-Gordon, *J. Chem. Phys.* **138**, 084102 (2013).
- [248] P. R. Horn and M. Head-Gordon, *J. Chem. Phys.* **143**, 114111 (2015).
- [249] N. C. Handy, C. W. Murray, and R. D. Amos, *J. Phys. Chem.* **97**, 4392 (1993).
- [250] H. Xiao, J. Tahir-Kheli, and I. William A. Goddard, *J. Phys. Chem. Lett.* **2**, 212 (2011).
- [251] H. M. Berman, J. Westbrook, Z. Feng, G. Gilliland, T. N. Bhat, H. Weissig, I. N. Shindyalov, and P. E. Bourne, *Nucleic Acids Res.* **28**, 235 (2000).
- [252] H. Nar, M. Bauer, A. Schmid, J.-M. Stassen, W. Wienen, H. W. Pripke, I. K. Kauffmann, U. J. Ries, and N. H. Hael, *Structure* **9**, 29 (2001).
- [253] P. Labute, *Proteins* **75**, 187 (2009).
- [254] B. Temelso, K. A. Archer, and G. C. Shields, *J. Phys. Chem. A* **115**, 12034 (2011).
- [255] M. Feyereisen, G. Fitzgerald, and A. Komornicki, *Chem. Phys. Lett.* **208**, 359 (1993).
- [256] D. E. Bernholdt and R. J. Harrison, *Chem. Phys. Lett.* **250**, 477 (1996).
- [257] M. T. Stubbs and W. Bode, *Thromb. Res.* **69**, 1 (1993).

- [258] E. Rühmann, M. Betz, A. Heine, and G. Klebe, *J. Med. Chem.* **58**, 6960 (2015).
- [259] N. H. Hael, H. Nar, H. Priepke, U. Ries, J.-M. Stassen, and W. Wienen, *J. Med. Chem.* **45**, 1757 (2002).
- [260] S. Izadi, B. Aguilar, and A. V. Onufriev, *J. Chem. Theory Comput.* **11**, 4450 (2015).
- [261] H. S. Karkov, B. O. Krogh, J. Woo, S. Parimal, H. Ahmadian, and S. M. Cramer, *Biotechnol. Bioeng.* **112**, 2305 (2015).
- [262] C. Hensen, J. C. Hermann, K. Nam, S. Ma, J. Gao, and H.-D. Höltje, *J. Med. Chem.* **47**, 6673 (2004).
- [263] Y. Mo, G. Subramanian, J. Gao, and D. M. Ferguson, *J. Am. Chem. Soc.* **124**, 4832 (2002).
- [264] B. Baum, L. Muley, A. Heine, M. Smolinski, D. Hangauer, and G. Klebe, *J. Mol. Biol.* **391**, 552 (2009).
- [265] Dziedzic, J., Helal, H. H., Skylaris, C.-K., Mostofi, A. A., and Payne, M. C., *Europhys. Lett.* **95**, 43001 (2011).
- [266] P. Su, H. Liu, and W. Wu, *J. Chem. Phys.* **137** (2012).
- [267] S. Miertuš, E. Scrocco, and J. Tomasi, *Chem. Phys.* **55**, 117 (1981).
- [268] S. Miertuš and J. Tomasi, *Chem. Phys.* **65**, 239 (1982).
- [269] J. Tomasi, B. Mennucci, and R. Cammi, *Chem. Rev.* **105**, 2999 (2005).
- [270] A. Albaugh, H. A. Boateng, R. T. Bradshaw, O. N. Demerdash, J. Dziedzic, Y. Mao, D. T. Margul, J. M. Swails, Q. Zeng, D. A. Case, P. K. Eastman, J. W. Essex, M. Head-Gordon, V. S. Pande, J. W. Ponder, Y. Shao, C.-K. Skylaris, I. T. Todorov, M. E. Tuckerman, and T. Head-Gordon, *J. Phys. Chem. B* (in press).